Evaluation of Long-Term Impacts of Early Opening of Concrete Pavements

NRRA RIGID TEAM

Authors: Lev Khazanovich, Katelyn Kosar, Haoran Li

A pooled fund project administered by the Minnesota Department of Transportation

Report No. NRRA202111

NRRA
National Road Research Alliance

m DEPARTMENT OF TRANSPORTATION

1. Report No. NRRA202111	2.	3. Recipients Accession No.	
4. Title and Subtitle Evaluation of Long-Term Impacts of Early Opening of Concrete Pavements		5. Report Date August 2021	
		6.	
7. Author(s) Lev Khazanovich, Katelyn Kosar, Haoran Li		8. Performing Organization Report No.	
9. Performing Organization Name and Address Department of Civil and Environmental Engineering University of Pittsburgh 3700 O'Hara Street, 703 Benedum Hall Pittsburgh, PA 15261-2294 USA		10. Project/Task/Work Unit No.	
		11. Contract (C) or Grant (G) No. (c) 1003327 (wo) 3	
12. Sponsoring Organization Name and Address Minnesota Department of Transportation Office of Research & Innovation 395 John Ireland Boulevard, MS 330 St. Paul, Minnesota 55155-1899		13. Type of Report and Period Covered Final Report	
		14. Sponsoring Agency Code	
15. Supplementary Notes https://www.mndot.gov/research/reports/2021/NRRA202111.pdf			

16. Abstract (Limit: 250 words)

Due to an increase in demand to shorten construction time as much as possible, the purpose of this project was to determine the optimum strength for concrete pavement before opening it to traffic and without jeopardizing long-term performance. Six test cells in MnDOT's MnROAD project were constructed in 2017 with varying degrees of early loading. Various tests were performed during and immediately following construction and, four years later, ride quality and load transfer efficiency were used to quantify long-term damage. A finite element analysis was then performed using ISLAB2000 to determine the effects of load location and temperature gradient on the Portland cement concrete (PCC) longitudinal stresses to explain the absence of premature failure. A mechanistic-based early opening damage analysis procedure was created to determine the optimum timing for opening of a concrete pavement to traffic. The procedure accounts for the effect of site conditions and pavement characteristics. A web-based tool was developed to facilitate implementation of this procedure.

17. Document Analysis/Descriptors Concrete pavements, Decision making, Strength of materials, Analysis, Pavement performance		18. Availability Statement No restrictions. Document available from: National Technical Information Services, Alexandria, Virginia 22312	
19. Security Class (this report) Unclassified	20. Security Class (this page) Unclassified	21. No. of Pages 190	22. Price

Evaluation of Long-Term Impacts of Early Opening of Concrete Pavements

FINAL REPORT

Prepared by:

Lev Khazanovich
Katelyn Kosar
Haoran Li
Department of Civil Engineering
University of Pittsburgh

August 2021

ACKNOWLEDGMENTS

TABLE OF CONTENTS

LIST OF FIGURES

LIST OF TABLES

LIST OF ABBREVIATIONS

AASHTO: American Association of State Highway and Transportation Officials

DPC: Dry point contact

EPRI: Electric Power Research Institute

ESAL: Equivalent single axle loading

FHWA: Federal Highway Association

FWD: Falling weight deflectometer

HTI: Hilbert transform indicator

IRI: International roughness index

LTE: Load transfer efficiency

MEPDG: Mechanistic-Empirical Pavement Design Guide

PCC: Portland cement concrete

SCM: Supplementary cementitious material

EXECUTIVE SUMMARY

Searching for cost-effective, low-risk solutions to reduce the time a conventional PCC pavement is closed for construction without compromising long-term performance is a popular concern in the pavement industry. Determining the earliest point of opening for a pavement can reduce total construction time and cost, improve driver satisfaction, and reduce the probability of premature pavement failures.

To evaluate the effect of early loading on pavement damage, six test cells were paved on Minnesota Department of Transportation's MnROAD and exposed to varying degrees of early loading by two levels of axle weight. To evaluate effects of early loading on the long-term performance of concrete pavement, the following information was collected for Cells 124-624: concrete maturity, concrete dynamic strains, concrete strains caused by environment, warp and curl measurements, concrete strength and durability, non-destructive testing (MIRA), international roughness index measurement, falling weight deflectometer testing, and petrographic data.

The maturity data was used to determine concrete strength at time of loading using the results of concrete strength and maturity testing performed by American Engineering Testing, Inc. (AET). To enable strength determination of concrete cured under different temperature conditions, concrete maturity was computed at the time of the concrete specimens' compressive and flexural strength testing using the Nurse-Saul method as described in ASTM C 1074. After the cells were subjected to early loading, multiple cores were retrieved by MnROAD personnel and durability testing was conducted by AET, Inc. No reduction of concrete durability due to early loading of Cells 124-424 was detected by this test. It can be observed that for both inside and outside lanes, MIRA testing in the wheel path did not result in low velocity indicating presence of significant damage. An initial comparison of HTI indexes computed from MIRA testing near core locations in the wheel path and between wheel paths was also conducted. It can be observed that wheel path locations did not exhibit HTI higher than HTIs between wheel path locations for the same slabs.

There was no decrease in international roughness index, short or long term, indicating no loss in serviceability from early loading. There was no increase in load transfer efficiency, short or long term, indicating no loss in serviceability from early loading. No visual damage occurred on the surface of the cells, but a petrographic analysis was performed for non-visible damage. According to the results of the petrographic analysis performed by AET, Inc., the overall condition of the six concrete core samples was judged to be good. None of the cores exhibited visual evidence of gross deterioration or large-scale cracking/fracturing. They were fairly well consolidated and purposefully air-entrained with expected signs of age and weathering.

Since the testing slabs at MnROAD did not exhibit any signs of early failure even though they were loaded when the concrete strength was lower than design strength, a finite element analysis was performed to determine the stresses in the Portland cement concrete (PCC). As would be expected, the combination of the positive temperature difference and heavier axle load placed at the slab/shoulder joint causes the highest maximum stress at the bottom PCC surface. Moving this load away from the joint or reducing the temperature difference would decrease the critical PCC stresses. Therefore, to

evaluate the risk of early opening of a concrete pavement to traffic, it is important to estimate the probability of application of the heavy axle load near the critical location with a significant positive temperature gradient.

Potential for slab damage from early opening depends highly on axle weights, wheel path, temperature gradients, and PCC strength at time of load application. The same level of traffic may or may not cause slab damage depending on how favorable conditions are and the loading location. This may be resolved by restricting traffic to lightweight/passenger vehicles and only loading under a small or negative temperature gradient and/or keeping vehicles off the pavement edge. To address this challenge, a probabilistic approach was applied to evaluate the risk of early opening. For each vehicle pass, the procedure predicts critical stresses due to traffic loading and compares it with the corresponding strength. A strength is then calculated based on the random time chosen to open to traffic. If the critical stress is greater than the corresponding strength, then the pass may cause damage and is counted as a failure. Each passing vehicle is simulated separately after which the total failures are summed. This total number of failures is then divided by the number of vehicles to obtain the probability of failure for a single opening of traffic simulation. This analysis is repeated multiple times and the average probability of failure from all simulations is computed. The reliability of the pavement to sustain early opening is then found by subtracting the average probability of failure from 100%.

Damage was considered in terms of transverse cracking and dowel damage. These considerations have similar procedures when determining the stress levels at which a slab would fail in either aspect as well as the reliability for this damage to occur. Both damage criteria will be used when determining the optimal time to open a pavement to traffic.

To implement the damage analysis, a web-based tool was developed for wide use. The tool uses the mechanistic-based early opening damage analysis to analyze the project based on its location, design features, and concrete maturity-strength relationships. It returns cracking performance reliability, dowel performance reliability, and equivalent single axle loads (ESALs) repetition to design strength. These results allow the user to analyze the risks involved with opening to traffic at the chosen maturity, and then if the reliabilities are below the desired level, to choose a better opening maturity value to repeat the analysis.

Chapter 1: INTRODUCTION

Searching for cost-effective, low-risk solutions to reduce the time a conventional Portland cement concrete (PCC) pavement is closed for construction without compromising long-term performance is a popular concern in the pavement industry. Determining the earliest point of opening for a pavement can reduce the total construction time and cost, improve driver satisfaction, and reduce the probability of premature pavement failures.

Increase in the modern commercial and passenger traffic demands minimizing the roadway closure time needed for construction and rehabilitation. One of the ways to achieve this objective is to make "early-opening-to-traffic" possible without unnecessary delays while not jeopardizing long-term pavement performance. The purpose of this project is to identify what strength is appropriate for opening to traffic and methods determining that concrete has achieved the appropriate strength. This brief provides a review of performance concerns, material and construction needs, and agency criteria for the early or rapid opening of rigid pavements to traffic.

The early-opening-to-traffic refers to all concepts that accelerate the timing window between the placement of pavement and its opening to traffic. This includes fast-track construction, which in pavement engineering refers to efforts that result in reduced closure times for construction and rehabilitation (Kohn and Tayabji, 2003). In general, as summarized in Lee et al. (2006), the goal of early-opening-to-traffic is to (1) minimize traffic disruption and road user costs; (2) provide a safe work environment for construction workers and roadway users; and (3) reduce impact on local businesses and the larger environment.

While early-opening-to-traffic methods require careful consideration, they are quite similar to traditional methods and thus are within the immediate reach of all agencies and contractors. Furthermore, early-opening-to-traffic methods can be applied to both low- and high-volume roadways. The use of early-opening-to-traffic requires minor modifications in a range of project planning issues; however, these small changes may result in a significant decrease in roadway closure time. Table 1.1 summarizes project needs and changes in implementing early-opening-to-traffic.

The objectives of this study are to:

- Create an experimental design, preferably a stepwise loading scenario, to replicate and simulate early loading of concrete (new construction and rehabilitation) in a sequence that maximizes and accentuates corresponding quantifiable damage to the concrete pavement
- Determine visible damage as well as intrinsic immediate and long-term damage due to early loading (through sensors and testing)
- Recommend strategies for avoidance, mitigation, or remediation of damage from early loading while evaluating what level of damage is of any consequence

Table 1.1 Sample changes to project activities to shorten concrete pavement construction time (from ACPA,1994)

Project Component	Possible Changes
Planning	• Implement partnering-based project management • Consider night construction and/or schedule extended closures • Use innovative equipment or procedures to expedite construction • Specify more than one concrete mixture for varied strength development • Develop alternate design sections that incorporate thicker slab and stronger base without requiring very high early strength concrete • Provide options to contractors, not step-by-step procedures. • Investigate use of time-of-completion incentives and disincentives
Concrete Materials	• Try different cement types (particularly Type III) • Use helpful admixtures • Use a uniform aggregate grading • Keep water-cement-plus-pozzolan ratio below 0.43
Jointing and Sealing	• Consider use of green sawing with ultra-light saws • Use dry-sa6*wing blades • Use step-cut blades for single pass joint sawing • Use a sealant compatible with high moisture and not sensitive to reservoir cleanliness
Concrete Curing and Temperature	• Specify blanket curing to aid strength gain when ambient temperatures are cool • Monitor concrete temperature and understand relationship of ambient, subgrade, and mixture temperature on strength gain • Elevate concrete temperature before placement
Strength Testing	• Use nondestructive methods to supplement cylinders/beams for strength testing • Use concrete maturity or pulse-velocity testing to predict strength
Opening Criteria	• Allow use of concrete strength criteria without concrete age restrictions • Channel initial traffic loads away from slab edges • Restrict use to automobile traffic during early age period

1.1 PERFORMANCE AND ISSUES

1.1.1 Performance considerations

Strength performance of the paving concrete is a significant consideration for timing the opening of a pavement to traffic. The strength performance targets for both conventional and early-opening-to-traffic projects are:

- the magnitude of strength at a certain time (e.g., 28 days)
- the rate of maturation (i.e., strength gain)

The use of high cement content, low water-cement ratios, accelerating admixtures, and/or high curing temperatures allows for accelerating concrete strength development and for addressing specific early-opening-to-traffic performance concerns. Various performance targets for the strength of high-performance concretes were proposed, including those of the Federal Highway Administration. State agencies have conducted similar work to develop their own performance considerations for early-opening-to-traffic concretes. Performance and criteria for traffic opening are naturally coupled. The sections below summarize the strength criteria.

1.1.2 Performance issues

1.1.2.1 Cracking/fatigue damage

Performance considerations for the timing of opening include the amount of fatigue damage immediately after opening (i.e., the allowable number of load repetitions for the early age pavement) and the effect of early damage on the long-term performance of the pavement (Olek et al., 2002). The possibility of damage resulting from early opening is a major concern. Recent research coupled models for concrete strength performance at early ages with fatigue damage and cracking models from the *AASHTO Mechanistic-Empirical Pavement Design Guide* to predict damage at early ages in rigid pavements and the long-term effects of opening timing (Freeseman et al., 2016). The resulting model is applicable to investigating the effects of opening timings in both early-opening-to-traffic and conventional projects. The model is also capable of analyzing early loading immediately after opening to traffic then looking at long-term performance with just normal traffic loads.

1.1.2.2 Durability

Concretes specifically targeted for early-opening are typically susceptible to durability issues. Because of the use of unconventional materials and/or design in the PCC mix — higher-than-normal cement contents or supplementary cementious materials (SCMs), admixtures, etc. — the microstructure and behavior of early-opening-to-traffic concretes are as different from conventional concretes as are its strength values and rates of maturity. Thus, one should anticipate issues that are associated with durability problems, such as increased shrinkage or a compromised microstructure.

Later sections detail early age behavior and materials/mix design and how these properties of early-opening-to-traffic concretes may affect durability.

1.1.2.3 Dowel looseness

Opening pavements too early to live traffic may be risky because of the possible excessive bearing stresses under dowels that develop due to the application of wheel loads at early ages. These stresses can lead to damage in the concrete surrounding the dowels that is not apparent at the surface yet compromises the load-transfer efficiency of all joints containing compromised dowels. However, a laboratory study of this phenomenon found little evidence of failure in the "compression zone" of paste surrounding the dowel after early age loading (Crovetti and Khazanovich, 2005). Nevertheless, the application of early-opening-to-traffic should emphasize the proper design and construction of joints to ensure adequate joint performance.

1.2 OVERVIEW OF EARLY AGE PAVEMENT BEHAVIOR

The early age behavior of early-opening-to-traffic mixes is often exacerbated by the use of unconventional or unfamiliar materials. Thus, the agency and contractor should closely monitor the early age behavior of the early-opening-to-traffic slab. Early age behavior for early-opening-to-traffic mixes, as with general PCC paving mixes, can be considered in three respects: hydration, maturation, and shrinkage.

1.2.1 Cement hydration/microstructure development

The macrostructure properties of PCC, such as strength and durability, are largely associated with interactions at the microscopic level between cement paste, water, and aggregates. Initially, the concrete mixture contains large voids of water and unhydrated cement; as hydration occurs, and more cement particles interact with water, these voids become incorporated into the larger matrix of hydrated cement paste and aggregates. "Hydrated cement" describes a variety of products of the chemical reaction between water and cement paste: most notably, calcium-silicate-hydrate (C-S-H), calcium hydroxide (CH), and calcium sulfo-aluminates (CSA) (Mehta and Monteiro, 2006; Mindness et al., 2003). The use of increased cement content and SCMs in early-opening-to-traffic mix designs is intended to result in better, faster gains in the development of these hydration products. However, these factors also lead to increased heat of hydration, and thus early age temperatures in early-opening-to-traffic concretes should be closely monitored.
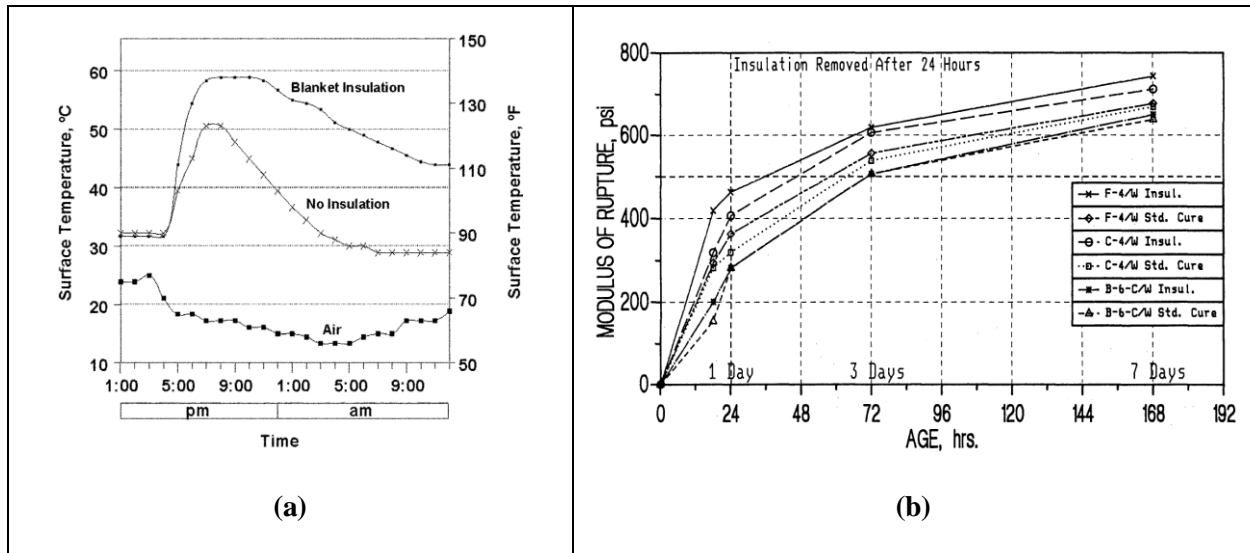
Figure 1.1 Sample (a) early age temperatures in early-opening-to-traffic concretes with and without blanket insulation (from ACI, 2001) and (b) strength gain in early strength concretes by cement type and insulation (from Grove, 1989)

1.2.2 Concrete maturity and strength gain

The hydration of cement depends on both time and temperature. As PCC strength is directly proportional to the level of hydration, strength can be expressed as a function of time and temperature. The relationship between PCC strength, time, and temperature is known as maturity. It has been shown that a very strong correlation exists between strength properties and maturity, thus monitoring of maturity in early-opening-to-traffic concretes is critical (Olek et al., 2002).

1.3 CRITERIA FOR OPENING TO TRAFFIC

1.3.1 Flexural and compressive strength

While opening times previously relied on engineering rules of thumb that could be reduced to arbitrary wait times, modern criteria generally rely on the strength of the concrete (FHWA, 1994; Olek et al., 2002). These criteria are generally either flexural or compressive strengths at certain times after placement. The use of both strength criteria is common given the perceived variability of flexural strength tests, which can be sensitive to test beams and testing procedures. Thus, many agencies' criteria include compressive strength, which is determined using a simpler, consistent test than those used for flexural strength testing.

Since the Federal Highway Administration initiated a demonstration project on accelerated rigid paving techniques in 1988, many states have initiated a concept of early-opening-to-traffic that is used to open a pavement within 12-48 hours (Olek et al., 2002). Table 1.2 illustrates early-opening-to-traffic criteria by state agency. While there is a wide range of criteria, for very early strength (6-8 hour) concretes, a rough minimum compressive strength at opening ranges from 1200 to 3500 psi, whereas a rough

minimum flexural strength (in third-point loading) for these concretes ranges from 260 to 400 psi (Van Dam et al., 2005).

MnDOT allows opening of a new pavement slab to general traffic after one of these three criteria is met (MnDOT Special Provision 2301.3.O):

- 7 days from concrete placement
- concrete reaches 3,000 psi compressive strength
- concrete flexural strength reaches the minimum value provided in Table 1.3.

Roesler et al. (2000) considered early opening from the perspective that flexural fatigue cracking is the main concern with early opening to traffic. Based on a simplified mechanistic-empirical analysis, the study recommended opening flexural strengths for a variety of pavement features (see Table 1.3), concluding that a minimum flexural strength for all pavements was 300 psi.

As noted in the discussion of performance issues, recent research has coupled models for concrete strength performance at early ages with fatigue damage and cracking models from the AASHTO Mechanistic-Empirical Pavement Design Guide (Freeseman et al., 2016). Simulations can be conducted with this model to investigate opening timing criteria in terms of strength for both early-opening-to-traffic projects and conventional paving projects.

There are profound variations from state to state in terms of mix proportioning, as well as in metrics (time and/or strength) and cut-off specification values used as the criteria for opening. At the same time, none of the current methods account for time of construction, design features, early age traffic loading conditions, climate conditions, and other factors that affect early age pavement performance. The existing methods do not quantify the effect of early opening on long-term pavement performance, which limits the engineer's ability to make cost/benefit decisions when determining the opening timing. Also, in some cases it is logistically feasible to allow for limited traffic opening to minimize long-term pavement damage, while also minimizing short-term traffic disruption. For example, none of the criteria rationally distinguish between opening traffic to lightweight (i.e., passenger) vehicle traffic only versus heavy load applications.

Table 1.2 State Highway Agency Specifications (adapted from Van Dam et al., 2005)

State	Mixture Designation	Opening Criterion
AR	Accelerated Strength	>14 MPa (2,000 psi) completed @ 6 hours
	HES	>21 MPa (3,000 psi) completed @ 24 hours
CA	Type FSHCC	>2.8 MPa (400 psi) flexural @ 8 hours
FL	Patching	>21 MPa (3,000 psi) completed @ 24 hours, 6-hour opening
GA	24-Hour Accelerated	>17 MPa (2,500 psi) completed @ 24 hours
IL	Class PP(1)	>22 MPa (3,100 psi) completed > 4.2 MPa (600 psi) flexural @ 48 hours
IN	High Early	>3.8 MPa (550 psi) flexural @ 48 hours

MD	6 hours or 7 hours	>17 MPa (2,500 psi) completed @ 12 hours
	24 hours	>17 MPa (2,500 psi) completed @ 12 hours
MI	Type SLP	>2.0 MPa (290 psi) flexural @ 8 hours
	Type P-MS	>3.5 MPa (500 psi) flexural @ 12 hours
MO	4 hours	>24 MPa (3,500 psi) completed
	24 hours	>24 MPa (3,500 psi) completed
NJ	VHES	>2.4 MPa (350 psi) flexural @ 6.5 hour
NY	Patch	Surface temperature of 65°C (150°F)
OH	Class FS	2.8 MPa (400 psi) flexural @ 4 hours
	Class MS	>2.8 MPa (400 psi) flexural @ 24 hours
PA	Accelerated	8.3 MPa (1,200 psi) completed @ opening, 10 MPa (1,450 psi) completed @ 7 hours
TX	Class K	2.9 MPa (420 psi) flexural @ 24 hours, Open @ 1.8 MPa (260 psi) flexural
	Class K "Modified"	>2.8 MPa (400 psi) flexural @ 24 hours
WI	Special HES	21 MPa (3,000 psi) completed @ 8 hours

Table 1.3 MnDOT Minimum Strength Flexural Strength Requirements

Slab Thickness, in	Flexural Strength, psi
≤ 7	500
7.5	480
8.0	460
8.5	440
9.0	390
≥9.5	350

Table 1.4 Recommended Flexural Strength, psi (MPa), for Opening (Roesler et al., 2000).

Slab Thickness in. (cm)	Foundation Support psi/in (kPa/cm)	Modulus of Rupture for Opening, psi (Mpa), to support estimated ESALs Repetitions to Specified Strength				
		100	500	1000	2000	5000
8 (20.3)	100 (271)	370 (2.55)	410 (2.83)	430 (2.96)	450 (3.10)	470 (3.24)
	200 (543)	310 (2.14)	340 (2.34)	350 (2.41)	370 (2.55)	390 (2.69)
	500 (1357)	300 (2.07)	300 (2.07)	300 (2.07)	300 (2.07)	310 (2.14)
8.5 (21.6)	100 (271)	340 (2.34)	370 (2.55)	380 (2.62)	400 (2.76)	430 (2.96)
	200 (543)	300 (2.07)	300 (2.07)	320 (2.21)	330 (2.28)	350 (2.41)
	500 (1357)	300 (2.07)	300 (2.07)	300 (2.07)	300 (2.07)	300 (2.07)
9 (22.9)	100 (271)	300 (2.07)	300 (2.07)	320 (2.21)	260 (2.48)	390 (2.69)
	200 (543)	300 (2.07)	300 (2.07)	300 (2.07)	300 (2.07)	320 (2.21)
	500 (1357)	300 (2.07)	300 (2.07)	300 (2.07)	300 (2.07)	300 (2.07)
9.5 (24.1)	100 (271)	300 (2.07)	300 (2.07)	300 (2.07)	330 (2.28)	350 (2.41)
	200 (543)	300 (2.07)	300 (2.07)	300 (2.07)	300 (2.07)	300 (2.07)
	500 (1357)	300 (2.07)	300 (2.07)	300 (2.07)	300 (2.07)	300 (2.07)
10 (25.4)	100 (271)	300 (2.07)	300 (2.07)	300 (2.07)	300 (2.07)	320 (2.21)
	200 (543)	300 (2.07)	300 (2.07)	300 (2.07)	300 (2.07)	300 (2.07)
	500 (1357)	300 (2.07)	300 (2.07)	300 (2.07)	300 (2.07)	300 (2.07)
10.5 (26.7)	100 (271)	300 (2.07)	300 (2.07)	300 (2.07)	300 (2.07)	300 (2.07)
	200 (543)	300 (2.07)	300 (2.07)	300 (2.07)	300 (2.07)	300 (2.07)
	500 (1357)	300 (2.07)	300 (2.07)	300 (2.07)	300 (2.07)	300 (2.07)

1.3.2 Maturity

The use of maturity as an opening timing criterion is uncommon, given the possibility of on-site changes to the job mix to address unforeseen difficulties (climatic conditions, workability, etc.). However, with adequate maturity testing in the laboratory using the job mix, a criterion can be developed that can be used to time opening to traffic based on maturity testing on-site. Figure 1.2 illustrates how the maturity concept can be transferred from the lab to the jobsite to be used as a basis for an opening criterion for either conventional or early-opening-to-traffic projects.
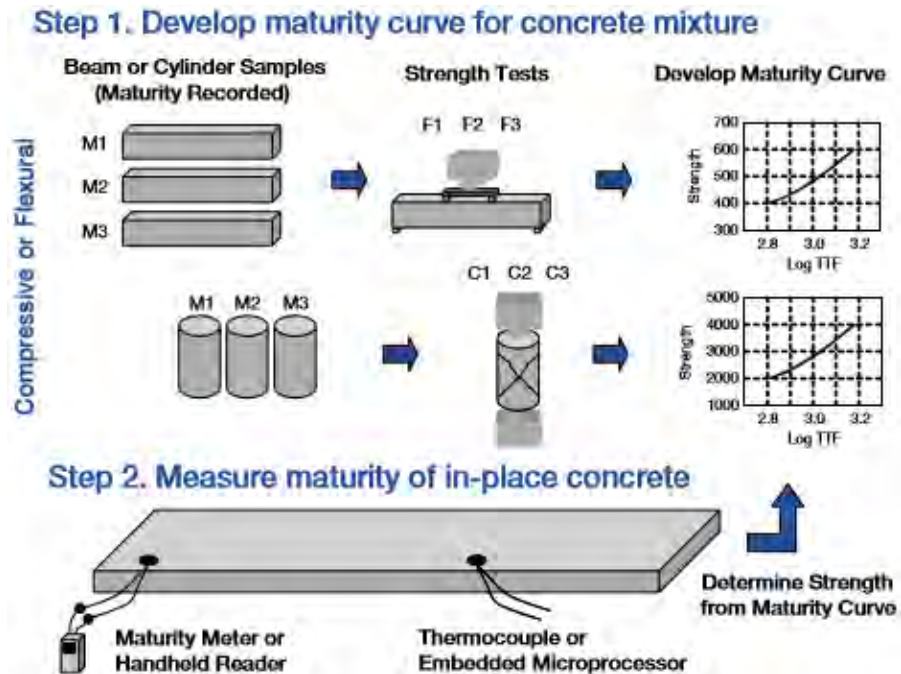
Figure 1.2 Moving from the laboratory to the field in the development of a maturity criterion (from ACPA, 2016)

1.4 TESTING

Testing of early-opening-to-traffic concrete specimens ensures that minimum strength levels are achieved in planned mix designs. In addition, in-situ tests save time and money and also reduce the efforts required in core extraction for testing representative samples from the in-situ slabs.

1.4.1 Flexural and compressive strength

The compressive strength test on cylindrical specimens, described in AASHTO T 22, is the most common strength test performed on early-opening-to-traffic concretes. The flexural strength test is often used in concert with compressive strength testing (AASHTO T 97 or AASHTO T 177). While flexural strength provides a more direct estimation of the structural resistance to failure, flexural strength testing specimens are more difficult to properly prepare, thus higher variability in flexural strength testing is observed. Regardless of the specific strength test adopted, strength testing is important for the mix design and later for construction monitoring.

1.4.2 Non-destructive testing

1.4.2.1 Maturity

Strength-maturity relationships established for a given early-opening-to-traffic mix can be used during construction to monitor strength development prior to opening. Maturity testing (ASTM C 1074) is valuable for construction monitoring, as conventional strength testing for early-opening-to-traffic projects is often not possible due to the narrow time window (Olek et al., 2002). Thorough laboratory

testing, using the actual job mix materials, is necessary before applying concrete maturity testing in the field. Field maturity evaluation then uses thermocouples along the project; placement of the thermocouples should include critical areas for joint sawing and opening to traffic. By taking readings at regular intervals with maturity meters or temperature recorders, the temperature-time relationship from preparatory laboratory work can be used to infer strength development (ACPA, 1994; ACI, 2001).

1.4.2.2   Pulse velocity

Pulse-velocity testing (ASTM C 597) also requires advance laboratory work prior to construction for reliable estimates of strength development. As with the preparatory work for maturity testing, lab batches must contain the job mix materials in the same proportions as used on-site. Relationships between pulse velocity readings and specimens with known strength (determined using traditional strength tests) can be used to monitor early strength development in the field given frequent field pulse-velocity testing (ACI, 2001).

1.4.2.3   Ultrasonic tomography

In addition to pulse velocity tests, other non-destructive tests such as ultrasonic tomography, can be used to quickly assess strength in concrete. These evaluations correlate shear wave velocity with Young's modulus, which in turn can be related to strength (Freeseman et al., 2016). Figure 1.3 presents flexural strength and seismic elastic moduli versus age obtained from laboratory testing of a typical MnDOT concrete mix. As expected, both flexural strength and elastic moduli increase with time. Notably, although this concrete is not specifically designed for early traffic opening, the beams exhibited flexural strength greater than 300 psi and 400 psi after two and three days, respectively.
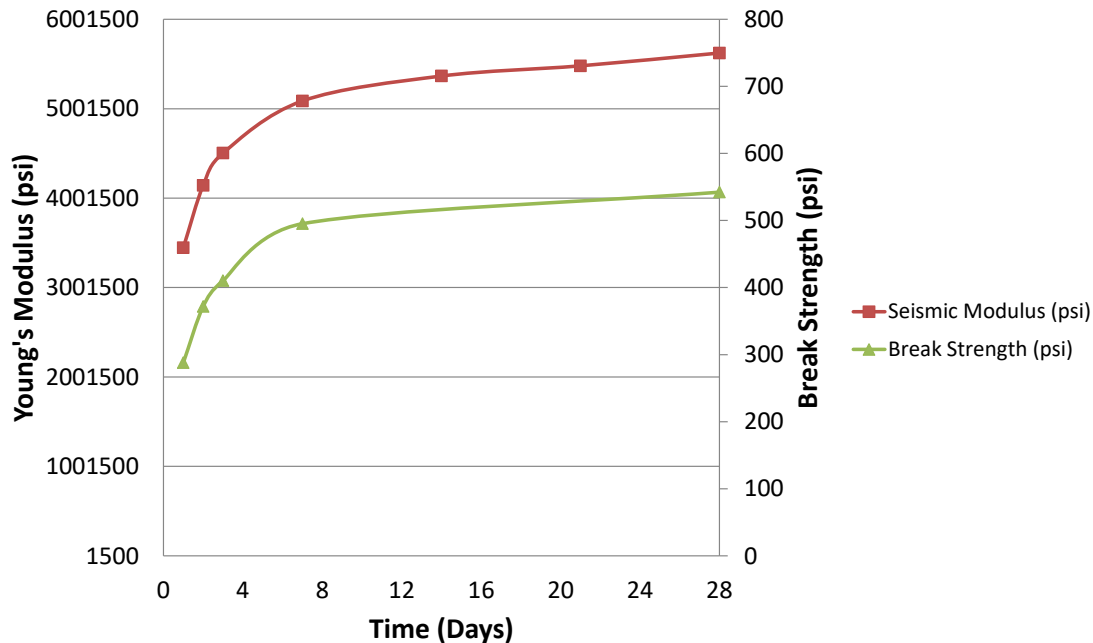
Figure 1.3 Small strain Young's modulus and strength development showed similar trends (Freeseman et al., 2016)

1.5   EARLY AGE FATIGUE DAMAGE ANALYSIS

Freeseman et al. (2016) re-examined the effect of early opening on pavement damage through a laboratory study and analytical modeling. The study developed a mechanistic-based procedure for evaluating the effect of early traffic opening on long-term damage accumulation, while accounting for critical factors such as climate, traffic level, and pavement design characteristics. The basis of this method is a modification of the *Mechanistic-Empirical Pavement Design Guide* (MEPDG) fatigue damage analysis to analyze traffic loading on the first 28 days of pavement life (AASHTO, 2015). The procedure provides the potential to update predictions based on as-built nondestructive testing measurements of the pavement.

The output of the analysis is a quantitative damage prediction that allows the road owner to do a cost/benefit analysis of the opening timing based on specific site and traffic characteristics. Providing the predicted effect of the potential opening decisions also allows for using the analysis as part of a larger cost-benefit evaluation, which is not possible with the current criteria. Although the procedure is tailored for Minnesota paving conditions, it can be adapted to meet the needs of other paving conditions. Also, the model allows for input of as-built conditions, which provides an opportunity to update damage predictions as nondestructive testing or other pavement performance measures become available. The method developed in this research provides an alternative to the rigidity of current methods and allows for the damage associated with chosen opening times to be predicted based on the inputted traffic and climate conditions.

Chapter 2: LABORATORY AND FIELD TESTING

2.1   CELL SPECIFICATIONS

To evaluate the effect of early loading on pavement damage, six test cells, with a total distance of 565 feet were constructed on MnROAD's low volume road in July 2017 (Figure 2.1). The length of cells varies slightly; Cells 124, 224, 324, 424, 524, and 624 are lengths 120, 120, 130, 115, 60, and 20 feet, respectively. Paving started from east to west, where Cell 624 was paved first and Cell 124 last. The cells were designed as 6 inch thick concrete slabs with 1 inch diameter dowels and sawed, non-skewed joints established at 15-foot intervals. The dense graded aggregate base is 6 in thick. The as-constructed PCC thickness measured by MITSCAN-T2 varied from 5.8 to 6.6 in (Table 2.2).
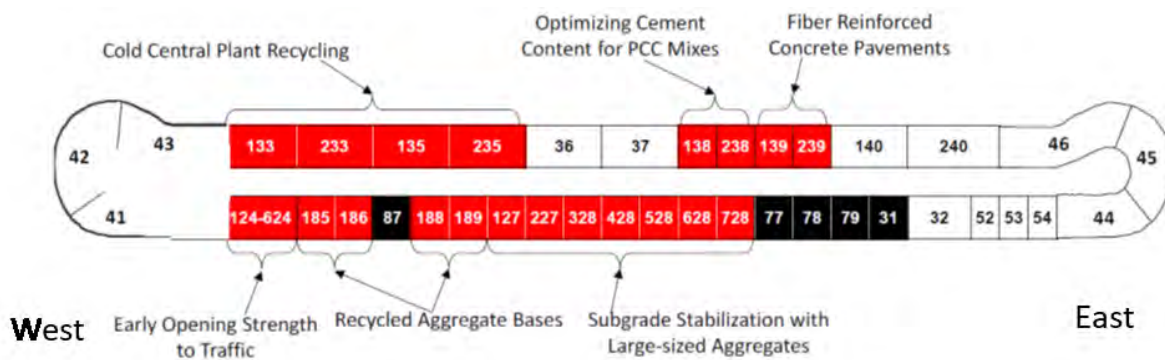
Figure 2.1 MnROAD Low Volume Road (LVR) NRRA sections (from Van Deusen 2017)

124 - 624

6 in. PCC
15 ft joints
24 ft width
1.0 in. dowels

6 in. Class 6
agg base

Sand subgrade
(existing)
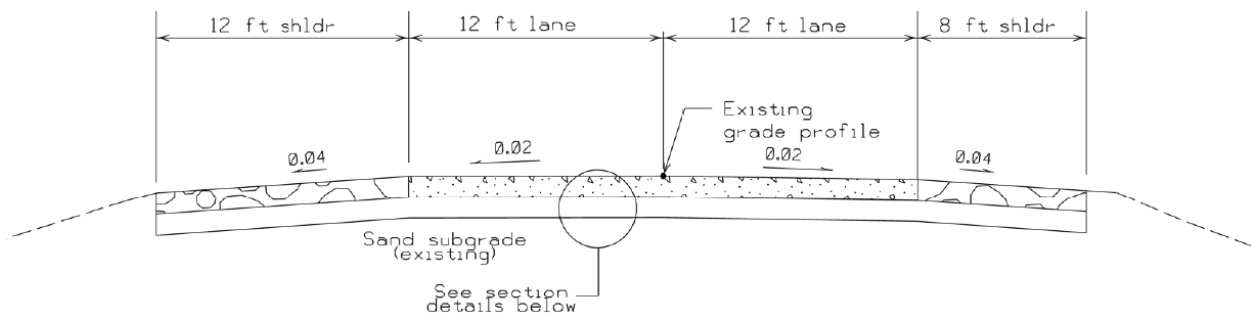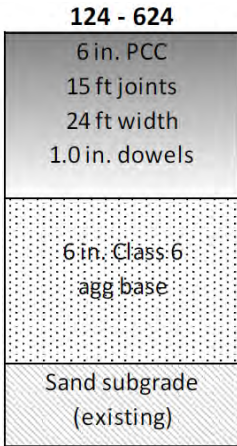
Figure 2.2 Concrete pavement section design for the early opening experiment (Cells 124-624) (from Van Deusen 2017)

Table 2.1 Lengths of cells

Cell	Length, ft
124	120
224	120
324	130
424	115
524	60
624	20

Table 2.2 As-built pavement thickness data – Cells 124-624 (Van Deusen 2017)

Cell	Station	Lane	Offset (ft)	Thickness (in)
124	15850	Outside	10	6.5
124	15850	Inside	-10	6.3
224	15950	Outside	10	6.1
224	15950	Inside	-10	5.8
224	16050	Outside	10	-
224	16050	Inside	-10	5.9
324	16150	Outside	10	6.1
324	16150	Inside	-10	6.1
424	16250	Outside	10	6.4
424	16250	Inside	-10	6.0
524	16350	Outside	10	6.6
524	16350	Inside	-10	6.5

2.2 STRENGTH MEASUREMENTS

Concrete strength and maturity testing was performed by American Engineering Testing, Inc. (AET). AET cast a set of various concrete test specimens using the same concrete mix design as the one used for MnROAD Cells 124-624. Compressive and flexural testing was conducted 6 hours, 12 hours, 1 day, 2 days, 3 days, 4 days, 5 days, and 7 days after the specimens were cast. The temperature of concrete specimens during curing varied between 23 and 30 °C. To enable strength determination of concrete cured under different temperature conditions, AET computed concrete maturity at the time of concrete specimens testing using the Nurse-Saul method as described in ASTM C 1074:

$$TTF = \sum (T_c - T_0)\Delta t \qquad (1)$$

where *TTF* is the time-temperature factor at age *t*, degree-hours, used as the maturity index in this study, Δt is time interval, hours, T_c is the average concrete temperature during time interval, Δt, °C, and T_0 is datum temperature assumed to be equal 0 °C.

Figure 2.3 shows development of compressive and flexural strengths for various maturity levels. This data was used to calibrate relationships between concrete strength and maturity using following functional form:

$$Strength = A\,ln(TTF) - B \qquad (2)$$

where A and B are regression coefficients.

Trendlines and corresponding predictive equations are also shown in Figure 2.3.
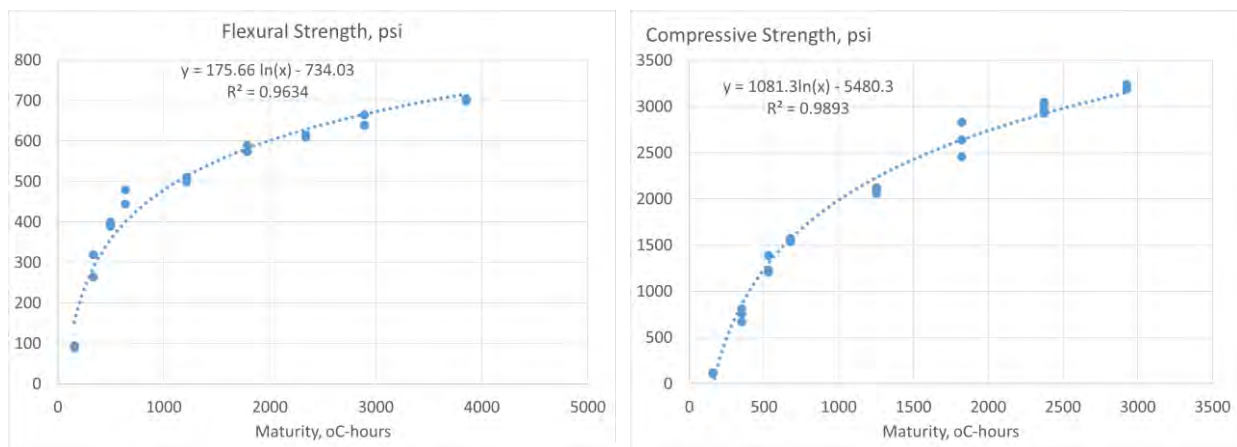
Figure 2.3 Predicted verses measured flexural (left) and compressive (right) strength gain as PCC matures

2.3 EARLY LOADING OF MNROAD CELLS

Shortly after paving, the inside lane of Cells 124-242 was loaded by an unloaded 31,000-lb MnDOT snowplow truck and the outside lane was loaded by a ¾-ton pickup truck. A load application contains one forward and one backward pass with the loading vehicles as shown by the black and white arrows in Figure 2.4. Cells 124, 224, 324, and 424 received 8, 6, 4, and 2 load passes, respectively.

The strength-maturity curves presented above were used to determine concrete strength at the time of loading. The first loading of Cell 124 was conducted when the maturity reached 100°-hr, approximately 3 hours after paving, when the flexural strength was estimated to be just 73 psi. The final loading, which was performed on Cells 124-424, was performed when the maturity reached 400°-hr, approximately 10 hours after paving, when the flexural strength was approximately 318 psi. Loading sequences with corresponding maturity and flexural strengths are shown in Table 2.3.

Cell 524 served as a control slab and was not loaded on the first day. Cell 624 was loaded by a ¾-ton pickup truck traversing the slab approximately 2 hours after paving while the PCC was still plastic (Figure 2.5). This was done to study the impact that visible ruts impart when drivers erroneously drive on freshly placed concrete. The remaining cells did not show any visible damage after early loading. Since the summer of 2017, all sections have been loaded with approximately 10,000 ESALs per year.
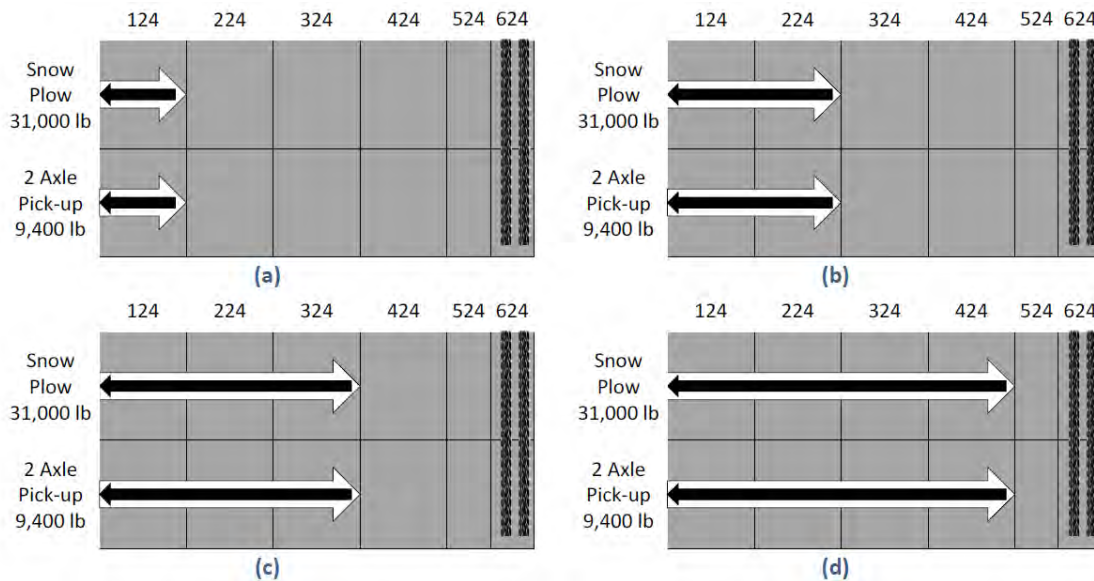
Figure 2.4 Primary loading scheme for early loading

Table 2.3 Loading sequencing for each maturity level.

Cell x24 Early Loading Sequence		
Maturity (Deg-Hr)	Flexural Strength (psi)	Load applied to lanes
100	73	1st load on Cell 124 (forward and back)
200	196	1st load on Cell 224, 2nd load on Cell 124

| 300 | 267 | 1st load on Cell 324, 2nd load on Cell 224, 3rd load on Cell 324 |
| 400 | 318 | 1st load on Cell 424, 2nd load on Cell 324, 3rd load on Cell 224, 4th load on Cell 124 |

Cell 624 was loaded by a ¾-ton, 2-axle pickup truck traversing across the plastic pavement approximately 2 hours after paving (to induce visible damage) as shown in Figure 2.5.

Figure 2.5 Damage in Cell 624 due to early loading

To evaluate effects of early loading on the long-term performance of concrete pavement, the following information had been collected for Cells 124-624:

- Concrete maturity
- Concrete dynamic strains
- Concrete strains caused by environment
- Warp and curl measurements
- Concrete strength and durability
- Non-destructive testing (MIRA)
- International roughness index measurement
- FWD testing
- Petrographic data

Chapter 3: STRAIN GAUGE DATA ANALYSIS

Eight dynamic strain sensors were installed in each of Cells 124 to 424 according to the sensor layout shown in Figure 3.1. Each sensor is labeled as X24CE00Y where X is 1, 2, 3, or 4 for cells 124, 224, 324, and 424, respectively, and Y is numbers 1 to 8. For each location, a top surface sensor is installed 0.5 to 1 in below the PCC slab surface and a bottom surface censor is installed 0.5 to 1 in above the PCC slab bottom. Top sensors installed are labeled with an odd Y, while bottom sensors are labeled with an even Y. Table 3.1 shows locations and orientations of the sensors. Environmental sensors were also placed near the slabs and recorded continuously days 2 through 6.
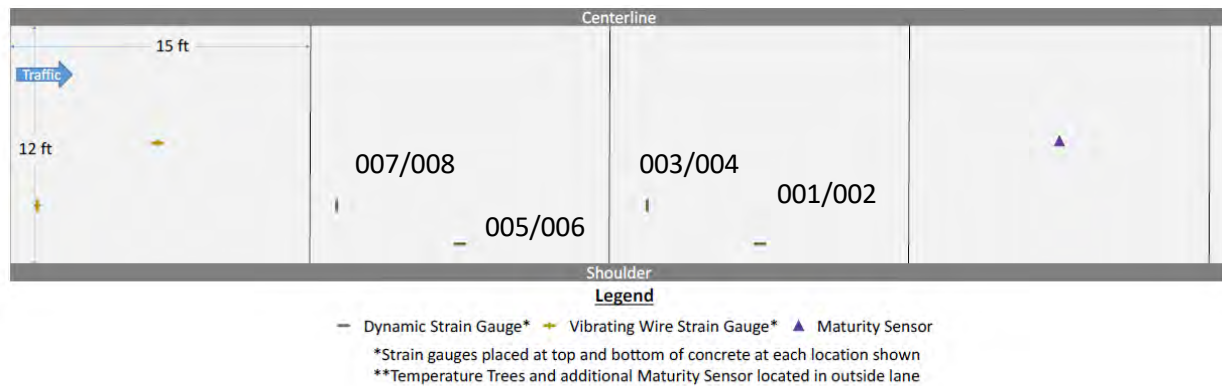
Figure 3.1 Dynamic Strain Gauges layout for Cell 124, 224, 324, and 424

Table 3.1 Locations and orientations of dynamic strain gauges

Location	Orientation	Top Surface	Bottom Surface
Center-slab, lane/shoulder joint	Longitudinal	X24CE001	X24CE002
Wheel path, transverse joint	Transverse	X24CE003	X24CE004
Center-slab, lane/shoulder joint	Longitudinal	X24CE005	X24CE006
Wheel path, transverse joint	Transverse	X24CE007	X24CE008

The dynamic strain gauges recorded strains induced in the concrete slabs by each truck loading; ¾ ton, 2 axle truck for the outer lane and an unloaded snow truck for the interior lane. The readings were taken with a frequency of 120 measurements per 0.1 seconds for 20 seconds in which the truck was passing. Figure 3.2 shows an example of the recorded strain history from sensor 124CE004 taken at the time of the third loading, shown in Figure 3.1. The computed moving average from fifty consecutive readings is also reported on this figure. It can be observed a presence of a distinct peak in recoded strains. A significant fluctuation in readings before and after the time of wheel passage indicates the presence of significant noise in the data, but the amplitude of the noise is less than the amplitude of the peak measured strain. However, this pattern was not observed for all sensors in this study.

Figure 3.3 shows an example of micro strain time histories for sensors 124CE001 and 124CE002. It can be observed that amplitude of peak for sensor 124CE002 is only moderately greater than amplitude of noise, while the time series for sensor 124CE001 does not exhibit any distinct peak. This example illustrates the challenges with the analysis of strain gauge data:

- Extraction of strains induced by wheel loading from a noisy signal may not be straightforward.
- Quality of data from some strain gauges may be poor. It is important to flag and remove unreliable data from the analysis.
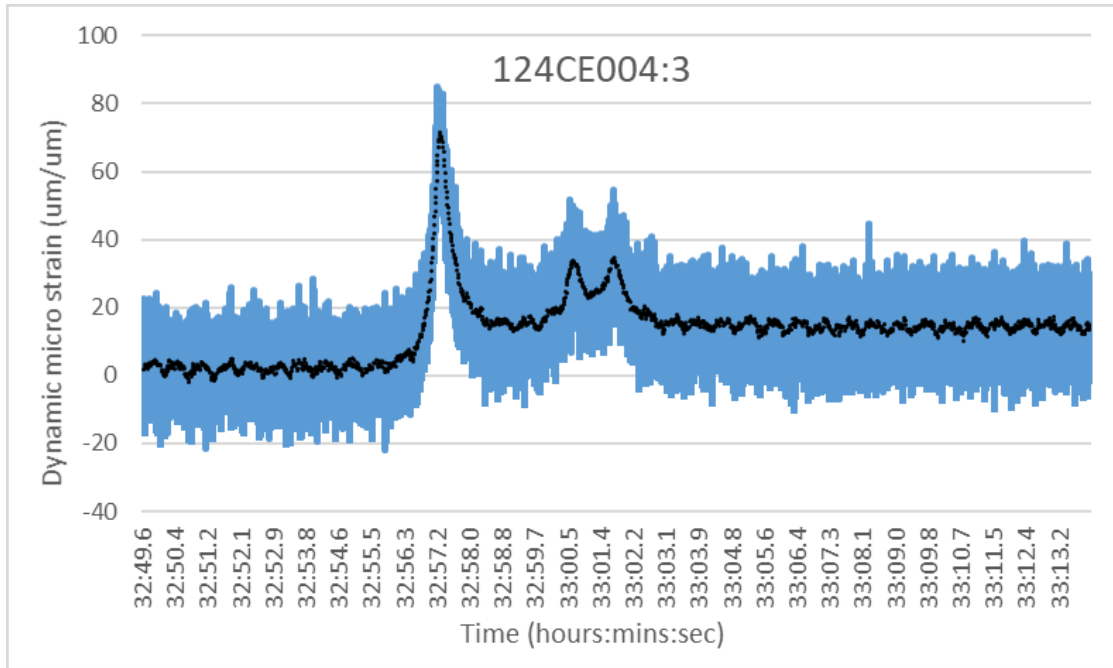
Figure 3.2 Strain time history from sensor 124CE004, loading 3 by the snow plow truck
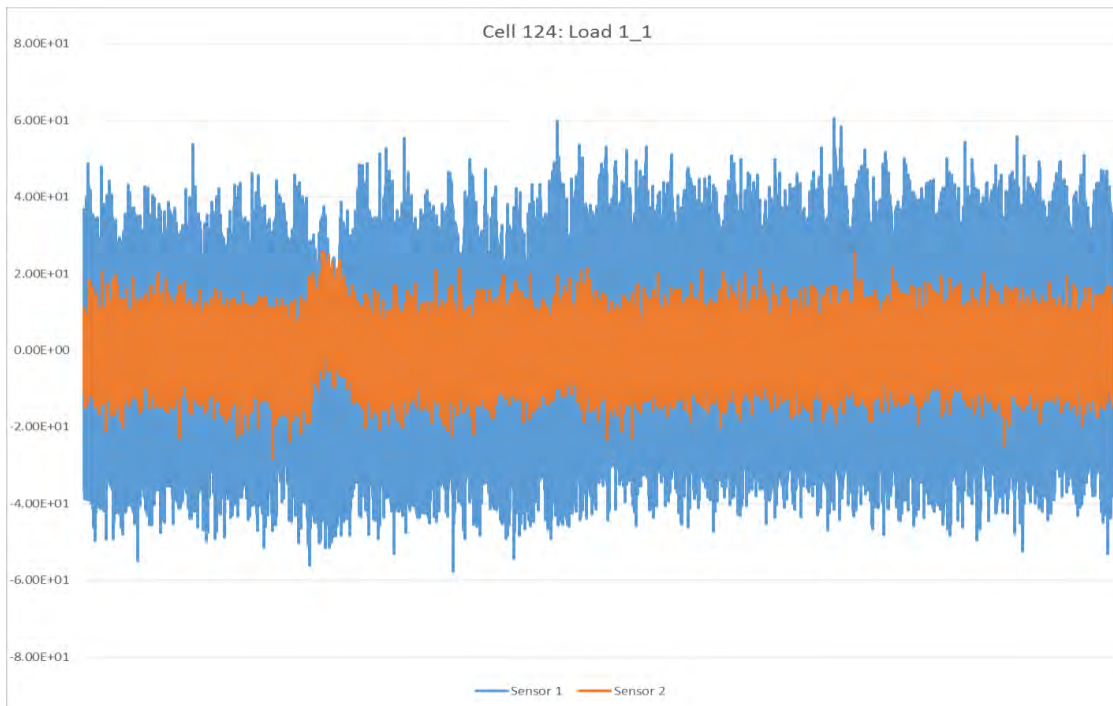
Figure 3.3 Reading from sensors 124CE001 and 124CE002, first loading by the snow plow truck

3.1 ESTIMATION OF THE WHEEL-INDUCED STRAINS

If the wheel load passes in close vicinity of the sensor, it will cause a significant deviation from strain state in the absence of the wheel loading. Therefore, maximum and the minimum values of the reading may be associated with the effect of axle loading. However, presence of noise in data may lead to misleading results. Figure 3.4 shows an example of the spike in data overshadowing the correct maximum signal. To reduce the effect of random noise, the moving average trendlines were evaluated for each sensor and loadings. Approximate timings of maximum moving average strains occurrence were determined for even sensors (sensors located near the bottom PCC surface) and minimum moving average strains for the odd sensors (sensors located near the top PCC surface). Subsequently, maximum or minimum values of the measured strains were determined.

As observed above, strain gauges do not exhibit constant zero readings in the absence of wheel loading. Therefore, to estimate wheel-induced strains, it is important to adjust measured strain gauge responses. It requires establishing the base line for each sensor for each loading, by using the reading value corresponding to a reading in an absence of load-induced strains.

In this study, it was assumed that the median value of the strain readings for the entire twenty seconds of reading corresponds to the strain gauge base line. The median is the value separating the higher half from the lower half of a data sample. It is much less sensitive to presence of outlier readings and short-term deviations caused by wheel loading. The following procedure was used for evaluation of the effect of axle loading on concrete strains:

- For each sensor time history, median and standard deviation values for each loading were determined. The resulting values are reported in Appendix A.
- The median value was subtracted from the maximum value to estimate maximum strain, and the medium value was subtracted from the minimum value to estimate minimum strain.

Table 3.2 presents the results of this analysis for sensor 124CE004. It can be observed that adjusting maximum and minimum values for the base line level may significantly change the estimate of strains induced by wheel loading.
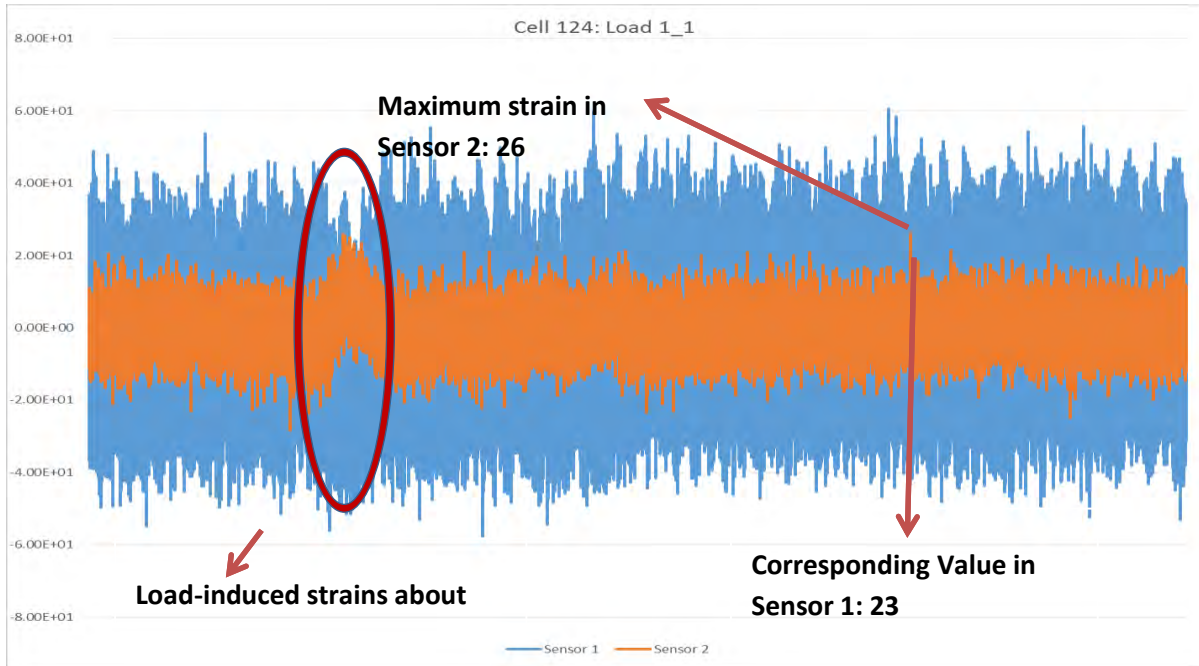
Figure 3.4 Example of data noise leading to erroneous maximum reading

Table 3.2 Estimation of wheel-induced strains for sensor 124CE004

Loading	Maturity, °C-hr	Load direction	Maximum, micro strain	Median, micro strain	Maximum-median, micro strain
1	100	Forward	109	42	67
		Back	134	46	88
2	200	Forward	85	13	72
		Back	N/A	N/A	N/A
3	300	Forward	53	2	51
		Back	54	3	51
4	400	Forward	71	17	54
		Back	71	18	53

3.2   DATA QUALITY ASSESSMENT

As discussed above, some sensors exhibited significant noise in the data. To quantify noise level, standard deviations for strain time histories were evalauted. Based on the review of strain gauge data, strain gauge time histories with standard deviations greater than 80 micro strains were flagged as unreliable measurements and were removed from subsequent analysis. The following time histories were flagged:

- Sensor 124CE001, loadings 4_1 and 4_2
- Sensor 324CE001, loadings 3_1, 3_2, 4_1 and 4_2
- Sensor 224CE003, loadings 3_1, 3_2, 4_1 and 4_2
- Sensor 324CE003, loadings 3_1, 3_2, 4_1 and 4_2
- Sensor 324CE006, loadings 3_1, 3_2, 4_1 and 4_2
- Sensor 124CE007, loadings 3_1, 3_2, 4_1 and 4_2

- Sensor 224CE003, loading 4_2

Figure 3.5 shows the time history from strain gauge 124CE007 from the second loading pass. The standard deviation for this time measurement is 33.1 micro strains, which is lower than the threshold level of 80 micro strains. A distinct minimum in measured strains corresponds to the minimum in the moving average of strain measurements indicating high quality data. Figure 3.6 shows a time history from sensor 124CE001, loading 4 (back). The standard deviation for this measurement is 116 micro strains, greater than 80 micro strains. It can be observed that the measurements have no distinct peak that can be attributed to the passage of the heavy axle load. Therefore, this measurement was removed from the analysis.
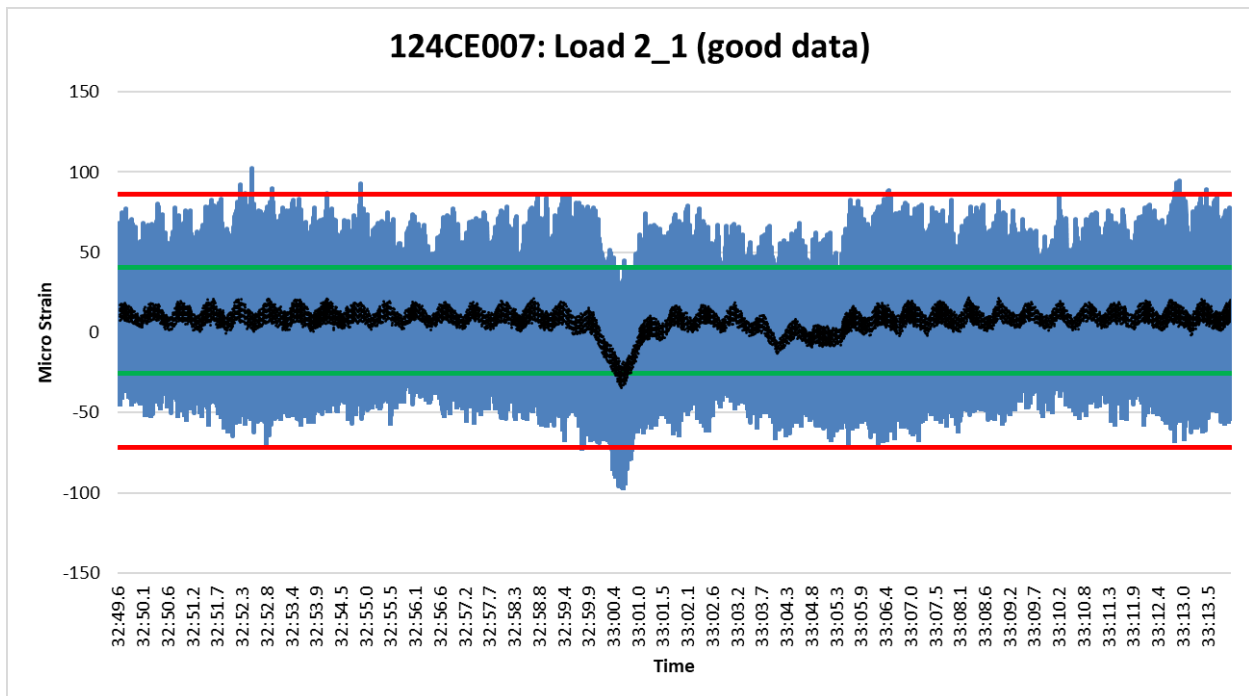
Figure 3.5 Strain time history for strain gauge 124CE007, load 2, forward pass.
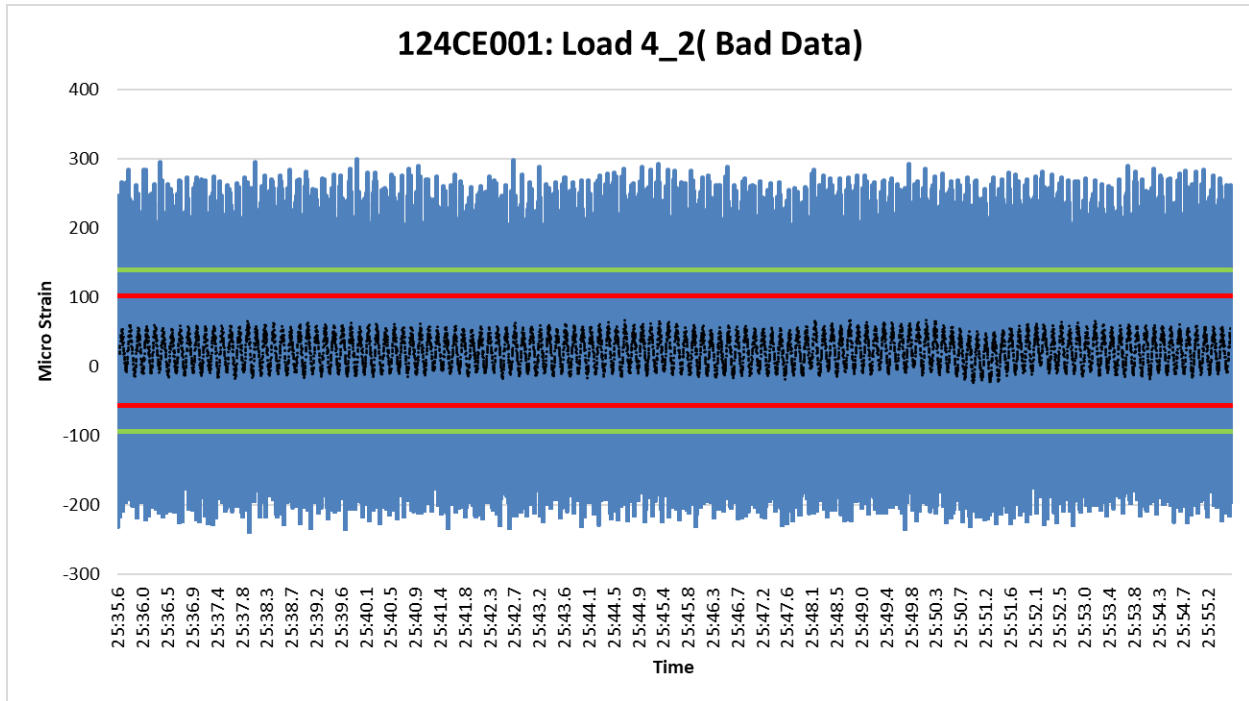
Figure 3.6 Strain time history for strain gauge 124CE001, load 5, back pass.

3.3   PEAK TO PEAK PROGRAM

Peak to Peak is a program utilized by MnDOT to identify critical peaks in a data set. This program was used to find the precise times the vehicle was over the sensor and the corresponding dynamic strain. Figure 3.7 shows an initial early loading of a cell and highlights three peaks marked by black points. Figure 3.8 is another graph example of a later loading date that finds five peaks. Peak values are

obtained by subtracting the baseline, indicated by the first white point, from the peak values. This sum is plotted and used in dynamic strain analysis.
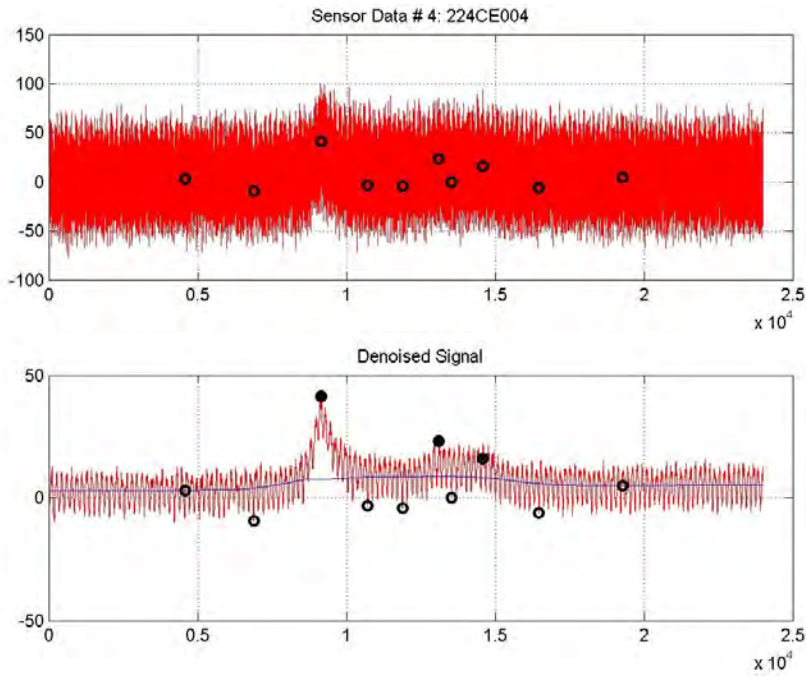
Figure 3.7 Cell 224, Run 5, Sensor 004, dynamic strain data for June 5, 2017
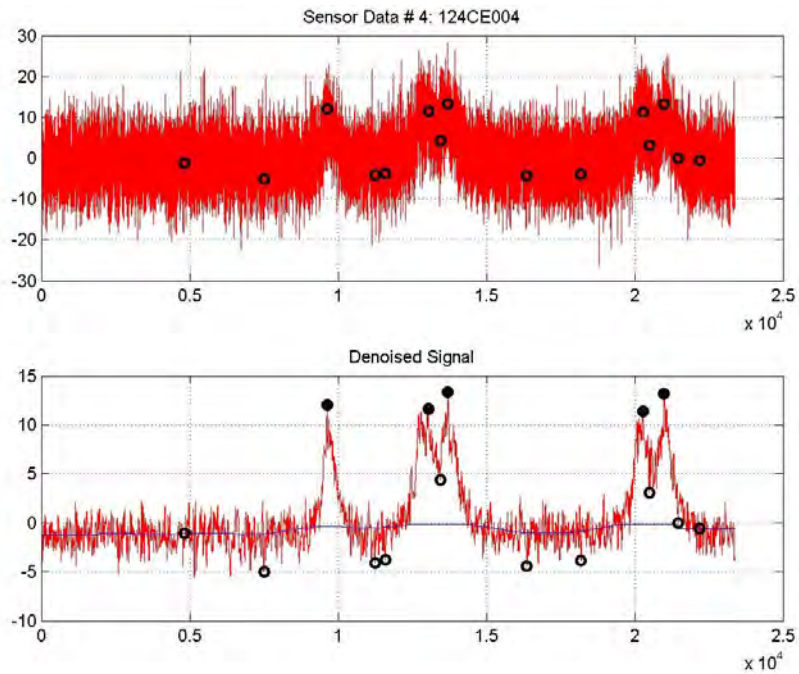
Figure 3.8 Cell 124, Run 1, Sensor 004, dynamic strain data for November 2017
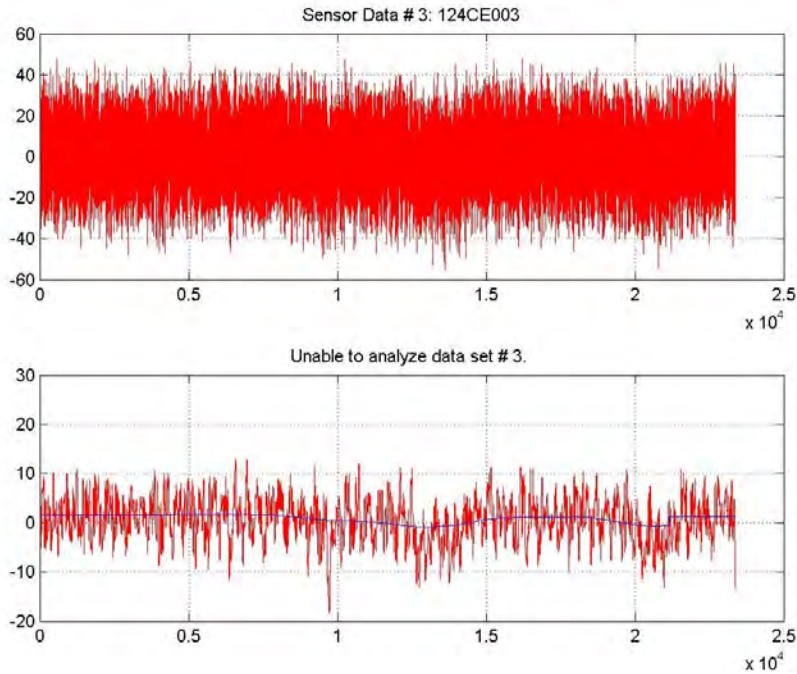
Figure 3.9 Cell 124, Run 1, Sensor 003, dynamic strain data for November 2017

The Peak to Peak program is not always able to identify peaks within the data, for example, Figure 3.9. The following sensors were identified by Peak to Peak as inconclusive:

- June 5, 2017
    - Sensor 124001, 003,
    - Sensor 224002
    - Sensor 324001, 003, 006
    - Sensor 424002
- November 2017
    - Sensor 124003
    - Sensor 324001, 002, 003, 004, 005, 006, 007, 008
    - Sensor 424002
- March 2018
    - Sensor 124003
    - Sensor 324001, 002, 003, 004, 005, 006, 007, 008
    - Sensor 424002, 006
- July 2018
    - Sensor 124001, 002, 003, 004, 005, 007, 008
    - Sensor 224001, 003, 004, 005, 007, 008
    - Sensor 324001, 002, 003, 004, 005, 006, 007, 008
    - Sensor 424001, 002, 003, 005, 006, 007, 008
- October 2018
    - Sensor 124001, 002, 003, 004, 005, 006, 007
    - Sensor 324001, 002, 003, 004, 005, 006, 007. 008
    - Sensor 424001, 002, 003, 005, 006, 007, 008

Previous analysis in used a moving average program in Excel to determine the peak positions. Many of the peaks identified with that method were similar to peaks found with the Peak to Peak program. The primary difference was Peak to Peak was able to identify smaller peaks that were previously lost in the surrounding noise.

3.4   REAL-TIME DYNAMIC STRAIN PEAK ANALYSIS

Cells 124 – 424 were loaded at different amounts and maturities with Cell 124 being loaded earliest and four times over several hours and Cell 424 was loaded latest and only once. Cells 224 and 324 being the increments in between the two extremes. During this loading, dynamic strain data was collected to understand the different strains that an immature concrete may experience. Figure 3.10 and Figure 3.11 show the dynamic strain peaks that occurred in each cell while the early loading was performed. Figure 3.10 shows sensors 1, 2, 5, and 6 near the pavement shoulder while Figure 3.11 shows sensors 3, 4, 7, and 8 near the pavement joint.
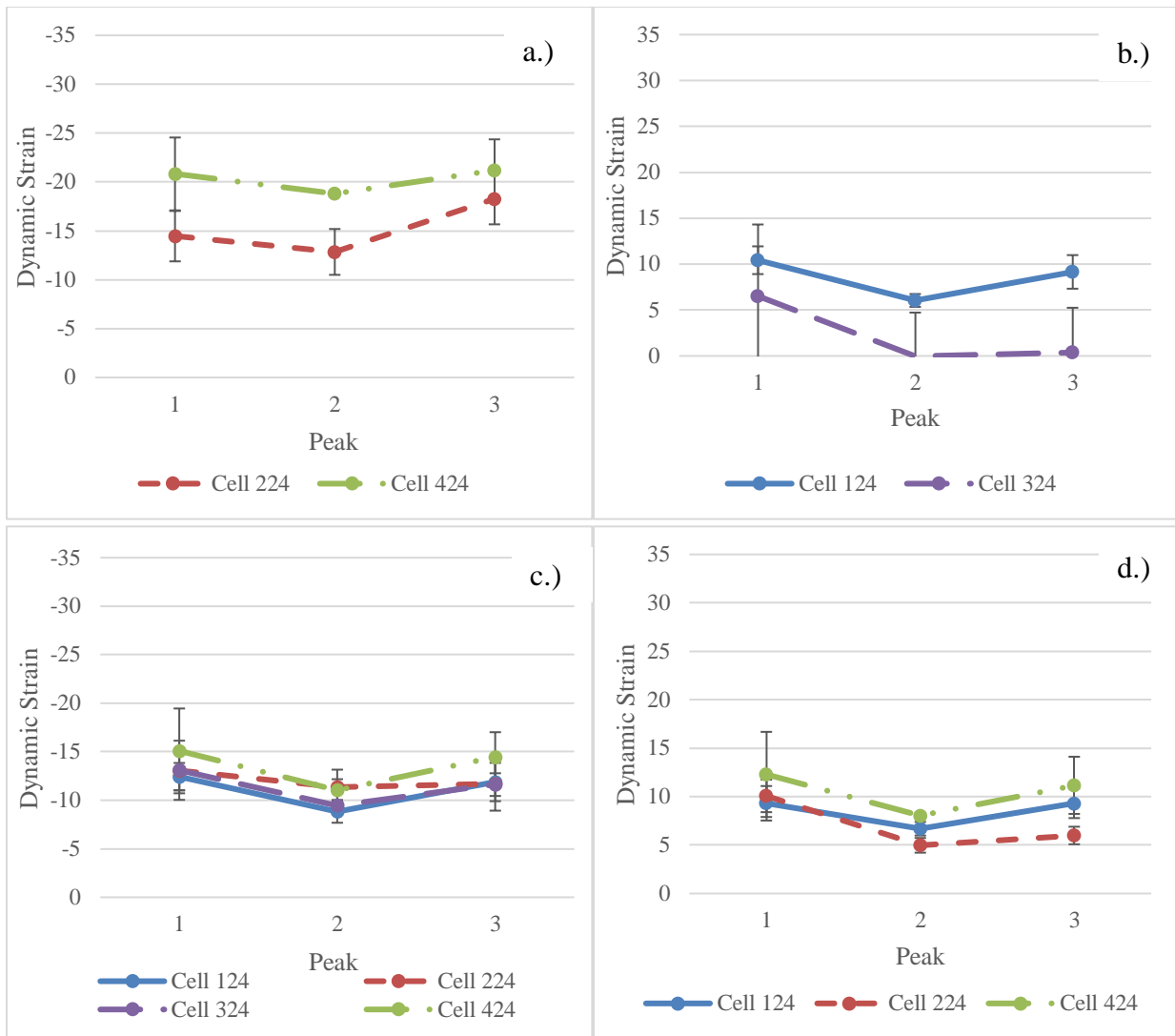
Figure 3.10 Real-time dynamic strain peaks for the longitudinal sensors near shoulder on June 5, 2017: a.) Sensor 1, b.) Sensor 2, c.) Sensor 5, and d.) Sensor 6
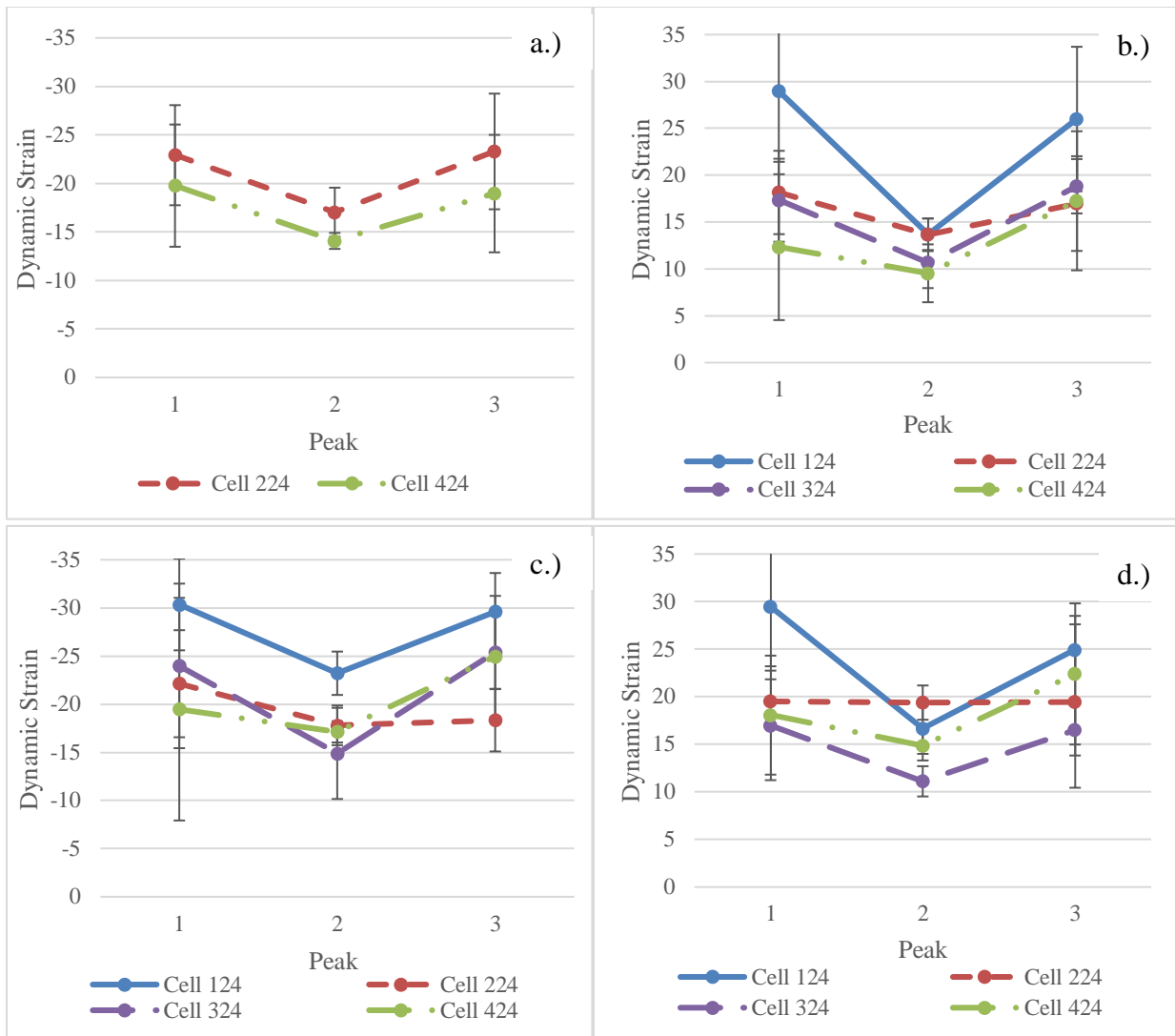
Figure 3.11 Real-time dynamic strain peaks for sensors near joint on June 5, 2017: a.) Sensor 3, b.) Sensor 4, c.) Sensor 7, and d.) Sensor 8

3.5   LONG-TERM DYNAMIC STRAIN ANALYSIS

Long-term data collection was done four more times over the course of a year: November 2017, March 2018, July 2018, and October 2018. This analysis will help predict premature failure due to excessive strains from an early opening. Data was collected by driving a snow-truck over the cells in several runs and was analyzed using the Peak to Peak program. Figure 3.12 and Figure 3.13 show the peaks identified by the program for each sensor in November 2017, approximately five months after paving. The other

data collected on is shown in Appendix D. Each sensor collects a lower dynamic strain than in the real-time loading, most likely from the pavement having additional time to cure.
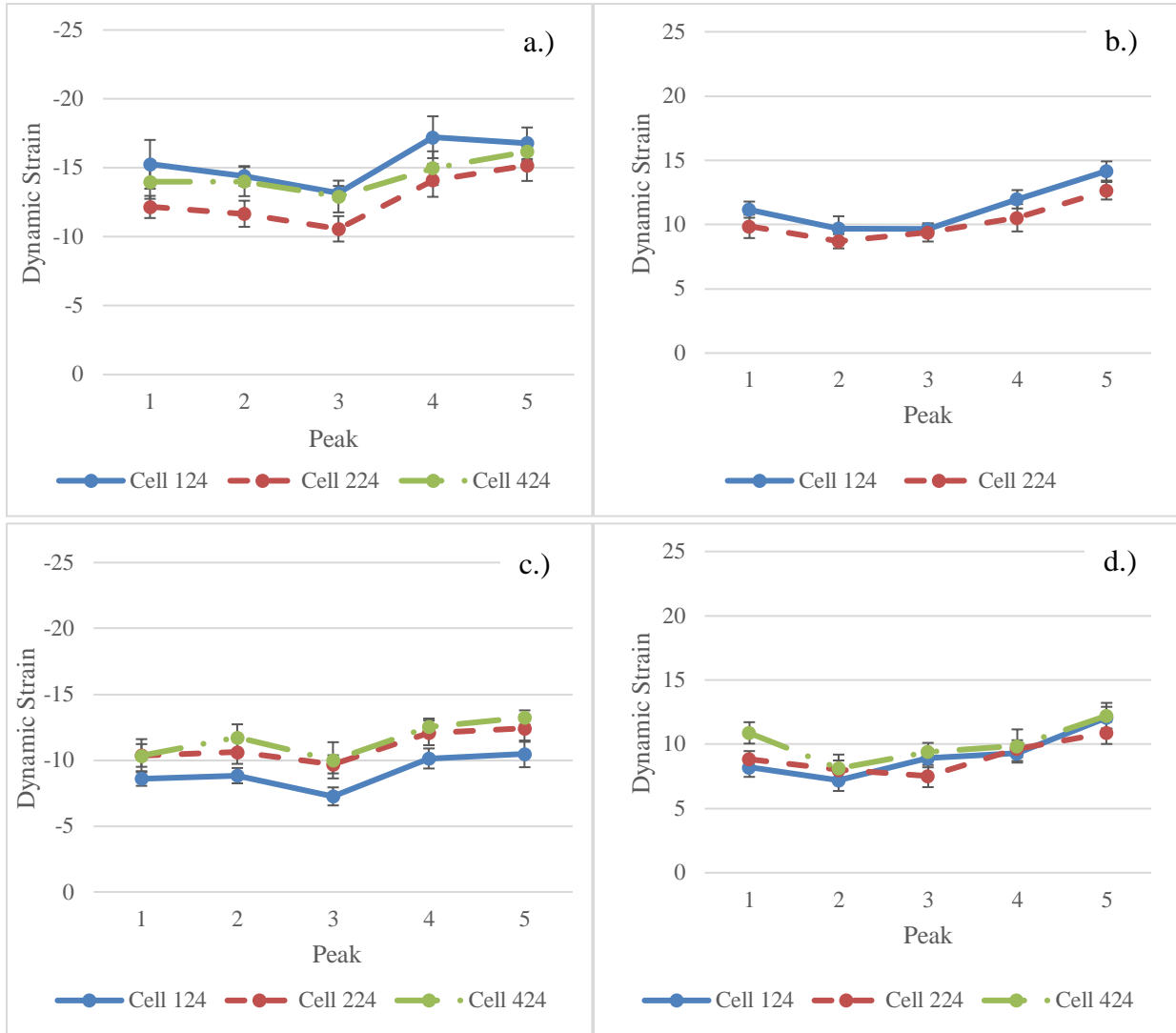
Figure 3.12 Dynamic strain peaks for the longitudinal sensors near shoulder on November 2017: a.) Sensor 1, b.) Sensor 2, c.) Sensor 5, and d.) Sensor 6
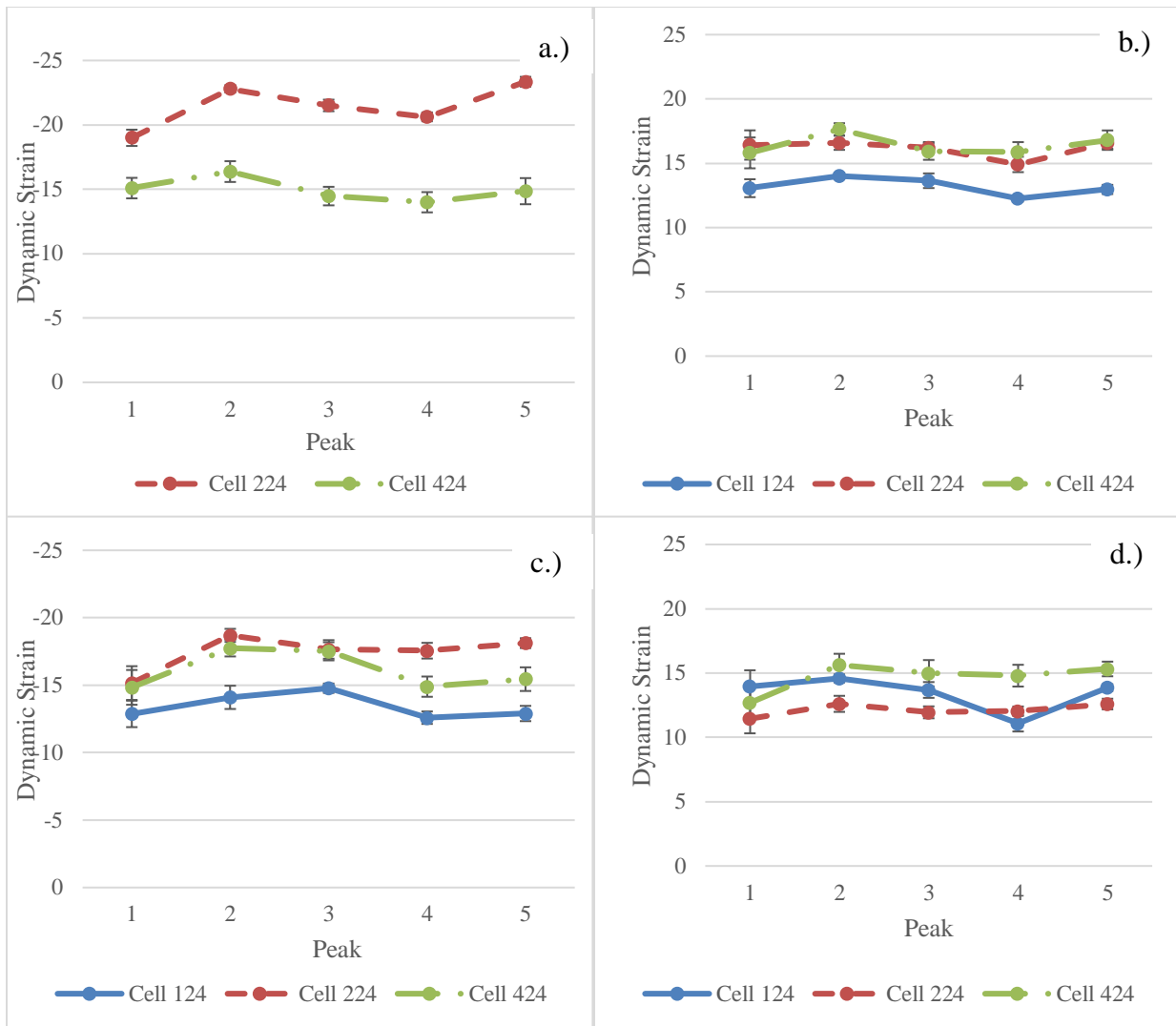
Figure 3.13 Dynamic strain peaks for sensors near joint on November 2017: a.) Sensor 3, b.) Sensor 4, c.) Sensor 7, and d.) Sensor 8

Chapter 4: COMPARISON OF MEASURED STRAINS

4.1   STATIC STRAIN GAUGE DATA ANALYSIS

Static strains are caused by environmental changes around the pavement, for example, temperature and moisture content. Concrete pavements are particularly susceptible to environmental changes and excessive fluctuations can accelerate cracking. Strain data was collected every second between the hours of 6:30 – 8:00 a.m. over the course of five days (July 6 to July 10). No loading is done on the pavement during this time. Figure 4.1, Figure 4.2, Figure 4.3, and Figure 4.4 show the strains collected over the allotted time. Cell 124 experiences the most fluctuation in strains but most cells experienced approximately 900.
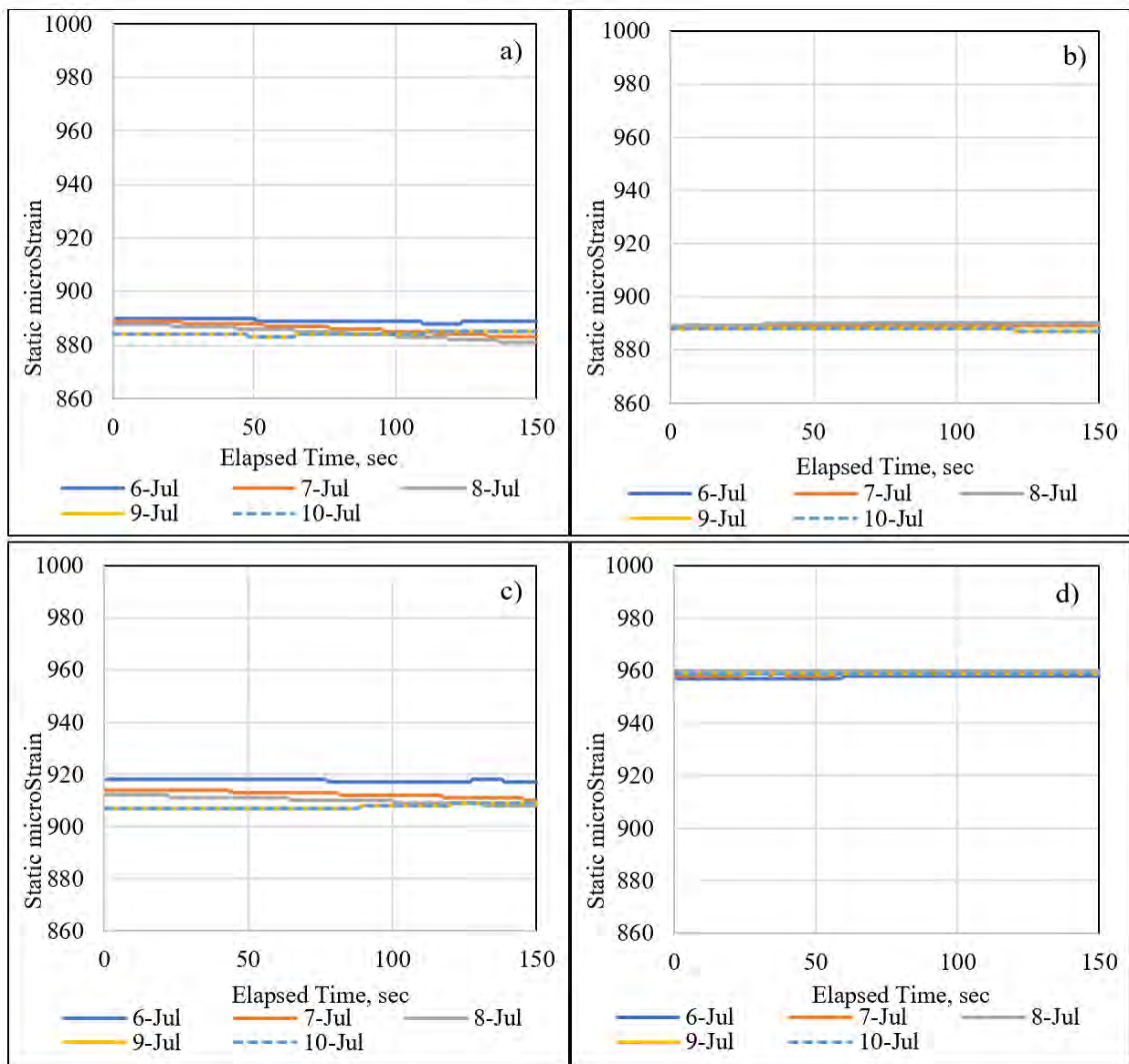
Figure 4.1 Static strain data for Cell 124 a) Sensor 001, b) Sensor 002, c) Sensor 003, and d) Sensor 004

30
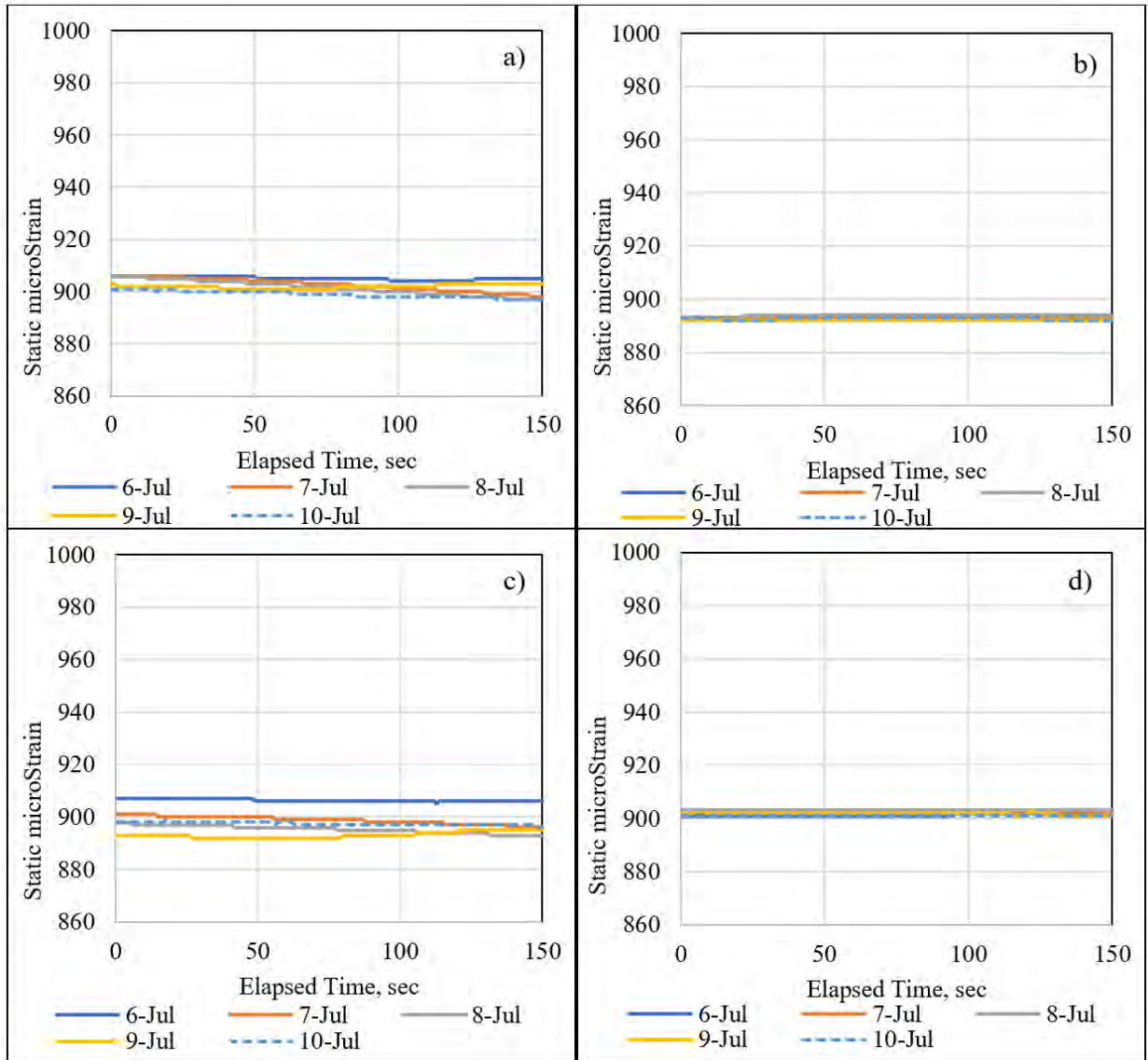
Figure 4.2 Static strain data for Cell 224 a) Sensor 001, b) Sensor 002, c) Sensor 003, and d) Sensor 004
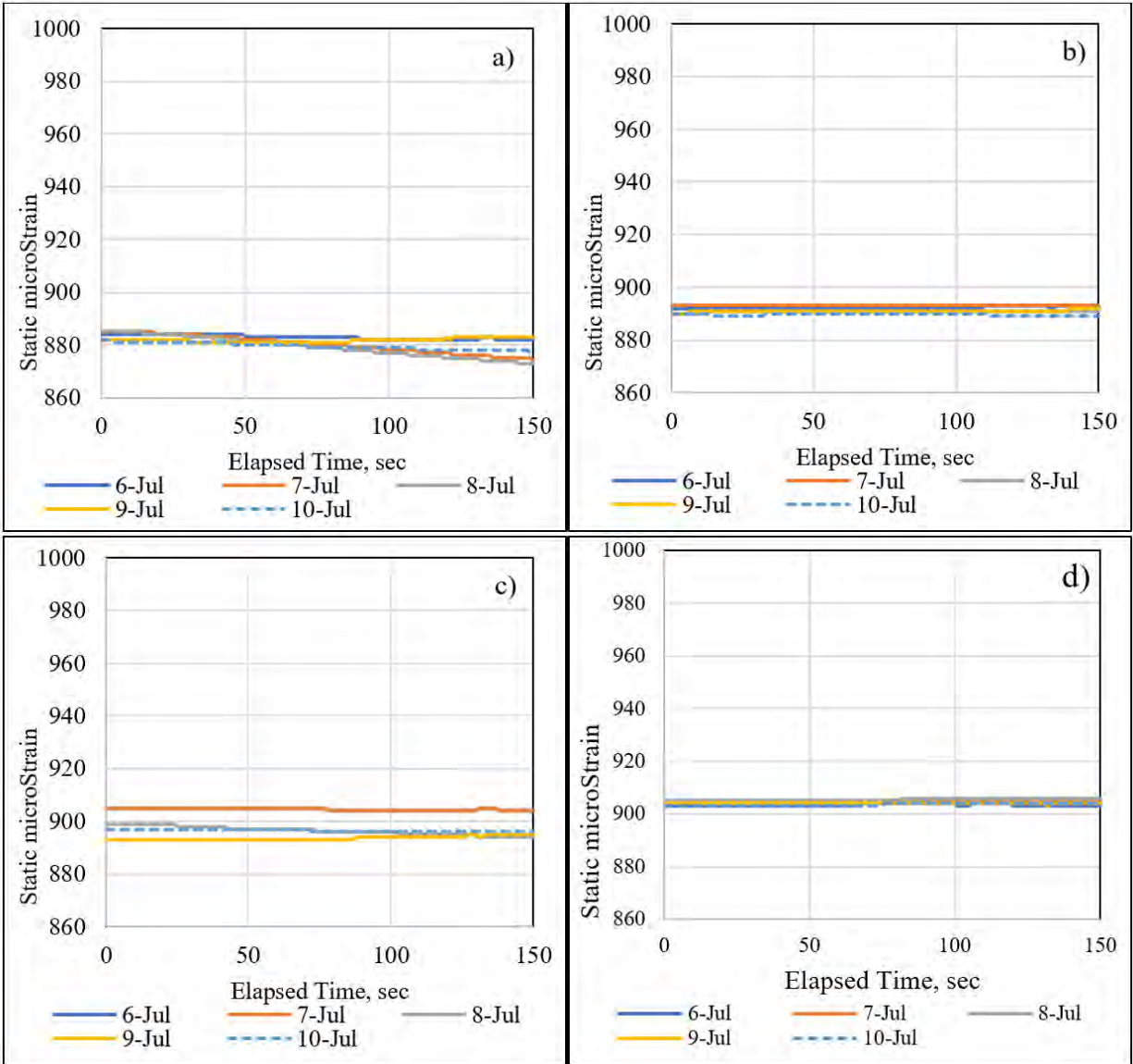
Figure 4.3 Static strain data for Cell 324 a) Sensor 001, b) Sensor 002, c) Sensor 003, and d) Sensor 004
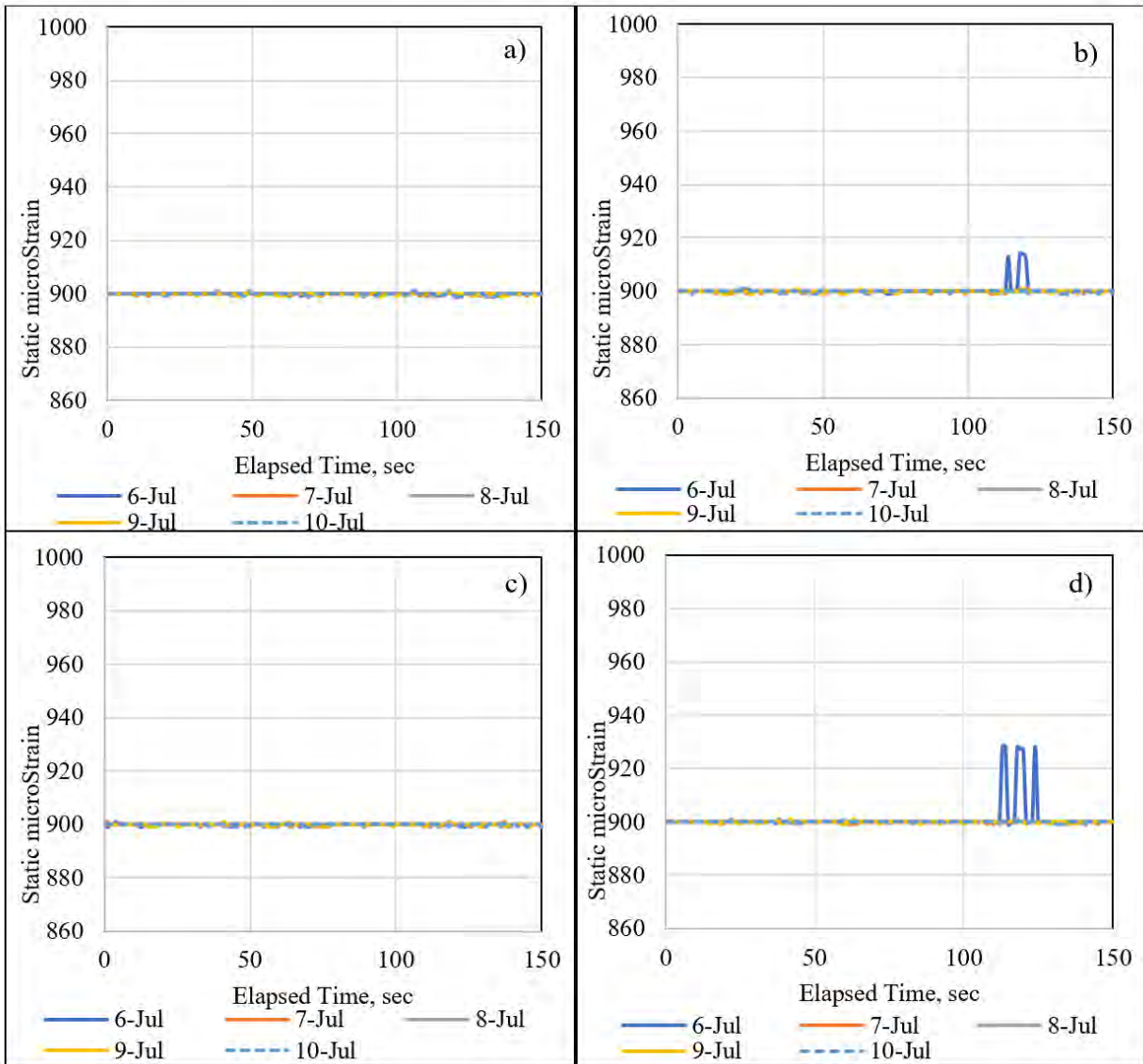
Figure 4.4 Static strain data for Cell 424 a) Sensor 001, b) Sensor 002, c) Sensor 003, and d) Sensor 004

4.2   MAXIMUM STRAIN GAUGE DATA ANALYSIS

The maximum strains measured from the snow plow truck loading on July 5, 2017, at various sections were compared. Figure 4.5 presents the results of this comparison.

The following observations can be made:

- High concrete strains were measured from early loading.
- Some replicate sensors pairs (for example, 324CE004 and 324CE008) showed similar values. At the same time, other replicate pairs (such as 224CE004 and 224CE008) exhibited significant discrepancy in the maximum responses under the same loading.
- Cell 224 exhibited the highest transverse strains.

- Several sensors did not show reliable readings. Early loading did not result in any visible damage.
- Several sensors exhibited an increase in the recorded strain values from loading to loading. It is possible that such increases are caused by accumulation of damage in concrete, but it could be also caused by many other factors, such as variation in the wheel path from loading to loading and variability in the slab curling. An analysis of the data taken at the latter times will be able to clarify this issues,
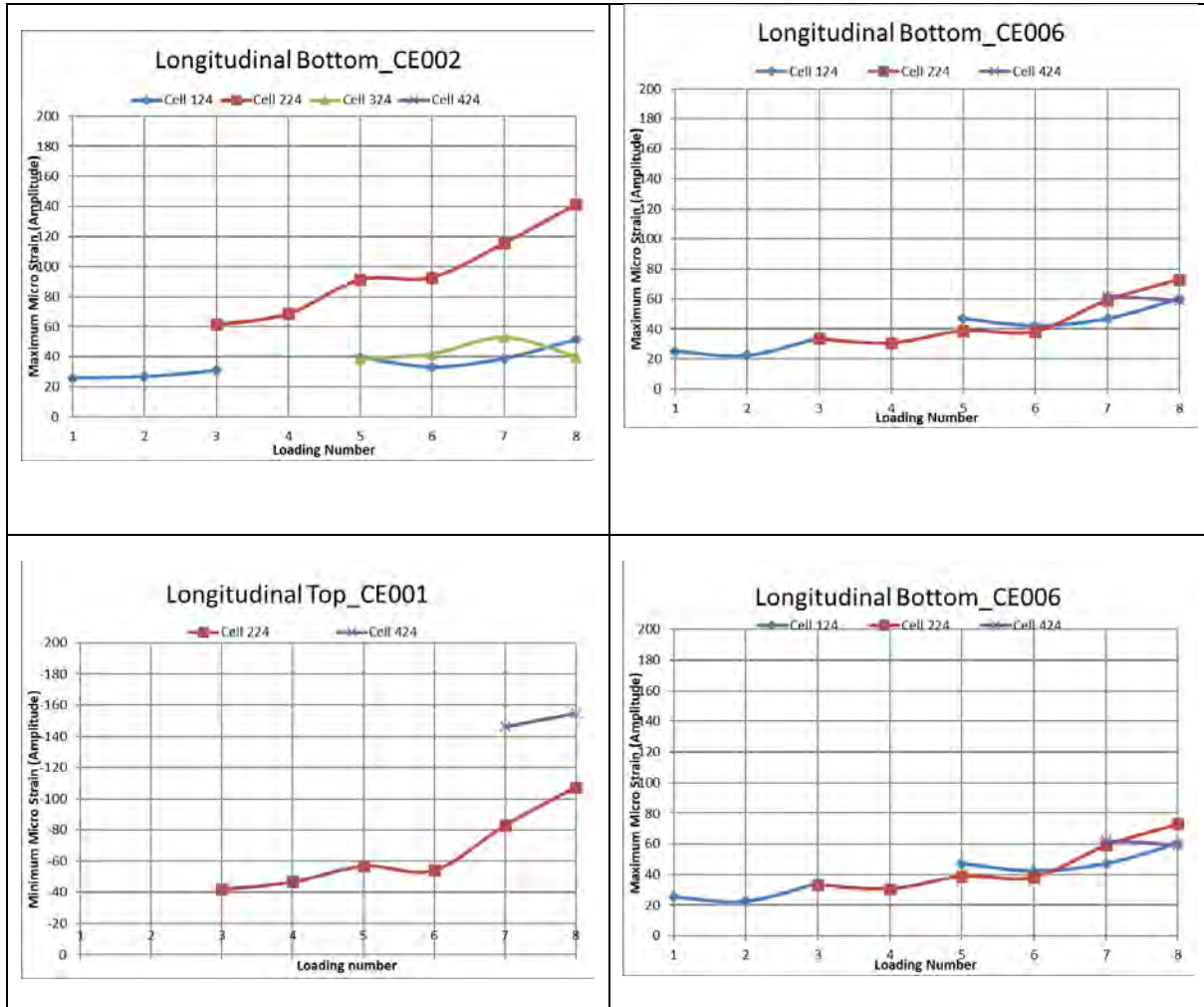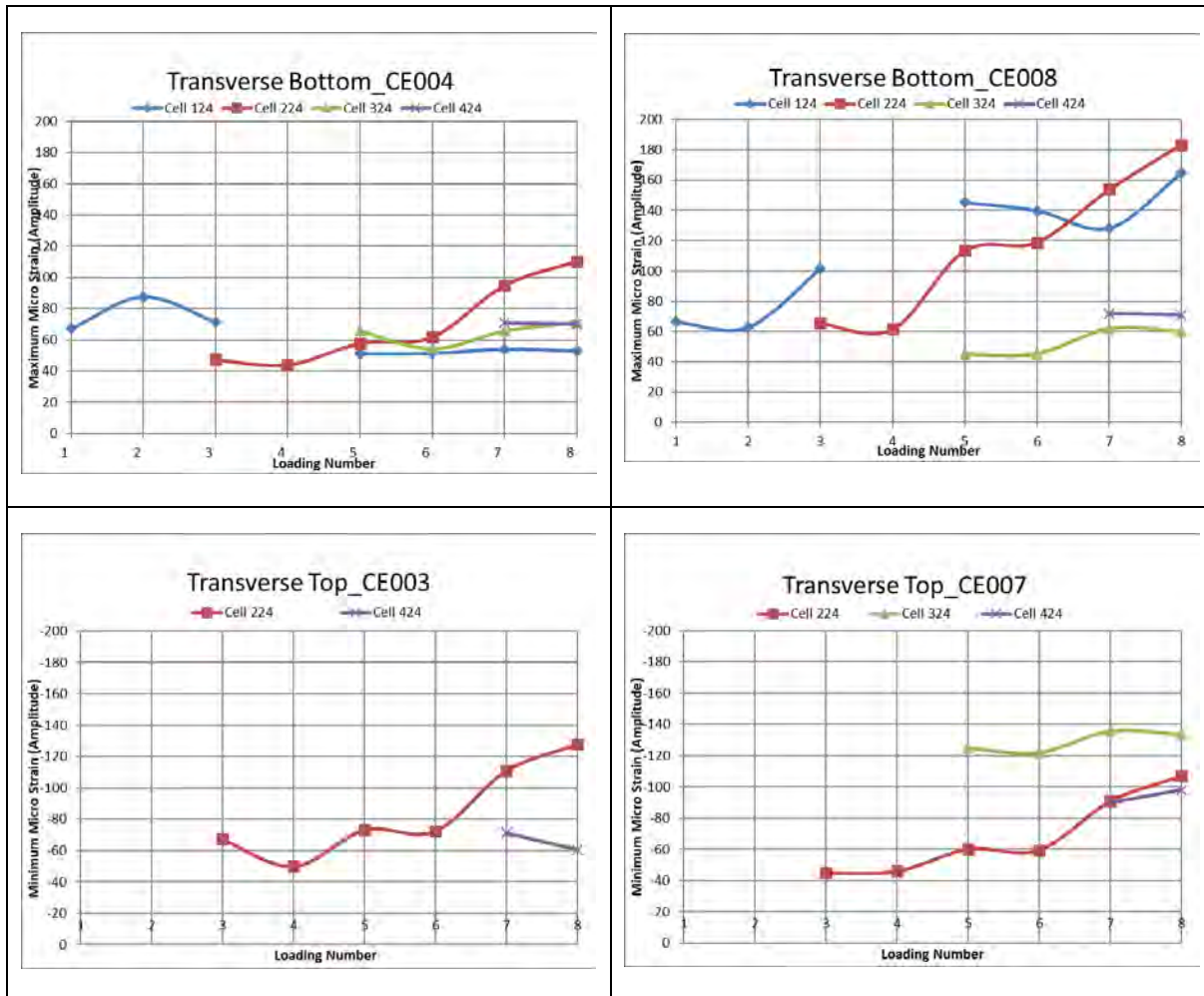
Figure 4.5 Comparison of maximum strains

Chapter 5: CONCRETE MATURITY AND STRENGTH AT THE TIME OF LOADING

The target loading times for Cells 124-424 were selected based on maturity levels shown in Table 5.1.

Table 5.1 Target concrete maturity at the loading time (Appendix B, Table B2, and Appendix E Table E1 and E2)

Cell x24 Early Loading Sequence		
Maturity (Deg-Hr)	Flexural (psi)	Loads applied to lanes
100	73	1st load on Cell 124 (forward and back)
200	196	1st load on Cell 224, 2nd load on Cell 124
300	267	1st load on Cell 324, 2nd load on Cell 224, 3rd load on Cell 124
400	318	1st load on Cell 424, 2nd load on Cell 324, 3rd load on Cell 242, 4th load on Cell 124

To determine actual concrete maturity at time of loading for every cell, the following analysis was performed:

- Using maturity measurements, the concrete placement time for each location was obtained. It was assumed that the first maturity measurement for each maturity meter was taken during concrete placement.
- Using the time stamp on dynamic strain gauge data, the time of maximum (or minimum) strain corresponding to the load-induced strain was determined for each cell where 1 refers to a forward pass and 2 refers to a reverse pass (Table 5.2).
- The concrete age for each location and loading was determined by subtracting the time of concrete placement from the time of maximum (or minimum) strain. Table 5.3 presents computed concrete age for each cell and each loading. Using concrete maturity meter data, quadratic relationships between measured maturity and time were obtained for each cell (Figure 5.1). Using these regression equations, concrete maturity for the times of maximum (or minimum) strains were identified.

- Table 5.4 presents measured maturity values for each cell and load application.

Table 5.2 Paving and loading time for each cell

Cells	Cell 124	Cell 224	Cell 324	Cell 424
Paving time	12:15 pm	11:15 am	10:40 am	9:50 am
Load number	Loading Time, h:min:sec (pm)			
Load 1_1	3:16:21			
Load 1_2	3:16:47			
Load 2_1	4:32:50	4:33:10		
Load 2_2	N/A	4:33:47		
Load 3_1	6:48:00	6:48:20	6:48:40	
Load 3_2	6:49:56	6:49:41	6:49:10	
Load 4_1	8:22:15	8:22:34	8:23:03	8:23:31
Load 4_2	8:25:36	8:25:09	8:24:41	8:24:18

Table 5.3 Concrete pavement age at the time of each load application

	Age at Loading (hrs)					
	Loaded Cells				Control	Tire Rut
	124 IL	224 IL	324 IL	424 IL	524 IL	624 IL
	124 OL	224 OL	324 OL	424 OL	524 OL	624 OL
Paving Time	12:15	11:15	10:40	9:50		
Paired Repetition 1	**3.00**	4.00	4.55	5.40		2 hr
Paired Repetition 2	4.25	**5.25**	5.80	6.65		
Paired Repetition 3	6.55	7.55	**8.10**	8.95		
Paired Repetition 4	8.15	9.15	9.70	**10.55**		

Maturity vs Elapsed Time

- ● 124_avg
- ● 224_avg
- ● 324
- ● 424
- —— Poly. (124_avg)
- – – – Poly. (224_avg)
- — — Poly. (324)
- —·— Poly. (424)

$y = 0.6829x^2 + 32.387x - 5.228$
$R^2 = 0.9987$

$y = 0.5868x^2 + 32.732x - 6.9794$
$R^2 = 0.9985$

$y = 0.8474x^2 + 29.528x - 5.3874$
$R^2 = 0.9986$

$y = 0.9895x^2 + 28.164x - 5.4615$
$R^2 = 0.9987$

Maturity, °C-Hrs

Time, (hrs)
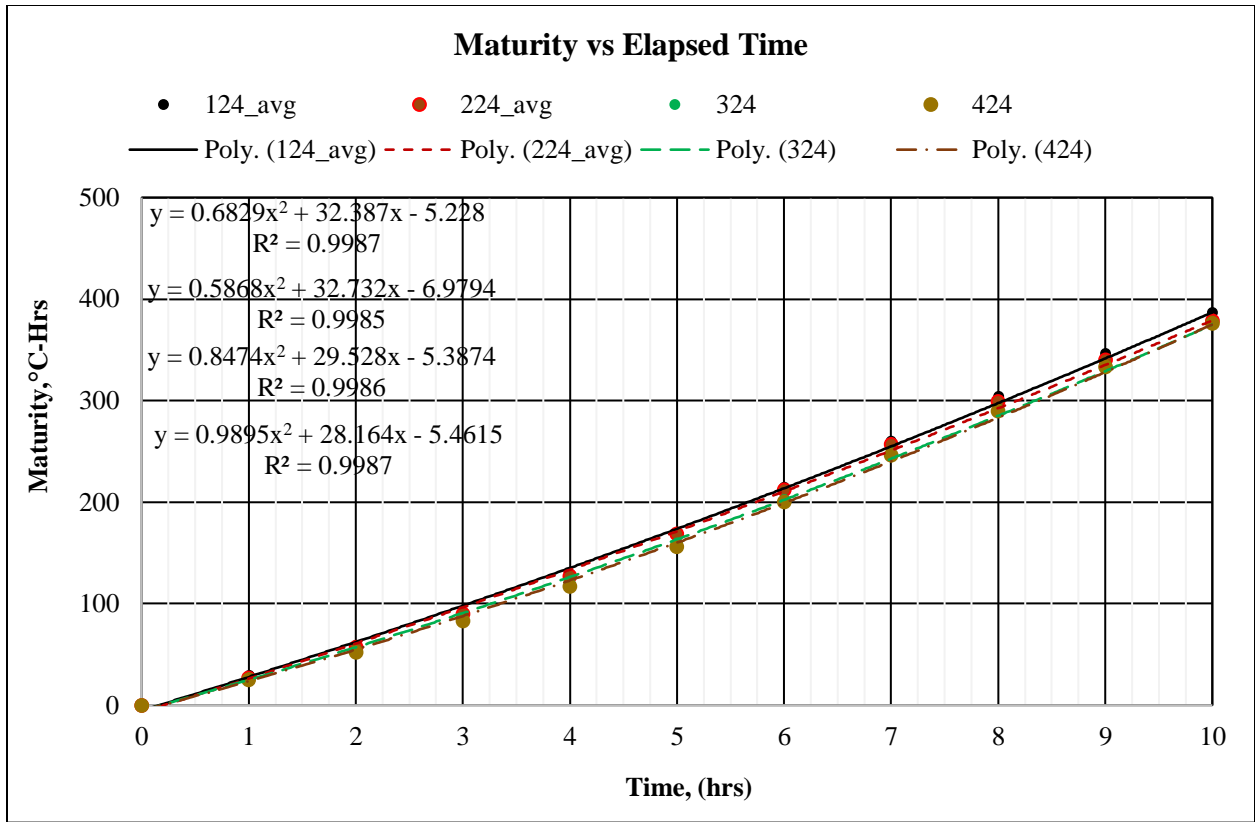
Figure 5.1 Measured concrete maturity vs time and corresponding regression equations

Table 5.4 Actual concrete maturity at the time of loading

Level	Load/ Rep	Loaded Cells			
31000 lb	SNOW PLOW → ←	124 IL	224 IL	324 IL	424 IL
9400 lb	PICK-UP → ←	124 0l	224 OL	324 OL	424 OL
		Maturity Level (°C-hr)			
	Paired Repetition 1	99.1	133.3	146.5	175.5
	Paired Repetition 2	144.8	181.0	194.4	225.6
	Paired Repetition 3	236.2	273.6	289.4	325.9
	Paired Repetition 4	304.1	341.6	360.8	401.8

The maturity data was used to determine concrete strength at time of loading using the results of concrete strength and maturity testing performed by American Engineering Testing, Inc. (AET). AET cast a set of various concrete test specimens using the same concrete mix design as the one used for MnROAD Cells 124-624. Figure 5.2 and Figure 5.3 show results of compressive and flexural tests, respectively, conducted 6 hours, 12 hours, 1 day, 2 days, 3 days, 4 days, 5 days, and 7 days after specimens were cast. The temperature of concrete specimens during curing varied between 23 and 30°C. To enable strength determination of concrete cured under different temperature conditions, AET computed concrete maturity at the time of concrete specimens testing. Figure 5.4 and Figure 5.5 show development of compressive and flexural strengths for various maturity levels, along with the corresponding trendlines and predictive equations. It can be observed that the predictive equation for flexural strength shown in Figure 5.5 is unreliable for maturity lower than 1000°C – hours. Figure 5.6 shows the trendline and predictive equation when only early maturity data were used. It can be observed that this predictive equation yields more realistic estimation of concrete strength.

Analysis of maturity and strength data suggests that concrete in Cell 124 had reached compressive strength of 430 psi and flexural strength of 210 psi only after the time of 3rd loading; concrete in Cell 224 had reached flexural strength of 290 psi only at the time of the fourth loading, and Cell 424 reached tensile strength 320 psi at the time of fourth loading (Figure 5.2, Figure 5.3).
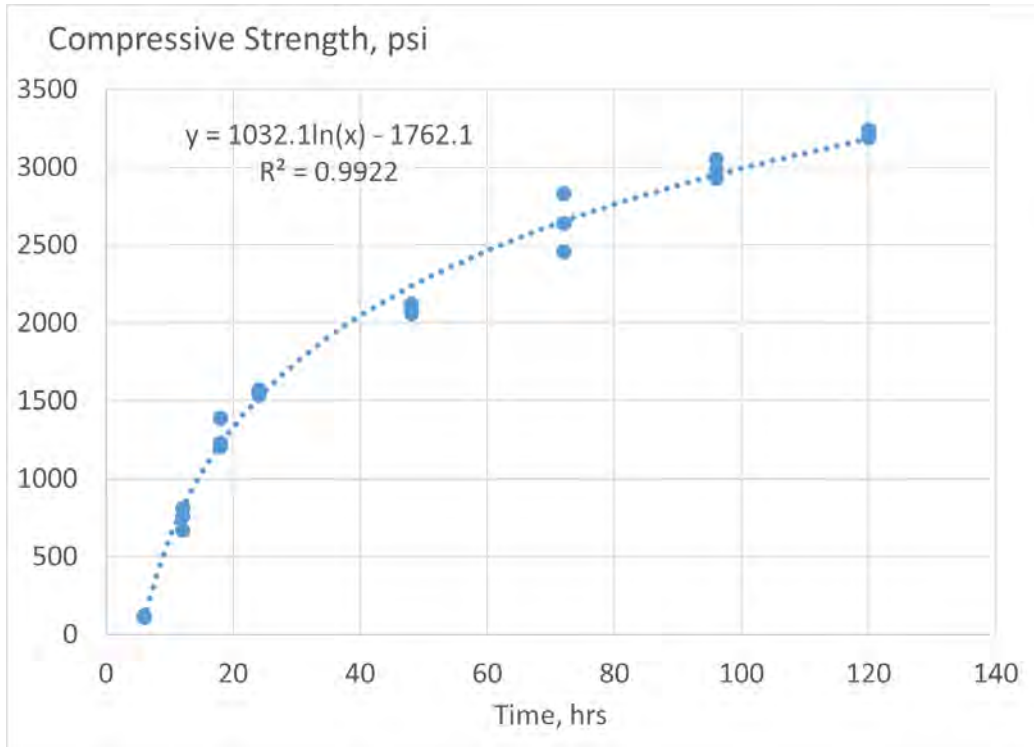
Figure 5.2 Compressive Strength at Various Ages
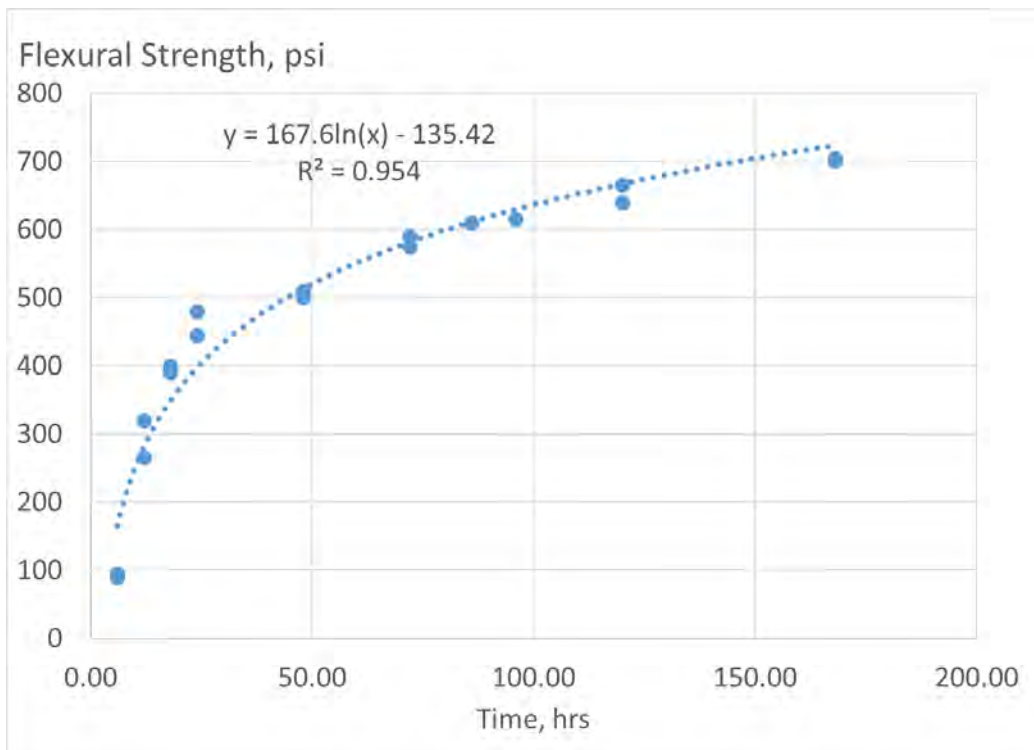
Figure 5.3 Flexural Strength at Various Ages

40
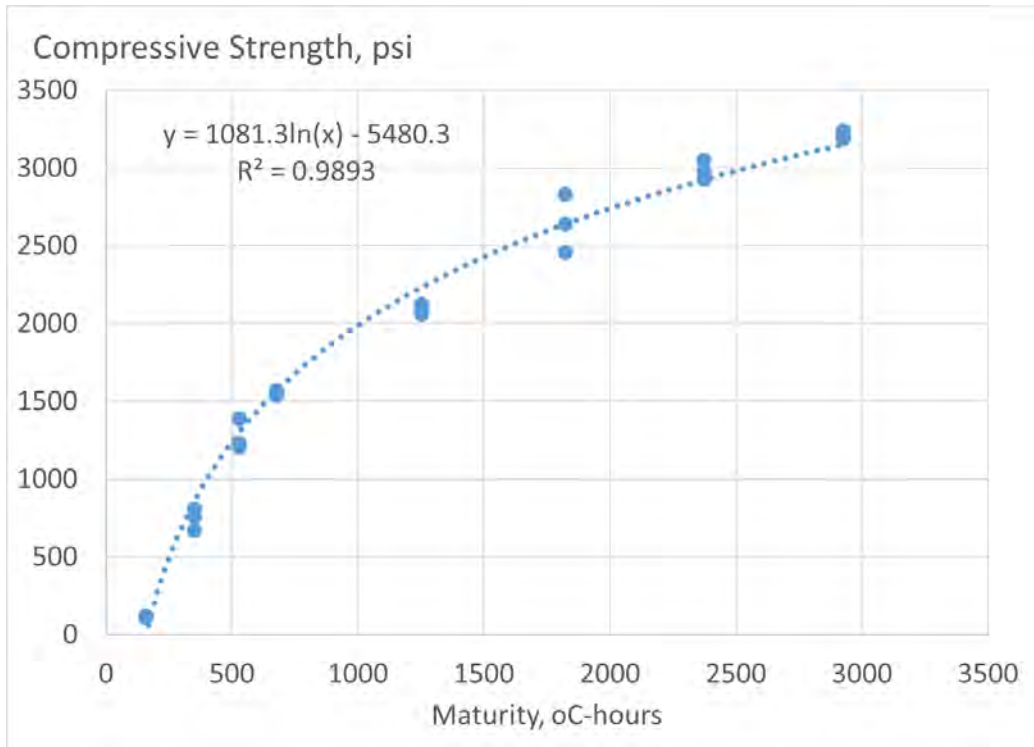
Figure 5.4 Concrete compressive strength vs maturity
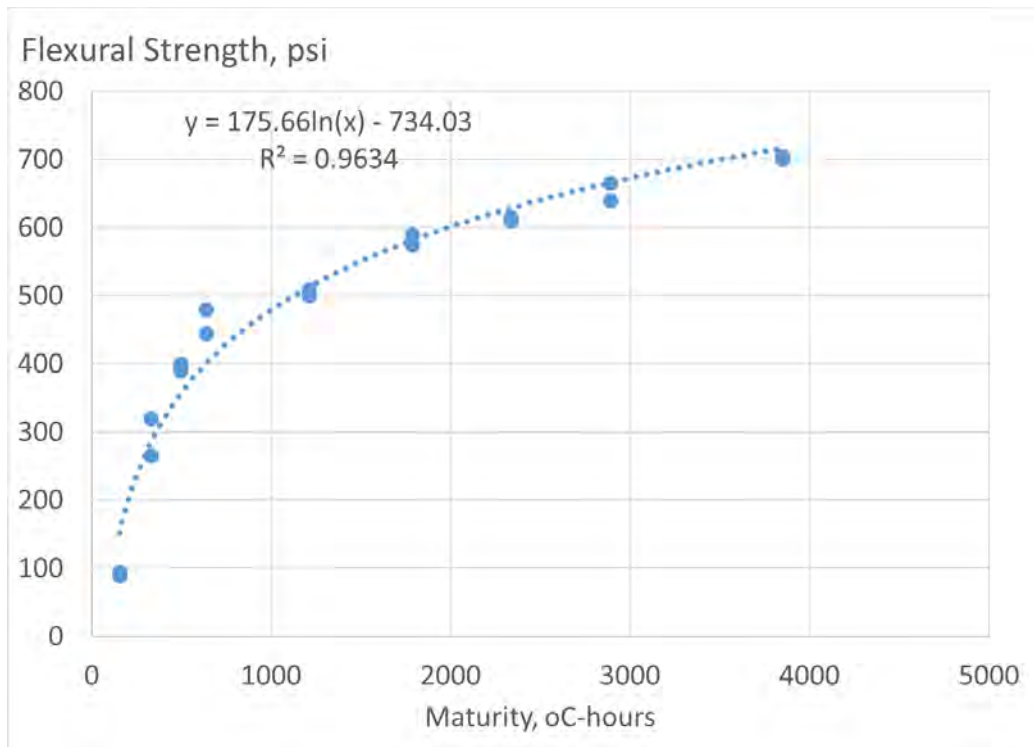
Figure 5.5 Concrete flexural strength vs maturity

41

Flexural Strength, psi

$$y = 208.82\ln(x) - 928.72$$
$$R^2 = 0.9333$$

Maturity, oC-hours
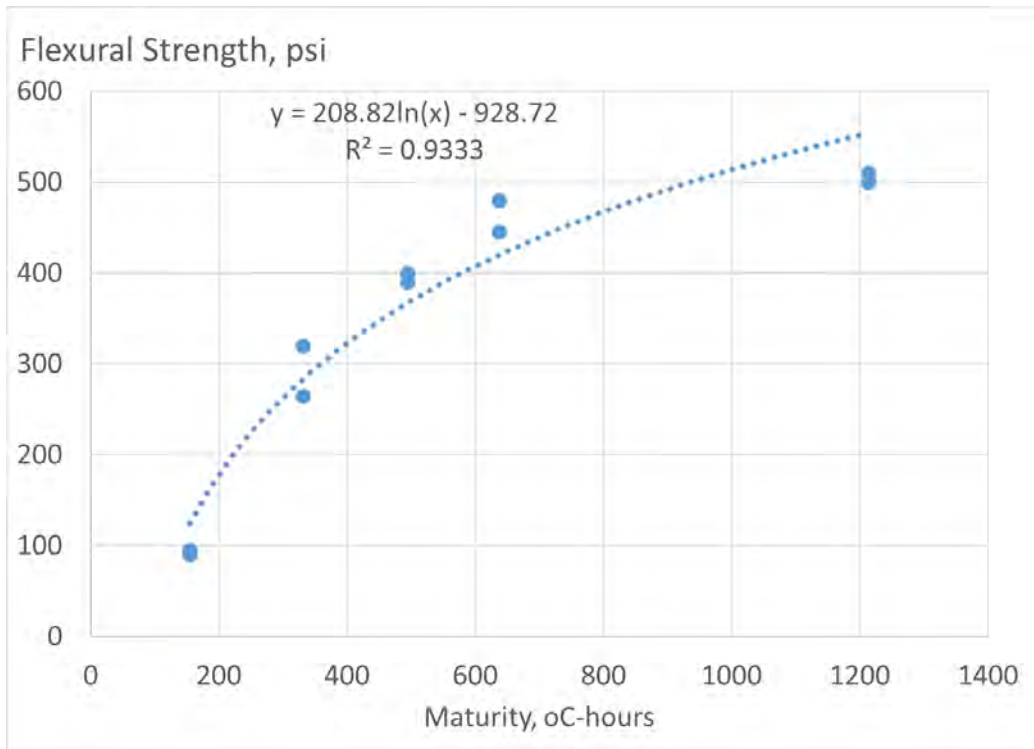
Figure 5.6 Concrete flexural strength vs maturity for low maturity levels

Table 5.5 In-place concrete flexural strength at the time of loading estimated from the maturity data.

Level	Load/ Rep	Loaded Cells			
31000 lb	SNOW PLOW → ←	124 IL	224 IL	324 IL	424 IL
9400 lb	PICK-UP → ←	124 0l	224 OL	324 OL	424 OL
		Flexural strength, psi			
	Paired Repetition 1	**73.3**			
	Paired Repetition 2	139.9	**179.1**		
	Paired Repetition 3	225.9	251.7	261.6	
	Paired Repetition 4	270.3	290.7	300.3	**319.2**

Chapter 6: EVALUATION OF THE EFFECT OF EARLY LOADING ON CONCRETE DURABILITY

After the cells were subjected to early loading, multiple cores were retrieved by MnROAD personnel and durability testing was conducted by AET, Inc. The total of 22 cores were subjected to ASTM C666, Procedure A, "Test Method for Resistance of Concrete to Rapid Freezing and Thawing." Four cores were extracted from Cells 124 through 524 and two cores were extracted from Cell 624. Since Cell 624 had transverse visible damage across both outside and inside lanes, only two cores were taken from the inside lane. Each core was labeled to denote the extraction cell and location from where each core was taken using the following nomenclature:

- IW: inside lane, wheel path
- IB: inside lane, between wheel paths
- OW: outside lane, wheel path
- OB: outside lane, between wheel paths

For example, core 324IB was taken from Cell 324, inside lane, between wheel paths. Specimens from Cell 624 were taken from the inside lane. One was taken within the rut created by early loading and another from between the wheel paths.

To fit cores in the ASTM C666 testing apparatus, each core was saw-cut vertically removing approximately one-quarter of the core. The specimens were subjected to 300 cycles of freezing and thawing. The mass change and relative dynamic moduli were measured.

Table 6.1 presents measured values for each core after 300 freezing-thawing cycles. The following observations can be made from

Table 6.1:

1. The mass change for cores taken from the control cell, Cell 524, varied from -0.63% to 0.12%.
2. The mass change for all other cores, except 424OB, 424OW, 624IB, and 624IR, were within the range of mass change of the cores from the control cell.
3. The relative dynamic modulus for cores taken from the control cell varied from 105% to 109%.
4. The relative dynamic modulus for all other cores, except cores 124IW, 424OB, and 424OW were within the range of the relative dynamic modulus for the cores from the control cell. For the core 124IW the relative dynamic modulus was slightly lower than the lower range (103% vs 105%), and for cores 424OB and 424OW it was slightly higher than the higher range.

Based on these observations it can be concluded that no reduction of concrete durability due to early loading of Cells 124-424 was detected by this test. The only cores that exhibited results different from those from the control cell were taken from Cell 424, outside lane, but this lane was loaded at higher

maturity than Cells 124-324 and by a lighter load than the inside lane of Cell 424. It is possible that deviation of properties of concrete from this location is due to variability in concrete placement.

Table 6.1 Summary of the ASTM C666 Freezing and Thawing Testing results

Core Identification	Mass Change, %	Relative Dynamic Modulus,%
124IB	-0.43	106
124IW	-0.33	103
124OB	-0.27	107
124OW	-0.56	105
224IB	-0.03	107
224IW	-0.17	107
224OB	-0.1	108
224OW	-0.12	108
324IB	0.12	108
324IW	0.02	107
324OB	-0.32	108
324OW	-0.23	108
424IB	0.05	106
424IW	-0.12	108
424OB	-1.61	111
424OW	-4.28	110
525IB	0.12	105
524IW	-0.57	107
525OB	-0.12	107
525OW	-0.63	109
624IB	-0.76	109
624IR	-1.13	Could not be obtained

Chapter 7: ULTRASOUND TOMOGRAPHY TESTING

The nondestructive testing technique utilized in this research is a linear array ultrasonic tomography device, MIRA. The version of MIRA used in this study incorporates ten channels, with each channel composed of four transmitting and four receiving dry point contact (DPC) transducers. No contact liquid couple is required for the transmission of horizontal shear waves to the tested medium (Shevaldykin et al, 2002). The distance between adjacent transducer channels is 40 mm (1.6 in.). When one transducer excites the slab surface, the wave propagates through the specimen and the receiving transducers record excitations at various locations. This linear array system generates 45 time-of-flight measurements from transmitting and receiving pairs at various distances in less than three seconds.

The ultrasound testing was conducted on July 6th, 2017 and on July 10th, 2017. The following MIRA settings were used:

- Frequency: 50 kHz
- Impulse duration: 2 half-periods
- Cycles: 1

Two types of testing were performed:

- Nine scans in the vicinity of the cores
- 10 scans along the width of the slab (see Figure 7.1)

For each type of the testing, shear wave velocity and Hilbert Transform Indicator were computed.

Figure 7.1 MIRA measurements

7.1 VELOCITY ANALYSIS

One advantage of the linear array system used in this study is its ability to record signals from pairs of sending and receiving transducers located at various distances. For each signal time history, the arrival time was determined as the time of maximum value of the arriving signal.

Figure 7.2 shows an example of determination of arrival time for sensor pairs located 40, 120, and 280 mm apart. Then a linear regression analysis was performed between arrival times and distances between sensors for each MIRA measurement. Figure 7.3 shows an example of the plot of distance between transducer pairs and the measured signal arrival time for one of the MIRA measurements. A clear linear relationship is observed for this data set and the slope of the line, 2.664 mm/microseconds = 2.402 km/s, is the shear wave velocity. A high R^2 of 99.97% indicated that the model explains 99.97% of the change in the arrival time with the change in distance between sensors.
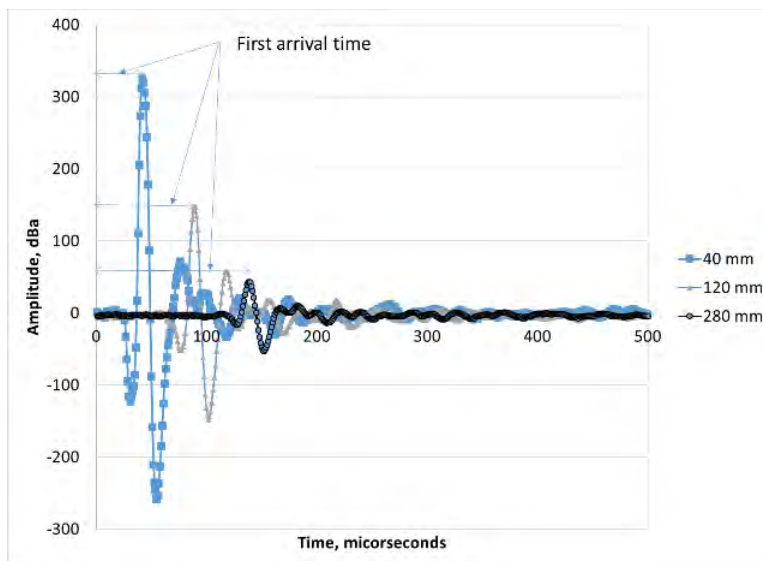
Figure 7.2 An example of MIRA signal time history for one sensor pair
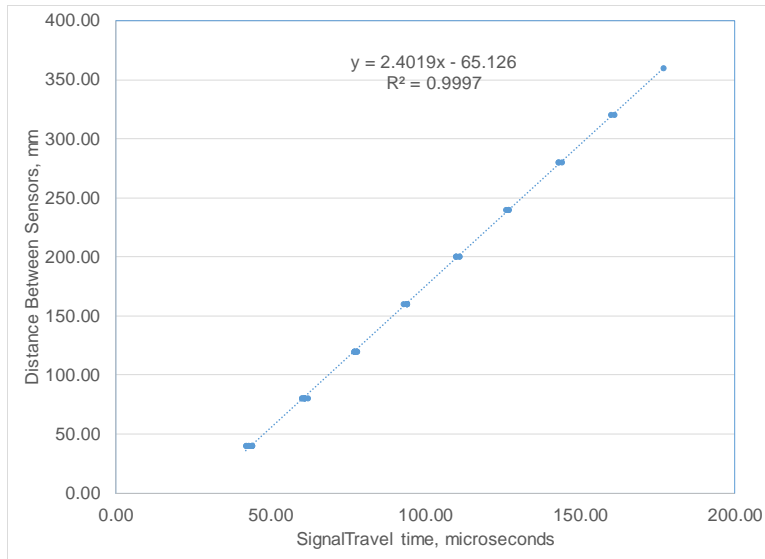
Figure 7.3 An example of shear wave velocity calculation

If concrete is approximated as an isotropic and elastic medium, the relationship between elastic parameters (Young's modulus and Poisson's ratio), density, and shear wave velocity in concrete has the form shown in Equation (3) (Carino, 2001):

$$C_S = \sqrt{\frac{E}{2(1+\mu)\rho}}$$
(3)

where E is initial Young's modulus of elasticity, μ is Poisson's ratio, ρ is density, and C_S is the shear wave (S-wave) velocity. Presence of micro cracking reduces Young's modulus of concrete resulting in reduction of the shear wave velocity.

The results of the velocity analysis for each MIRA scan are provided in Appendix C. Figure 7.4 presents the computed mean velocities for each cell from MIRA scans taken on July 6th along the width of the slabs. It can be observed that early loading of Cells 124 and 324 did not result in reduction of shear wave velocity of concrete compared to the velocity of concrete in the inside lane of control Cell 524. The mean measured velocity of concrete in the outside lane of Cell 224 was slightly lower than the velocity for the remaining slab, but this phenomenon was most likely caused by spatial variability of concrete velocities at early (less than 48 hours) age and not by 2-axle pickup truck damage.

47
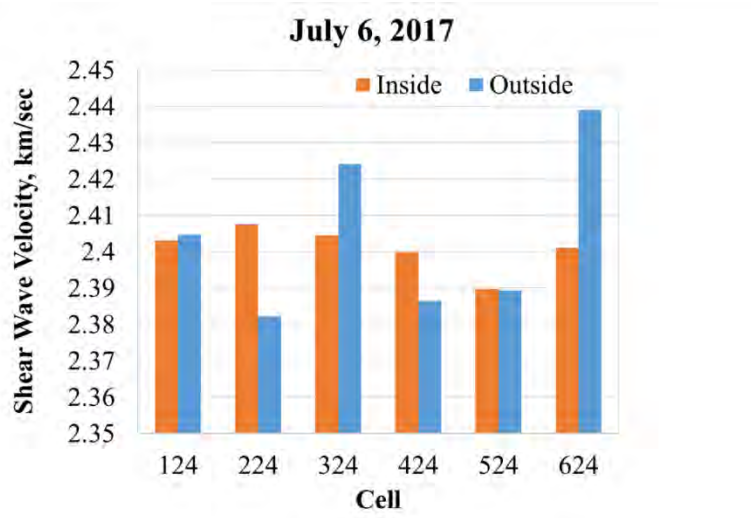
Figure 7.4 Comparison of Mean Shear Wave Velocities for Cells 124-624

Figure 7.5 and Figure 7.6 present comparison of the average shear wave velocities taken at the wheel path and between wheel paths near core locations, for inside and outside lanes, respectively. It can be observed that for both inside and outside lanes MIRA testing in the wheel path did not result in low velocity indicating presence of significant damage.
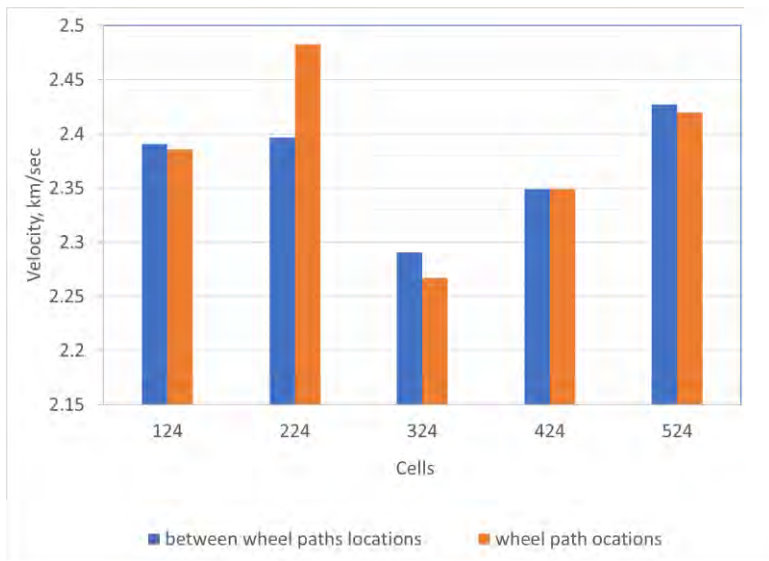
Figure 7.5 Comparison of velocities taken in the wheel path vs between wheel path for the inside lane
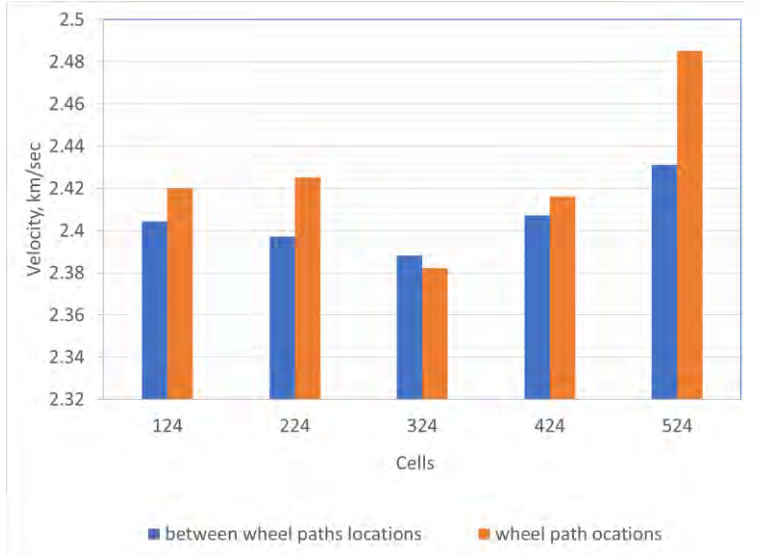
Figure 7.6 Comparison of velocities taken in the wheel path vs between wheel path for the outside lane

7.2   ANALYSIS OF THE SHAPE OF THE RECEIVED SIGNAL

In the past study, the Hilbert Transform Indicator (HTI) was successful in capturing the presence of damage in concrete slabs (Khazanovich et al, 2017). Those slabs commissioned by the Electric Power Research Institute (EPRI) were made of concrete with properties quite different from the properties of concrete used in this study.

The HTI is defined as follows:

$$HTI = \int_0^{500} \frac{HT(t)}{HT_{max}} \, dt \tag{4}$$

where HT(t) is the Hilbert transform of a signal f(t) defined as:

$$HT(t) = \sqrt{\left(f(t)\right)^2 + \left(\frac{1}{\pi}\int_{-\infty}^{\infty} \frac{f(\tau)}{t-\tau} d\tau\right)^2} \tag{5}$$

t is time and HT_{max} is the maximum value of the function HT(t) in the interval from 0 to 500 microseconds. A time window of 500 microseconds was selected to ensure that the direct arrival impulse as well as all subsequent oscillations were captured. A higher HTI value would be indicative of damaged concrete, while a low value represents sound concrete. Past studies showed that HTI lower than 80 indicates sound concrete while HTI greater than 100 indicates presence of significant of micro damage near the top surface.

Figure 7.7 presents mean values of computed HTI for Cells 124-624 from MIRA measurements taken on July 10, 2017. It can be observed that only the inside lane of Cell 224 exhibited mean HTI greater than 80. Figure 7.8 shows the maximum measured HTI for each cell from the same set of MIRA data. It can be observed that maximum HTIs for the inside lane of Cell 124 and outside lane of Cell 424 were greater than 100 indicating poor concrete condition near the surface. However, low maximum HTIs for Cells 124 and 224, and inside lane of Cell 424 suggest that those high values of HTI may have been a result of poor finishing and not be caused by early loading.

An initial comparison of HTI indexes computed from MIRA testing near core locations in the wheel path and between wheel paths was also conducted. It can be observed that wheel path locations did not exhibit HTI higher than HTIs between wheel path locations for the same slabs.

Analysis of MIRA data collected for these cells at later dates may help to clarify this issue.
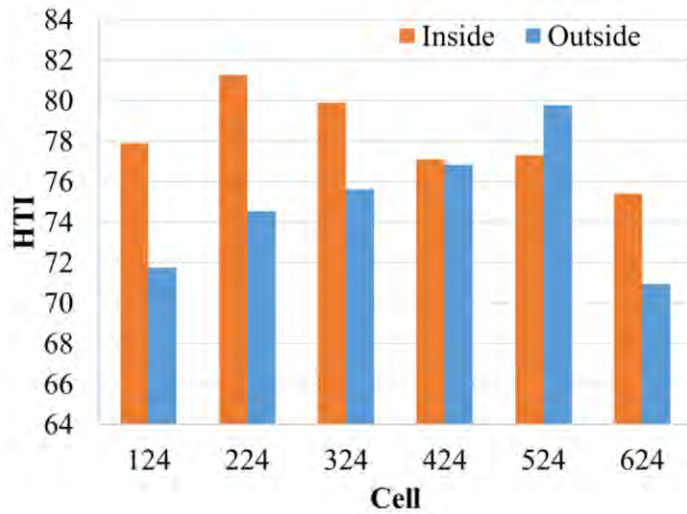
Figure 7.7 Mean HTIs for Cells 124-624 Measured on July 10, 2017
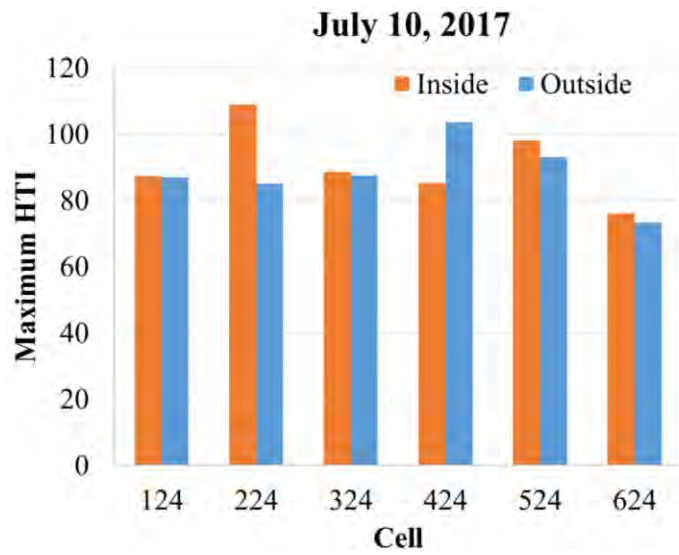
Figure 7.8 Maximum HTIs for Cells 124-624 Measured on July 10, 2017

Figure 7.9 Mean HTIs at the core locations, inside lane
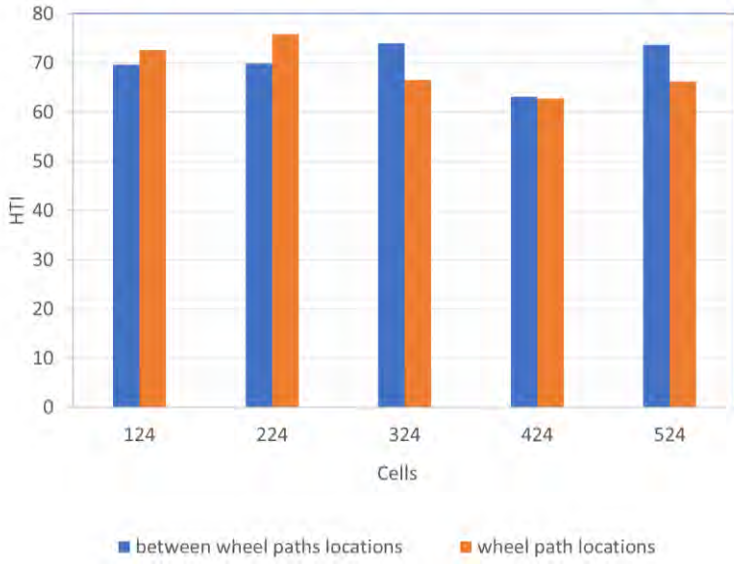
Figure 7.10 Mean HTIs at the core locations, outside lane

Chapter 8: RIDE QUALITY

8.1 EARLY AGE RIDE QUALITY

The serviceability was analyzed using the international roughness index (IRI). IRI analyzes the actual road surface rather than vehicle response. A higher IRI value signifies a rougher road surface which is an indicator of a lower ride quality. This method uses a model of a quarter of a car traversing the road at 50 mph. A 3K Laser Line sensor was used for data gathering in this experiment. Each cell was tested three times and the average IRI was used in analysis.

Cells 124 – 424 were loaded on the inside lane with a snow-plow truck (31,000 lbs) and the outer lane with a truck (9,000 lbs). The values shown in Figure 8.1 is an average IRI value from the entire pavement life of 22 months. The greatest IRI seen in the outside lane was cell 624, which was the slab with the visible truck wheel paths. These indents were observed by the laser surface scans creating a significantly higher IRI. Early loading on Cells 124 – 424 did not produce visible damage on the pavement to affect the IRI. There is also no difference in IRI between the inner and outer lanes.
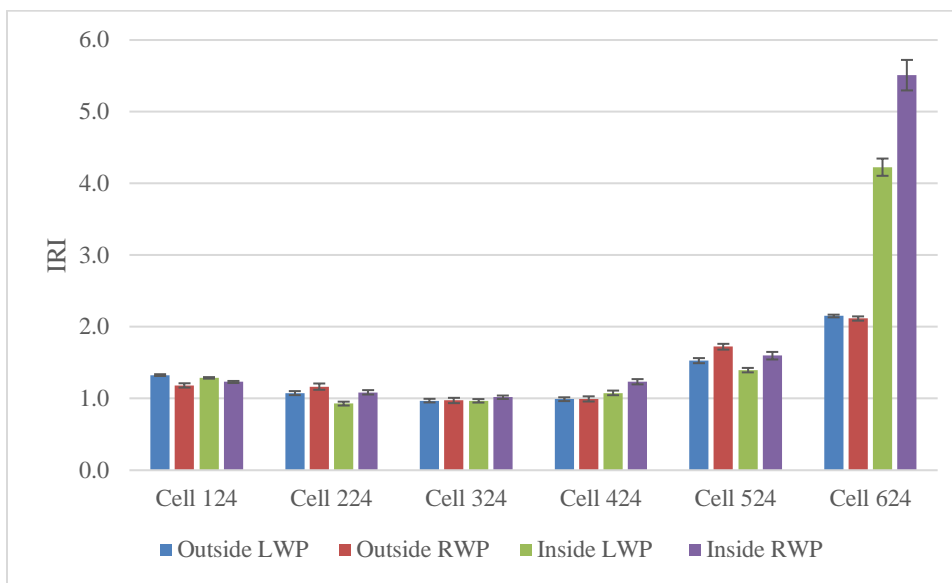
Figure 8.1 IRI for each cell

IRI data was taken seven times since originally paving and data collection is still on going. Figure 8.2 shows the IRI values up until October 2, 2018. In Cells 124 – 524 there is little increase in IRI with time indicating no drastic decline in serviceability. Cell 624 has more variability in values and is inconclusive.
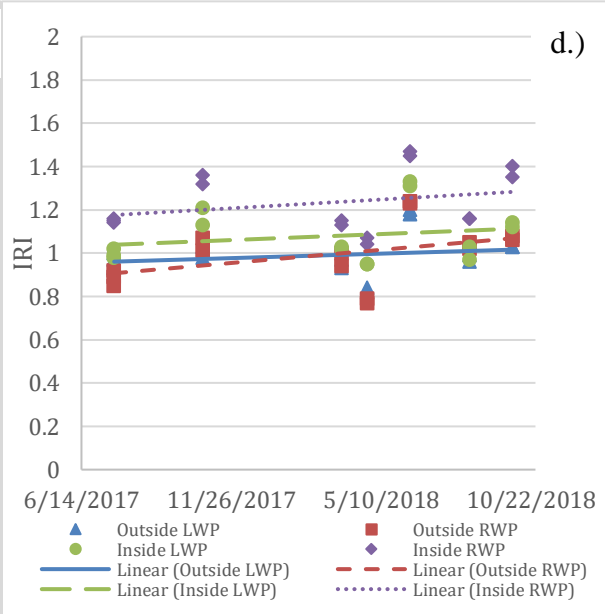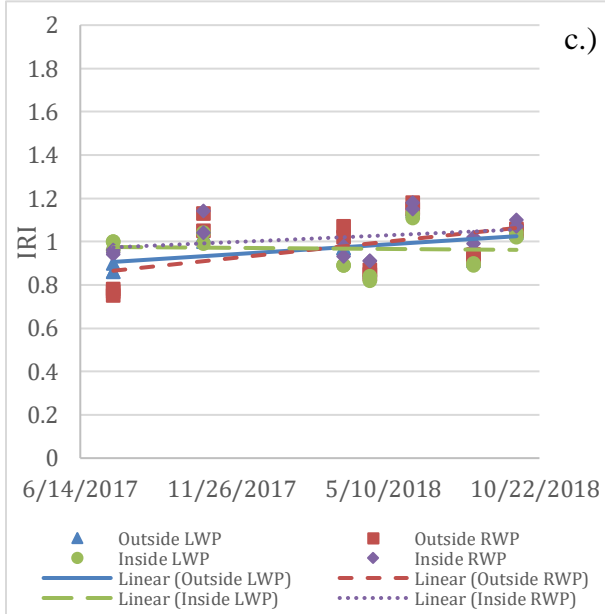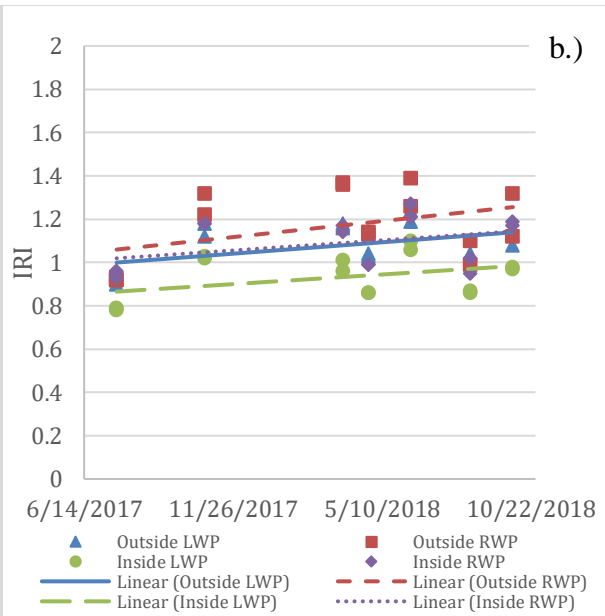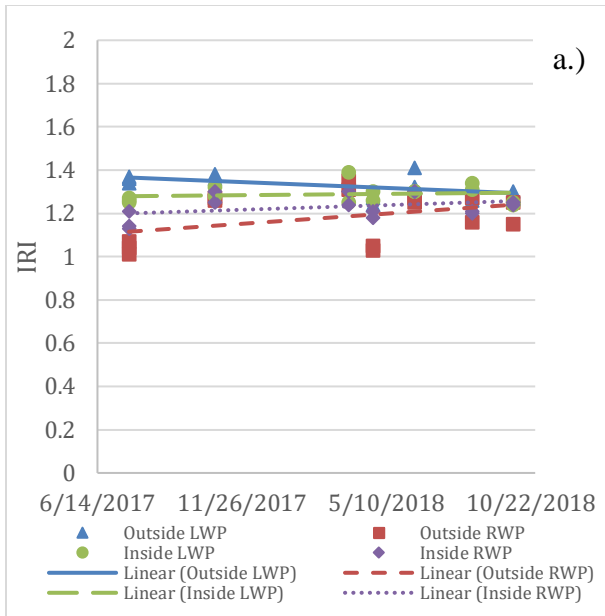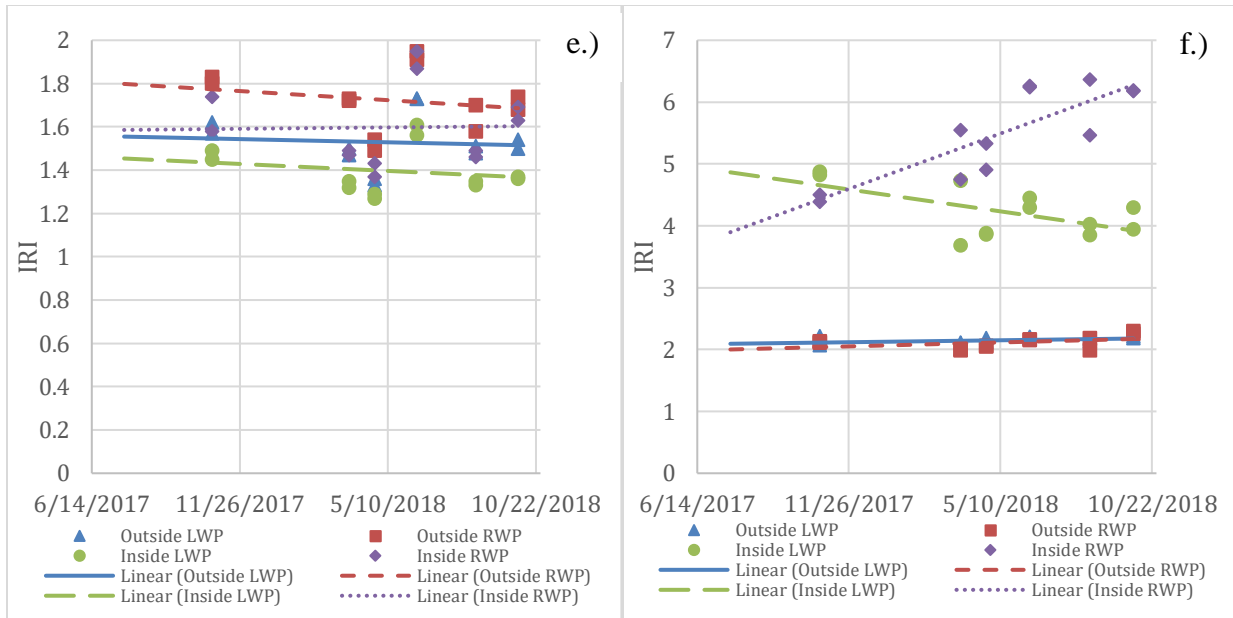
Figure 8.2 IRI values based on time where a.) Cell 124, b.) Cell 224, c.) Cell 324, d.) Cell 424, e.) Cell 524, and f.) Cell 624

8.2 LONG-TERM RIDE QUALITY

The ride quality in this study was quantified using the international roughness index (IRI). Reported in units of inches/mile, the IRI is a useful index for assessing overall pavement ride quality. It summarizes qualities of pavement surface deviations that impact vehicle suspension movement. A higher IRI value indicates a rougher road surface. A 3K Laser Line sensor was used to measure continuous profiles along the left wheel and right wheel path of each lane and the resulting profiles were processed to report IRIs.

Roughness profiles were measured 13 times between July 2017 and August 2020. Figure 8.3 and Figure 8.4 show average IRIs for each cell for the inside and outside lanes, respectively. As could be expected, Cell 624 shows the highest IRI due to the presence of the rut. Cell 524, which was not exposed to the early loading on the day of construction, exhibited significantly worse ride quality than the remaining Cells 124-424 for both inside and outside lanes, but this could be due to Cells 624 and 524 being measured consecutively and both having a shorter span. Since IRI is measured for each cell consecutively, the equipment may have had some residual vibration when scanning Cell 524 after traversing the especially rough surface of Cell 624. Therefore, the extremely poor ride quality measurements for Cell 624 could affect the ride quality measurements for Cell 524 even though the actual roughness of Cell 524 may be lower. Generally, MnDOT dictates that a typically loaded, good pavement has an IRI in the range of 55 to 105 in/mi.
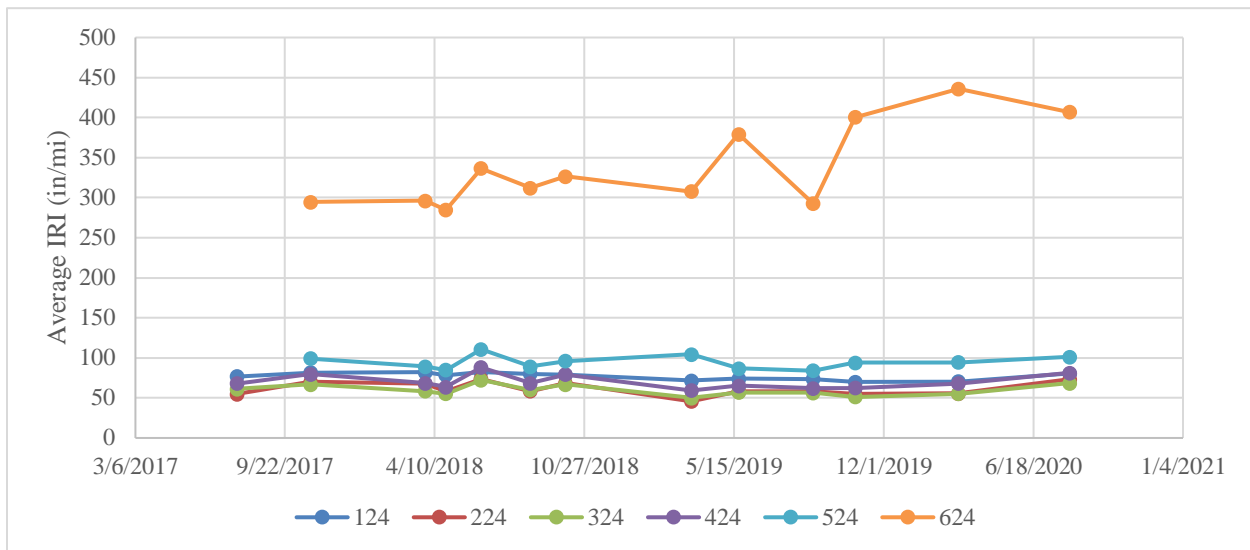
Figure 8.3 Average IRI of the inside lane
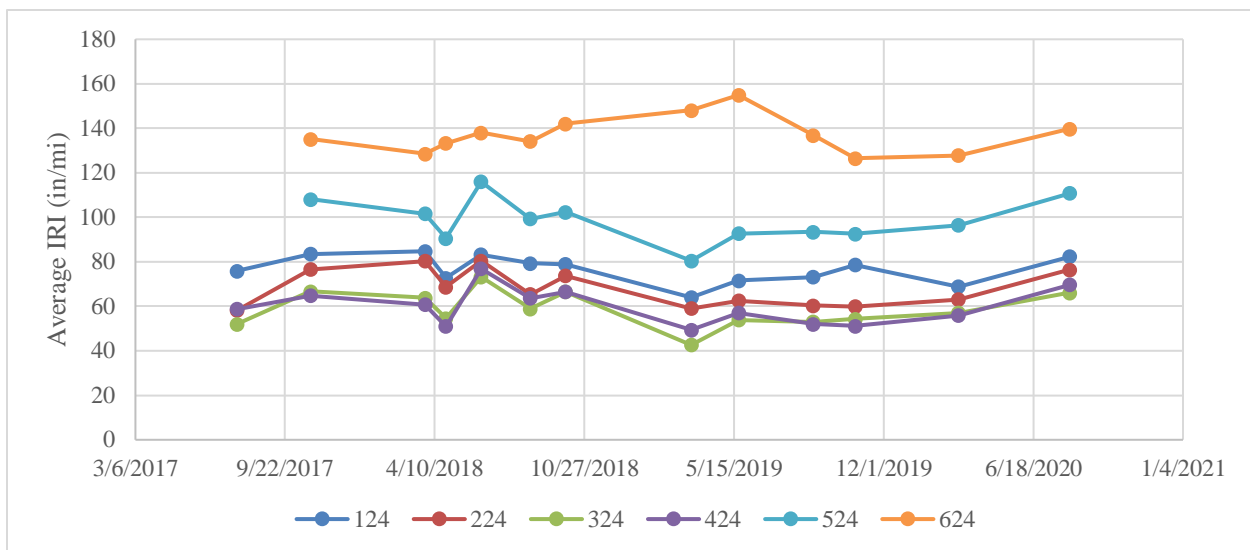
Figure 8.4 Average IRI of the outside lane

Analysis of Figure 8.3 and Figure 8.4 shows significant variability in IRI measurements and only a little increase in IRI with time indicating no significant decline in serviceability for Cells 124 – 424. Although the inside lane of Cell 124 initially exhibited a higher IRI than Cells 224, 324, and 424, at the time of the last observation it exhibited the same IRI as Cell 424. This indicates that although initially the heavy early loading, experienced by Cell 124, seems to be affecting the IRI, by the end of the observation period, IRI measurements of the most early loaded cell are congruent to the cell with least early loading.

Figure 8.5 shows that although the inside lane of Cell 124 was loaded at the very early age by a 31,000–lbs truck while the outside lane was loaded by a light pickup truck there is very little difference in ride quality between these two lanes. Early age loading of Cell 424 occurred only after the flexural concrete

strength reached 320 psi, but the difference in the measured IRI for the inside and outside lanes is much larger than for Cell 124, as shown in Figure 8.6. The difference in IRIs for these two lanes does not vary significantly between the measurements.

These observations lead to the conclusion that changes in ride quality over time for Cells 124, 224, 324, and 424 cannot be attributed to the early loading of these cells.
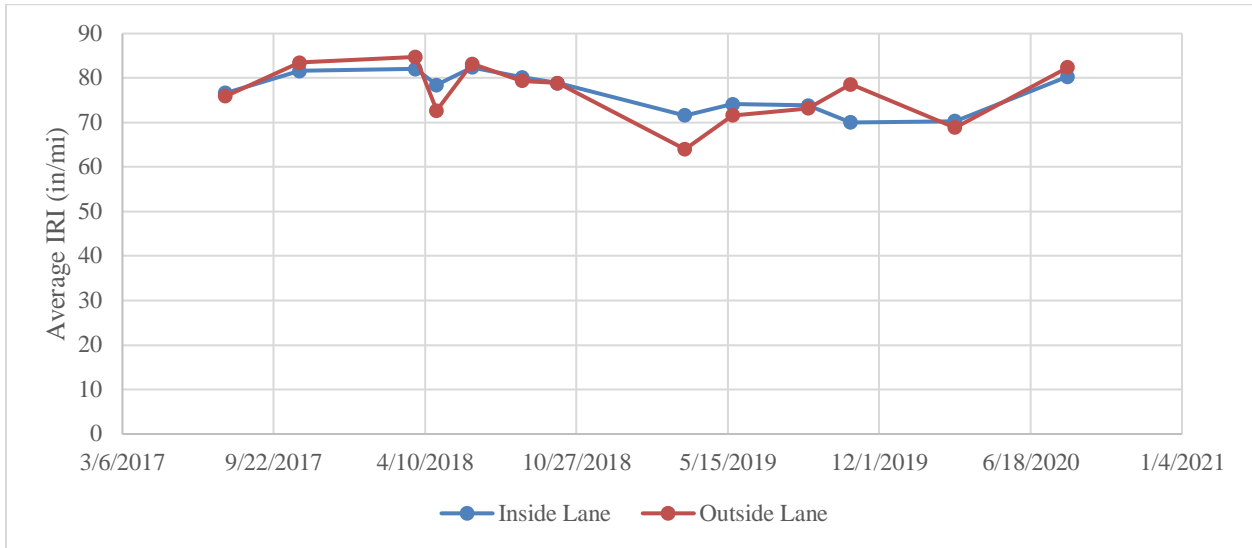
Figure 8.5 Average IRI for Cell 124
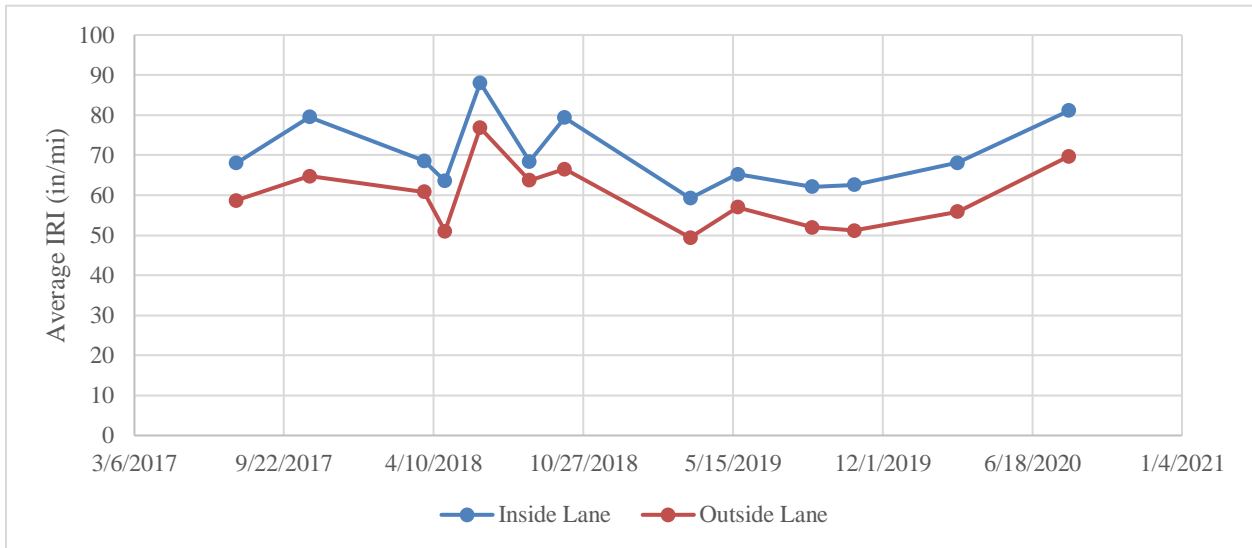
Figure 8.6 Average IRI for Cell 424

Chapter 9: ANALYSIS OF FWD DATA

9.1   EARLY AGE FWD DATA ANALYSIS

Nondestructive testing using a falling weight deflectometer (FWD) was done to determine the modulus of subgrade reaction (k), the elastic modulus of the concrete pavement (E_{PCC}), and the load transfer efficiency (LTE) of the joints. These calculations determine variation in base, subbase, subgrade, and pavement responses, structural capacity, and joint performance respectively. FWD data is obtained in three locations on a slab: the center and twelve inches on either side of a joint. A load plate is positioned and dropped three times with forces of 30, 45, and 60 kN on each location. Data is also collected systematically over 60 inches across the joint and -12 inches in the opposite direction, shown in Figure 9.1.
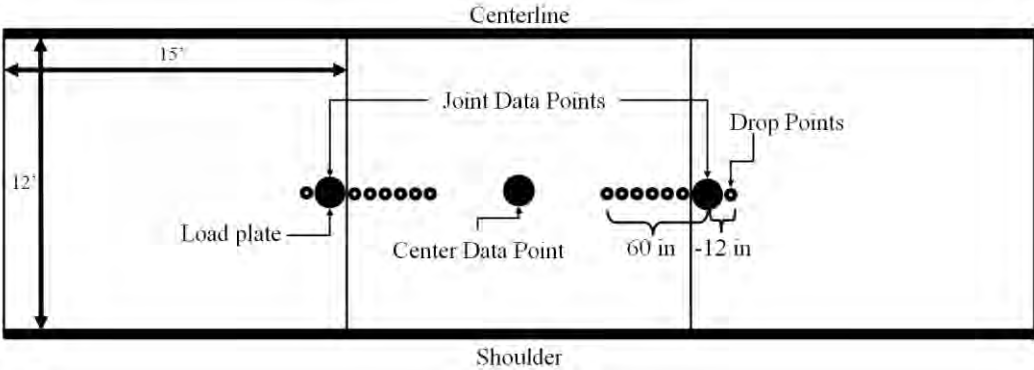
Figure 9.1 Locations FWD data was collected

9.1.1 Modulus of Subgrade Reaction

The modulus of subgrade reaction, k, is the deflection of the soil beneath the pavement under a normalized load. This is back-calculated from FWD data gathered at the center of the slab and changed to a static value using the following set of equations:

$$AREA_{60} = 4 + 6 \cdot \frac{d_8}{d_0} + 5 \cdot \frac{d_{12}}{d_0} + 6 \cdot \frac{d_{18}}{d_0} + 9 \cdot \frac{d_{24}}{d_0} + 18 \cdot \frac{d_{36}}{d_0} + 12 \cdot \frac{d_{60}}{d_0}$$

(6)

where $AREA_{60}$ is the area normalized under the deflection basin and d_X are the deflections X distance from the load point. This value is then used to find the radius of relative stiffness, ℓ, along with the values shown in Table 9.1.

$$\ell = \left[\frac{ln\left(\frac{k_1 - AREA}{k_2}\right)}{-k_3} \right]^{1/k_4}$$

(7)

Table 9.1 Regression coefficients for AREA versus radius of stiffness

	k_1	k_2	k_3	k_4
AREA60	60	289.708	0.698	2.566

The nondimensional deflection coefficient can then be determined using the regression coefficients shown in Table 9.2 and the following equation:

$$d_r \mathbin{*}= a \cdot e^{-b \cdot e^{-c \cdot \ell}}$$

(8)

where d_r is r inches away from center and ℓ is the radius of relative stiffness.

Table 9.2 Regression coefficients for nondimensional deflection coefficients

	a	b	c
d_0*	0.12450	0.14707	0.07565
d_8*	0.12323	0.46911	0.07209
d_{12}*	0.12188	0.79432	0.07074
d_{18}*	0.11933	1.38363	0.06909
d_{24}*	0.11634	2.06115	0.06775
d_{36}*	0.10960	3.62187	0.06568
d_{60}*	0.09521	7.41241	0.06255

The modulus of subgrade reaction, k, can now be calculated using the following equation:

$$k = \frac{P \cdot d_r *}{d_r \cdot \ell^2} \tag{9}$$

where P is the applied load (lbf), d_r* is the nondimensional deflection coefficient calculated above, d_r is the measured deflection at distance r from the load point, and ℓ is the radius of relative stiffness calculated above. The k value calculated is the dynamic value, to change to a static value, it is divided by two for the final result, shown in Figure 9.2.

The k values for the inside lane is consistently higher than the outside lane for each cell. Cell 424, the cell with the latest early loadings, is nearly the same as the control, while Cells 124 and 224, the cells with the earlier loadings, are closer to 200 lbf/in^2/in.
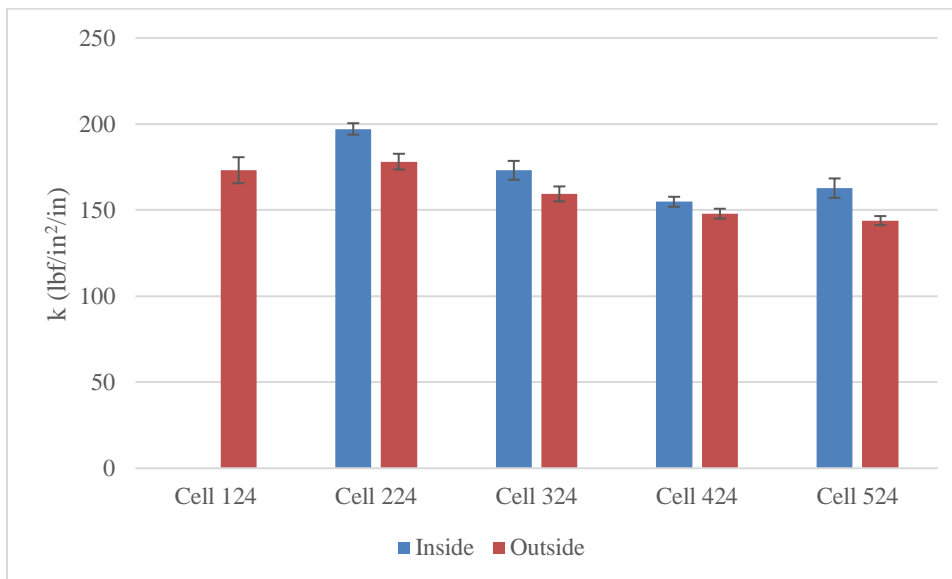
Figure 9.2 k-values for cells

9.1.2 Elastic Modulus of Concrete Pavement

The elastic modulus of the pavement is back-calculated using the FWD data from the center of the slab and changed to a static value using the following equation:

$$E_{PCC} = 0.8 \cdot \frac{12 \cdot \ell^2 \cdot (1 - \mu^2) \cdot k}{h^3} \tag{10}$$

where ℓ is the radius of stiffness, k is the modulus of subgrade reaction, μ is the Poisson's ratio, 0.15, and h is the height of the slab, 6 inches. The calculated values are shown in Figure 9.3. Values range from approximately 7.5 to 8 million psi with no discernable pattern between inside and outside lanes or between cells. Neither the number of loadings nor the different load sizes influence the elastic modulus.
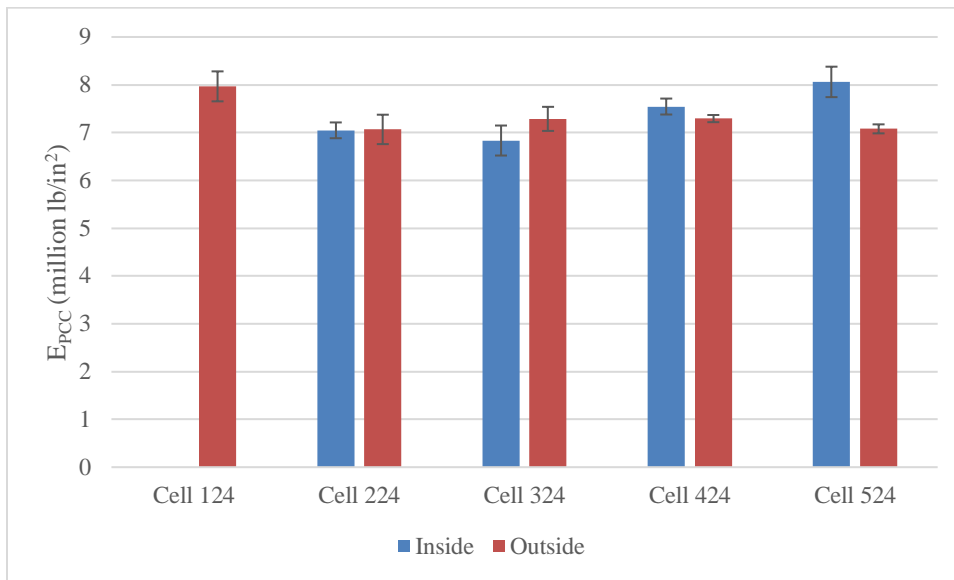
Figure 9.3 Elastic modulus for cells

9.1.3 Load Transfer Efficiency

The load transfer efficiency (LTE) is the ability for a joint to transfer a wheel load from one slab to another. This efficiency can affect the deflections of the slab and the overall structural performance of the pavement. LTE uses FWD data from either side of the joint. LTE was calculated using the following equation:

$$LTE = \frac{\Delta_{UL}}{\Delta_L} \times 100\% \tag{11}$$

where Δ_{UL} is the deflection on the unloaded slab and Δ_L is the deflection on the loaded slab. For example, Station 1, shown in Figure 9.4, will use the sensor located at +12 in (304 mm) from the load

point for the deflection under the unloaded slab. Station 2 (Figure 9.4) would use the sensor -12 in (-304 mm) from the load point.
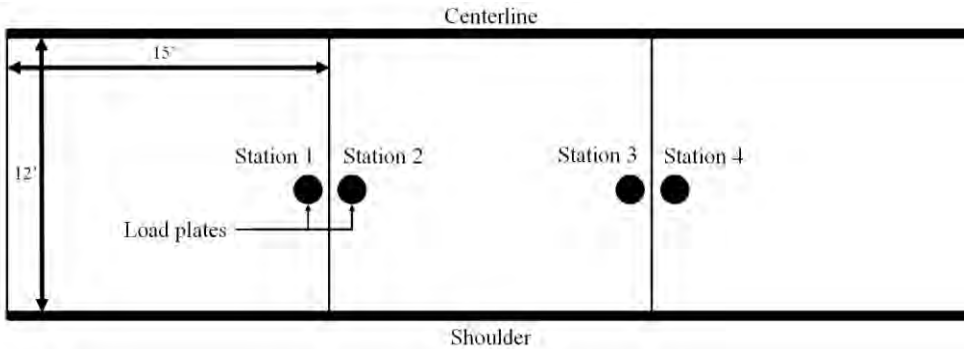
Figure 9.4 Location of LTE measurement stations within a cell

Within each cell, two joints were used for data collection and each joint had two stations as shown in Figure 9.4. Station 1 and 3 will be referred to as Approach and Stations 2 and 4 will be Leave. The calculated results for 2017 and 2018 are shown respectively in Figure 9.5 and Figure 9.6. There is no severe reduction in LTE between 2017 and 2018. For a majority of cells, the inside lane has a higher LTE than the outside lane, with the exception of Cell 224 and Cell 324 Leave Station in 2018.
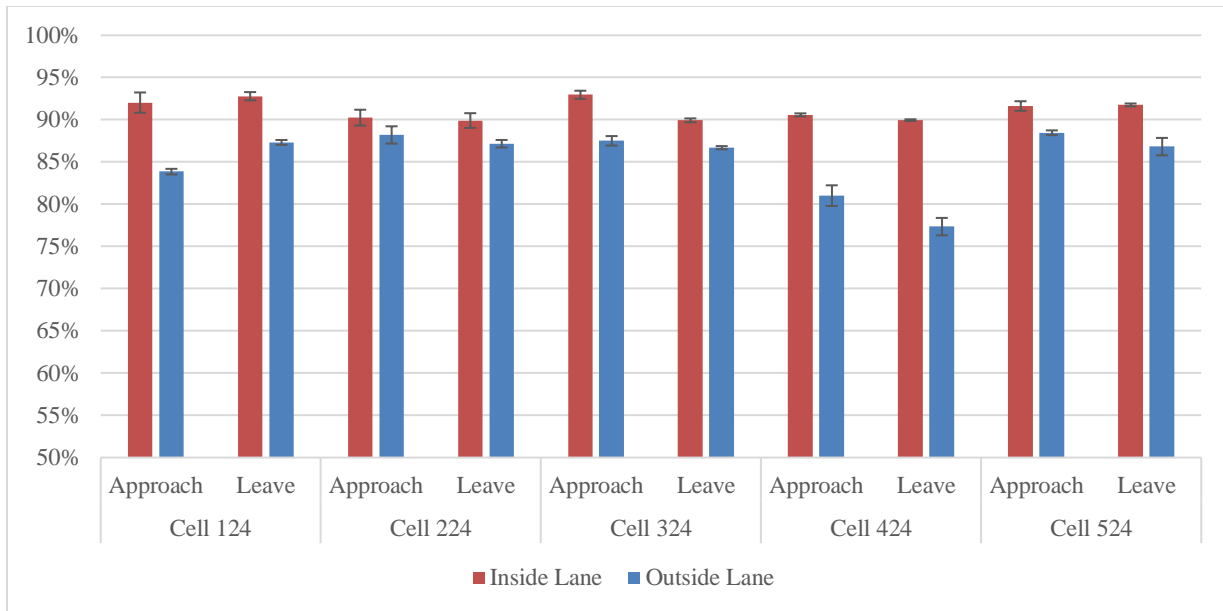
Figure 9.5 LTE results for cells in 2017
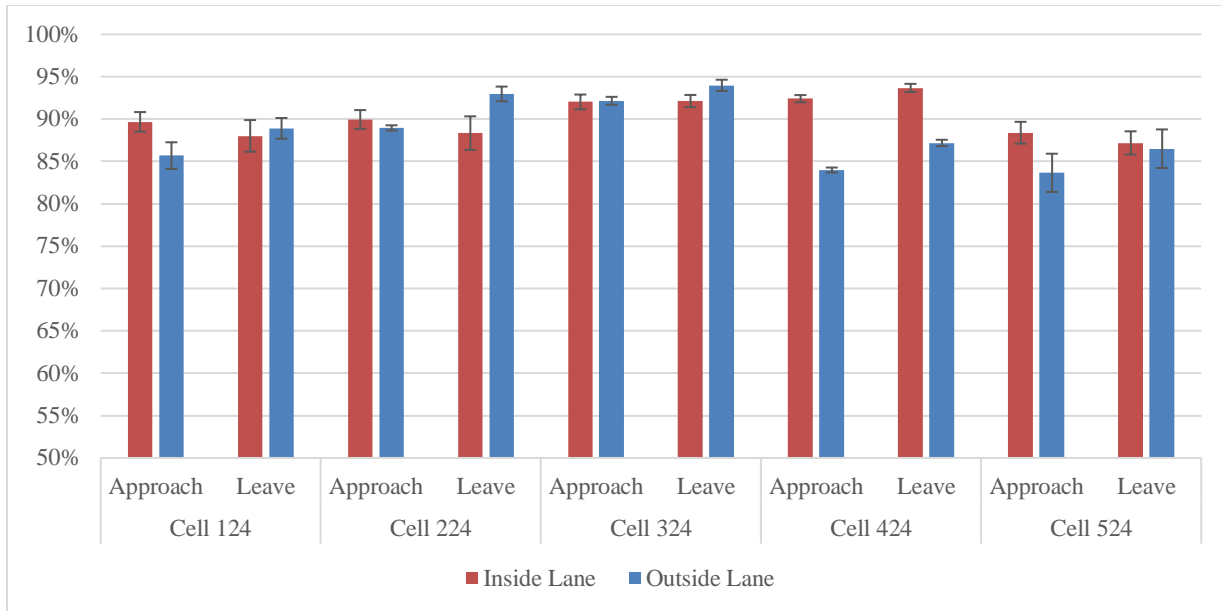
Figure 9.6 LTE results for cells in 2018

9.2 LONG-TERM FWD DATA ANALYSIS

The load transfer efficiency (LTE) of transverse joints profoundly affects the performance of jointed plain concrete pavements. Falling weight deflectometer (FWD) data collected by MnDOT was used to evaluate the effect of early loading on the LTE of transverse joints.

The LTEs were calculated from the results of the FWD tests when the load plate was placed tangentially to the edge of the joint. The loaded slab joint deflections were measured under the center of the load plate (6 inches [152 mm] away from the joint). The deflections of the unloaded slab were also measured at some distance (6 inches [152 mm]) from the joints. The ratio of the deflection of the unloaded slab to the deflection of the loaded slab was defined as the load transfer efficiency of the joint.

FWD testing was conducted nine times between October 2017 and April 2021. Deflections were measured for two joints in Cells 124-424 for both inside and outside lanes. The testing was performed both for the FWD loading applied on the approach slab and the leave slab surrounding the joint. Short lengths of Cells 524 and 624 did not allow for full FWD testing, so only one joint was tested for Cell 524.

Figure 9.7 and Figure 9.8 show computed load transfer efficiencies for the inside and outside lanes, respectively. It can be observed that the LTEs for both lanes exhibited a significant seasonal variability between 70% and 95% suggesting an adequate load transfer level. It is noted that in September of 2017, i.e., less than 3 months after construction, LTE for the inside lane, where the heavier early loads were applied, were higher than the outside lane LTEs. Moreover, LTEs for Cells 124 and 224 were similar or higher than LTEs for Cell 324 and 424 indicating that early loading by either size vehicle did not have a significant effect on initial joint performance.
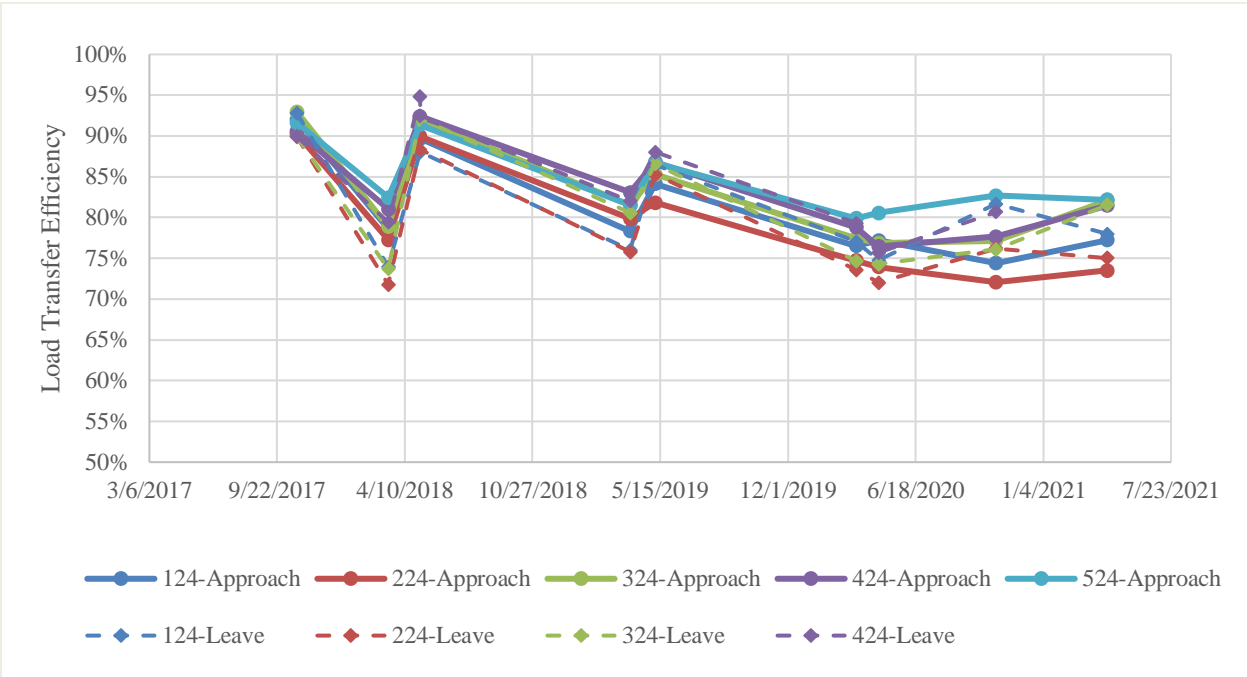
Figure 9.7 Load transfer efficiency for the inside lane
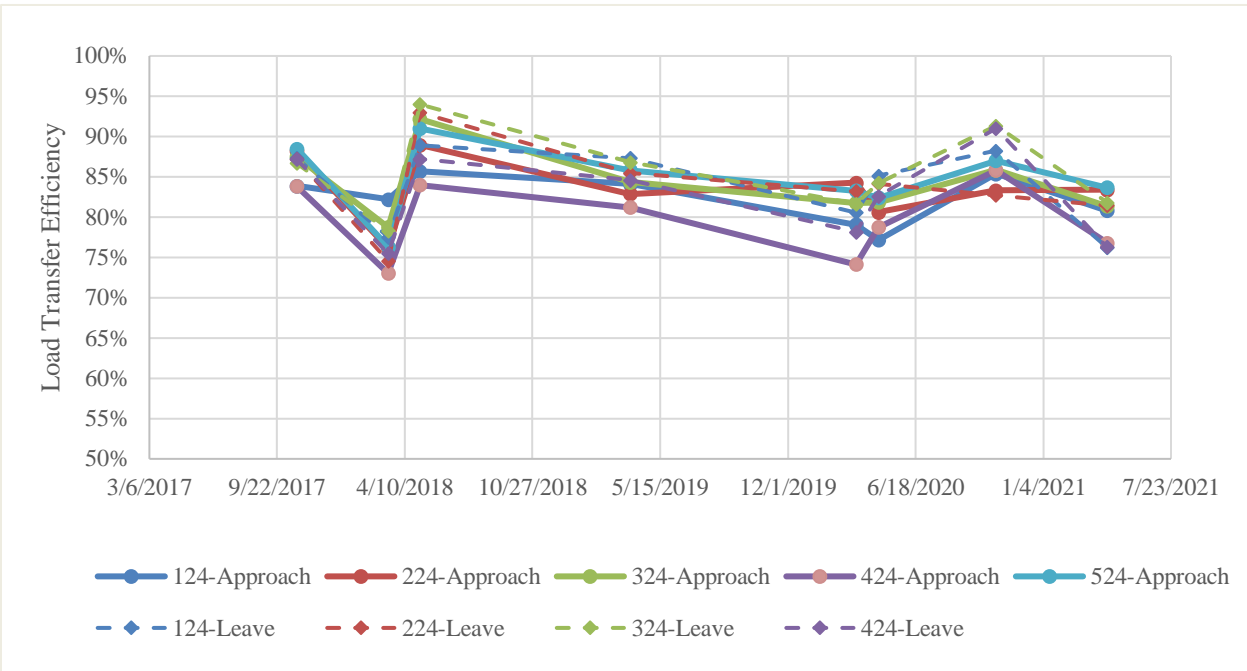
Figure 9.8 Load transfer efficiency for outside lane

It can be observed from Figure 9.7 that with time LTEs for Cells 124 and 224 become lower than LTEs for Cell 324 and 424. Moreover, all testing in 2020 and 2021 for the control Cell 524 resulted in LTEs not lower than LTEs for the remaining cells on the same day. That could potentially indicate a detrimental

effect of early loading on dowel performance. However, the analysis of Figure 9.8 shows that on April 14, 2021, the measured LTE for the outside lane of Cell 424 was similar to the inside lane LTEs for Cells 124 and 224. This indicates that other factors, such as construction or material quality or environmental factors, may have a greater influence on the joint load transfer efficiency than the early loading conducted shortly after construction of the MnROAD cells.

Chapter 10:   PETROGRAPHIC ANALYSIS

One of the concerns for early opening to traffic of concrete pavements is that friction loads generated by truck tires may cause damage of the concrete pavement surface due to dislocation of the aggregates while concrete strength is low. In addition, truck traffic may remove a portion of the curing compound reducing curing effectiveness and increasing the potential of durability problems.

To evaluate the effect of the concrete loading on the concrete surface damage after four years since the pavement placement, six cores were extracted by MnDOT from the locations subjected to various degrees of sequential early loading:

- Cell 124, early loading, wheel path location
- Cell 124, early loading, between the wheel paths location
- Cell 424, moderately early loading, wheel path location
- Cell 424, moderately early loading, between the wheel paths location
- Cell 524, no early loading, wheel path location
- Cell 524, no early loading, between the wheel paths location

According to the results of the petrographic analysis performed by American Engineering Testing, Inc., the overall condition of the six concrete core samples was judged to be good (Appendix H). None of the cores exhibited visual evidence of gross deterioration or large-scale cracking/fracturing. They were fairly well consolidated and purposefully air-entrained. However, the cores did exhibit signs of age and weathering.

The top surface condition of the cores was broom-finished/drag-textured. Mortar erosion and shallow scaling exposing numerous fine aggregates and a few coarse aggregate particles were observed for all cores. However, only about 5% of the area was shallowly scaled for cores from Cell 124 and from the wheel path location of Cell 424, while the cores from Cell 524 not exposed to early opening and between the wheel path of Cell 424 not directly exposed to friction tire loading exhibited approximately 10% of the area shallowly scaled. Moreover, the depth of the scaled surface for the core from the Cell 124 wheel path location was only 0.07 inches (2 mm), while for all other cores it was approaching 0.11 inches (3 mm). Therefore, it can be concluded that the early loading at MnROAD did not result in concrete surface scaling.

The cores also exhibited fine, sub-vertical microcracking. For Cell 124 cores the depth of the microcracks was 0.16 and 0.28 inches (4 and 7 mm) for the wheel path and between the wheel path locations, respectively. For the remaining cores, the depth of the microcracks varied from 0.2 to 0.51 inches (5 to 13 mm) while one microcrack of the core from Cell 424 between the wheel paths' location propagated to 1 inch (25 mm). While 1 inch is the deepest observed microcrack, it does not seem to be caused by early loading since Cell 424 had minimal exposure to early loading and cells with more severe load cycles did not display this depth of microcracking. The control, Cell 524, had a few microcracks that reached a depth of 0.43 inches (11 mm). The most common length of microcracking on typically loaded pavement is 0.4 to 0.8 inches (10 to 20 mm) into the core (Stutzman, 1999). It can be observed that the early loading did not increase the extent of microcracking of the top concrete pavement surface.

Finally, the cores from Cell 124 exhibited the lowest levels of carbonation. No carbonation was observed for the core taken from the wheel path. Carbonation ranged from negligible to 0.07 inches (2 mm) deep from the top surface and spiked to 0.24 inches (6 mm) deep along sub-vertical microcracks for the core taken between the wheel paths. Other cores exhibited carbonation up to 0.51 inches (13 mm) deep. Carbonation for control Cell 524 ranged from negligible to 9 mm along sub-vertical microcracks.

Based on these observations it can be concluded that the early age trafficking of Cells 124 and 424 did not cause top concrete surface damage or long-term durability problems.

Chapter 11:   FINITE ELEMENT ANALYSIS

Since the testing slabs at MnROAD did not fail even though it was loaded when the concrete strength was lower than design strength, a finite element analysis was performed to determine the stresses in the PCC. In pavements, when the tensile stress reaches the flexural strength, it does not necessarily mean that it will fail. Flexural strength of a pavement is measured using a simply supported beam which has a less effective stress distribution than a slab on grade. Therefore, the flexural strength of an in-situ pavement will be greater than measured with this method (Roesler, 1998). Also, Freeseman et al (2016) proved that the strength variability was greater at critical locations which could have also affected the PCC stresses.

To farther investigated PCC stresses, a finite element analysis was performed using ISLAB2000 to estimate the stresses caused to the MnDOT cells using the snowplow. The snowplow was simulated using two separate loadings by a 11-kip single axle and a 20-kip tandem axle. Different load locations and temperature gradients were used to farther examine potential stress simulations. The pavement structure created in ISLAB2000 was similar to the MnROAD with the following properties:

- Slab thickness: 6 in
- PCC modulus of elasticity and Poisson's ratio: 3,000,000 psi and 0.15, respectively.
- PCC coefficient of thermal expansion and unit weight: 5.0E-6 1/$^{\circ}$F and 0.087 lb/in^3, respectively
- Base thickness and modulus of elasticity: 6 in and 40,000 psi, respectively
- Interface condition between the PCC slab and base: unbonded
- Transverse joint spacing: 15 ft
- Subgrade stiffness: 250 psi/in
- Lane-shoulder joint LTE: 20%
- Linear temperature distribution through the slab thickness; the difference between the top and bottom PCC surfaces: 10 $^{\circ}$F or 0 $^{\circ}$F
- Axle type: single
- Axle weight: 12,000 lb or 18,000 lb
- Wheel tire pressure and wheel aspect ratio (length-to-width ratio): 100 psi and 1, respectively.
- Axle position: distance from the slab/shoulder joint: 0 in or 12 in

The first simulation shows longitudinal stresses at the critical location at the edge of the pavement with a 10°F temperature difference between the top and bottom surface. As can be seen in Figure 11.1, the critical stresses appear directly below the load on the slab edge. As it would be expected, the combination of the positive temperature difference and single axle load (11-kip) placed at the slab/shoulder joint causes the highest maximum stress (243 psi) at the bottom PCC surface. Heavier tandem axle load (20-kip) still causes a significant stress (205 psi) if it is placed at the slab edge in the presence of a positive temperature gradient. Since the flexural strength of the concrete pavement ranged between 70 to 200 psi during testing, these stress levels could have easily caused slab failure.
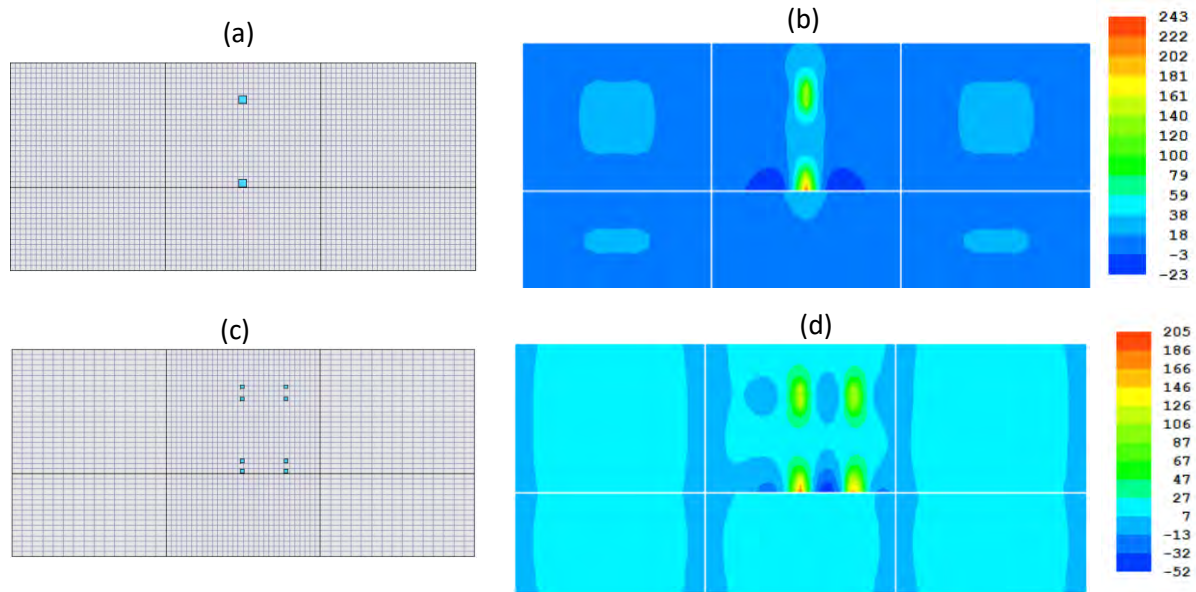
Figure 11.1 (a) ISLAB simulation with a single axle path on the edge with 10°F gradient and (b) bottom surface longitudinal stresses due to 11-kip single axle loading or (c) ISLAB simulation with a tandem axle path on the edge with 10°F gradient and (d) bottom surface longitudinal stresses due to 20-kip tandem axle loading.

When the original MnROAD was loaded early, the snowplow did not travel exactly on the edge. To simulate this, the load was moved 12 inches away from the edge maintaining the same snowplow loading and temperature gradient. This reduces the maximum stresses in the simulation to 150 and 127 psi for the single and tandem load, respectively (Figure 11.2). This move to a more favorable location also allows for the stresses at the slab edge to drop considerably, falling below 100 psi. This suggests that the wheel path in the experiment contributed to decreasing damage and preventing early failure.
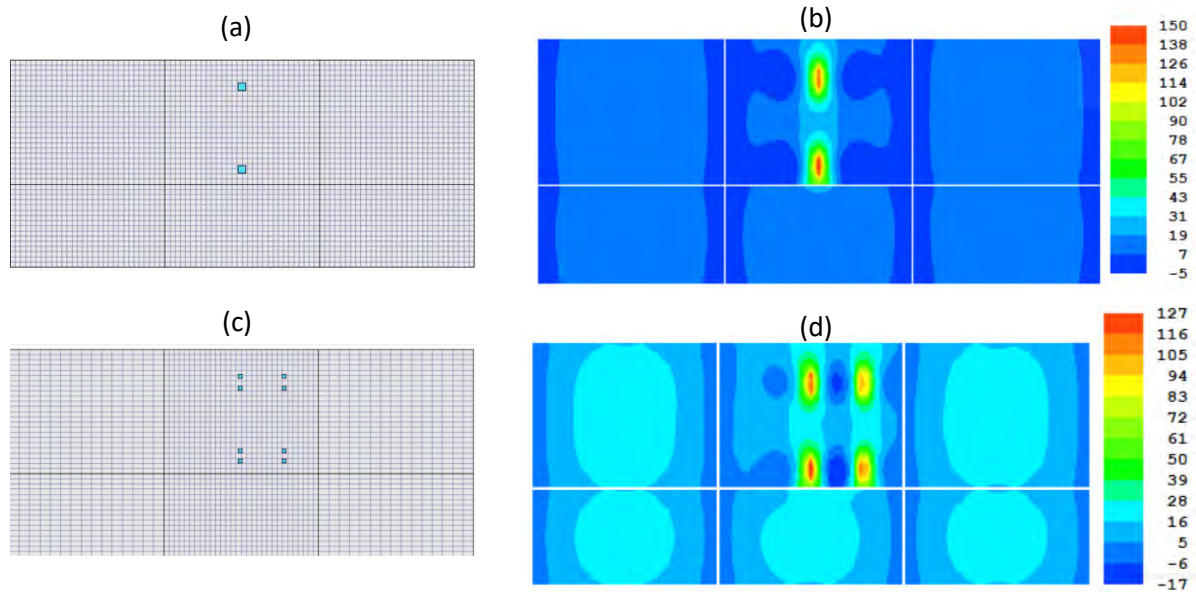
Figure 11.2 (a) ISLAB simulation with a single axle path 12 inches from the edge with 10°F gradient and (b) bottom surface longitudinal stresses due to 11-kip single axle loading or (c) ISLAB simulation with a tandem axle path 12 inches from the edge with 10°F gradient and (d) bottom surface longitudinal stresses due to 20-kip tandem axle loading.

Although MnROAD was initially loaded at 3 pm, the temperature gradient was not necessarily a high value like 10°F. While maintaining the snowplow loading and the loading location 12 inches away from the edge, the temperature gradient was changed from 10°F to 0°F. This caused the critical stresses to fall even lower, 132 and 110 psi for the single and tandem load, respectively (Figure 11.3). Changing the temperature gradient to a more favorable condition allows for an even greater decrease in stresses at the slab edge with stresses dropping to below 75 psi. The conditions of loading have a critical effect on the stresses within the PCC and may explain lack of visible damage and early failure.
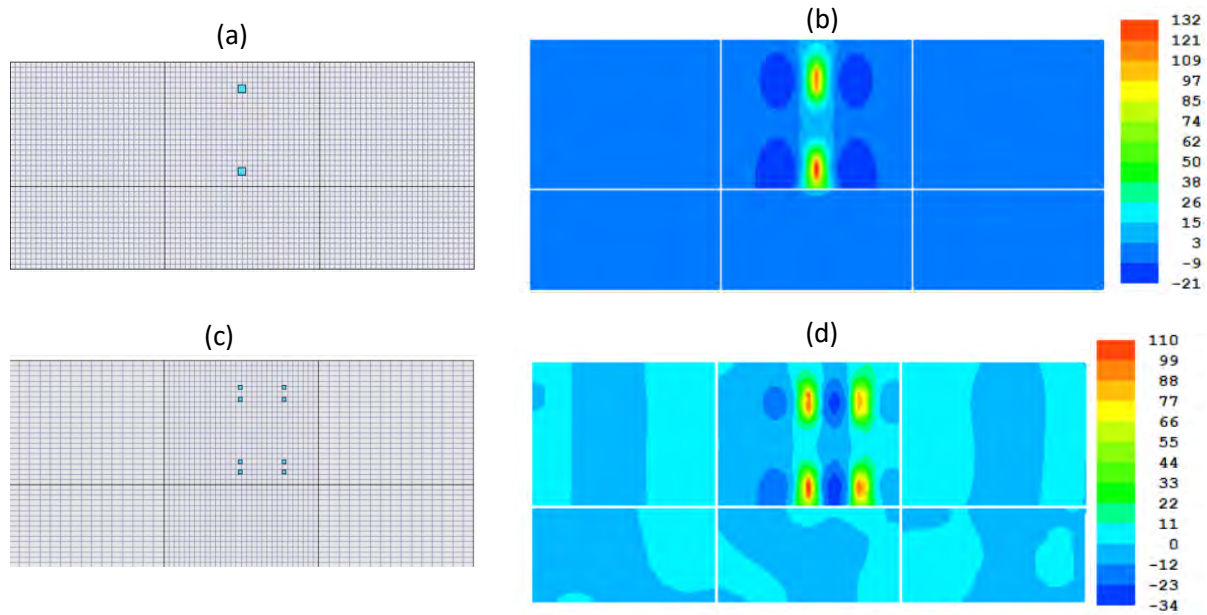
Figure 11.3 (a) ISLAB simulation with a single axle path 12 inches from the edge with 0°F gradient and (b) bottom surface longitudinal stresses due to 11-kip single axle loading or (c) ISLAB simulation with a tandem axle path 12 inches from the edge with 0°F gradient and (d) bottom surface longitudinal stresses due to 20-kip tandem axle loading.

Presence of the positive difference between the top and bottom concrete slab temperatures significantly increases the critical slab stresses. As it would be expected, the combination of the positive temperature difference and heavier axle load placed at the slab/shoulder joint causes the highest maximum stress at the bottom PCC surface. Moving this load away from the joint or reducing the temperature difference would decrease the critical PCC stresses. Lower axle load may cause a significant stress if it is placed at the slab edge in the presence of the positive temperature difference between the top and bottom PCC surface temperature. Therefore, to evaluate the risk of early opening of a concrete pavement to traffic it is important to estimate the probability of application of the heavy axle load near the critical location with a significant positive temperature gradient.

Chapter 12: MECHANISTIC-BASED EARLY OPENING DAMAGE ANALYSIS

As shown in the finite element analysis, potential for slab damage from early opening depends highly on axle weights, wheel path, temperature gradients, and PCC strength at time of load application. The same level of traffic may or may not cause slab damage depending on how favorable the conditions are and loading location. This may be resolved by restricting traffic to lightweight/passenger vehicles and only loading under a small or negative temperature gradient. While these methods would reduce the chance of damage, this makes it difficult to predict damage due to early opening while accounting for changeable traffic levels and environmental effects.

To address this challenge a probabilistic approach was applied to evaluate the risk of early opening. The user provides the initial strength at which the pavement is expected to be opened to traffic, the number of expected vehicles until the concrete strength reaches the design level, and the axle spectrum frequency. For each vehicle pass, the procedure predicts critical stresses due to traffic loading and compares it with the corresponding strength. To compute the stresses, the procedure selects the following parameters:

- Axle weights and types are randomly selected according to the user-provided axle spectrum frequency.
- Axle wheel path assuming the normal distribution with the given wheel path and standard deviation.
- Effective temperature gradient selected based on the effective temperature difference frequency for the location of the pavement section and the construction month.

A strength is then calculated based on the random time chosen to open to traffic. If the critical stress is greater than the corresponding strength then the pass may cause damage and is counted as a failure. Each passing vehicle is simulated separately after which the total failures summed up. This total number of failures is then divided by the number of vehicles to obtain the probability of failure for a single opening of traffic simulation. This analysis is repeated multiple times and the average probability of failure from all simulations is computed. The reliability of the pavement to sustain early opening is then found by subtracting the average probability of failure from 100%.

Damage was considered in terms of transverse cracking and dowel damage. These considerations have similar procedures when determining the stress levels at which a slab would fail in either aspect as well as the reliability for this damage to occur. Both damage criteria will be used when determining the optimal time to open a pavement to traffic. The details of this probabilistic simulation for the analysis of pavement reliability to resist damage is provided below.

12.1 PCC PROPERTIES ESTIMATION

For this analysis, concrete properties must be predicted at any time from when the pavement is opened to early traffic to when the PCC design strength is reached. The following concrete properties should be predicted:

1. Concrete flexural strength for transverse cracking damage analysis,
2. Concrete compressive strength for dowel damage analysis,
3. Concrete modulus of elasticity for analysis of both damage types.

It is necessary to determine the concrete maturity at any time after opening to traffic. The user is expected to provide the strength-maturity models similar to those reported in Figure 2.3. Generally, prediction of concrete maturity is quite complicated and demands extensive details on the ambient condition. However, the analysis of the maturity data collected at MnROAD shows that after concrete solidifies, the maturity development can be estimated from maturity based on the mean PCC temperature. In this study, the following simplified procedure was proposed:

$$TTF(t) = TTF_0 + T_m(t - t_0) \tag{12}$$

where TTF_0 is the concrete maturity at the time of opening to traffic, T_m is the estimated mean monthly PCC slab mid-depth temperature, and $t - t_0$ is the time from opening to traffic, hours.

The mean monthly PCC slab mid-depth temperature depends mainly on pavement location, construction month, and concrete strength. To simplify this step, a database was made to predict mean monthly PCC temperatures, assuming standard concrete thermal properties, as described in MEPDG, and concrete slab thicknesses, ranging 6 to 12 inches (AASHTO, 2015). Forty cities were chosen around the United States and the Enhanced Integrated Climate model, incorporated into the AASHTOWare Pavement ME Design software, was used to predict a generalized mean monthly PCC temperature for each location.

To determine the accuracy of this model, the concrete flexural strength development for MnROAD was made using the model shown in Figure 2.3 (left) and estimated using Equation (12). This prediction was compared with the flexural strength determined using the same strength-maturity model and field-measured maturity. Figure 12.1 shows a very good agreement between the strength predications.
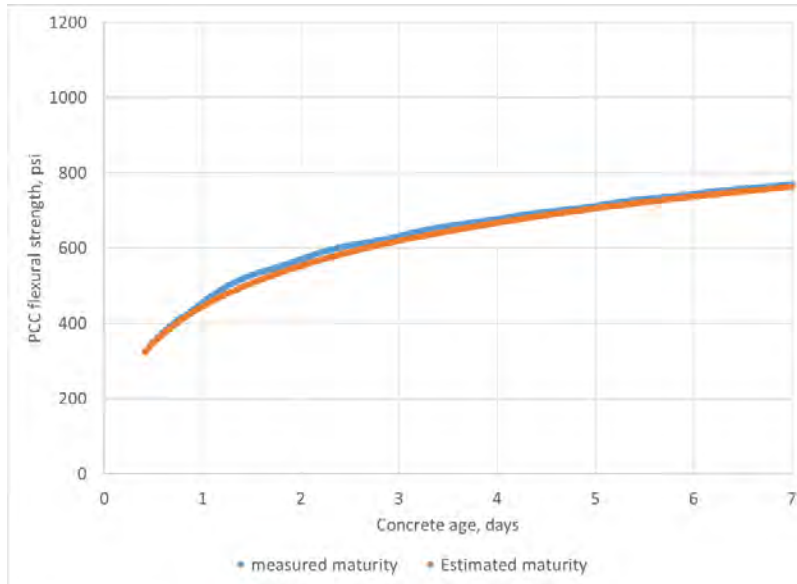
Figure 12.1 Predicted verses measured strength gain over time.

The maturity method will only predict the mean concrete temperature at any given time. The spatial variability of the concrete strength at an early age is much higher than for mature concrete and therefore must be accounted for in this analysis (Freeseman et al, 2016). A young concrete will have a high variability (typically about 25%), however as concrete matures, the variability becomes smaller (around 6%). The following model was developed to evaluate the strength coefficient of variation, COV_R:

$$COV_R = C \; Exp(-D \times TTF) + E \tag{13}$$

where *C, D, E* are calibration coefficients with default values of 0.25, 0.001, and 0.075, respectively. To account for the strength spatial variability, the following expression for the damage analysis strength is proposed:

$$R_C = R_M(1 - c \; COV_R) \tag{14}$$

where R_M is the maturity-estimated strength (flexural or compressive), R_c is the damage analysis strength (flexural or compressive), and *c* is a coefficient with a default of 1. The concrete modulus of elasticity can be estimated using the ACI equation:

$$E_c = 57{,}000 \; f'^{0.5}_c \tag{15}$$

where f'_c is the compressive strength, psi.

12.2 TRAFFIC CHARACTERIZATION

Traffic characterization is an important consideration when loading a concrete pavement early. A set level of traffic would not encompass all the possible loadings the pavement may be exposed to. If a set value is too high, the opening strength is not the most efficient whereas if the set traffic level is too low the pavement can easily be overloaded. Accounting for the expected traffic conditions for each pavement separately is critical to an accurate prediction.

To characterize the traffic, the user defines the daily truck traffic per lane and the type of roadway. Mean wheel path and traffic wander are assumed to be 18 and 10 inches, respectively. The traffic spectrum characterization for this study was adapted from Pavement Designer, a program developed by the American Concrete Pavements Association. This program is similar to that from MEPDG but is a simplified version that is less computationally expensive. This will populate the axle spectrum with single, tandem, and tridem axle loads as well as the axles per 1000 trucks for each axle type. If the number of axles is less than 1000, then the axle is ignored in this analysis.

12.3 CURLING/WARPING CHARACTERIZATION

A temperature gradient can cause curling or warping in a slab, where the edges or center of the slab may attempt to lift off the ground causing critical stress points. The effect of slab curling and warping was characterized through the effective temperature gradient distribution (Khazanovich, 2001). Temperature distributions and shrinkage strains through the PCC thickness is necessary to predict temperature distributions from the time of opening to when the PCC design strength is met. Typically, this would require sophisticated modeling, but a simplified procedure was used using the same database that predicts the mean monthly PCC temperature for 40 locations throughout the United States. To perform the analysis, the user should select the location and the construction month. The computed temperature differences are adjusted by the built-in curling temperature difference assumed to be equal to $10^{\circ}F$. Figure 12.2 shows an example of the resulting frequencies effective temperature gradient for July at MnROAD.
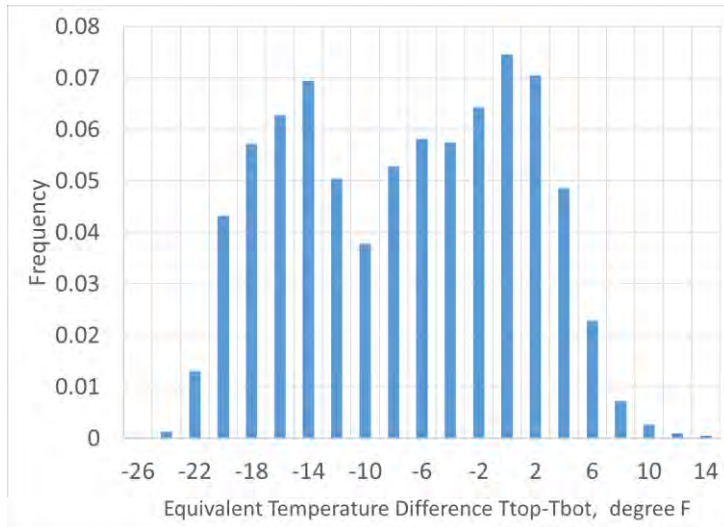
Figure 12.2 Temperature frequency analysis for July in Minnesota

12.4 TRANSVERSE CRACKING PERFORMANCE

Transverse cracking is a major damage in a slab loaded before the design strength has been met. Cracking initiates when the total mid-slab edge stress from the axle loading and temperature curling in greater than the flexural strength at the time of loading. To compute the axle loading stress independently from temperature curling stresses, it is assumed that an early age pavement does not significantly separate from the subgrade. This also permitted using the dynamic coefficient of subgrade reaction for the moving axle load stress calculation and the static coefficient of subgrade reaction in the curling analysis. The static coefficient of subgrade reaction was assumed to be half the dynamic coefficient of subgrade reaction. The total stress is obtained by summation of the axle-induced and temperature curling stresses.

An analysis was performed on a randomly selected time for each vehicle pass to determine the concrete modulus of elasticity and flexural strength using the following procedures:

a) Estimate concrete maturity using Equation (12);
b) Determine concrete flexural and compressive strength using corresponding strength-maturity relationships;
c) Adjust strengths to account for spatial variability using Equation (14); and
d) Determine the concrete modulus of elasticity using Equation (15).

The longitudinal stresses at the bottom of the concrete slab caused by axle loading are computed using the neural networks adapted from the rapid solutions developed under the NCHRP 1-37A project (Khazanovich, 2001). The temperature curling stresses were computed using Westergaard's solutions (Westergaard, 1926). Axle weight and traffic wander are randomly selected, and the temperature difference is randomly selected based on the effective temperature frequency analysis shown in Figure 12.2.

If the combination of axle-induced and temperature curling stresses exceeds the flexural strength then that run is counted as a failure. The total number of failures is summed for each expected vehicles and is used to compute the probability of failure for each simulation. It is recommended to conduct multiple simulations (between 100-800 simulations) and then average the probability of cracking failure between all simulations. The reliability that cracking will not occur is then calculated using the following equation:

$$CrRel = 100\% \times \left(1 - \frac{1}{N_{simulations}} \sum_{i=1}^{N_{sim}} \frac{N_{failures,i}}{n_{vehicles}}\right) \tag{16}$$

where $CrRel$ is the cracking resistance reliability, $N_{failures}$ is the total number of failures for simulation i, $n_{vehicles}$ is the total number of vehicles in one simulation, and N_{sim} is the total number of simulations.

12.5 DOWEL BAR PERFORMANCE

Heavy axle loading before the PCC reaches design strength may lead to excessive bearing stresses acting beneath the dowels in transverse joints. This may lead to micro or macro cracking in the PCC surrounding the dowels, will reduce dowel effectiveness, and compromise the long-term pavement performance.

Dowel-concrete interaction is a complex engineering problem. Tabatabae and Barenberg (1980) have proposed modeling dowel bars as beam elements based on the classical solution for a beam on Winkler foundation shown in Figure 12.3. This solution relates the shear force transmitted by the dowel with the concrete bearing stresses as shown in Figure 12.4.
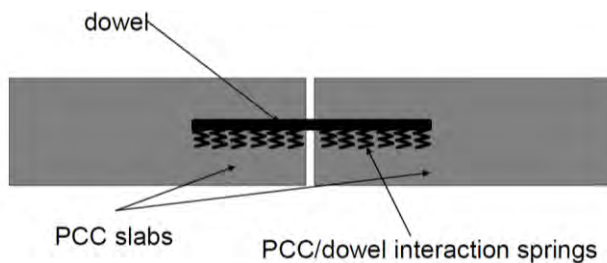
Figure 12.3 Tabatabaie and Barenberg model of doweled joints of PCC.
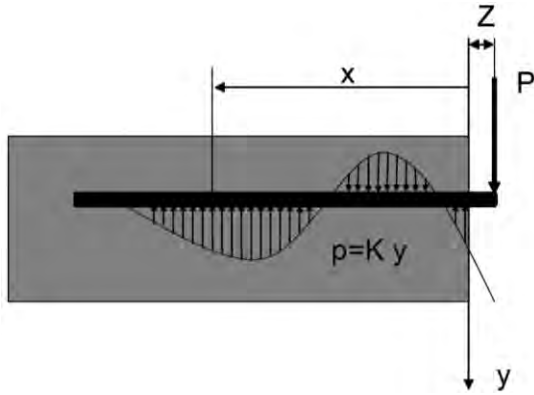
Figure 12.4 Dowel bearing stress distribution.

The maximum bearing stress can be obtained using the following equation:

$$\sigma_{c,max} = \frac{K_d\, P_d(2 + \beta\, Z)}{4\,\beta^3\, E_d\, I_d} \tag{17}$$

$$\beta = \sqrt[4]{\frac{K_d}{4\, E_d\, I_d}} \tag{18}$$

where σ_c is the maximum concrete bearing stress, P_d is the shear load transferred by the dowel, β is the relative stiffness of a dowel bar embedded in concrete, E_d is the modulus of elasticity of dowel. For a steel dowel E_d = 29,000,000 psi. K_d is the modulus of dowel support, psi/in, I_d is the moment of inertia of the dowel bar cross section (0.9 times the moment of inertia for a solid circular cross section), d is the dowel diameter, in, and Z is the joint opening.

The shear force transferred by a single dowel is related to the joint deflections of the leave and approach slab at the dowel location as follows:

$$P_d = J_d\, (w_a - w_l) \tag{19}$$

where w_a is the deflection of the approach side of the joint at the dowel location, w_l is the deflection of the leave side of the joint at the dowel location, and J_d is the dowel-concrete slab connection shear stiffness computed as

$$J_d = \frac{1}{Z^3 \frac{1+\Phi}{12\, E_d\, I_d} + \frac{2+\beta\, Z}{2\,\beta^3\, E_d\, I_d}} \tag{20}$$

$$\Phi = \frac{24(1 + \mu_d)}{A_d \, Z^2} \tag{21}$$

where μ_d is Poisson's ratio of the dowel material and A_d is the dowel cross-sectional area effective in shear.

Deflections of the leave and approach side of the joint are needed to determine the dowel bearing stresses. This can be determined through a finite element analysis, like ISLAB200, but for the purposes of this damage analysis, a rapid solution was developed to determine critical deflections due to single and tandem axle loading for three dowels located in the right wheel path.

To reduce the number of cases required for development of the rapid solutions, the principle of similarity was adapted in this study. The similar structure concept permits the computation of deflections in a multi-layer system (a concrete slab with a base on a subgrade) from those in a similar system. This concept has been used in the MEPDG for both the JPCP and continuously reinforced concrete pavement (CRCP) cracking models (Khazanovich, 2001). The two systems can be considered equivalent as long as their deflection basins are scalable, meaning that:

$$w_I(x_1, y_1) = \lambda_{def} w_{II}(x_2, y_2), \tag{22}$$

where w are deflections, x and y are horizontal coordinates, λ_{def} is the scaling factor for deflections (dependent only on properties of the pavement structure), and the subscripts I and II denote pavement systems I and II, respectively.

The analysis of numerous ISLAB2000 cases for the combined effect of axle loading and temperature gradient on deflections of the slabs revealed that presence of a temperature gradient thorough the slab thickness affects slab deflections it does not significantly affect the deflection difference between leave and approach sides of the joint, especially if there is no significant separation between the concrete slab and the base. Considering that at the early age the joint is not opened wide and the slab remains in full contact with the base, the effect of slab curling can be ignored in the dowel bearing stress calculation.

In the absence of temperature gradients, the following sufficient conditions for the slab similarities were identified:

- Two pavement systems have same in-plane geometry, i.e. number of slabs and slab horizontal dimensions.
- The load footprint geometries and load positions are the same for both systems.
- The corresponding slab joints, i.e. transfer joints, lane/shoulder joints, and longitudinal joints, have the same load transfer efficiency.
- The radii of relative stiffness, ℓ_I and ℓ_{II}, are equal. The radius of relative stiffness for a slab-on-grade system is defined as following:

$$\ell = \sqrt[4]{\frac{D}{k}} \tag{23}$$

where k is the coefficient of subgrade reaction and D is the flexural stiffness of the slab-on grade.

For a single layer slab, the flexural stiffness is defined as:

$$D = \frac{E\,h^3}{12(1 - \mu^2)} \tag{24}$$

where *h*, *E*, and μ are the slab thickness, modulus of elasticity, and Poisson's ratio, respectively.

For a two-layered slab consisting of a concrete layer and a base with an unbonded interface between the layers, the flexural stiffness is defined as a sum of the flexural stiffnesses of the individual layers. The deflections scaling factor has the following form:

$$\lambda_{def} = \frac{P_1 k_1}{P_2\,k_2} \tag{25}$$

where subscripts *1* and 2 denote the slab systems.

To develop a rapid solution for deflection calculation, the following ISLAB2000 finite element model of a six-slab system was adopted. The width for the slab modeling the effect of shoulder was set to 8 ft for a shoulder and the width for the slabs modeling traffic lanes was set to 12 ft. The slab length, i.e. transverse joint spacing, was set to 15 ft.

Two types of loading were considered: 18-kip single axle loading (see Figure 12.5) and 34-kip tandem axle loading (see Figure 12.6). The tire width and pressure were assumed to be equal to 8 in and 120 psi, respectively.
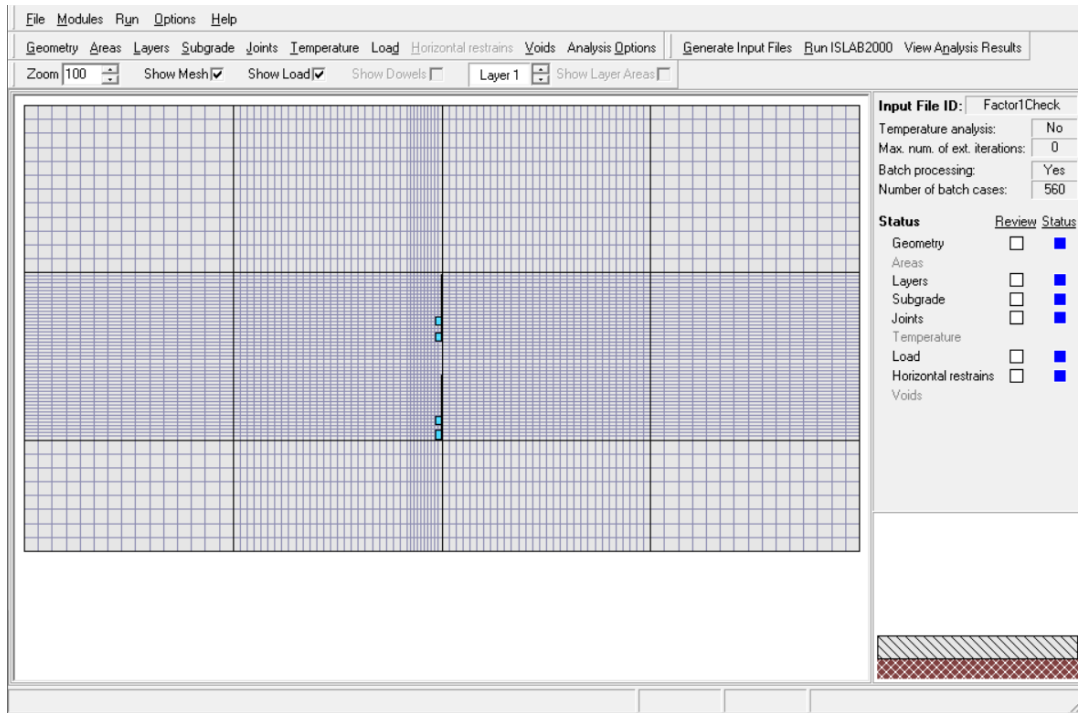
Figure 12.5 ISLAB2000 model for determination of transverse joint deflections due to single axle loading
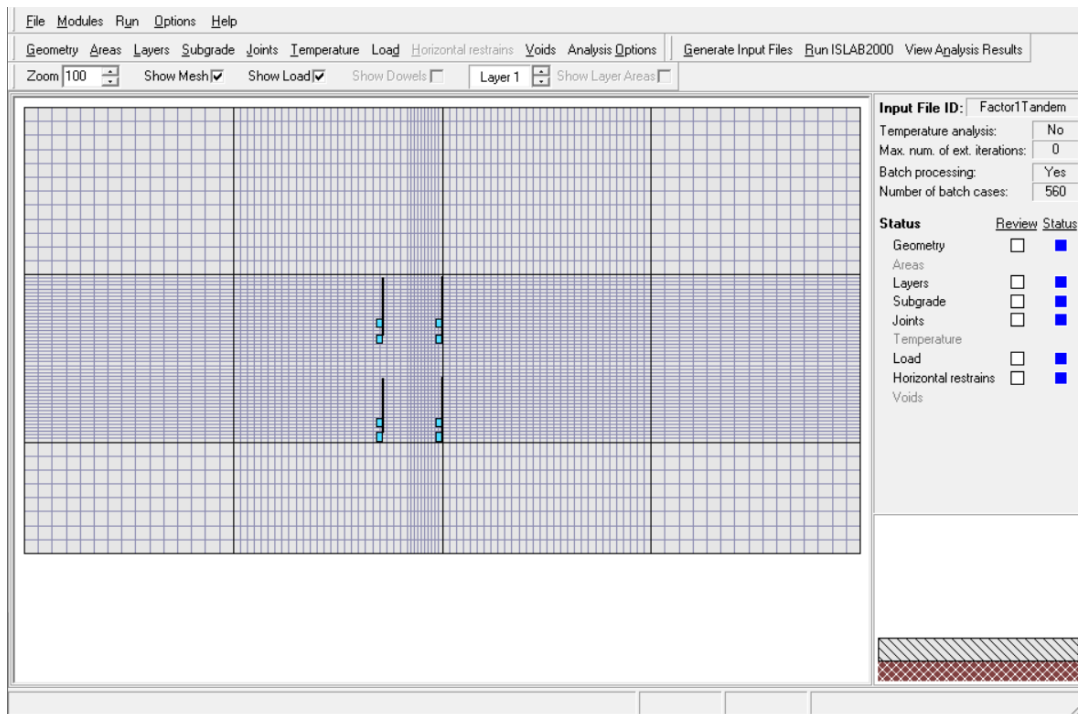
Figure 12.6 ISLAB2000 model for determination of transverse joint deflections due to tandem axle loading

A single layer slab system with the following parameters was considered:

- Slab thickness: 6 in
- Slab modulus of elasticity and Poisson's ratio: 4×10^6 psi and 0.15, respectively.
- The longitudinal joint deflection load transfer efficiency, LTE: 70%
- The lane/shoulder LTE: 20%
- The transverse joint LTE: varied between 20 and 95%.
- The distance between the axle load and the slab/shoulder joint varied from 0 to 36 in
- The coefficient of subgrade reaction varied between 3.125 psi/in and 1600 psi/in. It should be noted that this unrealistic range of this parameter permits to obtain solutions for pavement systems with the radii of relative stiffness ranging from 15 to 69 in.

The deflection at the loaded and unloaded side of the transverse joints 6, 18, and 30 in from the slab/shoulder joints were determined for each ISLAB2005 run and the rapid solutions were developed using modified MS-HARP neural network architecture (Banan and Hjelmstad, 1994; Khazanovich and Roesler, 1997).

The following procedure was used to calculate the deflections for this location for a two-layered pavements:

Step 1. Determine the flexural stiffness, D$_e$, for a two-layered pavement:

$$D_e = \frac{E_{pcc}\, h_{pcc}^3}{12(1 - \mu_{pcc}^2)} + \frac{E_{base}\, h_{base}^3}{12(1 - \mu_{base}^2)}$$

(26)

Step 2. Calculate the radius of relative stiffness:

$$\ell_1 = \sqrt[4]{\frac{D}{k_1}}$$

(27)

Step 3. Calculate the coefficient of subgrade reaction for the similar system using the condition $\ell_1 = \ell_2$

$$k_2 = \frac{D_e}{\ell_1^4}$$

(28)

Step 4. Using the rapid solutions, determine the differences between deflections at the loaded and unloaded sides of the joints 6, 18, and 30 in away from the slab/shoulder joint.

Step 5. Compute the temperature difference between deflections at the same location in the original two-layered system.

$$\Delta_{1,r} = \frac{P_1 k_1}{P_{ref}\, k_2} \Delta_{NN,r}$$

(29)

where $\Delta_{NN,r}$ is the difference between deflections of the loaded and unloaded sides of the joint at distance r from the longitudinal edge, P_{ref} is the axle load used to generate the training data for the Neural Networks (=17,000 lb for a single axle loading and 34,000 lb for the tandem axle loading), and P_{ref} is the axle load for the two-layered system.

Using these deflections, the maximum bearing stresses for dowels at this location can be determined using the following equation:

$$\sigma_{c,max} = \frac{K_d \ (2 + \beta \ Z)}{4 \ \beta^3 \ E_d \ I_d} J_d \ \Delta_{1,r} \tag{30}$$

The modulus of dowel support, K_d, is estimated using the following equations (Crovetti and Khazanovich, 2005):

$$K_d = 0.7651 \ E_{PCC} \tag{31}$$

where E_{PCC} is measured in psi and K_d is measured in psi/in.

Similar to the transverse cracking analysis, the early opening doweled joint damage analysis consist of two parts: comparison of bearing stress to allowable stress and a reliability analysis. Dowel bearing stress analysis due to loading be the standard legal truck having a 12-kip single axle load and two 34-kip tandem axle. In this analysis the dowel bearing stresses are compared with the allowable concrete bearing stresses, f_b, defined as

$$f_b = f_c' \frac{4 - d}{3} \tag{32}$$

where f_c' is concrete compressive strength at the time of traffic loading and d is the dowel diameter.

This maximum bearing stress is then compared to the allowable bearing stress. If the maximum is greater than the allowable, the simulation is a failure. The total number of failures is summed for each expected vehicle and is used to compute the probability of failure for each simulation. It is recommended to conduct multiple simulations (between 100-800 simulations) and then average the probability of dowel bar failure between all simulations. The reliability that dowel bar damage will not occur is then calculated using the following equation similar to that from cracking reliability:

$$DowelRel = 100\% \times \left(1 - \frac{1}{N_{simulations}} \sum_{i=1}^{N_{sim}} \frac{N_{failures,i}^d}{n_{vehicles}} \right) \tag{33}$$

where $DowelRel$ is the dowel performance reliability, $N^d{}_{failures}$ is the total number failures, i.e. bearing stresses exceed the bearing strength, for simulation i, $n_{vehicles}$ is the total number of vehicles in one simulation, and N_{sim} is the total number to simulations.

After opening to traffic, concrete strength, concrete modulus of elasticity, and allowable bearing stress will continue to increase with time. The increase in modulus of elasticity with also increase the dowel

bearing stresses under the same loading but at a slower pace than the allowable concrete bearing stresses.

To determine the optimal maturity or strength for early loading for the specified level of traffic requires considering both the cracking performance and dowel bar performance reliability. This allows the user to make an educated decision on when to open to traffic while understanding the risk of damage.

Chapter 13:   WEB-BASED TOOL

To implement the damage analysis, a web-based tool was developed for wide use. The computation models were implemented into a Fortran code while the web-based interface written in PHP and JavaScript permits the user to provide the input information for the analysis and displaces the analysis results. The application can be found at https://earlyopenpcc.azurewebsites.net. This tool requires users to input specific data about their project including location, construction month, traffic data, pavement structure properties, PCC design flexural strength, and maturity at time of opening (Figure 13.1). Strength relationships are defaulted based on MnROAD tests, but these settings and others can be modified as shown in Figure 13.2.

The tool then uses the mechanistic-based early opening damage analysis to analyze the project and returns cracking performance reliability, dowel performance reliability, and ESALs repetition to design strength (Figure 13.3). Plots show the increase in performance reliability with time if the pavement is opened at a higher compressive or flexural strength. Another plot shows the estimated number of ESALs the pavement will receive from a certain time after traffic opening until the PCC design strength is achieved. The final plot shows the predicted compressive and flexural strength gain with time. These results allow the user to analyze the risks involved with opening to traffic at the chosen maturity and then, if the reliabilities are below the desired level, to choose a better opening maturity value to repeat the analysis.

In this example shown in these figures, cracking and dowel bar performance reliability was calculated to be 86.3% and 72.8%, respectively. The pavement is expected to receive 757 ESALs after it opens to traffic when the PCC flexural strength is 295 psi and until it reaches the design flexural strength of 650

psi. If the traffic opening is delayed by 16 hours the PCC flexural strength would reach 422 psi, the cracking and dowel performance reliability would increase to 97.4% and 99.8%, respectively.

Figure 13.1 Opening screen for web-based damage analysis tool

Figure 13.2 Settings for the modulus of rupture in the maturity model
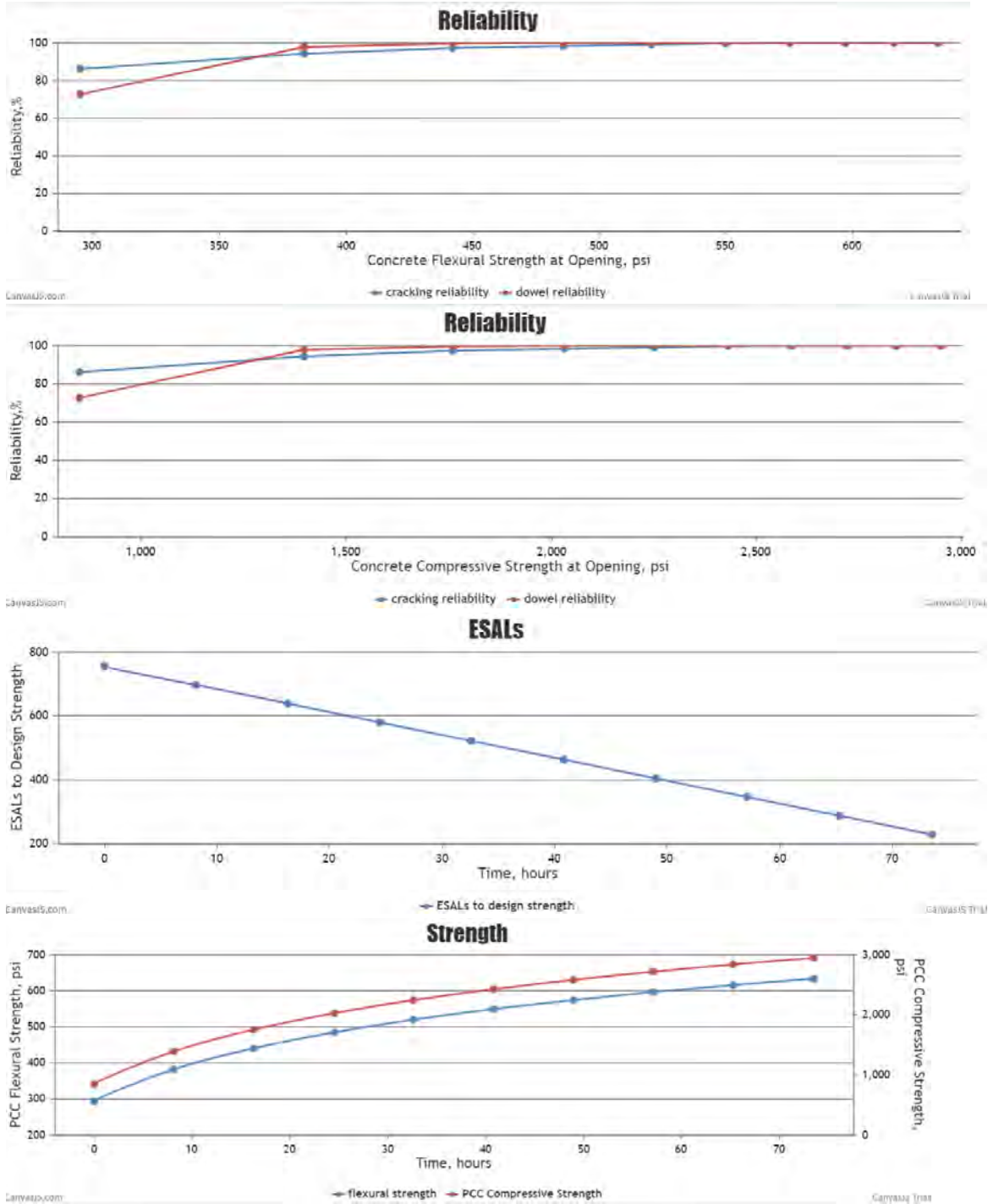
Figure 13.3 Graph outputs of the web-based tool

13.1 EXAMPLE SIMULATIONS

To demonstrate the effect of varying location, construction month, PCC thickness, and traffic level on the predicted opening time the following examples were simulated using the web tool. The remaining settings remain constant as shown in Figure 13.1 and Figure 13.2, the design PCC flexural strength is 650 psi, the maturity at time of opening is assumed to be 350°C-hr, and the opening flexural strength was found to be 295 psi.

- Case 1: Jacksonville, FL; paved in July; 6-inch PCC thickness; 200 trucks/day
- Case 2: Minnesota, MN; paved in October; 6-inch PCC thickness; 200 trucks/day
- Case 3: Minnesota, MN; paved in July; 9-inch PCC thickness; 200 trucks/day
- Case 4: Minnesota, MN; paved in July; 6-inch PCC thickness; 400 trucks/day

13.1.1 Case 1: Changing Location

For maturity prediction, a database of temperature data for 40 locations within the US was created. Case 1 investigates the effect of changing this location from Minneapolis, MN, to Jacksonville, FL. In this simulation, the cracking and dowel bar performance reliability raises to 93.9% and 76.5%, respectively. Because a higher anticipated mean monthly concrete temperature, the concrete would gain strength faster. The pavement will receive only 671 ESALs until the design strength is reached.

13.1.2 Case 2: Changing Construction Month

Cases 2 shows the effect of changing the construction month, in this case from July to October. Especially, in Minnesota, October is much colder than July which significantly slows the heat of hydration in the PCC, reducing the strength gain. In this simulation, cracking reliability does not change much with a value of 88.4%, however, dowel bar performance reliability falls significantly to 18% at the opening flexural strength of 295 psi. If the user were to delay opening until the flexural strength reached 450 psi, the dowel bar reliability rises to 99%. A second simulation should be run using this new opening criterion to adjust for this climatic change. This pavement will also receive 1935 ESALs before design strength is reached as compared to 757 ESALs in the initial example due to the slower strength gain rate.

13.1.3 Case 3: Changing PCC Thickness

Case 3 changes the PCC thickness from 6 inches to 9 inches. All other settings remain the same as the initial example. Since the PCC is thicker and therefore stronger, the cracking performance reliability and dowel performance reliability are 99.8% and 99.3%, respectively. This case also sees a slightly higher number of ESALs, 774, before design strength is reached.

13.1.4 Case 4: Changing Number of Trucks

Case 4 changes the traffic level from 200 to 400 trucks/day, both keeping a minor arterial traffic spectrum. All other settings remain the same as the initial example. When there are more expected truck loads, the cracking performance reliability falls to 75.1%, dowel performance reliability falls to 47.1%, and ESAL repetitions to design strength increases to 1513.7 ESALs. This simulation could benefit

from restricting traffic to smaller axle weights (changing the traffic spectrum) or to essential traffic only (lowering the number of trucks). If only essential trucks are allowed, lowering the trucks/day to 100, the cracking and dowel bar performance reliabilities raise to 96.2% and 84.9%, respectively.

These cases are summarized in Table 13.1.

Table 13.1 Example cases varying location, construction month, PCC thickness, and trucks/day

	Example	Case 1	Case 2	Case 3	Case 4
Location	Minneapolis, MN	Jacksonville, FL	Minneapolis, MN	Minneapolis, MN	Minneapolis, MN
Construction Month	July	July	October	July	July
PCC Thickness	6 in	6 in	6 in	9 in	6 in
Number of Trucks/day	200	200	200	200	400
Cracking Reliability	86.3%	93.9%	88.4%	99.8%	75.1%
Dowel Bar Reliability	72.8%	76.5%	18%	99.3%	47.1%
ESALs to design strength	756.9	670.9	1935.2	774.3	1513.7

Chapter 14:   CONCLUSIONS

The current strength criteria for opening concrete pavements to traffic are empirical and conservative. Data collected in this study review the behavior of modern concrete pavements when exposed to early opening. This extensive analysis of pavement performance, non-destructive testing, and embedded sensors could not identify any long-term damage associated with those early loadings, which includes the rutted concrete aside from roughness concerns. A summary of observations is presented below:

- Cells 124-424 and 624 were subjected to early loading: (2 to 10 hours after paving). No visible damage was observed in Cells 124-424.
- The analysis of strain gauge data and MIRA data did not reveal any significant difference in behavior of Cells 124, 324, and 424 compared to the control Cell 524, indicating absence of significant damage caused by the early loading.
- Some measured strains in Cell 224 were higher than the corresponding strains in other cells; therefore, presence of damage caused by early loading cannot be ruled out.
- The maximum HTI computed from MIRA measurements indicated possible presence of micro damage near the surface of Cell 224, but this phenomenon may have been caused by other factors and may not necessarily be a result of early loading.
- There is no effect on the Elastic Modulus or the modulus of subgrade reaction.
- Dynamic strain analysis was inconclusive.
- Static strain is unaffected from early loading.
- Different LTEs were observed in October 2017 for inside lane (subjected to traffic) and outside lane (no truck traffic). This trend was not confirmed in May 2018.
- No significant ride quality deterioration was observed.

Since the testing slabs at MnROAD did not fail even though they were loaded when the concrete strength was lower than design strength, a finite element analysis was performed to determine the stresses in the PCC. The finite element analysis has highlighted the area of primary concern, which is loading near the unsupported edge of the pavement. This concern may be resolved by 1) moving the load away from the edge to decrease the critical PCC stresses, 2) temporarily restricting traffic to lightweight/passenger vehicles, and/or 3) only loading the pavement edge under a small or negative temperature gradient.

Previous tasks in this study determined that the current criteria for traffic opening is overly conservative and that modern concrete pavements can safely open to traffic earlier than currently allowed. These conservative requirements can cause unnecessary delays and costs, especially for lightweight/passenger vehicles. This experiment showed no damage occurring at an estimated 73 psi flexural strength.

A mechanistic-based analytical tool was developed to better assess the risk of early opening by accounting for the rate of concrete strength gain, traffic volume, load characteristics, and pavement structure properties. Simulations performed with this tool compared well to data gathered at MnROAD. This tool can be used to open concrete pavements at the earliest strength or maturity without causing early damage or compromising long-term performance.

REFERENCES

AASHTO. (2017). AASHTO T 22 Standard Method of Test for Compressive Strength of Cylindrical Concrete Specimens, AASHTO Standards. Washington, DC: AASHTO.

AASHTO. (2018). AASHTO T 97 Standard Method of Test for Flexural Strength of Concrete (Using Simple Beam with Third-Point Loading), AASHTO Standards. Washington, DC: AASHTO.

AASHTO. (2017). AASHTO T 177 Standard Method of Test for Flexural Strength of Concrete (Using Simple Beam with Center-Point Loading), AASHTO Standards. Washington, DC: AASHTO.

AASHTO. (2015). *Mechanistic–Empirical Pavement Design Guide, Interim Edition: A Manual of Practice*. Washington, DC: AASHTO.

American Concrete Institute. (2001). *Accelerated Techniques for Concrete Paving* (ACI 325 11R-01). Farmington Hills, MI: ACI.

American Concrete Institute Committee 325. (1956-July). *Structural design considerations for pavement joints*. *Journal of the American Concrete Institute, 28*(1), 1-28.

American Concrete Pavement Association. (1994). *Fast-Track Concrete Pavements* (Report No. TB004.02P). Skokie, IL: American Concrete Pavement Association.

American Concrete Pavement Association. (n.d.). *Maturity testing*. Retrieved from http://wikipave.org/index.php?title=Maturity_Testing

American Engineering Testing. (2017). *Final Material Test Results for One Concrete Mix Identified as 3A21 AET* (Project No. 29-02550). Saint Paul, MN: American Engineering Testing.

ASTM International. (2016). ASTM C 597 Standard Test Method for Pulse Velocity Through Concrete, ASTM Standards. West Conshohocken, PA: ASTM International.

ASTM International. (2015). ASTM C 666 Standard Test Method for Resistance of Concrete to Rapid Freezing and Thawing, ASTM Standards. West Conshohocken, PA: ASTM International.

ASTM International. (2000). ASTM C 1074 Practice for Estimating Concrete Strength by the Maturity Method, ASTM Standards. West Conshohocken, PA: ASTM International.

Banan, M., & Hjelmstad, K. (1994). *Data-Based Mathematical Modeling: Development and Application* (SRS No. 590). Urbana, Il: Civil Engineering Studies, University of Illinois.

Carino, N. J. (2001). The Impact-Echo Method: An Overview. Paper presented at the American Society of Civil Engineers Structures Congress & Exposition, May 21-23, Washington, DC.

Crovetti, J. A., & Khazanovich L. (2005). *Early Opening of Portland Cement Concrete (PCC) Pavements to Traffic*. (WHRP Project 0092-01-04). Madison, WI: Wisconsin Department of Transportation.

Dave Van Deusen, T. B. (2018). *Report on 2017 MnROAD Construction Activities*. St. Paul, MN: Minnesota Department of Transportation, Research Services & Library.

Federal Highway Administration. (1994). *Accelerated Rigid Paving Techniques: State of the Art Report* (Special Project 201) (Report No. FHWA-SA-94-080). Washington, DC: Federal Highway Administration, U.S. Department of Transportation.

Freeseman, K., Hoegh, K., & Khazanovich, L. (2016) *Concrete Strength Required to Open to Traffic*. Minneapolis: Center for Transportation Studies, University of Minnesota. Retrieved from https://hdl.handle.net/11299/177641.

Grove, J. D. (1989). *Blanket curing to promote early strength concrete* (Report MLR-87-7). Ames, IA: Iowa Department of Transportation.

Khazanovich, L. (2018). Nondestructive Analysis of Alkali-Silica Reaction Damage in Concrete Slabs Using Shear Waves. *AIP Conference Proceedings*, 1949, 040003. doi: 10.1063/1.5031537

Khazanovich, L., & Roesler, J. (1997). DIPLOBACK: Neural Network-Based Backcalculation Program for Composite Pavements. *Transportation Research Record*, *1570,* 143–150

Khazanovich, L., Selezneva, O. I., Yu, H. T., & Darter, M. I. (2001). *Development of Rapid Solutions for Prediction of Critical Continuously Reinforced Concrete Pavement Stresses. Transportation Research Record, 1778*, 64–72.

Kohn, S. D., & Tayabji, S. (2003). *Best Practices for Airport Portland Cement Concrete Pavement Construction (Rigid Airport Pavement)* (Report IPRF-01-G-002-02-1). Skokie, IL: Innovative Pavement Research Foundation, Airport Concrete Pavement Technology Program.

Lee, E. B., Roesler, J., Harvey, J. T., & Ibbs, C. W. (2002). Case Study of Urban Concrete Pavement Reconstruction on Interstate 10. *J. Constr. Eng. Manage., 128*(1), 49-56.

Mindess, S., Young, J. F., & Darwin, D. (2003). *Concrete* (2nd Ed). Upper Saddle River, NJ: Prentice-Hall Pearson Education, Inc.

Mehta, P. K., & Monteiro, P. J. M. (2006). *Concrete: Microstructure, Properties, and Materials* (3rd Ed). New York: McGraw-Hill.

Minnesota Department of Transportation. (n.d.). MnROAD. Retrieved from http://www.dot.state.mn.us/mnroad/

Minnesota Department of Transportation. (n.d.) Special Provision 2301.3.O. Opening Pavement to Traffic. St. Paul, MN: MnDOT.

Olek, J., Cohen, M., Scholer, C., & Mandrekar, D. R. (2002). *Use of Modulus of Rupture, Fatigue Resistance and Maturity in Determining Opening to Traffic Time for Concrete Pavements* (Report No. FHWA/IN/JTRP-2000/25). Indianapolis, IN: Indiana Department of Transportation.

Roesler, J. (1998). *Fatigue of Concrete Beams and Slabs* (PhD thesis), University of Illinois, Urbana-Champaign, IL.

Roesler, J., Harvey, J. H., Farver, J., & Long F. (2000). *Investigation of design and construction issues for long life concrete pavement strategies* (Report No. FHWA/CA/OR-2000/04). Berkeley, CA: Pavement Research Center, Institute of Transportation Studies, University of California.

Shevaldykin, V. G. (2002). Ultrasonic Low-Frequency Transducers with Dry Dot Contact and Their Applications for Evaluation of Concrete Structures. *IEEE Ultrason. Symp. Proc., 1–2,* 793–798.

Stutzman P. E. (1999). *Deterioration of Iowa Highway Concrete Pavements: A Petrographic Study* (NISTR 6399). Gaithersburg, MD: National Institute of Standards and Technology.

Tabatabaie, A.M., & Barenberg, E.J. (1980). Structural Analysis of Concrete Pavement Systems. *Journal of Transportation Engineering, 106*(5), 493-506.

Van Dam, T. J., Peterson, K. R., Sutter, L. L., Panguluri, A., Sytsma, J., Buch, N., Kowli, R., & Desaraju, R. (2005). *Guidelines for Early-Opening-to-Traffic Portland Cement Concrete for Pavement Rehabilitation* (NCHRP Report 540). Washington, DC: National Highway Cooperative Research Program, Transportation Research Board, National Academies.

Westergaard, H. M. (1926). Stresses in Concrete Pavements Computed by Theoretical Analysis. *Public Roads, 7*(2), 25–35.

Youngbauer, P., & Morrison, W. (2017). *Report of Concrete Analysis*. St. Paul, MN: American Engineering Testing Inc.

APPENDIX A MEANS AND STANDARD DEVIATIONS FOR SENSORS

Table A1: Means and Standard Deviation for Sensors CE001

Sensor 001	Cell 124		Cell 224		Cell 324		Cell 424	
	Mean	Standard Deviation	Mean	Standard Deviation	Mean	Standard Deviation	Mean	Standard Deviation
Load 1_1	-0.4	20.5						
Load 1_2	2.0	20.5						
Load 2_1	6.0	35.8	12.6	12.9				
Load 2_2	N/A	N/A	13.5	12.9				
Load 3_1	13.1	71.2	-1.8	18.6	5.6	136.5		
Load 3_2	12.9	71.9	-2.6	18.8	5.6	136.5		
Load 4_1	23.6	85.6	-25.0	31.7	30.8	137.4	2085.8	70.9
Load 4_2	22.6	116.5	-28.4	36.6	29.6	135.4	2084.7	70.9

Table A2: Means and Standard Deviations for Sensors CE002

Sensor 002	Cell 124		Cell 224		Cell 324		Cell 424	
	Mean	Standard Deviation	Mean	Standard Deviation	Mean	Standard Deviation	Mean	Standard Deviation
Load 1_1	-0.4	20.5						
Load 1_2	2.0	20.5						
Load 2_1	6.0	35.8	12.6	12.9				
Load 2_2	N/A	N/A	13.5	12.9				
Load 3_1	-15.2	10.0	-12.0	45.4	-1.7	15.3		
Load 3_2	-14.5	10.0	-12.5	45.4	-1.6	15.2		
Load 4_1	56.2	11.4	45.0	46.7	5.6	15.6	N/A	N/A
Load 4_2	56.6	14.5	43.8	57.4	5.0	15.4	N/A	N/A

Table A3: Means and Standard Deviations for Sensors CE003

Sensor 003	Cell 124		Cell 224		Cell 324		Cell 424	
	Mean	Standard Deviation	Mean	Standard Deviation	Mean	Standard Deviation	Mean	Standard Deviation
Load 1_1	8.4	38.3						
Load 1_2	15.9	38.1						
Load 2_1	20.7	59.8	1.7	14.0				
Load 2_2	N/A	N/A	1.4	13.9				
Load 3_1	16.7	108.9	1.3	21.5	-0.5	127.3		
Load 3_2	18.1	109.9	0.7	21.7	-0.5	127.3		
Load 4_1	3.2	128.9	-21.1	33.2	7.1	129.2	1630.4	23.5
Load 4_2	3.5	176.1	-21.4	38.7	7.2	127.3	1630.5	23.6

Table A4: Means and Standard Deviations for Sensors CE004

Sensor	Cell 124	Cell 224	Cell 324	Cell 424

004	Mean	Standard Deviation	Mean	Standard Deviation	Mean	Standard Deviation	Mean	Standard Deviation
Load 1_1	33.9	22.8						
Load 1_2	49.9	14.1						
Load 2_1	13.4	12.1	2.4	11.9				
Load 2_2	N/A	N/A	3.3	11.9				
Load 3_1	2.6	11.2	3.5	17.4	-13.3	18.7		
Load 3_2	3.2	11.2	3.7	17.7	-13.1	18.7		
Load 4_1	17.4	12.7	6.5	28.1	-10.9	19.4	1780.0	22.3
Load 4_2	18.4	15.8	7.1	32.3	-9.8	19.2	1780.8	22.3

Table A5: Means and Standard Deviations for Sensors CE005

Sensor 005	Cell 124		Cell 224		Cell 324		Cell 424	
	Mean	Standard Deviation	Mean	Standard Deviation	Mean	Standard Deviation	Mean	Standard Deviation
Load 1_1	0.7	12.7						
Load 1_2	4.7	12.1						
Load 2_1	17.4	16.7	13.1	11.8				
Load 2_2	N/A	N/A	13.6	11.9				
Load 3_1	4.0	33.3	1.8	16.7	11.6	22.9		
Load 3_2	4.1	33.2	1.2	16.8	11.6	23.0		
Load 4_1	-3.9	33.8	-5.1	30.5	22.5	21.5	2840.1	24.0
Load 4_2	-6.3	43.9	-8.3	35.1	20.6	21.2	2839.0	24.1

Table A6: Means and Standard Deviations for Sensors CE006

Sensor 006	Cell 124		Cell 224		Cell 324		Cell 424	
	Mean	Standard Deviation	Mean	Standard Deviation	Mean	Standard Deviation	Mean	Standard Deviation
Load 1_1	-0.6	6.8						
Load 1_2	2.4	6.4						
Load 2_1	-8.0	7.8	-10.5	9.4				
Load 2_2	N/A	N/A	-11.2	9.4				
Load 3_1	-0.4	12.1	-7.6	13.3	-5.5	108.6		
Load 3_2	0.2	12.3	-7.3	13.4	-5.4	108.6		
Load 4_1	39.1	13.8	45.1	24.9	2.6	110.8	529.0	19.6
Load 4_2	38.0	17.7	42.9	28.6	1.1	109.1	527.9	19.7

Table A7: Means and Standard Deviations for Sensors CE007

Sensor 007	Cell 124		Cell 224		Cell 324		Cell 424	
	Mean	Standard Deviation	Mean	Standard Deviation	Mean	Standard Deviation	Mean	Standard Deviation

Load 1_1	-0.8	21.1						
Load 1_2	3.5	21.2						
Load 2_1	7.4	33.1	25.6	12.0				
Load 2_2	N/A	N/A	23.9	11.9				
Load 3_1	2.3	82.8	-17.0	16.6	-5.0	48.4		
Load 3_2	2.4	82.7	-17.6	16.8	-6.1	49.0		
Load 4_1	-2.0	95.0	35.3	29.8	28.6	50.9	2868.2	28.8
Load 4_2	-1.8	124.3	36.6	34.3	29.6	50.6	2867.7	28.8

Table A8: Means and Standard Deviations for Sensors CE008

Sensor 008	Cell 124		Cell 224		Cell 324		Cell 424	
	Mean	Standard Deviation	Mean	Standard Deviation	Mean	Standard Deviation	Mean	Standard Deviation
Load 1_1	3.6	23.2						
Load 1_2	11.6	21.5						
Load 2_1	26.6	28.9	8.0	23.1				
Load 2_2	N/A	N/A	10.2	23.2				
Load 3_1	3.7	62.8	2.8	58.2	-9.6	16.7		
Load 3_2	3.4	62.7	3.2	58.4	-9.3	16.8		
Load 4_1	-1.0	55.0	-6.5	67.0	16.0	17.4	1388.6	24.0
*Load 4_2	-0.7	71.5	-6.0	83.6	17.5	17.0	1389.4	24.1

APPENDIX B CONCRETE STRENGTH DATA

Table B1: Compressive Strength and Maturity Data (from AET, Inc.)

Concrete Age, hours	Specimen #	Maturity, ᵒC-days	Flexural Strength, psi
6	Cylinder 1	157	120
6	Cylinder 2	157	110
6	Cylinder 3	157	110
12	Cylinder 4	350	670
12	Cylinder 5	350	760
12	Cylinder 6	350	810
18	Cylinder 7	529	1390
18	Cylinder 8	529	1230
18	Cylinder 9	529	1210
24	Cylinder 10	674	1570
24	Cylinder 11	674	1540
24	Cylinder 12	674	1570
48	Cylinder 13	1,250	2060
48	Cylinder 14	1,250	2110
48	Cylinder 15	1,250	2120
72	Cylinder 16	1,820	2460
72	Cylinder 17	1,820	2830
72	Cylinder 18	1,820	2640
96	Cylinder 19	2,372	2930
96	Cylinder 20	2,372	2980
96	Cylinder 21	2,372	3050
120	Cylinder 22	2,924	3190
120	Cylinder 23	2,924	3230
120	Cylinder 24	2,924	3240

Table B2: Flexural Strength and Maturity Data (from AET, Inc.)

Concrete Age, hours	Specimen #	Maturity, ᵒC-days	Flexural Strength, psi
6.00	Beam 1	155	90
6.00	Beam 2	155	95
12.00	Beam 3	331	320
12.00	Beam 4	331	265
18.00	Beam 5	494	390
18.00	Beam 6	494	400
24.00	Beam 7	637	445
24.00	Beam 8	637	480
48.00	Beam 9	1,213	500
48.00	Beam 10	1,213	510
72.00	Beam 11	1,784	590
72.00	Beam 12	1,784	575
86.00	Beam 13	2,336	610
96.00	Beam 14	2,336	615
120.00	Beam 15	2,888	640
120.00	Beam 16	2,888	665

168.00	Beam 17	3,849	705
168.00	Beam 18	3,849	700

APPENDIX C CONCRETE SHEAR WAVE VELOCITY AND HTI

Table C1: Velocity and HTI from Measurements Near Core Locations

Core ID	scan	date	Time	Shear velocity. km/sec	HTI
124 IB	1	7/6/2017	9:38	2.357	85.565
124 IB	2	7/6/2017	9:38	2.354	75.485
124 IB	3	7/6/2017	9:38	2.362	78.233
124 IB	4	7/6/2017	9:38	2.398	83.409
124 IB	5	7/6/2017	9:38	2.368	85.048
124 IB	6	7/6/2017	9:38	2.349	78.68
124 IB	7	7/6/2017	9:38	2.486	75.934
124 IB	8	7/6/2017	9:38	2.452	78.65
124 IB	9	7/6/2017	9:38	2.388	75.372
124 IW	1	7/6/2017	9:38	2.439	76.868
124 IW	2	7/6/2017	9:38	2.359	70.673
124 IW	3	7/6/2017	9:38	2.414	69.594
124 IW	4	7/6/2017	9:38	2.387	69.759
124 IW	5	7/6/2017	9:38	2.371	73.093
124 IW	6	7/6/2017	9:38	2.364	73.138
124 IW	7	7/6/2017	9:38	2.372	75.901
124 IW	8	7/6/2017	9:38	2.351	76.462
124 IW	9	7/6/2017	9:38	2.415	72.848
124 OB	1	7/6/2017	9:38	2.418	68.99
124 OB	2	7/6/2017	9:38	2.413	70.369
124 OB	3	7/6/2017	9:38	2.424	66.598
124 OB	4	7/6/2017	9:38	2.395	74.102
124 OB	5	7/6/2017	9:38	2.393	71.798
124 OB	6	7/6/2017	9:38	2.415	70.797
124 OB	7	7/6/2017	9:38	2.376	75.664
124 OB	8	7/6/2017	9:38	2.39	67.531
124 OB	9	7/6/2017	9:38	2.416	61.116
124 OW	1	7/6/2017	9:28	2.443	69.164
124 OW	2	7/6/2017	9:28	2.404	76.903
124 OW	3	7/6/2017	9:28	2.416	78.237
124 OW	4	7/6/2017	9:28	2.409	71.932
124 OW	5	7/6/2017	9:28	2.412	69.794
124 OW	6	7/6/2017	9:28	2.41	74.462
124 OW	7	7/6/2017	9:28	2.428	69.963
124 OW	8	7/6/2017	9:28	2.436	71.391
124 OW	9	7/6/2017	9:28	2.423	71.707
224 IB	1	7/6/2017	9:38	2.381	79.219
224 IB	2	7/6/2017	9:38	2.409	80.092

Core ID	scan	date	Time	Shear velocity. km/sec	HTI
224 IB	3	7/6/2017	9:38	2.418	73.432
224 IB	4	7/6/2017	9:38	2.339	76.113
224 IB	5	7/6/2017	9:38	2.408	72.581
224 IB	6	7/6/2017	9:38	2.414	75.712
224 IB	7	7/6/2017	9:38	2.354	75.315
224 IB	8	7/6/2017	9:38	2.431	76.549
224 IB	9	7/6/2017	9:38	2.414	79.064
224 IW	1	7/6/2017	9:38	2.597	74.607
224 IW	2	7/6/2017	9:38	2.702	73.361
224 IW	3	7/6/2017	9:38	2.367	74.982
224 IW	4	7/6/2017	9:38	2.746	71.216
224 IW	5	7/6/2017	9:38	2.396	68.42
224 IW	6	7/6/2017	9:38	2.368	73.821
224 IW	7	7/6/2017	9:38	2.349	68.662
224 IW	8	7/6/2017	9:38	2.419	74.487
224 IW	9	7/6/2017	9:38	2.402	73.473
224 OB	1	7/6/2017	9:38	2.379	66.1
224 OB	2	7/6/2017	9:38	2.382	63.742
224 OB	3	7/6/2017	9:38	2.382	67.238
224 OB	4	7/6/2017	9:38	2.406	72.515
224 OB	5	7/6/2017	9:38	2.408	67.203
224 OB	6	7/6/2017	9:38	2.415	67.528
224 OB	7	7/6/2017	9:38	2.406	74.017
224 OB	8	7/6/2017	9:38	2.409	70.072
224 OB	9	7/6/2017	9:38	2.388	80.059
224 OW	1	7/6/2017	9:38	2.396	72.039
224 OW	2	7/6/2017	9:38	2.425	75.064
224 OW	3	7/6/2017	9:38	2.442	80.175
224 OW	4	7/6/2017	9:38	2.409	71.324
224 OW	5	7/6/2017	9:38	2.419	70.923
224 OW	6	7/6/2017	9:38	2.433	73.295
224 OW	7	7/6/2017	9:38	2.405	73.085
224 OW	8	7/6/2017	9:38	2.456	80.078
224 OW	9	7/6/2017	9:38	2.443	86.164
324 IB	1	7/6/2017	9:38	2.34	64.912
324 IB	2	7/6/2017	9:38	2.322	65.437
324 IB	3	7/6/2017	9:38	2.353	69.181
324 IB	4	7/6/2017	9:38	2.288	68.914
324 IB	5	7/6/2017	9:38	2.264	68.392
324 IB	6	7/6/2017	9:38	2.28	67.098

Core ID	scan	date	Time	Shear velocity. km/sec	HTI
324 IB	7	7/6/2017	9:38	2.211	61.452
324 IB	8	7/6/2017	9:38	2.274	65.86
324 IB	9	7/6/2017	9:38	2.283	68.587
324 IW	1	7/6/2017	9:38	2.265	61.27
324 IW	2	7/6/2017	9:38	2.28	65.666
324 IW	3	7/6/2017	9:38	2.287	62.222
324 IW	4	7/6/2017	9:38	2.297	61.277
324 IW	5	7/6/2017	9:38	2.298	64.123
324 IW	6	7/6/2017	9:38	2.287	68.183
324 IW	7	7/6/2017	9:38	2.252	66.492
324 IW	8	7/6/2017	9:38	2.212	70.477
324 IW	9	7/6/2017	9:38	2.226	72.649
324 OB	1	7/6/2017	10:14	2.366	74.326
324 OB	2	7/6/2017	10:14	2.393	75.896
324 OB	3	7/6/2017	10:14	2.403	73.578
324 OB	4	7/6/2017	10:14	2.384	74.293
324 OB	5	7/6/2017	10:14	2.38	73.483
324 OB	6	7/6/2017	10:14	2.396	71.867
324 OB	7	7/6/2017	10:14	2.382	75.724
324 OB	8	7/6/2017	10:14	2.393	76.187
324 OB	9	7/6/2017	10:14	2.396	70.253
324 OW	1	7/6/2017	10:14	2.409	63.93
324 OW	2	7/6/2017	10:14	2.372	64.948
324 OW	3	7/6/2017	10:14	2.384	64.27
324 OW	4	7/6/2017	10:14	2.41	60.182
324 OW	5	7/6/2017	10:14	2.376	64.135
324 OW	6	7/6/2017	10:14	2.346	65.02
324 OW	7	7/6/2017	10:14	2.397	63.307
324 OW	8	7/6/2017	10:14	2.378	65.725
324 OW	9	7/6/2017	10:14	2.368	78.32
324 OW	10	7/6/2017	10:14	2.382	75.561
424 IB	1	7/6/2017	9:38	2.603	65.955
424 IB	2	7/6/2017	9:38	2.402	69.225
424 IB	3	7/6/2017	9:38	2.363	71.121
424 IB	4	7/6/2017	9:38	2.252	68.103
424 IB	5	7/6/2017	9:38	2.37	64.972
424 IB	6	7/6/2017	9:38	2.368	64.963
424 IB	7	7/6/2017	9:38	2.247	71.696
424 IB	8	7/6/2017	9:38	2.299	70.485
424 IB	9	7/6/2017	9:38	2.24	66.213

Core ID	scan	date	Time	Shear velocity. km/sec	HTI
424 IW	1	7/6/2017	9:38	2.253	65.368
424 IW	2	7/6/2017	9:38	2.271	64.223
424 IW	3	7/6/2017	9:38	2.299	67.627
424 IW	4	7/6/2017	9:38	2.41	62.496
424 IW	5	7/6/2017	9:38	2.418	69.858
424 IW	6	7/6/2017	9:38	2.318	61.605
424 IW	7	7/6/2017	9:38	2.39	64.337
424 IW	8	7/6/2017	9:38	2.395	69.219
424 IW	9	7/6/2017	9:38	2.388	67.602
424 OB	1	7/6/2017	9:38	2.345	56.695
424 OB	2	7/6/2017	9:38	2.373	58.885
424 OB	3	7/6/2017	9:38	2.395	64.981
424 OB	4	7/6/2017	9:38	2.41	63.155
424 OB	5	7/6/2017	9:38	2.424	59.837
424 OB	6	7/6/2017	9:38	2.417	72.502
424 OB	7	7/6/2017	9:38	2.419	68.697
424 OB	8	7/6/2017	9:38	2.434	60.474
424 OB	9	7/6/2017	9:38	2.448	62.451
424 OW	1	7/6/2017	9:38	2.444	60.121
424 OW	2	7/6/2017	9:38	2.449	58.478
424 OW	3	7/6/2017	9:38	2.405	61.958
424 OW	4	7/6/2017	9:38	2.484	67.671
424 OW	5	7/6/2017	9:38	2.471	66.398
424 OW	6	7/6/2017	9:38	2.413	67.54
424 OW	7	7/6/2017	9:38	2.42	59.76
424 OW	8	7/6/2017	9:38	2.386	60.99
424 OW	9	7/6/2017	9:38	2.275	61.558
524 IB	1	7/6/2017	9:38	2.378	72.702
524 IB	1	7/6/2017	9:55	2.416	77.491
524 IB	2	7/6/2017	9:38	2.427	68.185
524 IB	2	7/6/2017	9:55	2.417	70.73
524 IB	3	7/6/2017	9:38	2.428	65.787
524 IB	3	7/6/2017	9:55	2.443	77.229
524 IB	4	7/6/2017	9:38	2.41	67.529
524 IB	4	7/6/2017	9:55	2.429	68.548
524 IB	5	7/6/2017	9:38	2.423	63.351
524 IB	5	7/6/2017	9:55	2.462	67.85
524 IB	6	7/6/2017	9:38	2.408	62.352
524 IB	6	7/6/2017	9:55	2.407	61.59
524 IB	7	7/6/2017	9:38	2.397	74.487

Core ID	scan	date	Time	Shear velocity. km/sec	HTI
524 IB	7	7/6/2017	9:55	2.433	69.413
524 IB	8	7/6/2017	9:38	2.41	66.551
524 IB	8	7/6/2017	9:55	2.426	69.38
524 IB	9	7/6/2017	9:38	2.428	67.018
524 IB	9	7/6/2017	9:55	2.409	68.676
524 IB	10	7/6/2017	9:38	2.314	59.267
524 IB	11	7/6/2017	9:38	2.313	63.946
524 IB	12	7/6/2017	9:38	2.325	62.418
524 IW	1	7/6/2017	9:55	2.408	71.219
524 IW	2	7/6/2017	9:55	2.409	68.78
524 IW	3	7/6/2017	9:55	2.404	68.82
524 IW	4	7/6/2017	9:55	2.384	67.685
524 IW	5	7/6/2017	9:55	2.412	69.569
524 IW	6	7/6/2017	9:55	2.424	69.318
524 IW	7	7/6/2017	9:55	2.436	68.145
524 IW	8	7/6/2017	9:55	2.465	65.536
524 IW	9	7/6/2017	9:55	2.434	65.763
524 OB	1	7/6/2017	9:55	2.417	73.961
524 OB	2	7/6/2017	9:55	2.421	73.743
524 OB	3	7/6/2017	9:55	2.431	75.005
524 OB	4	7/6/2017	9:55	2.533	72.152
524 OB	5	7/6/2017	9:55	2.451	74.568
524 OB	6	7/6/2017	9:55	2.436	74.781
524 OB	7	7/6/2017	9:55	2.419	69.097
524 OB	8	7/6/2017	9:55	2.421	69.444
524 OB	9	7/6/2017	9:55	2.352	79.827
524 OW	1	7/6/2017	9:55	2.366	68.111
524 OW	2	7/6/2017	9:55	2.496	71.85
524 OW	3	7/6/2017	9:55	2.484	66.846
524 OW	4	7/6/2017	9:55	2.521	64.684
524 OW	5	7/6/2017	9:55	2.71	68.367
524 OW	6	7/6/2017	9:55	2.473	68.228
524 OW	7	7/6/2017	9:55	2.506	63.772
524 OW	8	7/6/2017	9:55	2.385	61.964
524 OW	9	7/6/2017	9:55	2.426	61.856
624 IB	1	7/6/2017	9:55	2.332	83.239
624 IB	2	7/6/2017	9:55	2.317	88.695
624 IB	3	7/6/2017	9:55	2.276	85.653
624 IB	4	7/6/2017	9:55	2.355	71.703
624 IB	5	7/6/2017	9:55	3.111	126.764

Core ID	scan	date	Time	Shear velocity. km/sec	HTI
624 IB	6	7/6/2017	9:55	2.551	76.763
624 IB	7	7/6/2017	9:55	2.355	64.902
624 IB	8	7/6/2017	9:55	2.609	78.863
624 IB	9	7/6/2017	9:55	2.364	74.813
624 IR	1	7/6/2017	9:55	2.356	72.727
624 IR	2	7/6/2017	9:55	2.374	69.901
624 IR	3	7/6/2017	9:55	2.388	76.399
624 IR	4	7/6/2017	9:55	2.349	57.985
624 IR	5	7/6/2017	9:55	2.351	64.279
624 IR	6	7/6/2017	9:55	2.252	57.333
624 IR	7	7/6/2017	9:55	2.334	61.01
624 IR	8	7/6/2017	9:55	2.329	63.918
624 IR	9	7/6/2017	9:55	2.378	67.363
624 IR	10	7/6/2017	9:55	2.323	78.733
624 IR	11	7/6/2017	9:55	2.305	72.835
624 IR	12	7/6/2017	9:55	2.352	58.755
124 IB	1	7/10/2017	9:31	2.588	85.916
124 IB	2	7/10/2017	9:31	2.586	78.709
124 IB	3	7/10/2017	9:31	2.587	80.427
124 IB	4	7/10/2017	9:31	2.553	77.381
124 IB	5	7/10/2017	9:31	2.569	83.074
124 IB	6	7/10/2017	9:31	2.59	82.457
124 IB	7	7/10/2017	9:31	2.432	79.922
124 IB	8	7/10/2017	9:31	2.615	74.846
124 IB	9	7/10/2017	9:31	2.587	70.311
124 IB	10	7/10/2017	9:31	2.565	77.118
124 IB	11	7/10/2017	9:31	2.574	74.629
124 IW	1	7/10/2017	9:31	2.551	75.925
124 IW	2	7/10/2017	9:31	2.586	77.407
124 IW	3	7/10/2017	9:31	2.598	74.073
124 IW	4	7/10/2017	9:31	2.492	75.838
124 IW	5	7/10/2017	9:31	2.569	70.364
124 IW	6	7/10/2017	9:31	2.574	79.191
124 IW	7	7/10/2017	9:31	2.595	75.537
124 IW	8	7/10/2017	9:31	2.586	73.3
124 IW	9	7/10/2017	9:31	2.581	76.047
124 OB	1	7/10/2017	9:38	2.52	80.326
124 OB	2	7/10/2017	9:38	2.539	73.879
124 OB	3	7/10/2017	9:38	2.57	76.492
124 OB	4	7/10/2017	9:38	2.56	71.586

Core ID	scan	date	Time	Shear velocity. km/sec	HTI
124 OB	5	7/10/2017	9:38	2.561	73.143
124 OB	6	7/10/2017	9:38	2.57	70.973
124 OB	7	7/10/2017	9:38	2.522	80.579
124 OB	8	7/10/2017	9:38	2.531	75.333
124 OB	9	7/10/2017	9:38	2.551	69.499
124 OW	1	7/10/2017	9:38	2.578	68.221
124 OW	2	7/10/2017	9:38	2.544	66.548
124 OW	3	7/10/2017	9:38	2.539	67.863
124 OW	4	7/10/2017	9:38	2.577	68.195
124 OW	5	7/10/2017	9:38	2.553	79.965
124 OW	6	7/10/2017	9:38	2.57	76.432
124 OW	7	7/10/2017	9:38	2.589	77.838
124 OW	8	7/10/2017	9:38	2.586	76.67
124 OW	9	7/10/2017	9:38	2.557	72.673
224 IB	1	7/10/2017	9:38	2.505	72.442
224 IB	2	7/10/2017	9:38	2.527	76.136
224 IB	3	7/10/2017	9:38	2.541	72.876
224 IB	4	7/10/2017	9:38	2.54	78.858
224 IB	5	7/10/2017	9:38	2.371	72.493
224 IB	6	7/10/2017	9:38	2.544	76.938
224 IB	7	7/10/2017	9:38	2.534	73.979
224 IB	8	7/10/2017	9:38	2.534	78.557
224 IB	9	7/10/2017	9:38	2.537	74.959
224 IW	1	7/10/2017	9:38	2.543	80.783
224 IW	2	7/10/2017	9:38	2.392	80.111
224 IW	3	7/10/2017	9:38	2.528	80.154
224 IW	4	7/10/2017	9:38	2.567	74.34
224 IW	5	7/10/2017	9:38	2.564	75.555
224 IW	6	7/10/2017	9:38	2.561	89.905
224 IW	7	7/10/2017	9:38	2.384	73.61
224 IW	8	7/10/2017	9:38	2.568	86.043
224 IW	9	7/10/2017	9:38	2.586	81.044
224 OB	1	7/10/2017	9:38	2.535	73.586
224 OB	2	7/10/2017	9:38	2.512	68.283
224 OB	3	7/10/2017	9:38	2.554	73.89
224 OB	4	7/10/2017	9:38	2.496	67.62
224 OB	5	7/10/2017	9:38	2.504	67.188
224 OB	6	7/10/2017	9:38	2.517	74.458
224 OB	7	7/10/2017	9:38	2.561	78.683
224 OB	8	7/10/2017	9:38	2.555	78.753

Core ID	scan	date	Time	Shear velocity. km/sec	HTI
224 OB	9	7/10/2017	9:38	2.538	70.681
224 OW	1	7/10/2017	9:38	2.543	69.905
224 OW	2	7/10/2017	9:38	2.571	74.587
224 OW	3	7/10/2017	9:38	2.565	75.743
224 OW	4	7/10/2017	9:38	2.482	87.931
224 OW	5	7/10/2017	9:38	2.554	79.474
224 OW	6	7/10/2017	9:38	2.56	71.864
224 OW	7	7/10/2017	9:38	2.535	73.739
224 OW	8	7/10/2017	9:38	2.563	81.765
224 OW	9	7/10/2017	9:38	2.552	81.741
324 IB	1	7/10/2017	9:38	2.459	64.79
324 IB	2	7/10/2017	9:38	2.469	64.254
324 IB	3	7/10/2017	9:38	2.471	69.326
324 IB	4	7/10/2017	9:38	2.469	64.694
324 IB	5	7/10/2017	9:38	2.478	64.5
324 IB	6	7/10/2017	9:38	2.446	69.828
324 IB	7	7/10/2017	9:38	2.498	62.202
324 IB	8	7/10/2017	9:38	2.466	63.822
324 IB	9	7/10/2017	9:38	2.477	66.662
324 IW	1	7/10/2017	9:38	2.494	65.983
324 IW	2	7/10/2017	9:38	2.488	69.309
324 IW	3	7/10/2017	9:38	2.483	75.806
324 IW	4	7/10/2017	9:38	2.464	69.37
324 IW	5	7/10/2017	9:38	2.49	72.23
324 IW	6	7/10/2017	9:38	2.523	74.295
324 IW	7	7/10/2017	9:38	2.478	76.438
324 IW	8	7/10/2017	9:38	2.487	73.61
324 IW	9	7/10/2017	9:38	2.492	78.894
324 OB	1	7/10/2017	9:38	2.501	74.127
324 OB	2	7/10/2017	9:38	2.48	72.519
324 OB	3	7/10/2017	9:38	2.508	75.964
324 OB	4	7/10/2017	9:38	2.51	70.905
324 OB	5	7/10/2017	9:38	2.531	62.83
324 OB	6	7/10/2017	9:38	2.513	80.431
324 OB	7	7/10/2017	9:38	2.462	70.587
324 OB	8	7/10/2017	9:38	2.504	75.771
324 OB	9	7/10/2017	9:38	2.51	70.654
324 OW	1	7/10/2017	9:38	2.539	64.919
324 OW	2	7/10/2017	9:38	2.513	74.144
324 OW	3	7/10/2017	9:38	2.484	74.953

Core ID	scan	date	Time	Shear velocity. km/sec	HTI
324 OW	4	7/10/2017	9:38	2.531	62.668
324 OW	5	7/10/2017	9:38	2.498	61.112
324 OW	6	7/10/2017	9:38	2.514	70.739
324 OW	7	7/10/2017	9:38	2.533	66.238
324 OW	8	7/10/2017	9:38	2.517	68.979
324 OW	9	7/10/2017	9:38	2.494	76.005
424 IB	1	7/10/2017	9:38	2.5	72.26
424 IB	2	7/10/2017	9:38	2.512	73.49
424 IB	3	7/10/2017	9:38	2.508	71.694
424 IB	4	7/10/2017	9:38	2.476	68.359
424 IB	5	7/10/2017	9:38	2.469	66.399
424 IB	6	7/10/2017	9:38	2.456	64.201
424 IB	7	7/10/2017	9:38	2.513	67.155
424 IB	8	7/10/2017	9:38	2.503	65.328
424 IB	9	7/10/2017	9:38	2.501	64.159
424 IW	1	7/10/2017	9:38	2.526	73.97
424 IW	2	7/10/2017	9:38	2.511	77.269
424 IW	3	7/10/2017	9:38	2.513	73.719
424 IW	4	7/10/2017	9:38	2.524	71.791
424 IW	5	7/10/2017	9:38	2.505	70.97
424 IW	6	7/10/2017	9:38	2.5	69.582
424 IW	7	7/10/2017	9:38	2.537	67.189
424 IW	8	7/10/2017	9:38	2.558	76.646
424 IW	9	7/10/2017	9:38	2.513	79.917
424 OB	1	7/10/2017	9:59	2.505	63.017
424 OB	2	7/10/2017	9:59	2.506	62.001
424 OB	3	7/10/2017	9:59	2.541	64.825
424 OB	4	7/10/2017	9:59	2.501	61.99
424 OB	5	7/10/2017	9:59	2.471	59.998
424 OB	6	7/10/2017	9:59	2.514	65.461
424 OB	7	7/10/2017	9:59	2.518	67.964
424 OB	8	7/10/2017	9:59	2.523	61.841
424 OB	9	7/10/2017	9:59	2.541	62.167
424 OW	1	7/10/2017	9:59	2.558	58.932
424 OW	2	7/10/2017	9:59	2.533	59.974
424 OW	3	7/10/2017	9:59	2.494	64.631
424 OW	4	7/10/2017	9:59	2.525	64.334
424 OW	5	7/10/2017	9:59	2.51	61.151
424 OW	6	7/10/2017	9:59	2.509	63.744
424 OW	7	7/10/2017	9:59	2.549	60.992

Core ID	scan	date	Time	Shear velocity. km/sec	HTI
424 OW	8	7/10/2017	9:59	2.523	59.891
424 OW	9	7/10/2017	9:59	2.518	63.719
524 IB	1	7/10/2017	9:59	2.512	64.595
524 IB	2	7/10/2017	9:59	2.52	67.225
524 IB	3	7/10/2017	9:59	2.533	61.535
524 IB	4	7/10/2017	9:59	2.506	67.97
524 IB	5	7/10/2017	9:59	2.523	66.695
524 IB	6	7/10/2017	9:59	2.521	64.314
524 IB	7	7/10/2017	9:59	2.503	59.434
524 IB	8	7/10/2017	9:59	2.523	62.59
524 IB	9	7/10/2017	9:59	2.518	65.139
524 IW	1	7/10/2017	9:59	2.517	68.424
524 IW	2	7/10/2017	9:59	2.495	66.008
524 IW	3	7/10/2017	9:59	2.492	67.351
524 IW	4	7/10/2017	9:59	2.5	68.617
524 IW	5	7/10/2017	9:59	2.5	70.453
524 IW	6	7/10/2017	9:59	2.502	68.10/20177
524 IW	7	7/10/2017	9:59	2.501	63.03
524 IW	8	7/10/2017	9:59	2.513	62.57
524 IW	9	7/10/2017	9:59	2.537	66.356
524 OB	1	7/10/2017	9:59	2.531	63.396
524 OB	2	7/10/2017	9:59	2.49	67.347
524 OB	3	7/10/2017	9:59	2.515	64.671
524 OB	4	7/10/2017	9:59	2.507	64.55
524 OB	5	7/10/2017	9:59	2.519	69.304
524 OB	6	7/10/2017	9:59	2.494	65.793
524 OB	7	7/10/2017	9:59	2.482	63.53
524 OB	8	7/10/2017	9:59	2.495	69.268
524 OB	9	7/10/2017	9:59	2.529	69.016
524 OW	1	7/10/2017	9:59	2.595	61.446
524 OW	2	7/10/2017	9:59	2.581	64.782
524 OW	3	7/10/2017	9:59	2.582	67.844
524 OW	4	7/10/2017	9:59	2.633	64.183
524 OW	5	7/10/2017	9:59	2.599	63.561
524 OW	6	7/10/2017	9:59	2.542	67.921
524 OW	7	7/10/2017	9:59	2.615	63.389
524 OW	8	7/10/2017	9:59	2.568	64.509
524 OW	9	7/10/2017	9:59	2.587	66.375
624 IB	1	7/10/2017	9:59	2.373	91.21
624 IB	2	7/10/2017	9:59	2.189	108.745

Core ID	scan	date	Time	Shear velocity. km/sec	HTI
624 IB	3	7/10/2017	9:59	2.264	110.615
624 IB	4	7/10/2017	9:59	2.449	84.755
624 IB	5	7/10/2017	9:59	2.501	69.424
624 IB	6	7/10/2017	9:59	2.487	64.526
624 IB	7	7/10/2017	9:59	2.513	63.197
624 IB	8	7/10/2017	9:59	2.484	64.75
624 IB	9	7/10/2017	9:59	2.496	64.846
624 IR	1	7/10/2017	9:59	2.505	62.927
624 IR	2	7/10/2017	9:59	2.471	62.479
624 IR	3	7/10/2017	9:59	2.514	64.027
624 IR	4	7/10/2017	9:59	2.506	66.172
624 IR	5	7/10/2017	9:59	2.512	71.033
624 IR	6	7/10/2017	9:59	2.528	74.152
624 IR	7	7/10/2017	9:59	2.529	68.618
624 IR	8	7/10/2017	9:59	2.51	79.137
624 IR	9	7/10/2017	9:59	2.51	67.949
624 IR	10	7/10/2017	9:59	2.484	68.711
624 IR	11	7/10/2017	9:59	2.519	71.199
624 IR	12	7/10/2017	9:59	2.514	69.053

Table C2: Velocity and HTI from Measurements the Width of the Slab

Cell	scan	Date	Time	Shear velocity. km/sec	HTI
124	1	7/6/2017	10:45	2.418	79.94
124	1	7/6/2017	12:22	2.465	131.693
124	2	7/6/2017	10:45	2.407	83.474
124	2	7/6/2017	12:22	2.385	123.309
124	3	7/6/2017	10:45	2.448	88.87
124	3	7/6/2017	12:22	2.416	131.392
124	4	7/6/2017	10:45	2.439	81.821
124	4	7/6/2017	12:22	2.367	90.807
124	5	7/6/2017	10:45	2.426	100.211
124	5	7/6/2017	12:22	2.392	98.235
124	6	7/6/2017	10:45	2.42	87.328
124	6	7/6/2017	12:22	2.364	98.395
124	7	7/6/2017	10:45	2.422	92.032
124	7	7/6/2017	12:22	2.392	94.027
124	8	7/6/2017	10:45	2.419	85.367

Cell	scan	Date	Time	Shear velocity. km/sec	HTI
124	8	7/6/2017	12:22	2.42	94.529
124	9	7/6/2017	10:45	2.376	85.815
124	9	7/6/2017	12:22	2.414	131.476
124	10	7/6/2017	10:45	2.397	74.441
124	10	7/6/2017	12:22	2.411	127.446
124	11	7/6/2017	10:45	2.408	80.45
124	11	7/6/2017	12:22	2.419	103.755
124	12	7/6/2017	10:45	2.381	81.348
124	12	7/6/2017	12:22	2.389	119.47
124	13	7/6/2017	10:45	2.424	81.624
124	13	7/6/2017	12:22	2.406	93.599
124	14	7/6/2017	10:45	2.38	74.929
124	14	7/6/2017	12:22	2.413	104.776
124	15	7/6/2017	10:45	2.346	75.943
124	15	7/6/2017	12:22	2.422	119.521
124	16	7/6/2017	10:45	2.34	76.53
124	16	7/6/2017	12:22	2.4	99.983
224	1	7/6/2017	10:45	2.383	75.723
224	1	7/6/2017	12:22	2.346	74.465
224	2	7/6/2017	10:45	2.36	71.82
224	2	7/6/2017	12:22	2.369	93.891
224	3	7/6/2017	10:45	2.418	78.311
224	3	7/6/2017	12:22	2.374	108.295
224	4	7/6/2017	10:45	2.42	76.119
224	4	7/6/2017	12:22	2.373	80.488
224	5	7/6/2017	10:45	2.411	77.533
224	5	7/6/2017	12:22	2.385	117.715
224	6	7/6/2017	10:45	2.381	79.739
224	6	7/6/2017	12:22	2.434	109.623
224	7	7/6/2017	10:45	2.404	71.097
224	7	7/6/2017	12:22	2.406	129.585
224	8	7/6/2017	10:45	2.398	79.896
224	8	7/6/2017	12:22	2.374	109.786
224	9	7/6/2017	10:45	2.386	91.889
224	9	7/6/2017	12:22	2.397	109.735
224	10	7/6/2017	10:45	2.392	74.601
224	10	7/6/2017	12:22	2.413	114.851

Cell	scan	Date	Time	Shear velocity. km/sec	HTI
224	11	7/6/2017	10:45	2.43	78.797
224	11	7/6/2017	12:22	2.375	108.423
224	12	7/6/2017	10:45	2.442	81.021
224	12	7/6/2017	12:22	2.408	131.246
224	13	7/6/2017	10:45	2.432	82.399
224	13	7/6/2017	12:22	2.382	114.108
224	14	7/6/2017	10:45	2.416	80.191
224	14	7/6/2017	12:22	2.391	112.076
224	15	7/6/2017	10:45	2.428	84.647
224	15	7/6/2017	12:22	2.365	96.402
224	16	7/6/2017	10:45	2.416	81.233
224	16	7/6/2017	12:22	2.351	92.447
224	17	7/6/2017	10:45	2.413	80.732
224	17	7/6/2017	12:22	2.353	92.599
324	1	7/6/2017	10:45	2.426	91.764
324	1	7/6/2017	12:22	2.338	119.285
324	2	7/6/2017	10:45	2.42	94.497
324	2	7/6/2017	12:22	2.334	114.142
324	3	7/6/2017	10:45	2.459	86.338
324	3	7/6/2017	12:22	2.4	140.474
324	4	7/6/2017	10:45	2.446	87.276
324	4	7/6/2017	12:22	2.39	123.219
324	5	7/6/2017	10:45	2.463	77.744
324	5	7/6/2017	12:22	2.363	126.928
324	6	7/6/2017	10:45	2.44	79.722
324	6	7/6/2017	12:22	2.382	122.701
324	7	7/6/2017	10:45	2.382	76.9
324	7	7/6/2017	12:22	2.418	116.93
324	8	7/6/2017	10:45	2.348	76.687
324	8	7/6/2017	12:22	2.417	136.907
324	9	7/6/2017	10:45	2.398	92.548
324	9	7/6/2017	12:22	2.402	121.378
324	10	7/6/2017	10:45	2.423	83.948
324	10	7/6/2017	12:22	2.406	94.994
324	11	7/6/2017	10:45	2.407	78.57
324	11	7/6/2017	12:22	2.415	98.101
324	12	7/6/2017	10:45	2.368	81.787
324	12	7/6/2017	12:22	2.891	140.991

Cell	scan	Date	Time	Shear velocity. km/sec	HTI
324	13	7/6/2017	10:45	2.379	75.792
324	13	7/6/2017	12:22	2.437	93.83
324	14	7/6/2017	10:45	2.352	82.515
324	14	7/6/2017	12:22	2.451	108.578
324	15	7/6/2017	10:45	2.384	90.211
324	15	7/6/2017	12:22	2.381	95.369
324	16	7/6/2017	10:45	2.376	83.714
324	16	7/6/2017	12:22	2.361	99.12
424	1	7/6/2017	10:45	2.408	80.711
424	1	7/6/2017	10:45	2.388	77.462
424	2	7/6/2017	10:45	2.399	78.672
424	2	7/6/2017	10:45	2.395	78.344
424	3	7/6/2017	10:45	2.421	78.485
424	3	7/6/2017	10:45	2.388	71.902
424	4	7/6/2017	10:45	2.4	80.636
424	4	7/6/2017	10:45	2.391	75.017
424	5	7/6/2017	10:45	2.435	79.568
424	5	7/6/2017	10:45	2.414	73.455
424	6	7/6/2017	10:45	2.431	80.473
424	6	7/6/2017	10:45	2.416	90.176

Cell	scan	Date	Time	Shear velocity. km/sec	HTI
424	7	7/6/2017	10:45	2.35	82.644
424	7	7/6/2017	10:45	2.379	68.526
424	8	7/6/2017	10:45	2.374	76.085
424	8	7/6/2017	10:45	2.379	82.611
424	9	7/6/2017	10:45	2.369	71.76
424	9	7/6/2017	10:45	2.385	83.624
424	10	7/6/2017	10:45	2.364	84.233
424	10	7/6/2017	10:45	2.397	90.661
424	11	7/6/2017	10:45	2.406	79.907
424	11	7/6/2017	10:45	2.382	74.677
424	12	7/6/2017	10:45	2.417	78.541
424	12	7/6/2017	10:45	2.385	77.078
424	13	7/6/2017	10:45	2.404	83.792
424	13	7/6/2017	10:45	2.379	75.74
424	14	7/6/2017	10:45	2.4	81.614
424	14	7/6/2017	10:45	2.363	75.075
424	15	7/6/2017	10:45	2.41	69.934
424	15	7/6/2017	10:45	2.376	72.796
424	16	7/6/2017	10:45	2.41	71.837
424	16	7/6/2017	10:45	2.366	87.39
524	1	7/6/2017	10:45	2.365	69.652
524	1	7/6/2017	10:45	2.42	80.483
524	2	7/6/2017	10:45	2.384	68.729
524	2	7/6/2017	10:45	2.424	74.492
524	3	7/6/2017	10:45	2.368	90.707
524	3	7/6/2017	10:45	2.411	83.098
524	4	7/6/2017	10:45	2.424	90.16
524	4	7/6/2017	10:45	2.404	76.546
524	5	7/6/2017	10:45	2.362	72.003
524	5	7/6/2017	10:45	2.381	74.817
524	6	7/6/2017	10:45	2.394	73.523
524	6	7/6/2017	10:45	2.394	85.78
524	7	7/6/2017	10:45	2.419	82.292
524	7	7/6/2017	10:45	2.374	70.524
524	8	7/6/2017	10:45	2.402	75.136
524	8	7/6/2017	10:45	2.307	79.891
624	1	7/6/2017	10:45	2.409	81.699

Cell	scan	Date	Time	Shear velocity. km/sec	HTI
624	1	7/6/2017	10:45	2.435	71.193
624	2	7/6/2017	10:45	2.393	76.218
624	2	7/6/2017	10:45	2.443	73.418
124	1	7/10/2017	10:13	2.487	72.393
124	1	7/10/2017	10:13	2.553	74.689
124	2	7/10/2017	10:13	2.472	68.463
124	2	7/10/2017	10:13	2.55	77.019
124	3	7/10/2017	10:13	2.567	70.968
124	3	7/10/2017	10:13	2.582	81.972
124	4	7/10/2017	10:13	2.58	69.237
124	4	7/10/2017	10:13	2.535	87.278
124	5	7/10/2017	10:13	2.48	73.674
124	5	7/10/2017	10:13	2.57	77.29
124	6	7/10/2017	10:13	2.509	66.755
124	6	7/10/2017	10:13	2.553	74.947
124	7	7/10/2017	10:13	2.579	68.644
124	7	7/10/2017	10:13	2.528	81.137
124	8	7/10/2017	10:13	2.584	74.187
124	8	7/10/2017	10:13	2.556	79.112
124	9	7/10/2017	10:13	2.566	71.699
124	9	7/10/2017	10:13	2.458	78.136
124	10	7/10/2017	10:13	2.554	66.439
124	10	7/10/2017	10:13	2.553	79.616
124	11	7/10/2017	10:13	2.534	67.074
124	11	7/10/2017	10:13	2.579	73.841
124	12	7/10/2017	10:13	2.53	72.56
124	12	7/10/2017	10:13	2.55	75.513
124	13	7/10/2017	10:13	2.551	69.491
124	13	7/10/2017	10:13	2.413	83.321
124	14	7/10/2017	10:13	2.569	70.507
124	14	7/10/2017	10:13	2.599	72.044
124	15	7/10/2017	10:13	2.522	87.032
124	15	7/10/2017	10:13	2.496	74.784
124	16	7/10/2017	10:13	2.511	78.97
124	16	7/10/2017	10:13	2.534	75.717
224	1	7/10/2017	10:13	2.624	65.162
224	1	7/10/2017	10:13	2.462	108.923
224	2	7/10/2017	10:13	2.53	67.776

Cell	scan	Date	Time	Shear velocity. km/sec	HTI
224	2	7/10/2017	10:13	2.548	84.469
224	3	7/10/2017	10:13	2.517	73.812
224	3	7/10/2017	10:13	2.587	84.016
224	4	7/10/2017	10:13	2.539	80.839
224	4	7/10/2017	10:13	2.577	74.434
224	5	7/10/2017	10:13	2.55	76.547
224	5	7/10/2017	10:13	2.547	79.018
224	6	7/10/2017	10:13	2.509	82.548
224	6	7/10/2017	10:13	2.546	78.825
224	7	7/10/2017	10:13	2.515	73.027
224	7	7/10/2017	10:13	2.535	85.898
224	8	7/10/2017	10:13	2.553	85.024
224	8	7/10/2017	10:13	2.538	73.289
224	9	7/10/2017	10:13	2.535	75.352
224	9	7/10/2017	10:13	2.538	79.027
224	10	7/10/2017	10:13	2.51	73.67
224	10	7/10/2017	10:13	2.579	77.071
224	11	7/10/2017	10:13	2.5	69.715
224	11	7/10/2017	10:13	2.502	78.588
224	12	7/10/2017	10:13	2.499	77.627
224	12	7/10/2017	10:13	2.54	74.816
224	13	7/10/2017	10:13	2.52	71.09
224	13	7/10/2017	10:13	2.563	83.468
224	14	7/10/2017	10:13	2.515	82.129
224	14	7/10/2017	10:13	2.533	78.445
224	15	7/10/2017	10:13	2.504	66.612
224	15	7/10/2017	10:13	2.553	77.667
224	16	7/10/2017	10:13	2.496	71.474
224	16	7/10/2017	10:13	2.41	82.406
324	1	7/10/2017	10:13	2.495	87.421
324	1	7/10/2017	10:13	2.418	80.683
324	2	7/10/2017	10:13	2.464	80.662
324	2	7/10/2017	10:13	2.579	79.751
324	3	7/10/2017	10:13	2.506	79.101
324	3	7/10/2017	10:13	2.419	86.971
324	4	7/10/2017	10:13	2.47	82.092
324	4	7/10/2017	10:13	2.565	80.175
324	5	7/10/2017	10:13	2.503	65.8

Cell	scan	Date	Time	Shear velocity. km/sec	HTI
324	5	7/10/2017	10:13	2.421	83.002
324	6	7/10/2017	10:13	2.516	70.36
324	6	7/10/2017	10:13	2.578	82.472
324	7	7/10/2017	10:13	2.579	76.714
324	7	7/10/2017	10:13	2.377	77.144
324	8	7/10/2017	10:13	2.539	74.913
324	8	7/10/2017	10:13	2.542	78.322
324	9	7/10/2017	10:13	2.542	81.386
324	9	7/10/2017	10:13	2.543	88.619
324	10	7/10/2017	10:13	2.526	85.29
324	10	7/10/2017	10:13	2.538	86.899
324	11	7/10/2017	10:13	2.541	77.263
324	11	7/10/2017	10:13	2.519	79.556
324	12	7/10/2017	10:13	2.534	61.713
324	12	7/10/2017	10:13	2.515	78.303
324	13	7/10/2017	10:13	2.562	72.679
324	13	7/10/2017	10:13	2.471	72.201
324	14	7/10/2017	10:13	2.551	73.486
324	14	7/10/2017	10:13	2.501	71.389
324	15	7/10/2017	10:13	2.532	71.489
324	15	7/10/2017	10:13	2.473	77.307
324	16	7/10/2017	10:13	2.497	69.181
324	16	7/10/2017	10:13	2.485	75.7
424	1	7/10/2017	10:13	2.482	71.34
424	1	7/10/2017	10:13	2.518	80.366
424	1	7/10/2017	10:13	2.47	71.987
424	2	7/10/2017	10:13	2.447	79.016
424	2	7/10/2017	10:13	2.498	79.273
424	2	7/10/2017	10:13	2.505	81.426
424	3	7/10/2017	10:13	2.528	74.045
424	3	7/10/2017	10:13	2.518	76.971
424	3	7/10/2017	10:13	2.492	73.854
424	4	7/10/2017	10:13	2.521	79.589
424	4	7/10/2017	10:13	2.54	85.179
424	4	7/10/2017	10:13	2.521	83.431
424	5	7/10/2017	10:13	2.505	71.622
424	5	7/10/2017	10:13	2.533	76.001
424	5	7/10/2017	10:13	2.563	69.161

Cell	scan	Date	Time	Shear velocity. km/sec	HTI
424	6	7/10/2017	10:13	2.461	103.496
424	6	7/10/2017	10:13	2.533	83.686
424	6	7/10/2017	10:13	2.502	70.097
424	7	7/10/2017	10:13	2.469	65.679
424	7	7/10/2017	10:13	2.499	81.405
424	8	7/10/2017	10:13	2.487	65.201
424	8	7/10/2017	10:13	2.513	80.593
424	9	7/10/2017	10:13	2.506	77.19
424	9	7/10/2017	10:13	2.51	70.038
424	10	7/10/2017	10:13	2.509	71.706
424	10	7/10/2017	10:13	2.496	70.128
424	11	7/10/2017	10:13	2.711	93.916
424	12	7/10/2017	10:13	2.503	68.571
424	13	7/10/2017	10:13	2.511	70.587
424	14	7/10/2017	10:13	2.661	84.821
424	15	7/10/2017	10:13	2.519	76.418
424	16	7/10/2017	10:13	2.466	76.283
524	1	7/10/2017	10:13	2.533	75.874
524	1	7/10/2017	10:13	2.492	72.644
524	2	7/10/2017	10:13	2.539	76.63
524	2	7/10/2017	10:13	2.465	68.334
524	3	7/10/2017	10:13	2.513	77.889
524	3	7/10/2017	10:13	2.496	89.384
524	4	7/10/2017	10:13	2.504	84.554
524	4	7/10/2017	10:13	2.534	84.092
524	5	7/10/2017	10:13	2.481	82.203
524	5	7/10/2017	10:13	2.523	70.737
524	6	7/10/2017	10:13	2.516	77.051
524	6	7/10/2017	10:13	2.498	65.065
524	7	7/10/2017	10:13	2.481	93.081
524	7	7/10/2017	10:13	2.464	98.103
524	8	7/10/2017	10:13	2.495	71.021
524	8	7/10/2017	10:13	2.521	70.084
624	1	7/10/2017	10:13	2.551	68.614
624	1	7/10/2017	10:13	2.522	74.648
624	2	7/10/2017	10:13	2.527	73.289
624	2	7/10/2017	10:13	2.535	76.145

APPENDIX D LONG-TERM DYNAMIC DATA
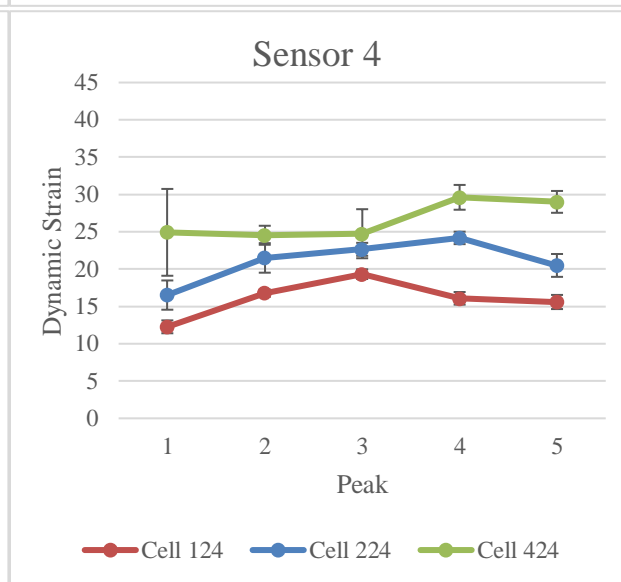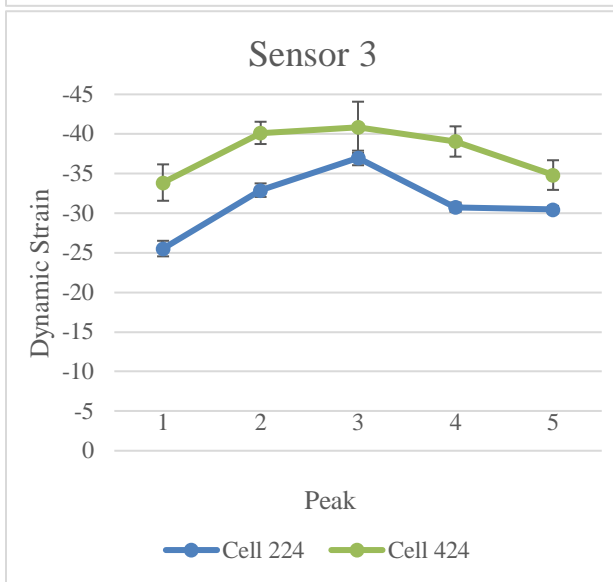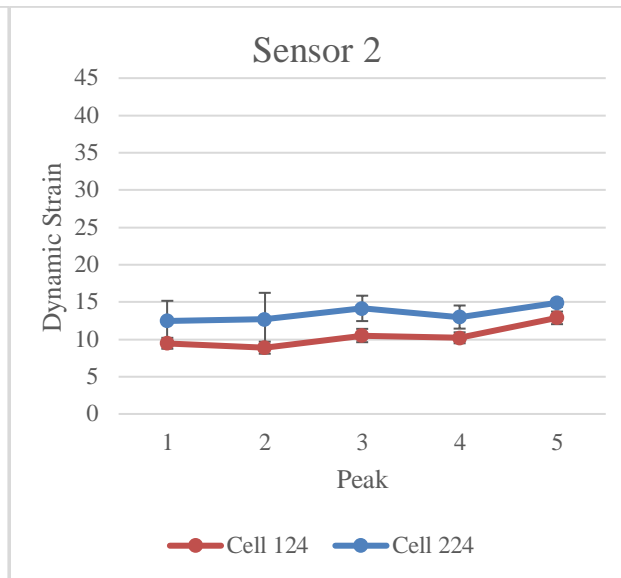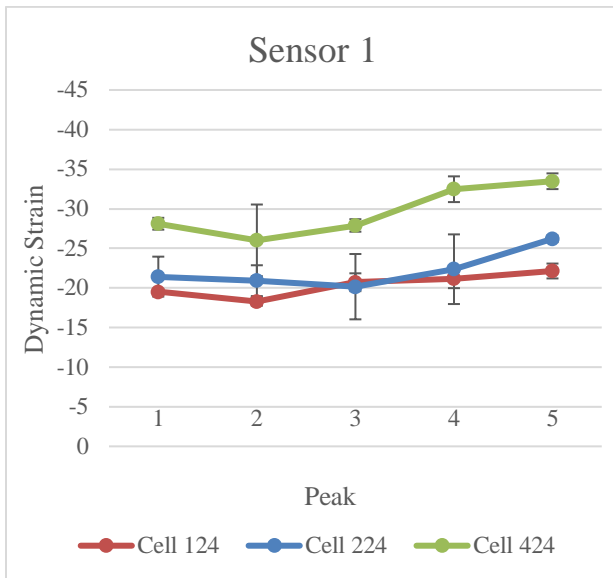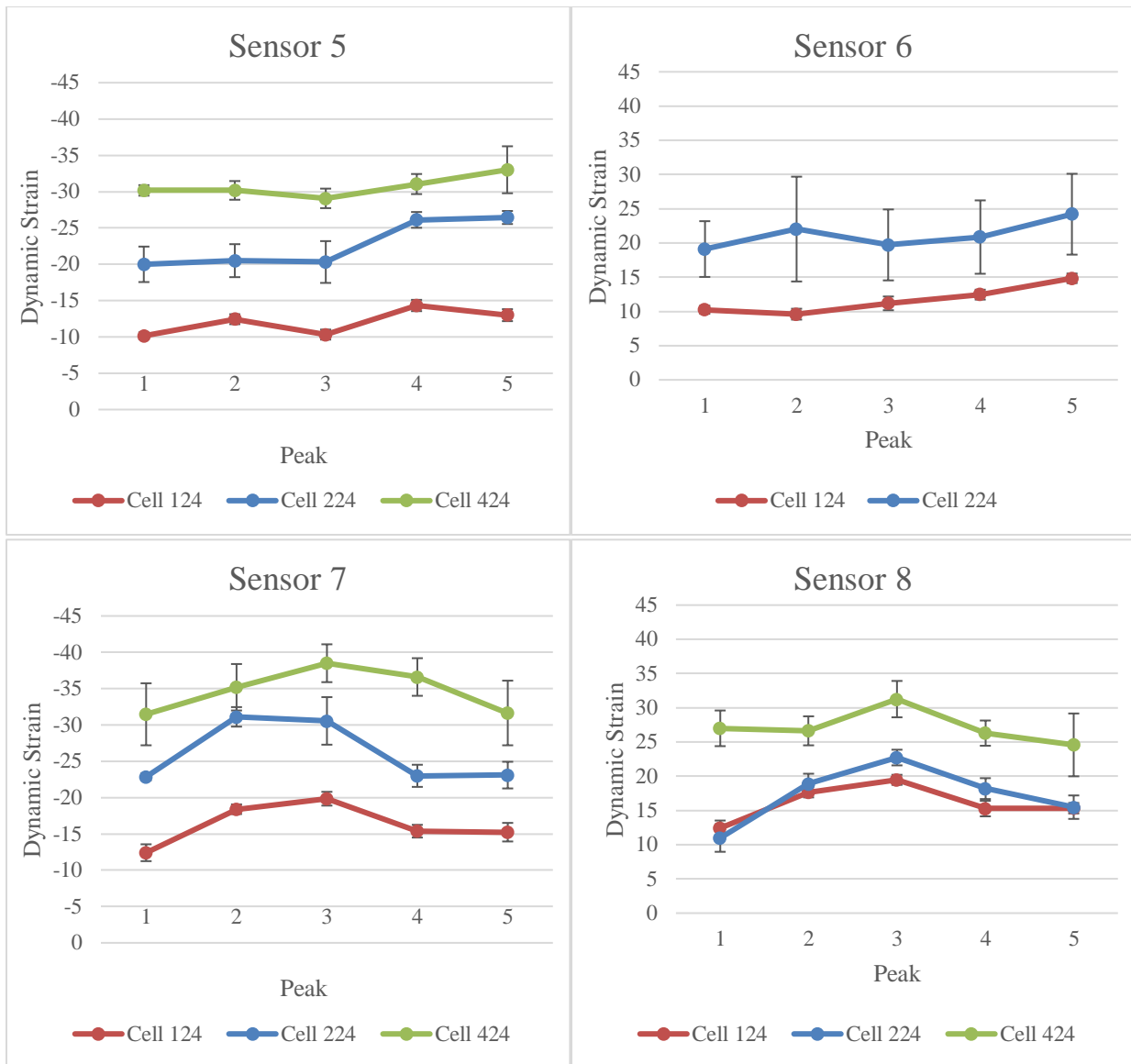
Figure D1: Long-term dynamic strain data for March 2018
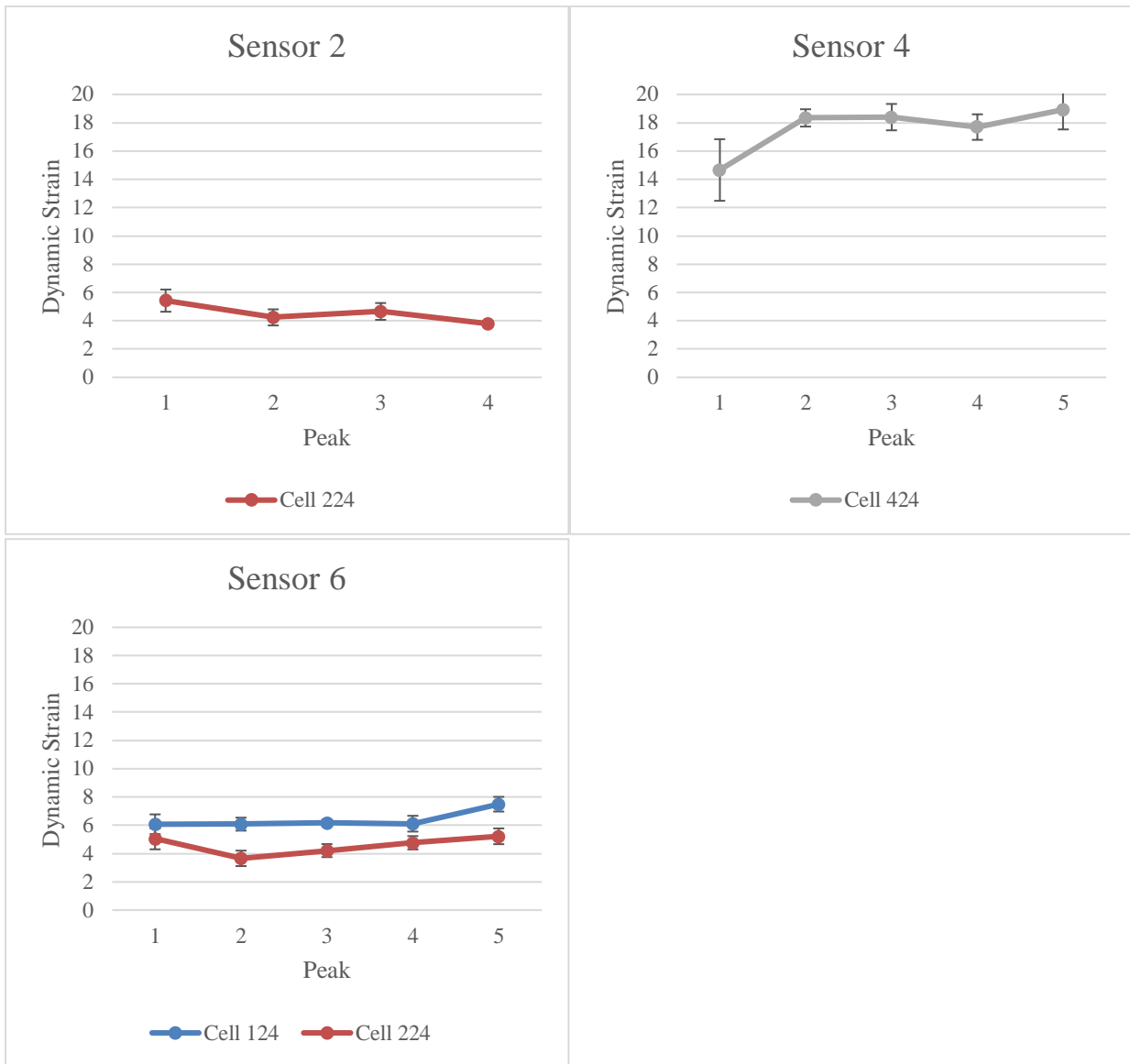
Figure D2: Long-term dynamic strain data for July 2018
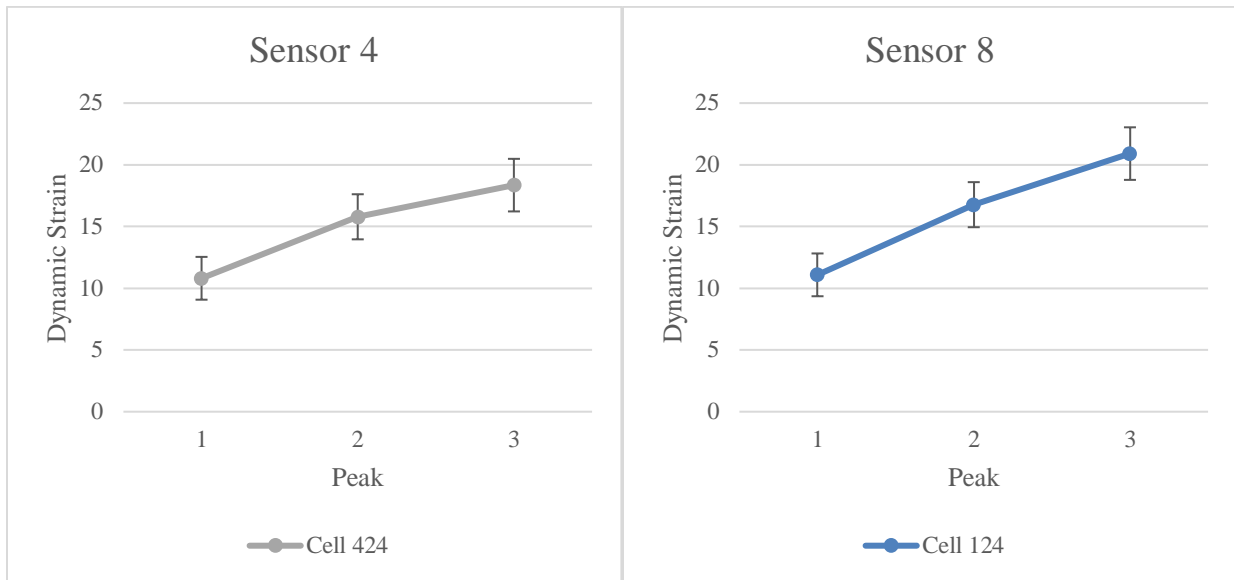
Figure D3: Long-term dynamic strain data for October 2018

APPENDIX E AMERICAN ENGINEERING TESTING INC. EARLY AGE MNROAD MIX

Table E1: Summary of flexural strength test results

Test Method	3A21	Specification
ASTM C78, Flexural Strength, Average psi		
6 hours		
Sample 1	90	
Sample 2	95	-
Average	95	
12 hours		
Sample 1	320	
Sample 2	265	-
Average	295	
18 hours		
Sample 1	390	
Sample 2	400	-
Average	395	
1 day		
Sample 1	445	
Sample 2	480	-
Average	465	
2 days		
Sample 1	500	
Sample 2	510	-
Average	505	
3 days		
Sample 1	590	
Sample 2	575	-
Average	585	
4 days		
Sample 1	610	
Sample 2	615	-
Average	615	
5 days		
Sample 1	640	
Sample 2	665	-
Average	655	
7 days		
Sample 1	705	
Sample 2	700	-
Average	705	

Table E2: Final test results of ASTM C1074, estimating concrete flexural strength by the maturity method [6]

Maturity Level	Specimen #	Specimen Strength (psi)	Average Specimen Strength (psi)	Maturity Elapsed Time (hh:mm)	Specimen Maturity (°C-hrs)	Temperature (°C)	Average Maturity (°C-hrs)	Average Temperature (°C)	Average Age (days)
1	Beam 1	90	90	6:00	155	28	155	28	0.25
1	Beam 2	95		6:00	155	28			
2	Beam 3	320	290	12:00	331	28	331	28	0.50
2	Beam 4	265		12:00	331	28			
3	Beam 5	390	400	18:00	494	25	494	25	0.75
3	Beam 6	400		18:00	494	25			
4	Beam 7	445	460	24:00	637	24	637	24	1.00
4	Beam 8	480		24:00	637	24			
5	Beam 9	500	510	48:00	1,213	24	1,213	24	2.00
5	Beam 10	510		48:00	1,213	24			
6	Beam 11	590	583	72:00	1,784	23	1,784	23	3.00
6	Beam 12	575		72:00	1,784	23			
7	Beam 13	610	613	96:00	2,336	23	2,336	23	4.00
7	Beam 14	615		96:00	2,336	23			
8	Beam 15	640	653	120:00	2,888	23	2,888	23	5.00
8	Beam 16	665		120:00	2,888	23			
9	Beam 17	705	703	168:00	3,849	22	3,849	22	7.00
9	Beam 18	700		168:00	3,848	22			

APPENDIX F IRI DATA

Table F1 IRI data with each date averaging 2 to 3 runs in each wheel path

Cell	Date	IRI (in/mi)					
		Inside Lane			Outside Lane		
		LWP	RWP	Average	LWP	RWP	Average
124	7/20/2017	79.83	73.50	76.67	85.96	65.89	75.93
	10/26/2017	82.37	80.78	81.58	86.80	80.15	83.48
	3/28/2018	83.64	80.47	82.05	85.22	84.27	84.74
	4/25/2018	81.10	75.72	78.41	79.52	65.89	72.71
	6/11/2018	82.37	82.37	82.37	86.49	79.83	83.16
	8/16/2018	83.95	76.35	80.15	81.73	76.98	79.36
	10/2/2018	78.88	78.88	78.88	81.73	76.03	78.88
	3/19/2019	75.08	68.11	71.60	71.28	56.71	63.99
	5/21/2019	76.67	71.60	74.13	77.93	65.26	71.60
	8/29/2019	74.45	73.18	73.81	76.67	69.70	73.18
	10/24/2019	72.55	67.48	70.01	80.78	76.35	78.57
	3/10/2020	73.18	67.48	70.33	70.65	67.16	68.90
	8/6/2020	79.20	81.42	80.31	83.64	81.10	82.37
224	7/20/2017	49.84	59.98	54.91	57.87	58.50	58.19
	10/26/2017	64.94	74.76	69.85	72.86	80.47	76.67
	3/28/2018	62.41	73.18	67.80	74.13	86.49	80.31
	4/25/2018	54.49	62.73	58.61	65.58	71.91	68.75
	6/11/2018	68.43	78.57	73.50	76.98	83.95	80.47
	8/16/2018	54.81	62.41	58.61	64.63	66.21	65.42
	10/2/2018	61.78	74.76	68.27	70.01	77.30	73.66
	3/19/2019	37.70	53.86	45.78	58.29	59.88	59.08
	5/21/2019	53.54	62.41	57.97	62.41	62.73	62.57
	8/29/2019	49.42	67.16	58.29	59.24	61.46	60.35
	10/24/2019	46.25	63.36	54.81	58.61	61.14	59.88
	3/10/2020	47.84	63.36	55.60	61.78	64.31	63.04
	8/6/2020	64.63	81.73	73.18	71.60	81.31	76.45
324	7/20/2017	62.52	60.19	61.35	55.33	48.58	51.96
	10/26/2017	64.31	69.06	66.69	64.31	69.06	66.69
	3/28/2018	56.39	60.51	58.45	61.46	66.21	63.84
	4/25/2018	52.59	57.66	55.12	54.81	54.49	54.65
	6/11/2018	70.96	73.81	72.39	72.55	73.81	73.18
	8/16/2018	56.71	63.68	60.19	58.92	58.92	58.92
	10/2/2018	65.26	68.75	67.00	66.21	66.84	66.53
	3/19/2019	46.89	53.54	50.21	46.57	38.65	42.61
	5/21/2019	55.44	58.61	57.02	55.76	51.96	53.86
	8/29/2019	54.81	57.97	56.39	53.86	52.27	53.06
	10/24/2019	50.37	51.96	51.16	54.81	53.86	54.33
	3/10/2020	53.54	57.34	55.44	58.29	55.76	57.02
	8/6/2020	63.36	73.50	68.43	65.47	66.74	66.11

	7/20/2017	63.15	72.86	68.01	61.25	56.18	58.71
	10/26/2017	74.13	84.90	79.52	63.68	65.89	64.79
	3/28/2018	64.94	72.23	68.59	60.19	61.46	60.83
	4/25/2018	60.19	66.84	63.52	52.59	49.42	51.00
	6/11/2018	83.64	92.51	88.07	75.40	78.25	76.82
	8/16/2018	63.36	73.50	68.43	61.78	65.58	63.68
424	10/2/2018	71.60	87.12	79.36	65.26	67.80	66.53
	3/19/2019	55.12	63.36	59.24	51.96	46.89	49.42
	5/21/2019	60.19	70.33	65.26	57.34	56.71	57.02
	8/29/2019	56.07	68.11	62.09	52.91	51.00	51.96
	10/24/2019	60.19	64.94	62.57	51.32	51.00	51.16
	3/10/2020	64.31	71.91	68.11	56.07	55.76	55.92
	8/6/2020	73.81	88.39	81.10	69.06	70.33	69.70
	10/26/2017	93.14	105.18	99.16	101.06	115.00	108.03
	3/28/2018	84.59	93.77	89.18	94.09	109.30	101.69
	4/25/2018	81.10	88.70	84.90	85.22	95.99	90.60
	6/11/2018	100.43	121.02	110.72	109.61	122.28	115.95
	8/16/2018	84.90	93.46	89.18	94.72	103.91	99.32
524	10/2/2018	86.49	105.18	95.83	96.31	108.35	102.33
	3/19/2019	96.31	112.15	104.23	76.35	84.59	80.47
	5/21/2019	80.78	92.51	86.64	86.49	98.84	92.66
	8/29/2019	76.35	91.56	83.95	86.80	100.11	93.46
	10/24/2019	85.54	102.33	93.93	85.85	99.16	92.51
	3/10/2020	86.17	102.96	94.56	90.92	102.01	96.47
	8/6/2020	93.46	109.30	101.38	103.49	118.06	110.77
	10/26/2017	307.30	281.64	294.47	135.91	134.32	135.12
	3/28/2018	266.43	326.30	296.37	130.52	126.40	128.46
	4/25/2018	245.20	324.40	284.80	136.22	130.20	133.21
	6/11/2018	277.20	396.00	336.60	139.39	136.54	137.97
	8/16/2018	249.64	374.46	312.05	135.91	132.42	134.16
624	10/2/2018	261.04	391.88	326.46	139.71	144.46	142.08
	3/19/2019	266.11	349.11	307.61	147.95	148.26	148.10
	5/21/2019	312.36	446.05	379.21	153.33	156.50	154.92
	8/29/2019	227.78	357.67	292.72	139.08	134.64	136.86
	10/24/2019	318.70	482.17	400.44	131.47	121.65	126.56
	3/10/2020	366.54	505.30	435.92	138.12	117.53	127.83
	8/6/2020	308.88	504.66	406.77	140.45	138.97	139.71

APPENDIX G LTE DATA

Table G1 LTE data for the approach slab in the inside lane with each date averaging 3 runs

		Slab 1	Slab 2	Average
124	10/23/2017	95%	89%	92%
	3/15/2018	81%	76%	79%
	5/4/2018	92%	87%	90%
	3/29/2019	82%	74%	78%
	5/7/2019	85%	83%	84%
	3/17/2020	82%	71%	77%
	4/21/2020	83%	72%	77%
	10/22/2020	79%	69%	74%
	4/14/2021	71%	84%	77%
224	10/23/2017	92%	88%	90%
	3/15/2018	80%	74%	77%
	5/4/2018	92%	88%	90%
	3/29/2019	85%	75%	80%
	5/7/2019	83%	81%	82%
	3/17/2020	79%	71%	75%
	4/21/2020	78%	70%	74%
	10/22/2020	75%	69%	72%
	4/14/2021	78%	69%	73%
324	10/23/2017	94%	92%	93%
	3/15/2018	78%	80%	79%
	5/4/2018	94%	90%	92%
	3/29/2019	82%	81%	82%
	5/7/2019	86%	85%	85%
	3/17/2020	78%	76%	77%
	4/21/2020	78%	76%	77%
	10/22/2020	79%	75%	77%
	4/14/2021	81%	83%	82%
424	10/23/2017	91%	90%	91%
	3/15/2018	82%	80%	81%
	5/4/2018	93%	92%	92%
	3/29/2019	79%	87%	83%
	5/7/2019	86%	87%	87%
	3/17/2020	80%	78%	79%
	4/21/2020	76%	77%	76%
	10/22/2020	78%	78%	78%
	4/14/2021	80%	83%	81%
524	10/23/2017	93%	90%	92%
	3/15/2018	87%	78%	82%
	5/4/2018	93%	90%	91%
	3/29/2019	89%	74%	82%
	5/7/2019	89%	85%	87%

		Slab 1	Slab 2	Average
	3/17/2020	85%	75%	80%
	4/21/2020	87%	74%	81%
	10/22/2020	88%	77%	83%
	4/14/2021	91%	73%	82%

Table G2 LTE data for the approach slab in the outside lane with each date averaging 3 runs

		Slab 1	Slab 2	Average
	10/23/2017	84%	84%	84%
	3/15/2018	85%	80%	82%
	5/4/2018	89%	82%	86%
124	3/29/2019	85%	83%	84%
	3/17/2020	84%	74%	79%
	4/21/2020	81%	73%	77%
	10/22/2020	86%	84%	85%
	4/14/2021	86%	75%	81%
	10/23/2017	90%	86%	88%
	3/15/2018	77%	76%	76%
	5/4/2018	89%	89%	89%
224	3/29/2019	84%	82%	83%
	3/17/2020	83%	86%	84%
	4/21/2020	81%	80%	81%
	10/22/2020	86%	80%	83%
	4/14/2021	80%	87%	83%
	10/23/2017	87%	88%	87%
	3/15/2018	78%	79%	79%
	5/4/2018	92%	93%	92%
324	3/29/2019	85%	84%	84%
	3/17/2020	83%	81%	82%
	4/21/2020	83%	81%	82%
	10/22/2020	86%	86%	86%
	4/14/2021	83%	80%	81%
	10/23/2017	84%	84%	84%
	3/15/2018	70%	76%	73%
	5/4/2018	84%	84%	84%
424	3/29/2019	81%	82%	81%
	3/17/2020	71%	77%	74%
	4/21/2020	77%	81%	79%
	10/22/2020	86%	86%	86%
	4/14/2021	76%	78%	77%
	10/23/2017	88%	89%	88%
524	3/15/2018	78%	75%	76%
	5/4/2018	92%	90%	91%
	3/29/2019	88%	83%	86%

		Slab 1	Slab 2	Average
	3/17/2020	86%	80%	83%
	4/21/2020	87%	78%	82%
	10/22/2020	87%	87%	87%
	4/14/2021	88%	79%	84%

Table G3 LTE data for the leave slab in the inside lane with each date averaging 3 runs

		Slab 1	Slab 2	Average
	10/23/2017	94%	92%	93%
	3/15/2018	80%	68%	74%
	5/4/2018	92%	84%	88%
	3/29/2019	78%	74%	76%
124	5/7/2019	88%	85%	86%
	3/17/2020	79%	75%	77%
	4/21/2020	76%	73%	75%
	10/22/2020	81%	82%	82%
	4/14/2021	81%	75%	78%
	10/23/2017	92%	88%	90%
	3/15/2018	74%	70%	72%
	5/4/2018	93%	84%	88%
	3/29/2019	84%	68%	76%
224	5/7/2019	87%	83%	85%
	3/17/2020	77%	71%	74%
	4/21/2020	76%	68%	72%
	10/22/2020	80%	72%	76%
	4/14/2021	79%	71%	75%
	10/23/2017	90%	90%	90%
	3/15/2018	74%	73%	74%
	5/4/2018	93%	91%	92%
	3/29/2019	82%	79%	81%
324	5/7/2019	88%	85%	87%
	3/17/2020	76%	73%	75%
	4/21/2020	75%	74%	74%
	10/22/2020	76%	76%	76%
	4/14/2021	80%	83%	82%
	10/23/2017	90%	90%	90%
	3/15/2018	79%	80%	79%
	5/4/2018	95%	95%	95%
	5/4/2018	92%	93%	92%
424	3/29/2019	81%	83%	82%
	5/7/2019	88%	88%	88%
	3/17/2020	79%	80%	79%
	4/21/2020	76%	76%	76%
	10/22/2020	79%	82%	81%

Table G4 LTE data for the leave slab in the outside lane with each date averaging 3 runs

		Slab 1	Slab 2	Average
124	10/23/2017	88%	87%	87%
	3/15/2018	81%	74%	78%
	5/4/2018	91%	86%	89%
	3/29/2019	89%	86%	87%
	3/17/2020	86%	75%	81%
	4/21/2020	88%	82%	85%
	10/22/2020	91%	85%	88%
	4/14/2021	83%	69%	76%
224	10/23/2017	88%	86%	87%
	3/15/2018	75%	75%	75%
	5/4/2018	94%	92%	93%
	3/29/2019	87%	84%	85%
	3/17/2020	83%	84%	83%
	4/21/2020	84%		84%
	10/22/2020	89%	76%	83%
	4/14/2021	76%	86%	81%
324	10/23/2017	86%	87%	87%
	3/15/2018	79%	77%	78%
	5/4/2018	93%	95%	94%
	3/29/2019	89%	85%	87%
	3/17/2020	83%	80%	82%
	4/21/2020	86%	83%	84%
	10/22/2020	91%	91%	91%
	4/14/2021	84%	80%	82%
424	10/23/2017	87%	87%	87%
	3/15/2018	74%	76%	75%
	5/4/2018	86%	88%	87%
	3/29/2019	82%	87%	85%
	3/17/2020	76%	80%	78%
	4/21/2020	82%	83%	83%
	10/22/2020	90%	92%	91%
	4/14/2021	76%	76%	76%

APPENDIX H PETROGRAPHIC DATA

AMERICAN ENGINEERING TESTING, INC.

REPORT OF CONCRETE ANALYSIS

PROJECT:

PERFORMANCE OF EARLY LOADED
CONCRETE SECTIONS AFTER 4 YEARS
STATE PROJECT NO. (SP): 8821-331
TRUNK HIGHWAY NUMBER (TH): 999

AET PROJECT NO: P-0002628

REPORTED TO:

MN DEPT OF TRANSPORTATION
1123 MESABA AVENUE
DULUTH, MN 55811

ATTN: AMY THORSON

DATE: MAY 21, 2021

INTRODUCTION

This report presents the results of laboratory work performed by our firm on six concrete core samples submitted by Dr. Bernard Izevbekhai of Minnesota Department of Transportation on May 7, 2021. We understand the cores were obtained from concrete road pavement of various locations subjected to various degrees of sequential early loading. The concrete was reportedly about 4 years old. The scope of our work was limited to performing petrographic analysis on the six core samples to document the general overall condition of the concrete.

CONCLUSIONS

Based on our observations and testing, we believe:

1. The overall condition of the six concrete core samples was judged to be good. The six samples were full depth cores through the concrete pavement placed on grade with broom finished/drag textured top surfaces. The six core samples did not exhibit any visual evidence of gross deterioration and were free of large-scaled cracking/fracturing. We observed no evidence of any detrimental effects of early loading of the concrete pavements.

2. The six concrete cores did exhibit signs of age and weathering. The top surfaces of the core samples were mortar eroded and shallowly (< 3 mm depth) scaled which exposed numerous fine aggregates and a few coarse aggregate particles. Also, topographic highs of core 521 424B were worn slightly smooth. Remnant flakes of curing compound were documented residing in the topographic lows of the top surfaces of the cores. A few to several, fine, sub-vertical drying shrinkage microcracks proceeded to 25 mm (1") maximum depth from the top surfaces. Carbonation ranged from negligible to 9 mm (3/8") maximum depth along sub-vertical microcracks. Intermittent carbonation was documented to 15 mm (9/16") maximum depth along sub-vertical microcracking in 521 424B and 521 424W. Carbonation, in general, is a reaction between calcium hydroxide present in the concrete paste along with carbona dioxide and moisture to form calcium carbonate, resulting in a lowering of the pH of the concrete paste. Carbonation in well cured concrete of a moderate to cementitious materials ratio (w/cm) typically progresses < 1 mm (1/32") per year.

3.   The six concrete cores were fairly well consolidated and purposefully air entrained. The concrete in the cores exhibited fairly well to fairly distributed, 'fine,' air void systems that were consistent with current American Concrete Institute (ACI) recommendations for freeze-thaw resistance. The total air content of the concrete cores ranged from 6.3 to 8.4% with 0.002" spacing factor. A few to several, innocuous, irregular shaped, entrapped-sized, air voids were documented throughout the samples with some concentration along paste/aggregate boundaries. A notable lesser amount of coarse aggregate particles, > 13 mm (1/2") in size, were documented in the top approximately 76 mm (3") of 521 424B, 521 424W, 521 524B, and 521 524W.

SAMPLE IDENTIFICATION

Sample ID:	521 124B	521 124W
Sample Type:	102 mm (4") Diameter Hardened Concrete Cores	
Sample Length:	165 mm (6-1/2")	165 mm (6-1/2")
Sample ID:	521 424B	521 424W
Sample Type:	102 mm (4") Diameter Hardened Concrete Cores	
Sample Length:	165 mm (6-1/2")	159 mm (6-1/4")
Sample ID:	521 524B	521 524W
Sample Type:	102 mm (4") Diameter Hardened Concrete Cores	
Sample Length:	171 mm (6-3/4")	165 mm (6-1/2")

TEST RESULTS

Our complete petrographic analysis documentation appears on the attached sheets entitled 24-LAB-001 "Petrographic Examination of Hardened Concrete, ASTM C856." A brief summary of the general physical characteristics of the concrete is as follows:

1.   The coarse aggregate in the six cores was comprised of natural glacial gravel. The nominal aggregate size was 38 mm (1-1/2") in 521 424B and 25 mm (1") in the remaining cores. The coarse aggregate appeared well graded and exhibited good to fair overall distribution. A lesser amount of coarse aggregate particles, > 13 mm (1/2") in size, were documented in the top approximately 76 mm (3") of 521 424B, 521 424W, 521 524B, and 521 524W. The fine aggregate in the cores was a natural glacial sand.

2.   The overall paste color of the six cores was medium light gray and the paste hardness was judged to be moderate. The paste/aggregate bond was considered good to fair in 521 124B and 521 424B, fair in 521 124W and 521 424W, and fair to poor in 521 524B and 521 524W.

3.   The top surface condition of the cores was broom finished/drag textured exhibiting mortar erosion and shallow scaling exposing numerous fine aggregate and a few coarse aggregate particles. Also, the topographic highs of core 521 424B were worn slightly smooth. Carbonation ranged negligible to 9 mm (3/8") maximum depth from the top surfaces along sub-vertical microcracking. Intermittent carbonation was documented to 15 mm (9/16") maximum depth along sub-vertical microcracking in 521 424B and 521 424W.

4.   The w/cm of the six concrete cores was similar and estimated to be between 0.40 and 0.45 with approximately 7 to 9% residual portland cement clinker particles and an amount of fly ash visually consistent with 25 to 35% replacement of portland cement.

Air Content Testing

Sample ID	521 124B	521 124W
Total Air Content (%)	7.5	6.3
"Entrained" Air (%) voids < 1mm (0.040")	5.5	5.1
"Entrapped" Air (%) voids > 1mm (0.040")	2.0	1.2
Spacing Factor, in.	0.002	0.002

Sample ID	521 424B	521 424W
Total Air Content (%)	8.4	8.2
"Entrained" Air (%) voids < 1mm (0.040")	6.6	6.4
"Entrapped" Air (%) voids > 1mm (0.040")	1.8	1.8
Spacing Factor, in.	0.002	0.002

Sample ID	521 524B	521 524W
Total Air Content (%)	7.9	7.6
"Entrained" Air (%) voids < 1mm (0.040")	6.5	6.0
"Entrapped" Air (%) voids > 1mm (0.040")	1.4	1.6

Spacing Factor, in.	0.002	0.002

TEST PROCEDURES

Laboratory testing was performed on May 10, 2021 and subsequent dates. Our procedures were as follows:

Petrographic Analysis

A petrographic analysis was performed in accordance with AET Standard Operating Procedure 24- LAB-001, "Petrographic Examination of Hardened Concrete," ASTM C856-latest revision. The petrographic analysis consisted of reviewing the cement paste and aggregate qualities on a whole basis on saw cut, lapped, and fractured sections. Reflected light microscopy was performed under an Olympus SZX-12 binocular stereozoom microscope at magnifications up to 160x. The depth of carbonation was documented using a phenolphthalein pH indicator solution applied on freshly saw cut and lapped surfaces of the concrete sample. The paste-coarse aggregate bond quality was determined by fracturing a sound section of the concrete in the laboratory with a rock hammer.

The water/cementitious of the concrete was estimated by viewing a thin section of the concrete under an Olympus BX-51 polarizing light microscope at magnifications of up to 1000x. Thin section analysis was performed in accordance with Standard Operating Procedure 24-LAB-009, "Determining the Water/Cement of Portland Cement Concrete, AET Method." An additional, smaller, saw cut subdivision of the concrete sample is epoxy impregnated, highly polished, and then attached to a glass slide using an optically clear epoxy. Excess sample is saw cut from the glass and the thin slice remaining on the slide is lapped and polished until the concrete reaches 25 microns or less in thickness. Thin section analysis allows for the observation of portland cement morphology, including: phase identification, an estimate of the amount of residual material, and spatial relationships. Also, the presence and relative amounts of supplementary cementitious materials and pozzolans may be identified and estimated.

Air Content Testing

Air content testing was performed using Standard Operating Procedure 24-LAB-003, "Microscopical Determination of Air Void Content and Parameters of the Air Void System in Hardened Concrete, ASTM C457-latest revision." The linear traverse method was used. The concrete core was saw cut perpendicular with respect to the horizontal plane of the concrete as placed and then lapped prior to testing.

REMARKS
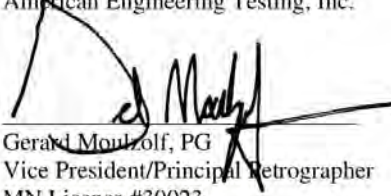
The test samples will be retained for a period of at least sixty days from the date of this report. Unless further instructions are received by that time, the samples may be discarded. Test results relate only to the items tested. No warranty, express or implied, is made.

Report Prepared By:
American Engineering Testing, Inc.

Sherry Malecha

Sherry Malecha
Petrographer
smalecha@amengtest.com

Report Reviewed By:
American Engineering Testing, Inc.

Gerard Moulzolf, PG
Vice President/Principal Petrographer
MN License #30023
Phone:651-659-1346
gmoulzolf@amengtest.com

24-LAB-001 Petrographic Examination of Hardened Concrete
ASTM C856

Project No.	P-0002628	Date:	5-12-2021	Date reviewed:	5-21-2021
Sample ID:	521 124B	Performed by:	S. Malecha	Reviewed by:	G. Moulzolf

I. **General Observations**

1. Sample Dimensions: Our analysis was performed on a 165 mm (6-1/2") x 98 mm (3-7/8") x 44 mm (1-3/4") thick lapped profile section and a 76 mm (3") x 52 mm (2") thin section that were saw-cut and prepared from the original 102 mm (4") diameter x 165 mm (6-1/2") long core.

2. Surface Conditions:
   Top: Fairly rough, broom finished/drag textured surface exhibiting mortar erosion and shallow scaling.
   Bottom: Rough, slightly irregular, formed; placed on grade.

3. Reinforcement: None observed.

4. General Physical Conditions: Remnants of orange marker paint were observed on the top surface of the core sample. The top surface of the core sample was mortar eroded exposing numerous fine aggregate particles and approximately 5% of its surface area was shallowly (< 3 mm depth) scaled. A few remnant flakes of curing compound exhibiting fine craze cracking were observed within the topographic lows of the top surface. A few, fine, sub-vertical microcracks proceeded to 4 mm (5/32") depth from the top surface. A few shale fine aggregate particles exhibited expansive microcracking which propagated into the surrounding paste. Carbonation ranged from negligible to 6 mm (1/4") depth from the top surface along sub-vertical microcracks and along paste/aggregate boundaries. The concrete was air entrained and contained a fairly well distributed air void system with 7.5% total air content and 0.002" spacing factor. The concrete was fairly well consolidated. Several, irregular shaped, entrapped-sized, air voids were observed throughout the sample with some concentration along paste/aggregate boundaries.

II. **Aggregate**

1. Coarse: 25 mm (1") nominal sized naturally occurring glacial gravel consisting of granite, gabbro, chert, felsite, sandstone, carbonate, and basalt with a few iron oxide particles. The coarse aggregate was mostly sub-rounded to rounded with several sub-angular to angular particles. The coarse aggregate appeared well graded and exhibited good overall distribution.

2. Fine: Natural quartz, feldspar, and lithic sand (carbonates, chert, granite, gabbro, and basalt with a few iron oxide and shale particles). The grains were mostly sub-rounded to sub-angular with many smaller angular particles. The fine aggregate appeared fairly graded and exhibited good overall uniform distribution. A few shale fine aggregate particles exhibited a dark rim and expansive microcracking which propagated into the surrounding paste.

III. **Cementitious Properties**

1. Air Content: 7.5% total
2. Depth of carbonation: Ranged from negligible to 6 mm (1/4") depth from the top surface along sub-vertical microcracks and along paste/aggregate boundaries.
3. Paste/aggregate bond: Good to fair.
4. Paste color: Medium light gray (Munsell® N6) overall. Medium gray (Munsell® N5) in the bottom approximately 13 mm (1/2") of the sample.
5. Paste hardness: Moderate (Mohs ≈ 3).
6. Microcracking: A few, fine, sub-vertical microcracks proceeded to 4 mm (5/32") depth from the top surface. A few shale fine aggregate particles exhibited expansive microcracking which propagated into the surrounding paste.
7. Secondary deposits: Ettringite was observed lining to filling air voids in thin section of the concrete sample.
8. w/cm: Estimated at between 0.40 and 0.45 with approximately 7 to 9% residual portland cement clinker particles and an amount of fly ash visually consistent with a 25 to 35% replacement of portland cement.
9. Cement hydration: Alites: moderate to fully
   Belites: negligible to low

24-LAB-001 Petrographic Examination of Hardened Concrete
ASTM C856

Project No.	P-0002628	Date:	5-12-2021	Date reviewed:	5-21-2021
Sample ID:	521 124W	Performed by:	S. Malecha	Reviewed by:	G. Moulzolf

I. **General Observations**

1. Sample Dimensions: Our analysis was performed on a 165 mm (6-1/2") x 98 mm (3-7/8") x 48 mm (1-7/8") thick lapped profile section and a 76 mm (3") x 52 mm (2") thin section that were saw-cut and prepared from the original 102 mm (4") diameter x 165 mm (6-1/2") long core.

2. Surface Conditions:
   Top: Fairly rough, broom finished/drag textured surface exhibiting mortar erosion and shallow scaling.
   Bottom: Rough, slightly irregular, formed; placed on grade.

3. Reinforcement: None observed.

4. General Physical Conditions: Remnants of orange marker paint were observed on the top surface of the core sample. The top surface of the core sample was mortar eroded exposing numerous fine aggregate particles and approximately 5% of its surface area was shallowly scaled to 2 mm (1/16") depth exposing a few coarse aggregate particles. A few remnant flakes of curing compound exhibiting fine craze cracking were observed within the topographic lows of the top surface. A few, fine, sub-vertical microcracks proceeded to 7 mm (1/4") depth from the top surface. A few shale fine aggregate particles exhibited expansive microcracking which propagated into the surrounding paste. Carbonation ranged from negligible to 2 mm (1/16") depth from the top surface and spiked to 6 mm (1/4") depth along sub-vertical microcracks. The concrete was air entrained and contained a fairly well distributed air void system with 6.3% total air content and 0.002" spacing factor. The concrete was fairly well consolidated. Several, irregular shaped, entrapped-sized, air voids were observed throughout the sample with some concentration along paste/aggregate boundaries.

II. **Aggregate**

1. Coarse: 25 mm (1") nominal sized naturally occurring glacial gravel consisting of granite, gabbro, chert, felsite, sandstone, carbonate, and basalt with a few iron oxide particles. The coarse aggregate was mostly sub-rounded to rounded with several sub-angular to angular particles. The coarse aggregate appeared well graded and exhibited good overall distribution.

2. Fine: Natural quartz, feldspar, and lithic sand (carbonates, chert, granite, gabbro, and basalt with a few iron oxide and shale particles). The grains were mostly sub-rounded to sub-angular with many smaller angular particles. The fine aggregate appeared fairly graded and exhibited good overall uniform distribution. A few shale fine aggregate particles exhibited a dark rim and expansive microcracking which propagated into the surrounding paste.

III. **Cementitious Properties**

1. Air Content: 6.3% total
2. Depth of carbonation: Ranged from negligible to 2 mm (1/16") depth from the top surface and spiked to 6 mm (1/4") depth along sub-vertical microcracks.
3. Paste/aggregate bond: Fair.
4. Paste color: Medium light gray (Munsell® N6) overall. Medium gray (Munsell® N5) in the bottom approximately 13 mm (1/2") of the sample.
5. Paste hardness: Moderate (Mohs ≈ 3).
6. Microcracking: A few, fine, sub-vertical microcracks proceeded to 7 mm (1/4") depth from the top surface. A few shale fine aggregate particles exhibited expansive microcracking which propagated into the surrounding paste.
7. Secondary deposits: None observed.
8. w/cm: Estimated at between 0.40 and 0.45 with approximately 7 to 9% residual portland cement clinker particles and an amount of fly ash visually consistent with a 25 to 35% replacement of portland cement.
9. Cement hydration: Alites: moderate to fully
                          Belites: negligible to low

| Project No. | P-0002628 | Date: | 5-12-2021 | Date reviewed: | 5-21-2021 |
| Sample ID: | 521 424B | Performed by: | S. Malecha | Reviewed by: | G. Moulzolf |

I. **General Observations**

1. Sample Dimensions: Our analysis was performed on a 165 mm (6-1/2") x 98 mm (3-7/8") x 48 mm (1-7/8") thick lapped profile section and a 76 mm (3") x 52 mm (2") thin section that were saw-cut and prepared from the original 102 mm (4") diameter x 165 mm (6-1/2") long core.

2. Surface Conditions:
   Top: Fairly rough, broom finished/drag textured surface exhibiting mortar erosion, traffic wear, and shallow scaling.
   Bottom: Rough, slightly irregular, formed; placed on grade.

3. Reinforcement: None observed.

4. General Physical Conditions: Remnants of orange marker paint were observed on the top surface of the core sample. The top surface was mortar eroded and traffic worn exposing numerous fine aggregate particles with topographic highs worn slightly smooth. Approximately 10% of its surface area was shallowly scaled away to approximately 3 mm (1/8") depth exposing a few coarse aggregate particles. A few remnant flakes of curing compound exhibiting fine craze cracking were observed within the topographic lows of the top surface. A lesser amount of coarse aggregate particles, > 13 mm (1/2") in size, were observed in the top approximately 25 mm (1") up to 32 mm (1-1/4") of the sample. A few, fine, sub-vertical microcracks proceeded to 9 mm (3/8") depth from the top surface and one microcrack proceeded to 25 mm (1") depth. A few shale fine aggregate particles exhibited expansive microcracking which propagated into the surrounding paste. Carbonation ranged from negligible to 7 mm (1/4") depth from the top surface. Intermittent carbonation proceeded to 15 mm (9/16") depth from the top surface along sub-vertical microcracks. The concrete was air entrained and contained a fairly well distributed air void system with 8.4% total air content and 0.002" spacing factor. The concrete was fairly well consolidated. Several, irregular shaped, entrapped-sized, air voids were observed throughout the sample with some concentration along paste/aggregate boundaries.

II. **Aggregate**

1. Coarse: 38 mm (1-1/2") nominal sized naturally occurring glacial gravel consisting of granite, gabbro, chert, felsite, sandstone, carbonate, and basalt with a few iron oxide particles. The coarse aggregate was mostly sub-rounded to rounded with several sub-angular to angular particles. The coarse aggregate appeared well graded and exhibited good to fair overall distribution. A lesser amount of coarse aggregate particles, > 13 mm (1/2") in size, were observed in the top approximately 25 mm (1") up to 32 mm (1-1/4") of the sample.

2. Fine: Natural quartz, feldspar, and lithic sand (carbonates, chert, granite, gabbro, and basalt with a few iron oxide and shale particles). The grains were mostly sub-rounded to sub-angular with many smaller angular particles. The fine aggregate appeared fairly graded and exhibited good overall uniform distribution. A few shale fine aggregate particles exhibited a dark rim and expansive microcracking which propagated into the surrounding paste.

III. **Cementitious Properties**

1. Air Content: 8.4% total
2. Depth of carbonation: Ranged from negligible to 7 mm (1/4") depth from the top surface along sub-vertical microcracks. Intermittent carbonation proceeded to 15 mm (9/16") depth from the top surface along sub-vertical microcracks.
3. Paste/aggregate bond: Good to fair.
4. Paste color: Medium light gray (Munsell® N6) overall. Medium gray (Munsell® N5) in the bottom approximately 13 mm (1/2") of the sample.
5. Paste hardness: Moderate (Mohs ≈ 3).
6. Microcracking: A few, fine, sub-vertical microcracks proceeded to 9 mm (3/8") depth from the top surface and one microcrack proceeded to 25 mm (1") depth. A few shale fine aggregate particles exhibited expansive microcracking which propagated into the surrounding paste.
7. Secondary deposits: None observed.
8. w/cm: Estimated at between 0.40 and 0.45 with approximately 7 to 9% residual portland cement clinker particles and an amount of fly ash visually consistent with a 25 to 35% replacement of portland cement.
9. Cement hydration: Alites: moderate to fully
   Belites: negligible to low

24-LAB-001 Petrographic Examination of Hardened Concrete
ASTM C856

Project No.	P-0002628	Date:	5-12-2021	Date reviewed:	5-21-2021
Sample ID:	521 424W	Performed by:	S. Malecha	Reviewed by:	G. Moulzolf

I. **General Observations**

1. Sample Dimensions: Our analysis was performed on a 156 mm (6-1/8") x 98 mm (3-7/8") x 48 mm (1-7/8") thick lapped profile section and a 76 mm (3") x 52 mm (2") thin section that were saw-cut and prepared from the original 102 mm (4") diameter x 159 mm (6-1/4") long core.

2. Surface Conditions:
   Top: Fairly rough, broom finished/drag textured surface exhibiting mortar erosion and shallow scaling.
   Bottom: Rough, slightly irregular, formed; placed on grade.

3. Reinforcement: None observed.

4. General Physical Conditions: Remnants of orange marker paint were observed on the top surface of the core sample. The top surface of the core sample was mortar eroded exposing numerous fine aggregate particles and approximately 5% of its surface area was shallowly (< 3 mm depth) scaled. Several remnant flakes of curing compound exhibiting fine craze cracking were observed within the topographic lows of the top surface. A lesser amount of coarse aggregate particles, > 13 mm (1/2") in size, were observed in the top approximately 70 mm (2-3/4") up to 76 mm (3") of the sample. A few, fine, sub-vertical microcracks proceeded to 8 mm (5/16") depth from the top surface. A few shale fine aggregate particles exhibited expansive microcracking which propagated into the surrounding paste. Carbonation ranged from negligible to 2 mm (1/16") depth from the top surface. Intermittent carbonation proceeded to 9 mm (3/8") depth from the top surface along sub-vertical microcracks. The concrete was air entrained and contained a fairly well distributed air void system with 8.2% total air content and 0.002" spacing factor. The concrete was fairly well consolidated. A few, irregular shaped, entrapped-sized, air voids were observed throughout the sample with some concentration along paste/aggregate boundaries.

II. **Aggregate**

1. Coarse: 25 mm (1") nominal sized naturally occurring glacial gravel consisting of granite, gabbro, chert, felsite, sandstone, carbonate, and basalt with a few iron oxide particles. The coarse aggregate was mostly sub-rounded to rounded with several sub-angular to angular particles. The coarse aggregate appeared well graded and exhibited good to fair overall distribution. A lesser amount of coarse aggregate particles, > 13 mm (1/2") in size, were observed in the top approximately 70 mm (2-3/4") up to 76 mm (3") of the sample.

2. Fine: Natural quartz, feldspar, and lithic sand (carbonates, chert, granite, gabbro, and basalt with a few iron oxide and shale particles). The grains were mostly sub-rounded to sub-angular with many smaller angular particles. The fine aggregate appeared fairly graded and exhibited good overall uniform distribution. A few shale fine aggregate particles exhibited a dark rim and expansive microcracking which propagated into the surrounding paste.

III. **Cementitious Properties**

1. Air Content: 8.2% total
2. Depth of carbonation: Ranged from negligible to 2 mm (1/16") depth from the top surface. Intermittent carbonation proceeded to 9 mm (3/8") depth from the top surface along sub-vertical microcracks.
3. Paste/aggregate bond: Fair.
4. Paste color: Medium light gray (Munsell® N6) overall. Medium gray (Munsell® N5) in the bottom approximately 106 mm (3/8") of the sample.
5. Paste hardness: Moderate (Mohs ≈ 3).
6. Microcracking: A few, fine, sub-vertical microcracks proceeded to 8 mm (5/16") depth from the top surface. A few shale fine aggregate particles exhibited expansive microcracking which propagated into the surrounding paste.
7. Secondary deposits: None observed.
8. w/cm: Estimated at between 0.40 and 0.45 with approximately 7 to 9% residual portland cement clinker particles and an amount of fly ash visually consistent with a 25 to 35% replacement of portland cement.
9. Cement hydration: Alites: moderate to fully
   Belites: negligible to low

24-LAB-001 Petrographic Examination of Hardened Concrete
ASTM C856

| Project No. | P-0002628 | Date: | 5-12-2021 | Date reviewed: | 5-21-2021 |
| Sample ID: | 521 524B | Performed by: | S. Malecha | Reviewed by: | G. Moulzolf |

I. General Observations

1. Sample Dimensions: Our analysis was performed on a 171 mm (6-3/4") x 98 mm (3-7/8") x 46 mm (1-13/16") thick lapped profile section and a 76 mm (3") x 52 mm (2") thin section that were saw-cut and prepared from the original 102 mm (4") diameter x 171 mm (6-3/4") long core.

2. Surface Conditions:
   Top: Fairly rough, broom finished/drag textured surface exhibiting mortar erosion and shallow scaling.
   Bottom: Rough, slightly irregular, formed; placed on grade.

3. Reinforcement: None observed.

4. General Physical Conditions: Remnants of orange marker paint were observed on the top surface of the core sample. The top surface of the core sample was mortar eroded exposing numerous fine aggregate particles and approximately 10% of its surface area was shallowly (< 3 mm depth) scaled exposing a few coarse aggregate particles. A few remnant flakes of curing compound exhibiting fine craze cracking were observed within the topographic lows of the top surface. A lesser amount of coarse aggregate particles, > 13 mm (1/2") in size, were observed in the top approximately 19 mm (3/4") up to 76 mm (3") of the sample. A few, fine, sub-vertical microcracks proceeded to 11 mm (7/16") depth from the top surface. A few shale fine aggregate particles exhibited expansive microcracking which propagated into the surrounding paste. Carbonation ranged from negligible to 7 mm (1/4") depth from the top surface along sub-vertical microcracks. The concrete was air entrained and contained a fairly well distributed air void system with 7.9% total air content and 0.002" spacing factor. The concrete was fairly well consolidated. Several, irregular shaped, entrapped-sized, air voids were observed throughout the sample.

II. Aggregate

1. Coarse: 25 mm (1") nominal sized naturally occurring glacial gravel consisting of granite, gabbro, chert, felsite, sandstone, carbonate, and basalt with a few iron oxide particles. The coarse aggregate was mostly sub-rounded to rounded with several sub-angular to angular particles. The coarse aggregate appeared well graded and exhibited good to fair overall distribution. A lesser amount of coarse aggregate particles, > 13 mm (1/2") in size, were observed in the top approximately 19 mm (3/4") up to 76 mm (3") of the sample.

2. Fine: Natural quartz, feldspar, and lithic sand (carbonates, chert, sandstone, granite, gabbro, and basalt with a few iron oxide and shale particles). The grains were mostly sub-rounded to sub-angular with many smaller angular particles. The fine aggregate appeared fairly graded and exhibited good overall uniform distribution. A few shale fine aggregate particles exhibited a dark rim and expansive microcracking which propagated into the surrounding paste.

III. Cementitious Properties

1. Air Content: 7.9% total
2. Depth of carbonation: Ranged from negligible to 7 mm (1/4") depth from the top surface along sub-vertical microcracks.
3. Paste/aggregate bond: Fair to poor.
4. Paste color: Medium light gray (Munsell® N6) overall. Medium gray (Munsell® N5) in the bottom approximately 13 mm (1/2") of the sample.
5. Paste hardness: Moderate (Mohs ≈ 3).
6. Microcracking: A few, fine, sub-vertical microcracks proceeded to 11 mm (7/16") depth from the top surface. A few shale fine aggregate particles exhibited expansive microcracking which propagated into the surrounding paste.
7. Secondary deposits: Ettringite was observed lining to filling air voids in thin section of the concrete sample.
8. w/cm: Estimated at between 0.40 and 0.45 with approximately 7 to 9% residual portland cement clinker particles and an amount of fly ash visually consistent with a 25 to 35% replacement of portland cement.
9. Cement hydration: Alites: moderate to fully
                           Belites: negligible to low

24-LAB-001 Petrographic Examination of Hardened Concrete
ASTM C856

| Project No. | P-0002628 | Date: | 5-12-2021 | Date reviewed: | 5-21-2021 |
| Sample ID: | 521 524W | Performed by: | S. Malecha | Reviewed by: | G. Moulzolf |

I. **General Observations**

1. Sample Dimensions: Our analysis was performed on a 165 mm (6-1/2") x 98 mm (3-7/8") x 44 mm (1-3/4") thick lapped profile section and a 76 mm (3") x 52 mm (2") thin section that were saw-cut and prepared from the original 102 mm (4") diameter x 165 mm (6-1/2") long core.

2. Surface Conditions:
   Top: Fairly rough, broom finished/drag textured surface exhibiting mortar erosion and shallow scaling.
   Bottom: Rough, slightly irregular, formed; placed on grade.

3. Reinforcement: None observed.

4. General Physical Conditions: Remnants of orange marker paint were observed on the top surface of the core sample. The top surface of the core sample was mortar eroded exposing numerous fine aggregate particles and approximately 10% of its surface area was shallowly scaled to 3 mm (1/8") depth. Residual curing compound exhibiting fine craze cracking was observed within the topographic lows of the top surface. A few topographic highs were worn relatively smooth. Minor corrosion product was observed on a few topographic highs on the top surface. A slightly lesser amount of coarse aggregate particles, > 13 mm (1/2") in size, were observed in the top approximately 38 mm (1-1/2") up to 76 mm (3") of the sample. A few, fine, sub-vertical microcracks proceeded to 5 mm (3/16") depth from the top surface. A few shale fine aggregate particles exhibited expansive microcracking which propagated into the surrounding paste. Carbonation ranged from negligible to 9 mm (3/8") depth from the top surface along sub-vertical microcracks. The concrete was air entrained and contained a fairly distributed air void system with 7.6% total air content and 0.002" spacing factor. The concrete was fairly well consolidated. Several, irregular shaped, entrapped-sized, air voids were observed throughout the sample with some concentration along paste/aggregate boundaries.

II. **Aggregate**

1. Coarse: 25 mm (1") nominal sized naturally occurring glacial gravel consisting of granite, gabbro, chert, felsite, sandstone, carbonate, and basalt with a few iron oxides and a shale particle. The coarse aggregate was mostly sub-rounded to rounded with several sub-angular to angular particles. The coarse aggregate appeared well graded and exhibited good to fair overall distribution. A slightly lesser amount of coarse aggregate particles, > 13 mm (1/2") in size, were observed in the top approximately 38 mm (1-1/2") up to 76 mm (3") of the sample.

2. Fine: Natural quartz, feldspar, and lithic sand (carbonates, chert, sandstone, granite, gabbro, and basalt with a few iron oxide and shale particles). The grains were mostly sub-rounded to sub-angular with many smaller angular particles. The fine aggregate appeared fairly graded and exhibited good overall uniform distribution. A few shale fine aggregate particles exhibited a dark rim and expansive microcracking which propagated into the surrounding paste.

III. **Cementitious Properties**

1. Air Content: 7.6% total
2. Depth of carbonation: Ranged from negligible to 9 mm (3/8") depth from the top surface along sub-vertical microcracks.
3. Paste/aggregate bond: Fair to poor.
4. Paste color: Medium light gray (Munsell® N6) overall. Medium gray (Munsell® N5) in the bottom approximately 19 mm (3/4") of the sample.
5. Paste hardness: Moderate (Mohs ≈ 3).
6. Microcracking: A few, fine, sub-vertical microcracks proceeded to 5 mm (3/16") depth from the top surface. A few shale fine aggregate particles exhibited expansive microcracking which propagated into the surrounding paste.
7. Secondary deposits: None observed.
8. w/cm: Estimated at between 0.40 and 0.45 with approximately 7 to 9% residual portland cement clinker particles and an amount of fly ash visually consistent with a 25 to 35% replacement of portland cement.
9. Cement hydration: Alites: moderate to fully
   Belites: negligible to low

![American Engineering Testing, Inc. logo]

AIR VOID ANALYSIS

PROJECT:

PERFORMANCE OF EARLY LOADED
CONCRETE SECTIONS AFTER 4 YEARS
STATE PROJECT NO. (SP): 8821-331
TRUNK HIGHWAY NUMBER (TH): 999

AET PROJECT NO: P-0002628

REPORTED TO:

MN DEPT OF TRANSPORTATION
1123 MESABA AVENUE
DULUTH, MN 55811

ATTN: AMY THORSON
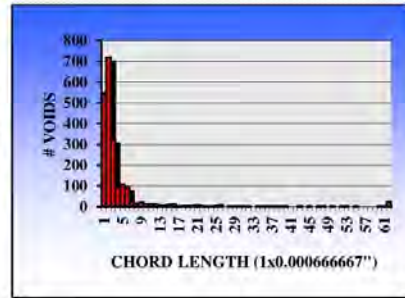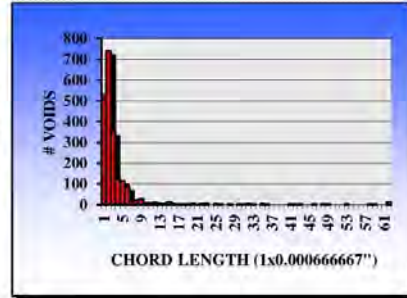
DATE: MAY 21, 2021

Sample ID: 521 124B

Conformance: The concrete contains an air void system which is consistent with current American Concrete Institute (ACI) recommendations for freeze-thaw resistance.

Sample Data

Description:	Hardened Concrete Core
Dimensions:	102 mm (4") diameter by 165 mm (6-1/2") long

Test Data: By ASTM C457, Procedure A

Air Void Content %	7.5
Entrained, % < 0.040" (1mm)	5.5
Entrapped, %> 0.040" (1mm)	2.0
Air Voids/inch	21.3
Specific Surface, in²/in³	1140
Spacing Factor, inches	0.002
Paste Content, % estimated	18
Magnification	75x
Traverse Length, inches	100
Test Date	5/12/2021
Test Performed By:	S. Malecha

Magnification: 30x
Description: Hardened air void system

AMERICAN ENGINEERING TESTING, INC.

AIR VOID ANALYSIS

PROJECT:

PERFORMANCE OF EARLY LOADED
CONCRETE SECTIONS AFTER 4 YEARS
STATE PROJECT NO. (SP): 8821-331
TRUNK HIGHWAY NUMBER (TH): 999

AET PROJECT NO: P-0002628

REPORTED TO:

MN DEPT OF TRANSPORTATION
1123 MESABA AVENUE
DULUTH, MN 55811

ATTN: AMY THORSON

DATE: MAY 21, 2021
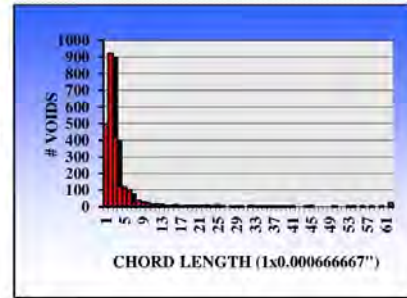

Sample ID: 521 124W

Conformance: The concrete contains an air void system which is consistent with current American Concrete Institute (ACI) recommendations for freeze-thaw resistance.

Sample Data

Description:	Hardened Concrete Core
Dimensions:	102 mm (4") diameter by 165 mm (6-1/2") long

CHORD LENGTH (1x0.000666667")

Test Data: By ASTM C457, Procedure A

Air Void Content %	6.3
Entrained, % < 0.040" (1mm)	5.1
Entrapped, % > 0.040" (1mm)	1.2
Air Voids/inch	21.4
Specific Surface, in²/in³	1360
Spacing Factor, inches	0.002
Paste Content, % estimated	17
Magnification	75x
Traverse Length, inches	100
Test Date	5/12/2021
Test Performed By:	S. Malecha

Magnification: 30x
Description: Hardened air void system

AIR VOID ANALYSIS

| **PROJECT:**	**REPORTED TO:**
PERFORMANCE OF EARLY LOADED	MN DEPT OF TRANSPORTATION
CONCRETE SECTIONS AFTER 4 YEARS	1123 MESABA AVENUE
STATE PROJECT NO. (SP): 8821-331	DULUTH, MN 55811
TRUNK HIGHWAY NUMBER (TH): 999	

ATTN: AMY THORSON

AET PROJECT NO: P-0002628   **DATE:**   MAY 21, 2021
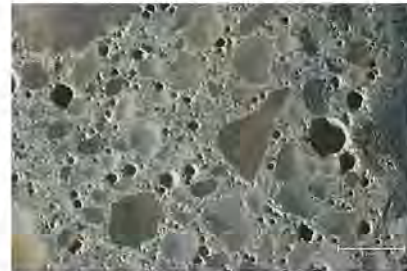
Sample ID: 521 424B

Conformance: The concrete contains an air void system which is consistent with current American Concrete Institute (ACI) recommendations for freeze-thaw resistance.
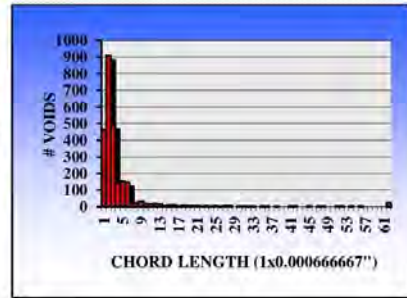
Sample Data

Description:	Hardened Concrete Core
Dimensions:	102 mm (4") diameter by 165 mm (6-1/2") long

Test Data: By ASTM C457, Procedure A

Air Void Content %	8.4
Entrained, % < 0.040" (1mm)	6.6
Entrapped, %> 0.040" (1mm)	1.8
Air Voids/inch	25.8
Specific Surface, in²/in³	1230
Spacing Factor, inches	0.002
Paste Content, % estimated	16
Magnification	75x
Traverse Length, inches	100
Test Date	5/14/2021
Test Performed By:	S. Malecha

Magnification: 30x
Description: Hardened air void system

AMERICAN ENGINEERING TESTING, INC.

AIR VOID ANALYSIS

PROJECT:

PERFORMANCE OF EARLY LOADED
CONCRETE SECTIONS AFTER 4 YEARS
STATE PROJECT NO. (SP): 8821-331
TRUNK HIGHWAY NUMBER (TH): 999

AET PROJECT NO: P-0002628

**REPORTED TO:**

MN DEPT OF TRANSPORTATION
1123 MESABA AVENUE
DULUTH, MN 55811

ATTN: AMY THORSON

DATE: MAY 21, 2021

Sample ID: 521 424W

Conformance: The concrete contains an air void
system which is consistent with
current American Concrete Institute
(ACI) recommendations for freeze-
thaw resistance.
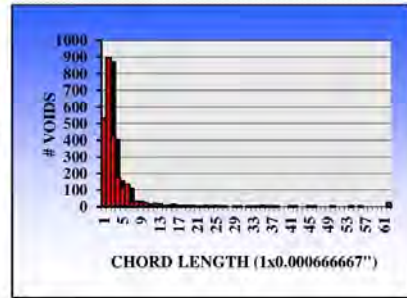
Sample Data
Description:	Hardened Concrete Core
Dimensions:	102 mm (4") diameter by
	159 mm (6-1/4") long

CHORD LENGTH (1x0.000666667")

Test Data: By ASTM C457, Procedure A

Air Void Content %	8.2
Entrained, % < 0.040" (1mm)	6.4
Entrapped, %> 0.040" (1mm)	1.8
Air Voids/inch	25.6
Specific Surface, in²/in³	1250
Spacing Factor, inches	0.002
Paste Content, % estimated	18
Magnification	75x
Traverse Length, inches	100
Test Date	5/14/2021
Test Performed By:	S. Malecha

Magnification: 30x
Description: Hardened air void system

AMERICAN ENGINEERING TESTING, INC.

AIR VOID ANALYSIS

PROJECT:

PERFORMANCE OF EARLY LOADED
CONCRETE SECTIONS AFTER 4 YEARS
STATE PROJECT NO. (SP): 8821-331
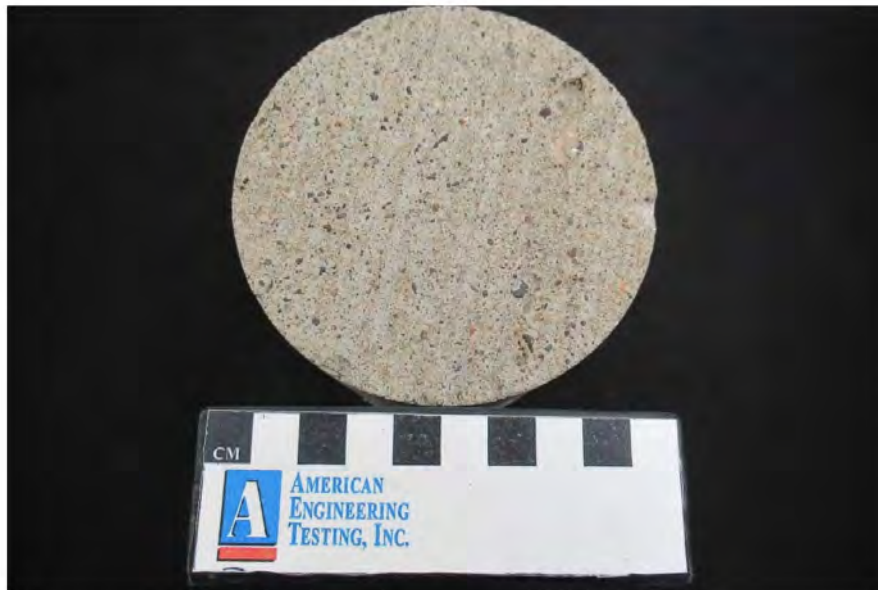TRUNK HIGHWAY NUMBER (TH): 999

AET PROJECT NO: P-0002628

REPORTED TO:

MN DEPT OF TRANSPORTATION
1123 MESABA AVENUE
DULUTH, MN 55811

ATTN: AMY THORSON

DATE: MAY 21, 2021

Sample ID: 521 524B

Conformance: The concrete contains an air void system which is consistent with current American Concrete Institute (ACI) recommendations for freeze-thaw resistance.

CHORD LENGTH (1x0.000666667")

Sample Data

Description:	Hardened Concrete Core
Dimensions:	102 mm (4") diameter by 171 mm (6-3/4") long

Test Data: By ASTM C457, Procedure A

Air Void Content %	7.9
Entrained, % < 0.040" (1mm)	6.5
Entrapped, %> 0.040" (1mm)	1.4
Air Voids/inch	24.6
Specific Surface, in²/in³	1250
Spacing Factor, inches	0.002
Paste Content, % estimated	17
Magnification	75x
Traverse Length, inches	100
Test Date	5/17/2021
Test Performed By:	S. Malecha

Magnification: 30x
Description: Hardened air void system

AIR VOID ANALYSIS

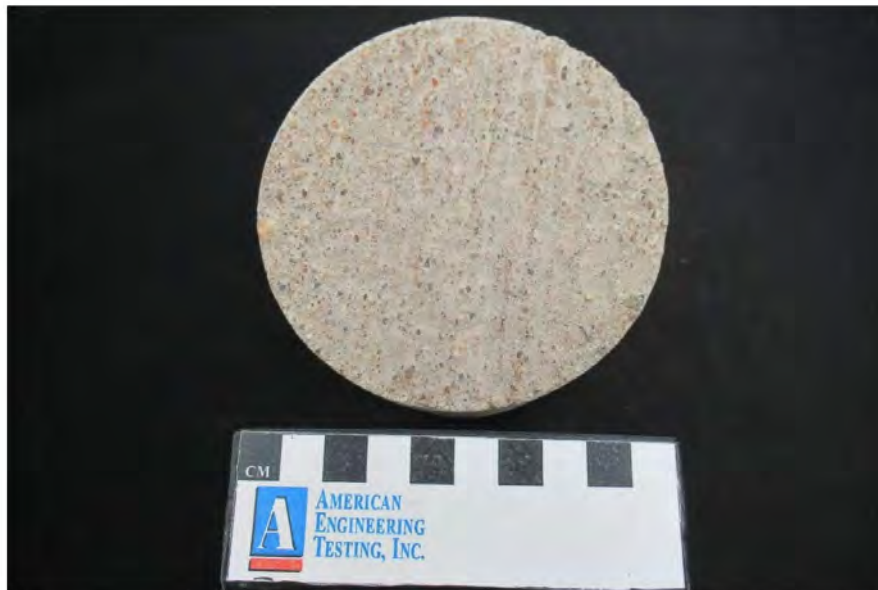| PROJECT:	REPORTED TO:
PERFORMANCE OF EARLY LOADED CONCRETE SECTIONS AFTER 4 YEARS STATE PROJECT NO. (SP): 8821-331 TRUNK HIGHWAY NUMBER (TH): 999	MN DEPT OF TRANSPORTATION 1123 MESABA AVENUE DULUTH, MN 55811

ATTN: AMY THORSON

AET PROJECT NO: P-0002628

DATE: MAY 21, 2021

Sample ID: 521 524W

Conformance: The concrete contains an air void system which is consistent with current American Concrete Institute (ACI) recommendations for freeze-thaw resistance.
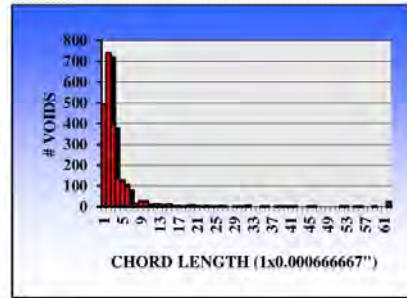
Sample Data

Description:	Hardened Concrete Core
Dimensions:	102 mm (4") diameter by 165 mm (6-1/2") long

Test Data: By ASTM C457, Procedure A

Air Void Content %	7.6
Entrained, % < 0.040" (1mm)	6.0
Entrapped, %> 0.040" (1mm)	1.6
Air Voids/inch	22.5
Specific Surface, in^2/in^3	1180
Spacing Factor, inches	0.002
Paste Content, % estimated	18
Magnification	75x
Traverse Length, inches	100
Test Date	5/18/2021
Test Performed By:	S. Malecha

Magnification: 30x
Description: Hardened air void system

AET PROJECT NO: P-0002628   DATE: MAY 21, 2021

PROJECT: PERFORMANCE OF EARLY LOADED CONCRETE SECTIONS AFTER 4 YEARS
STATE PROJECT NO. (SP): 8821-331, TRUNK HIGHWAY NUMBER (TH): 999
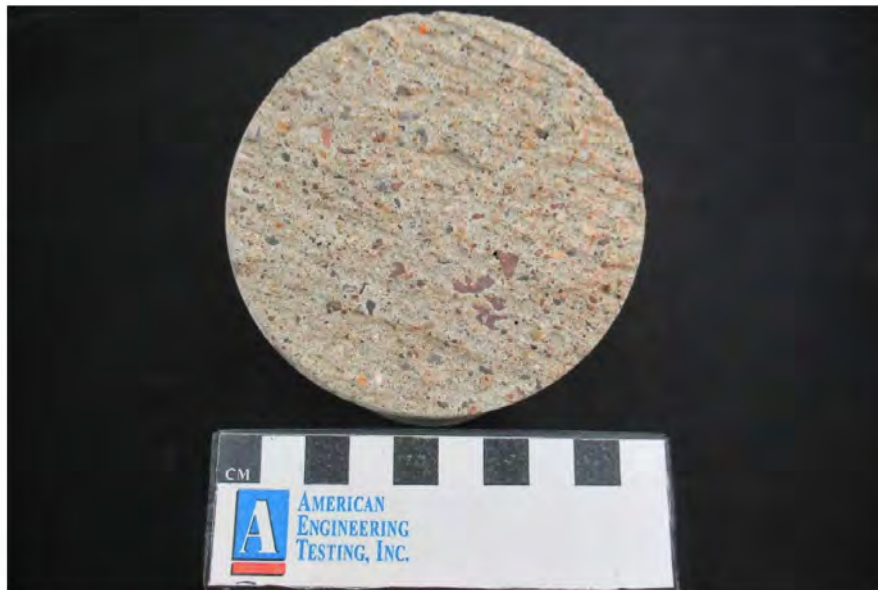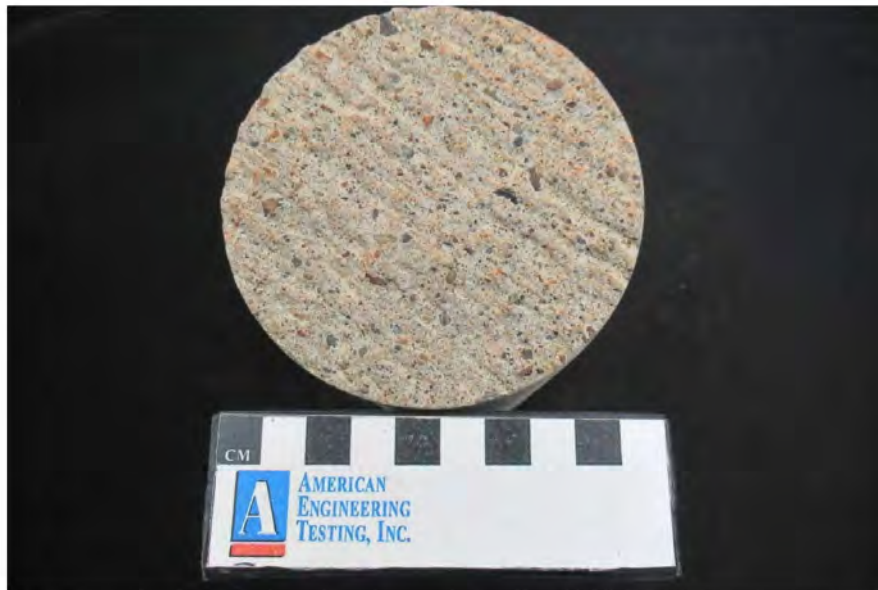
PHOTO: 1

SAMPLE ID: 521 124B   **DESCRIPTION:**   Profile of the concrete core sample as received with the top surface to the left.
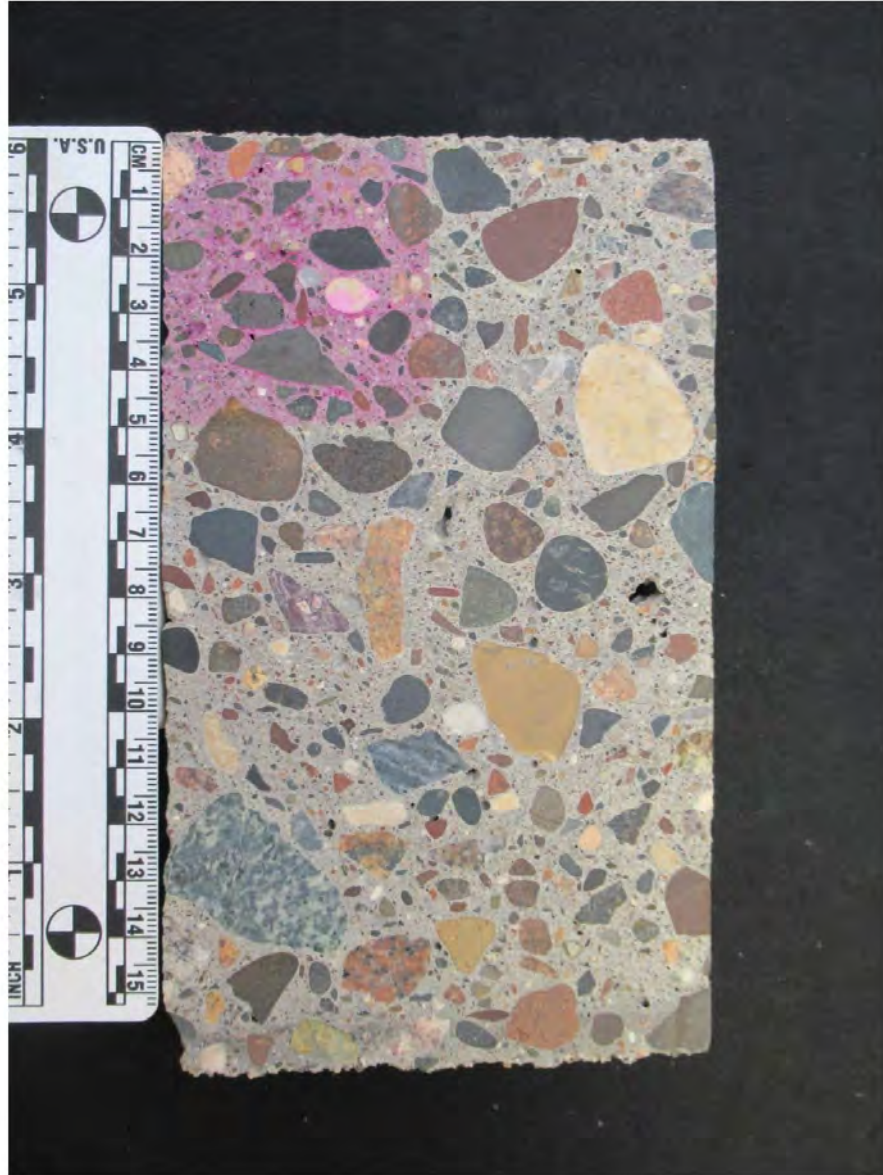
PHOTO: 2
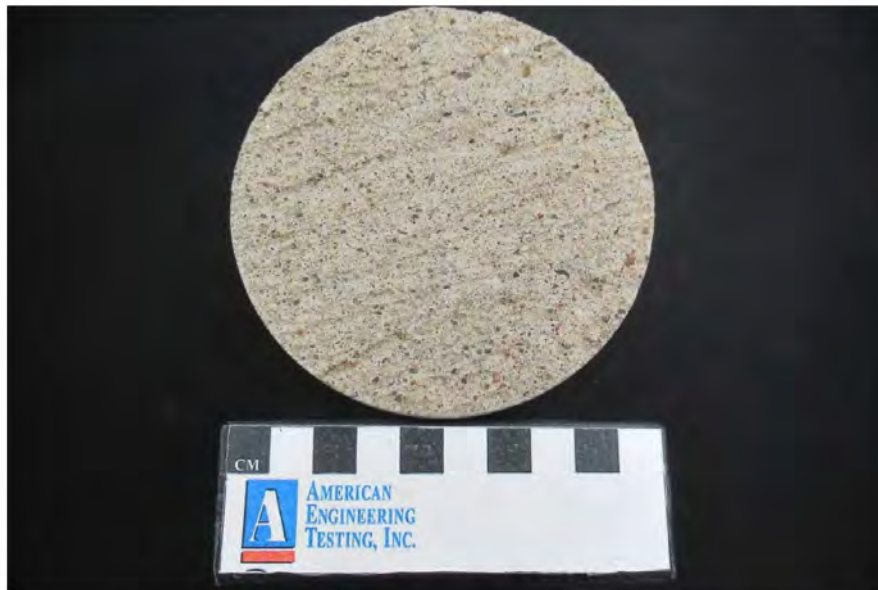
SAMPLE ID: 521 124B   **DESCRIPTION:**   Top surface of the core sample as received.

PHOTO: 3

SAMPLE ID: 521 124W   **DESCRIPTION:**   Profile of the concrete core sample as received with the top surface to the left.

PHOTO: 4

SAMPLE ID: 521 124W   **DESCRIPTION:**   Top surface of the core sample as received.

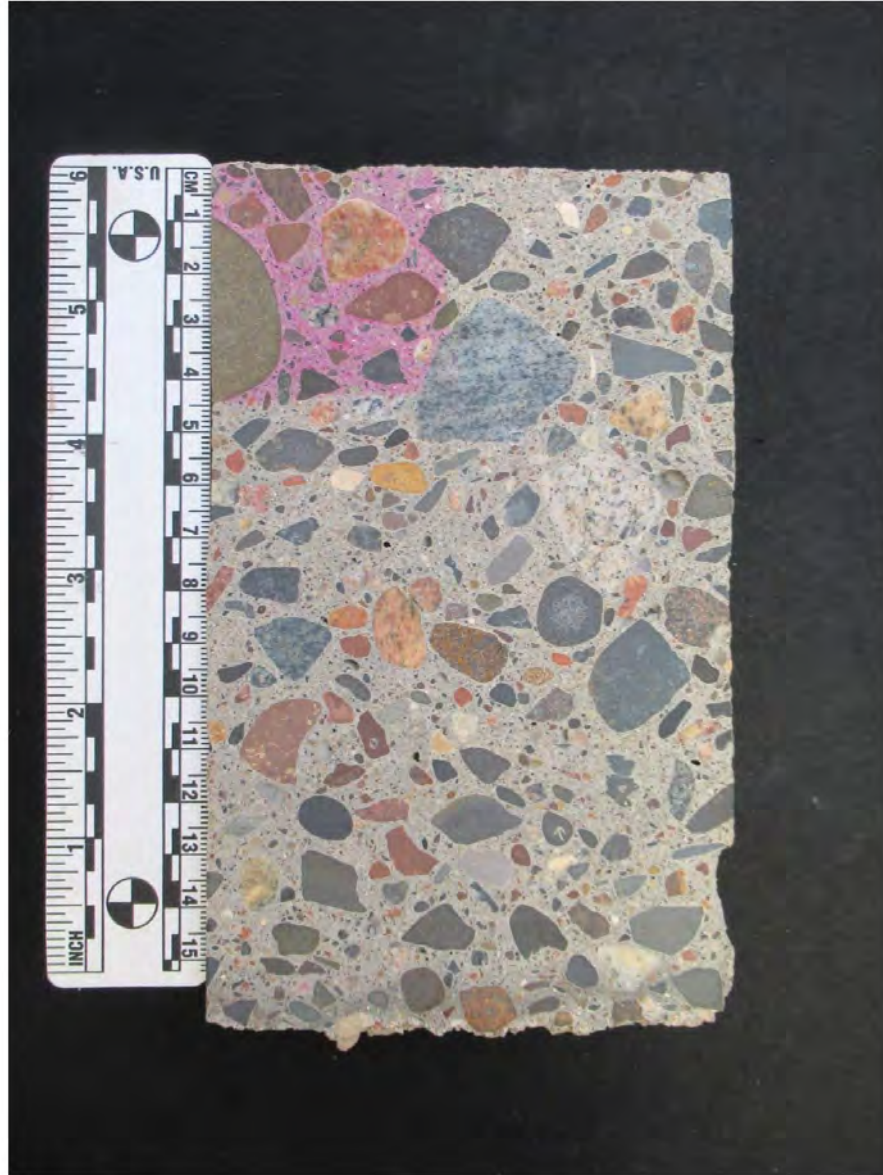AET PROJECT NO: P-0002628   **DATE:** MAY 21, 2021

PROJECT: PERFORMANCE OF EARLY LOADED CONCRETE SECTIONS AFTER 4 YEARS
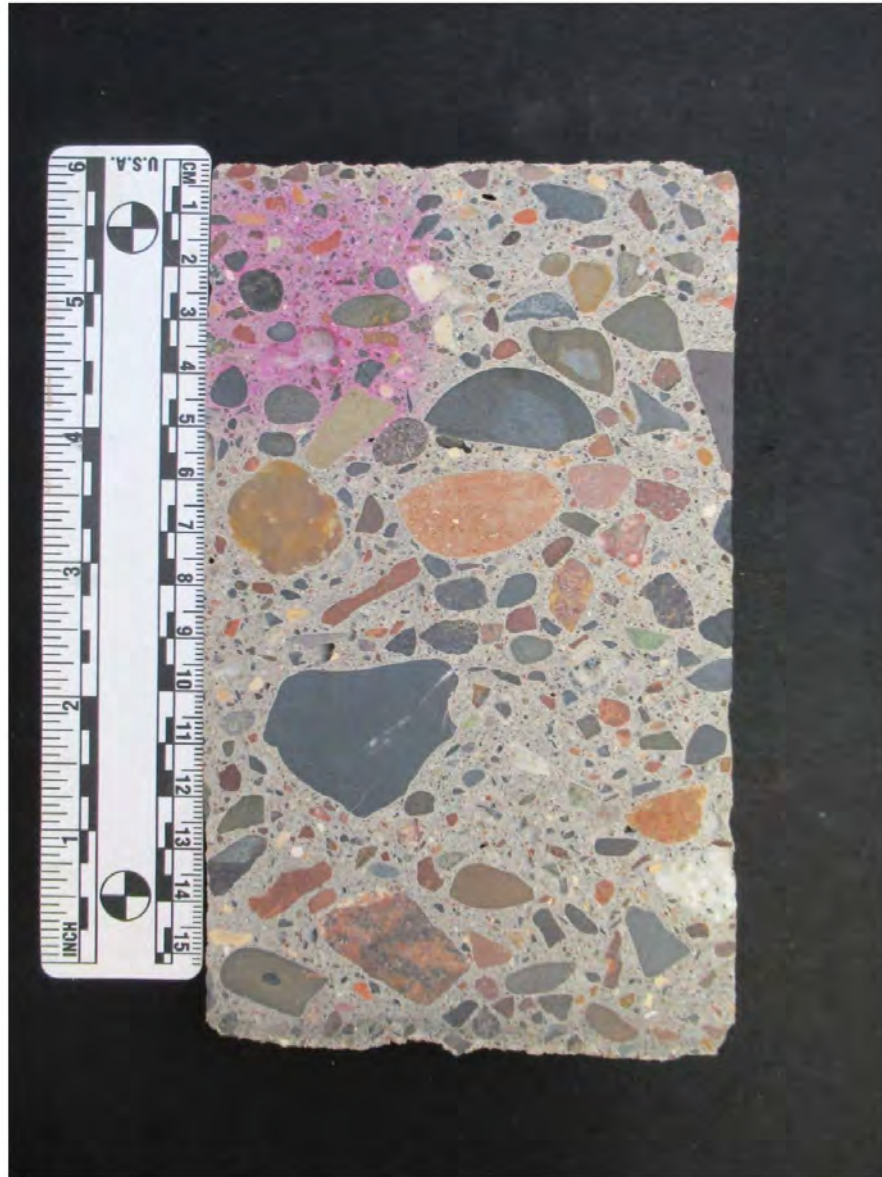STATE PROJECT NO. (SP): 8821-331, TRUNK HIGHWAY NUMBER (TH): 999

PHOTO: 5

SAMPLE ID: 521 424B   **DESCRIPTION:**   Profile of the concrete core sample as received with the top surface to the left.

PHOTO: 6

SAMPLE ID: 521 424B   **DESCRIPTION:**   Top surface of the core sample as received.

AET PROJECT NO: P-0002628   **DATE:**   MAY 21, 2021
PROJECT: PERFORMANCE OF EARLY LOADED CONCRETE SECTIONS AFTER 4 YEARS
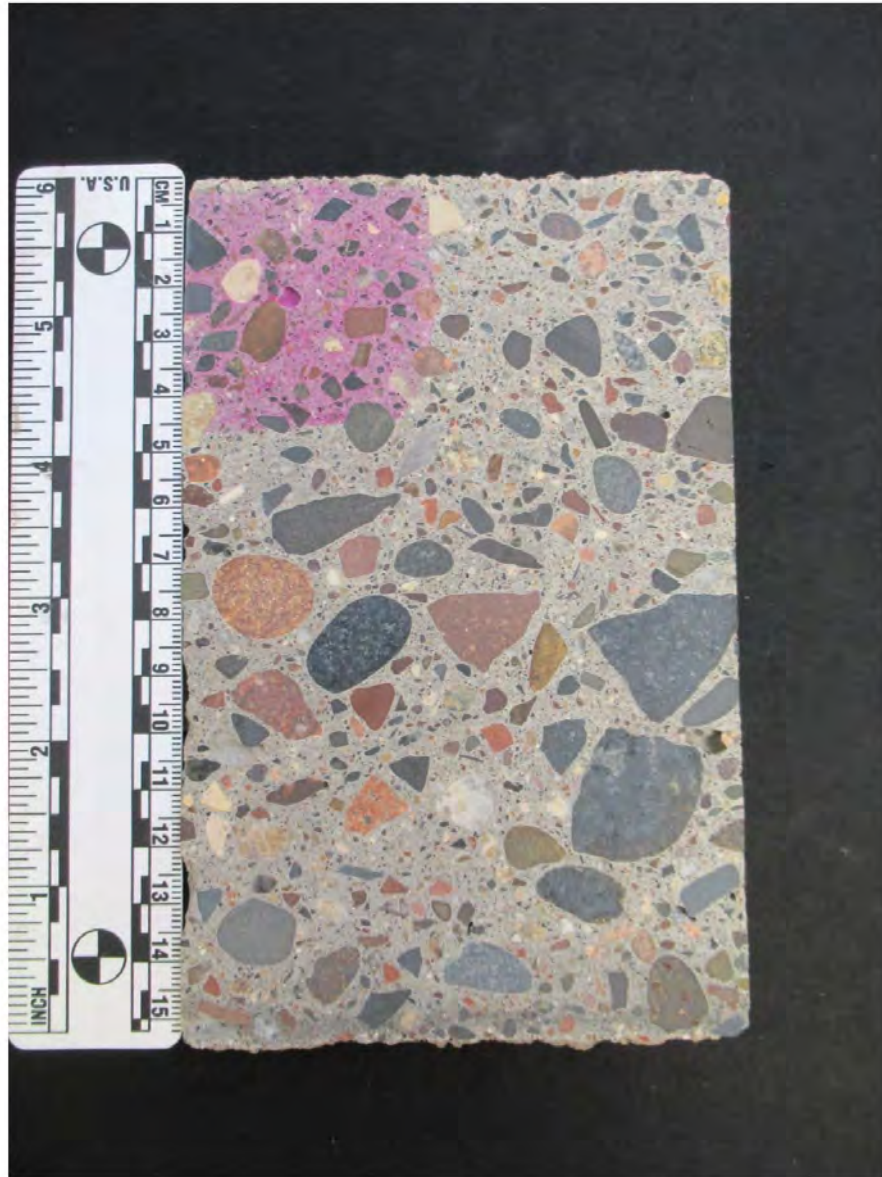STATE PROJECT NO. (SP): 8821-331, TRUNK HIGHWAY NUMBER (TH): 999

PHOTO: 7

SAMPLE ID: 521 424W   **DESCRIPTION:**   Profile of the concrete core sample as received with the top surface to the left.

PHOTO: 8

SAMPLE ID: 521 424W   **DESCRIPTION:**   Top surface of the core sample as received.

AET PROJECT NO: P-0002628   **DATE:** MAY 21, 2021

PROJECT: PERFORMANCE OF EARLY LOADED CONCRETE SECTIONS AFTER 4 YEARS
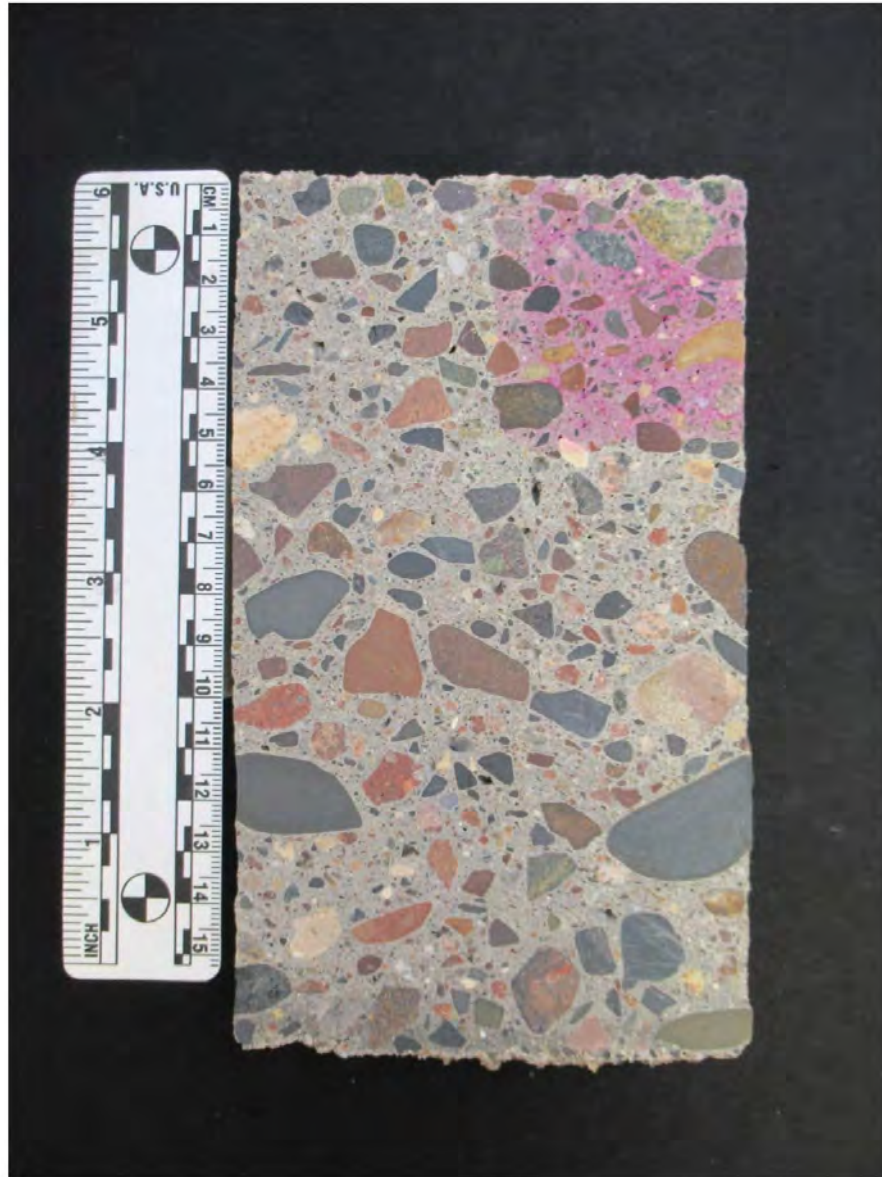STATE PROJECT NO. (SP): 8821-331, TRUNK HIGHWAY NUMBER (TH): 999

PHOTO: 9

SAMPLE ID: 521 524B   **DESCRIPTION:**   Profile of the concrete core sample as received with the top surface to the left.

PHOTO: 10

SAMPLE ID: 521 524B   **DESCRIPTION:**   Top surface of the core sample as received.

AET PROJECT NO: P-0002628   DATE: MAY 21, 2021

PROJECT: PERFORMANCE OF EARLY LOADED CONCRETE SECTIONS AFTER 4 YEARS
                    STATE PROJECT NO. (SP): 8821-331, TRUNK HIGHWAY NUMBER (TH): 999

PHOTO: 11

SAMPLE ID: 521 524W   DESCRIPTION: Profile of the concrete core sample as received with the top surface to the left.

PHOTO: 12

SAMPLE ID: 521 524W   DESCRIPTION: Top surface of the core sample as received.

AET PROJECT NO: P-0002628   **DATE:** MAY 21, 2021

PROJECT: PERFORMANCE OF EARLY LOADED CONCRETE SECTIONS AFTER 4 YEARS
                      STATE PROJECT NO. (SP): 8821-331, TRUNK HIGHWAY NUMBER (TH): 999
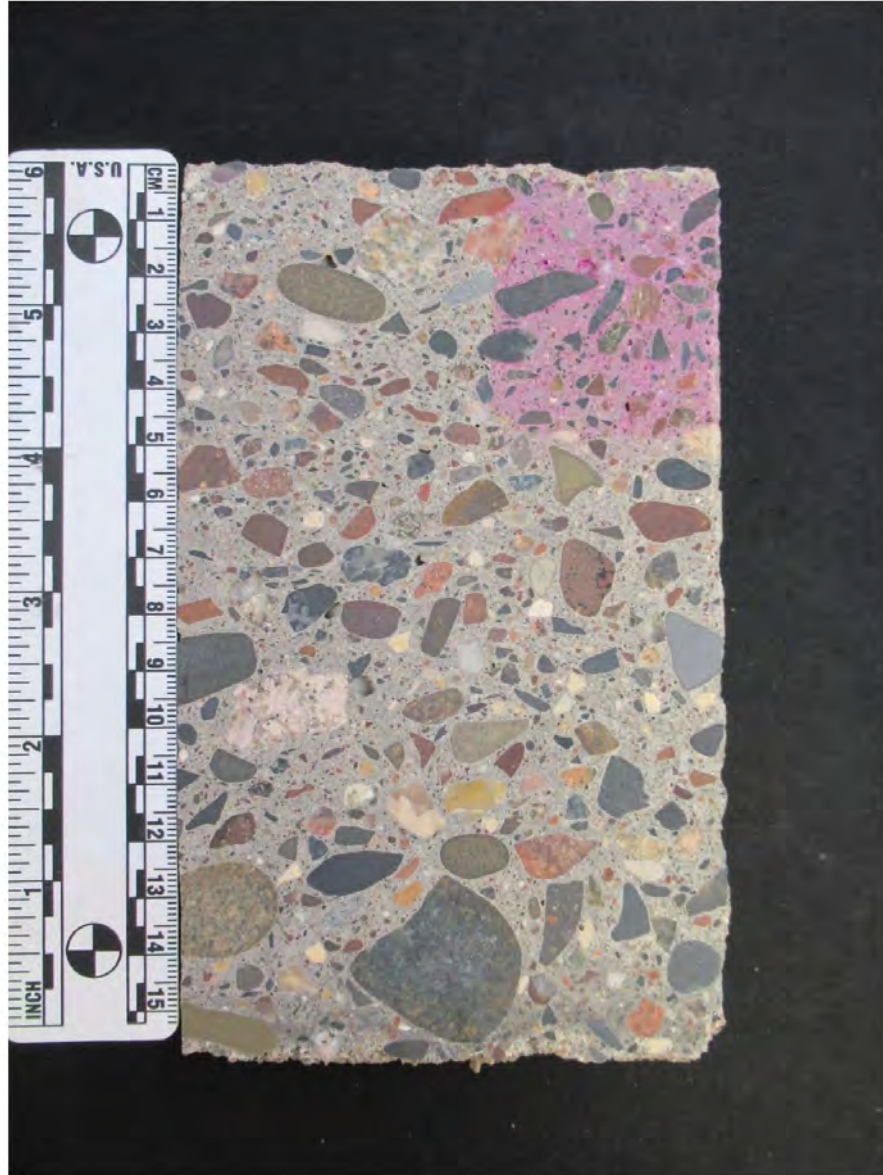
PHOTO: 13

SAMPLE ID: 521 124B   **DESCRIPTION:**   A saw-cut and lapped cross section of the concrete core sample with the top surface oriented to the top of the photo. The upper left corner was treated with phenolphthalein pH indicator (pink stain).

AET PROJECT NO: P-0002628   **DATE:** MAY 21, 2021

PROJECT: PERFORMANCE OF EARLY LOADED CONCRETE SECTIONS AFTER 4 YEARS
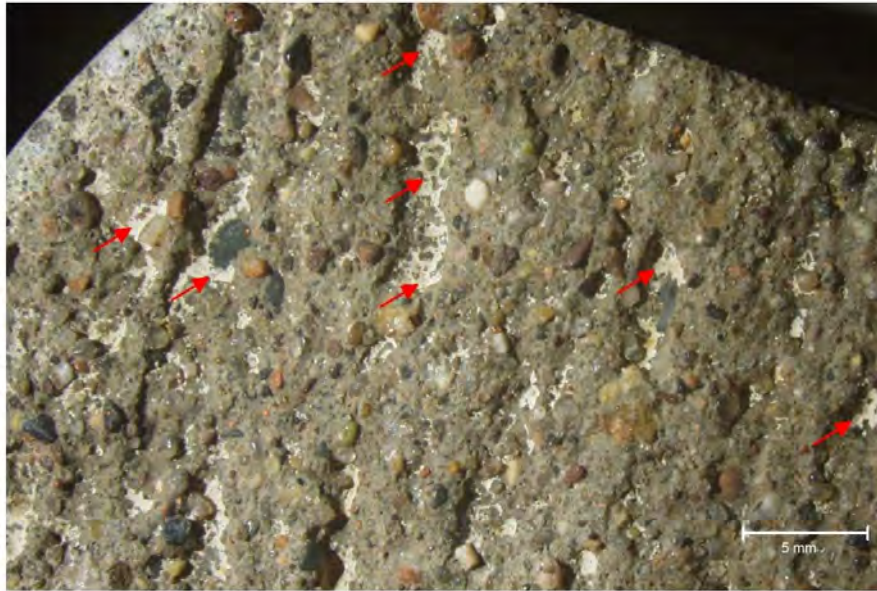STATE PROJECT NO. (SP): 8821-331, TRUNK HIGHWAY NUMBER (TH): 999

PHOTO: 14

SAMPLE ID: 521 124W   **DESCRIPTION:**   A saw-cut and lapped cross section of the concrete core sample with the top surface oriented to the top of the photo. The upper left corner was treated with phenolphthalein pH indicator (pink stain).

AET PROJECT NO: P-0002628   **DATE:** MAY 21, 2021

PROJECT: PERFORMANCE OF EARLY LOADED CONCRETE SECTIONS AFTER 4 YEARS
                                  STATE PROJECT NO. (SP): 8821-331, TRUNK HIGHWAY NUMBER (TH): 999

PHOTO: 15

SAMPLE ID: 521 424B   **DESCRIPTION:**   A saw-cut and lapped cross section of the concrete core sample with the top surface oriented to the top of the photo. The upper left corner was treated with phenolphthalein pH indicator (pink stain).

PROJECT: PERFORMANCE OF EARLY LOADED CONCRETE SECTIONS AFTER 4 YEARS
STATE PROJECT NO. (SP): 8821-331, TRUNK HIGHWAY NUMBER (TH): 999

PHOTO: 16

SAMPLE ID: 521 424W   **DESCRIPTION:**   A saw-cut and lapped cross section of the concrete core sample with the top surface oriented to the top of the photo. The upper left corner was treated with phenolphthalein pH indicator (pink stain).

PROJECT: PERFORMANCE OF EARLY LOADED CONCRETE SECTIONS AFTER 4 YEARS
                  STATE PROJECT NO. (SP): 8821-331, TRUNK HIGHWAY NUMBER (TH): 999

PHOTO: 17

SAMPLE ID: 521 524B   DESCRIPTION: A saw-cut and lapped cross section of the concrete core sample with the top surface oriented to the top of the photo. The upper right corner was treated with phenolphthalein pH indicator (pink stain).

PROJECT: PERFORMANCE OF EARLY LOADED CONCRETE SECTIONS AFTER 4 YEARS
                                  STATE PROJECT NO. (SP): 8821-331, TRUNK HIGHWAY NUMBER (TH): 999

PHOTO: 18

SAMPLE ID: 521 524W   **DESCRIPTION:**   A saw-cut and lapped cross section of the concrete core sample with the top surface oriented to the top of the photo. The upper right corner was treated with phenolphthalein pH indicator (pink stain).

AET PROJECT NO: P-0002628 **DATE:** MAY 21, 2021

**PROJECT:** PERFORMANCE OF EARLY LOADED CONCRETE SECTIONS AFTER 4 YEARS
STATE PROJECT NO. (SP): 8821-331, TRUNK HIGHWAY NUMBER (TH): 999

PHOTO: 19

| **SAMPLE ID:** | 521 124B | **DESCRIPTION:** A magnified view of the top surface. Note the remnant flakes of curing compound (red |
| **MAG:** | 5x | arrows) within the topographic lows of the top surface. |

PHOTO: 20

| **SAMPLE ID:** | 521 124W | **DESCRIPTION:** A magnified view of the top surface. Note the exposed coarse and fine aggregate |
| **MAG:** | 5x | particles. |

AET PROJECT NO: P-0002628   **DATE:**   MAY 21, 2021

PROJECT: PERFORMANCE OF EARLY LOADED CONCRETE SECTIONS AFTER 4 YEARS
                                STATE PROJECT NO. (SP): 8821-331, TRUNK HIGHWAY NUMBER (TH): 999
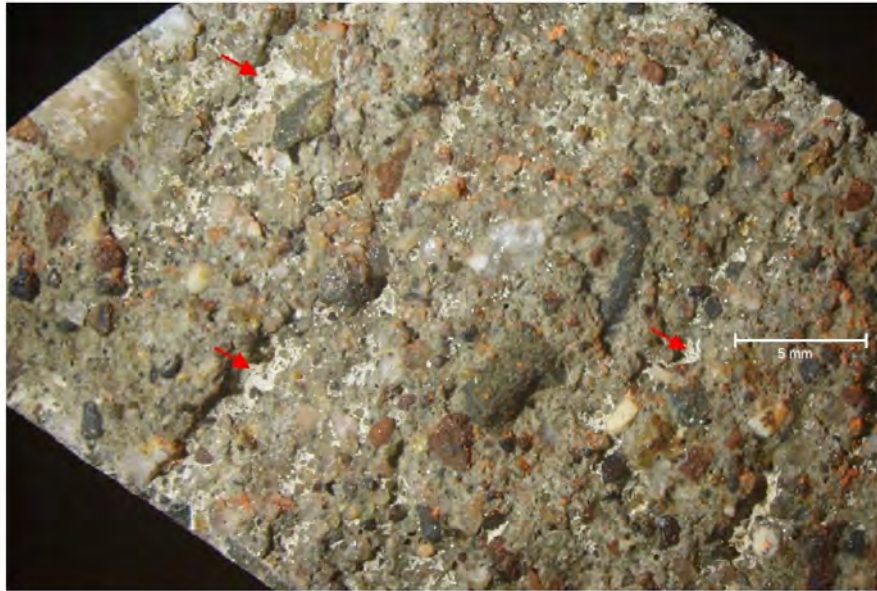
PHOTO: 21

SAMPLE ID: 521 424B   **DESCRIPTION:**   A magnified view of the top surface. Note the remnant flakes of curing compound (red
MAG: 5x   arrows) within the topographic lows of the top surface.

PHOTO: 22
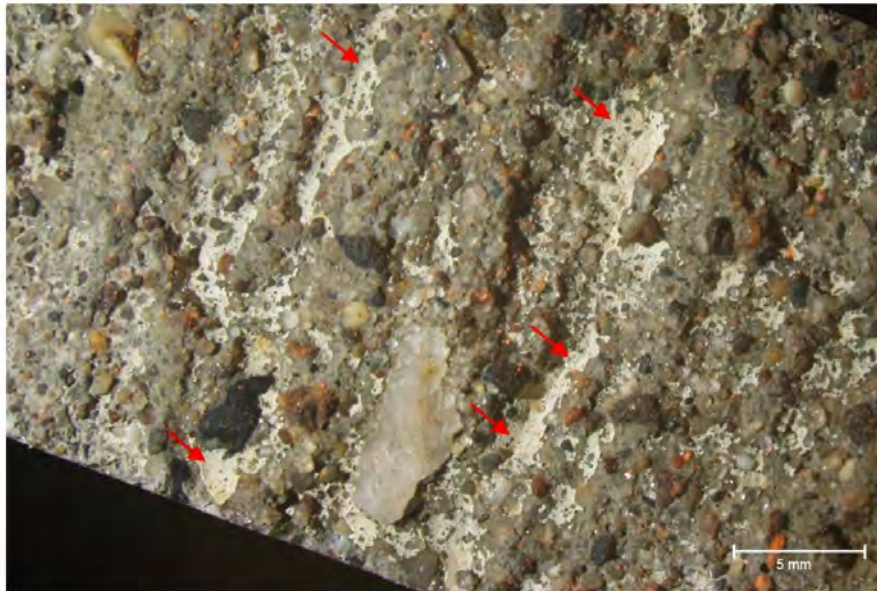
SAMPLE ID: 521 424W   **DESCRIPTION:**   A magnified view of the top surface. Note the remnant flakes of curing compound (red
MAG: 5x   arrows) within the topographic lows of the top surface.

AET PROJECT NO: P-0002628   **DATE:** MAY 21, 2021
PROJECT: PERFORMANCE OF EARLY LOADED CONCRETE SECTIONS AFTER 4 YEARS
STATE PROJECT NO. (SP): 8821-331, TRUNK HIGHWAY NUMBER (TH): 999

PHOTO: 23

SAMPLE ID: 521 524B   **DESCRIPTION:**   A magnified view of the top surface. Note the exposed coarse and fine aggregate
MAG: 5x   particles.

PHOTO: 24

SAMPLE ID: 521 524W   **DESCRIPTION:**   A magnified view of the top surface. Note the exposed coarse and fine aggregate
MAG: 5x   particles and residual curing compound within the topographic lows of the top surface.
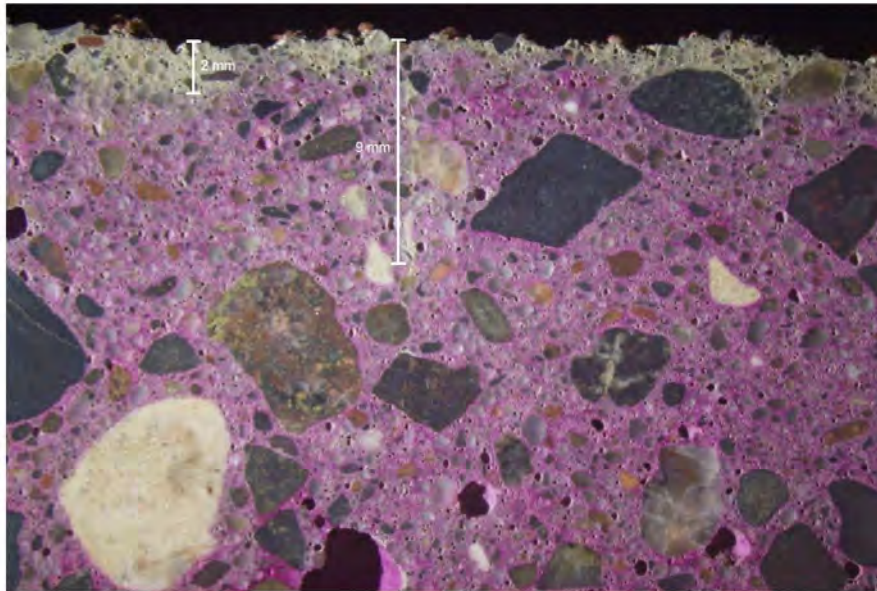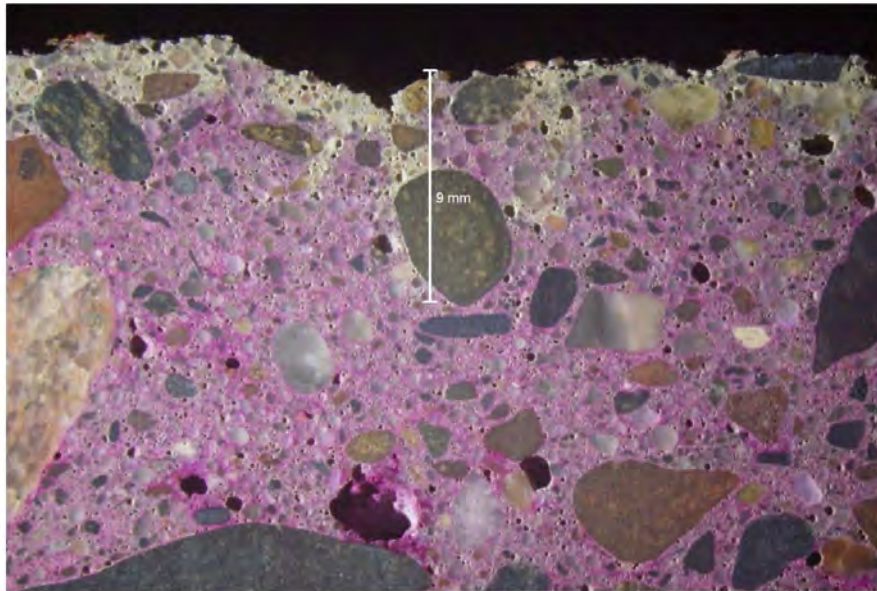
PHOTO: 25

6 mm
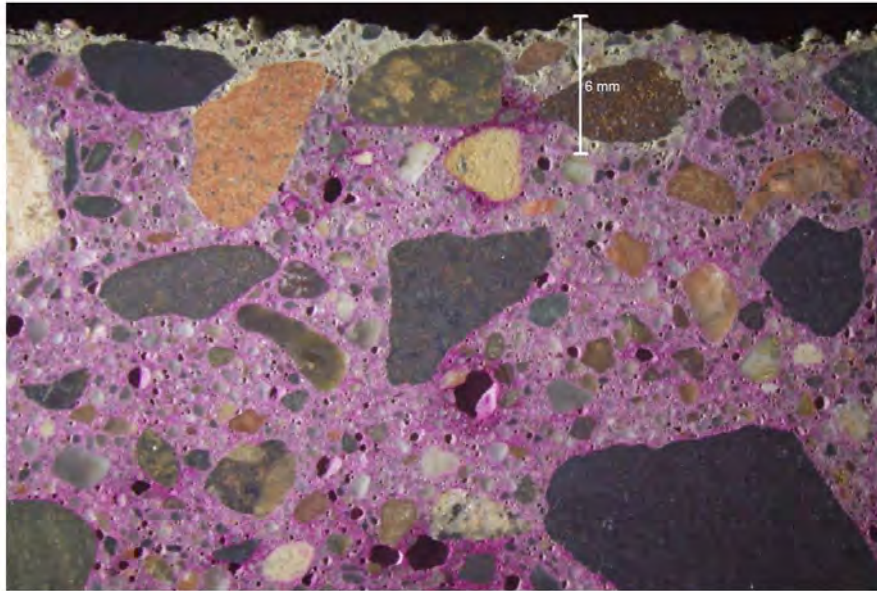
| **SAMPLE ID:** | 521 124B | **DESCRIPTION:** | Carbonation (unstained paste) ranged from negligible to 6 mm (1/4") depth from the top surface along a sub-vertical microcrack and along paste/aggregate boundary on a freshly saw-cut and lapped cross section of concrete treated with phenolphthalein pH indicator. |
| **MAG:** | 5x | | |

PHOTO: 26

6 mm
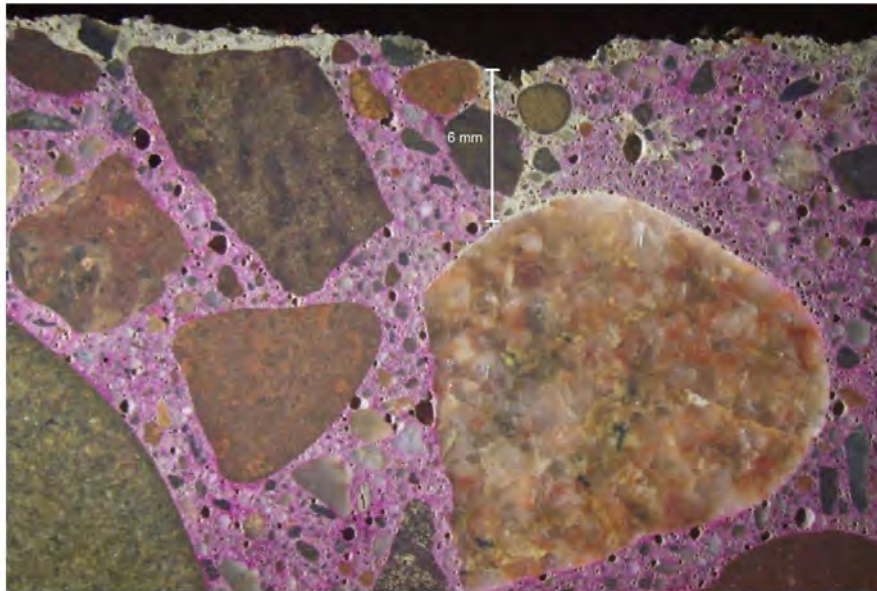
| **SAMPLE ID:** | 521 124W | **DESCRIPTION:** | Carbonation (unstained paste) spiked to 6 mm (1/4") depth from the top surface along a sub-vertical microcrack on a freshly saw-cut and lapped cross section of concrete treated with phenolphthalein pH indicator. |
| **MAG:** | 5x | | |

PHOTO: 27
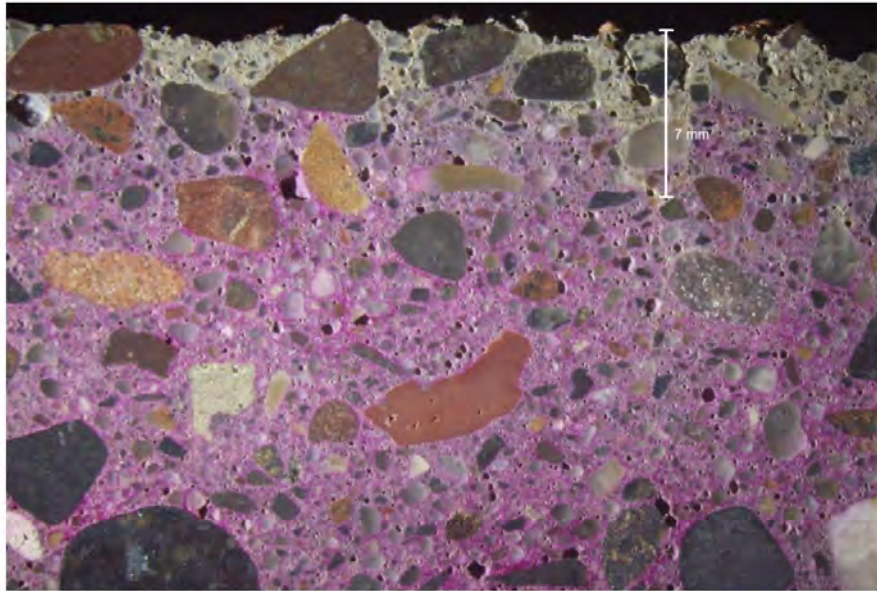
SAMPLE ID: 521 424B   **DESCRIPTION:** Carbonation (unstained paste) ranged from negligible to 7 mm (1/4") depth from the top
MAG: 5x   surface along a sub-vertical microcrack on a freshly saw-cut and lapped cross section of concrete treated with phenolphthalein pH indicator.

PHOTO: 28

SAMPLE ID: 521 424W   **DESCRIPTION:** Carbonation (unstained paste) ranged from negligible to 2 mm (1/16") depth from the
MAG: 5x   top surface. Intermittent carbonation proceeded to 9 mm (3/8") depth along a sub-vertical microcrack on a freshly saw-cut and lapped cross section of concrete treated with phenolphthalein pH indicator.

PHOTO: 29

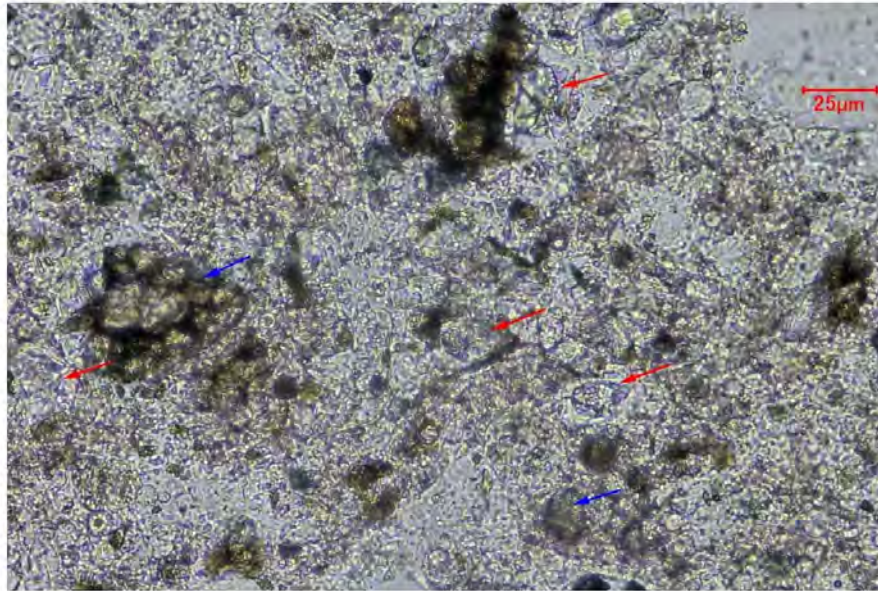| SAMPLE ID: | 521 524B | DESCRIPTION: | Carbonation (unstained paste) ranged from negligible to 7 mm (1/4") depth from the top surface along a sub-vertical microcrack on a freshly saw-cut and lapped cross section of concrete treated with phenolphthalein pH indicator. |
| MAG: | 5x | | |

PHOTO: 30

| SAMPLE ID: | 521 524W | DESCRIPTION: | Carbonation (unstained paste) ranged from negligible to 9 mm (3/8") depth from the top surface along a sub-vertical microcrack on a freshly saw-cut and lapped cross section of concrete treated with phenolphthalein pH indicator. |
| MAG: | 5x | | |

AET PROJECT NO: P-0002628   **DATE:**   MAY 21, 2021

PROJECT: PERFORMANCE OF EARLY LOADED CONCRETE SECTIONS AFTER 4 YEARS
STATE PROJECT NO. (SP): 8821-331, TRUNK HIGHWAY NUMBER (TH): 999

PHOTO: 31

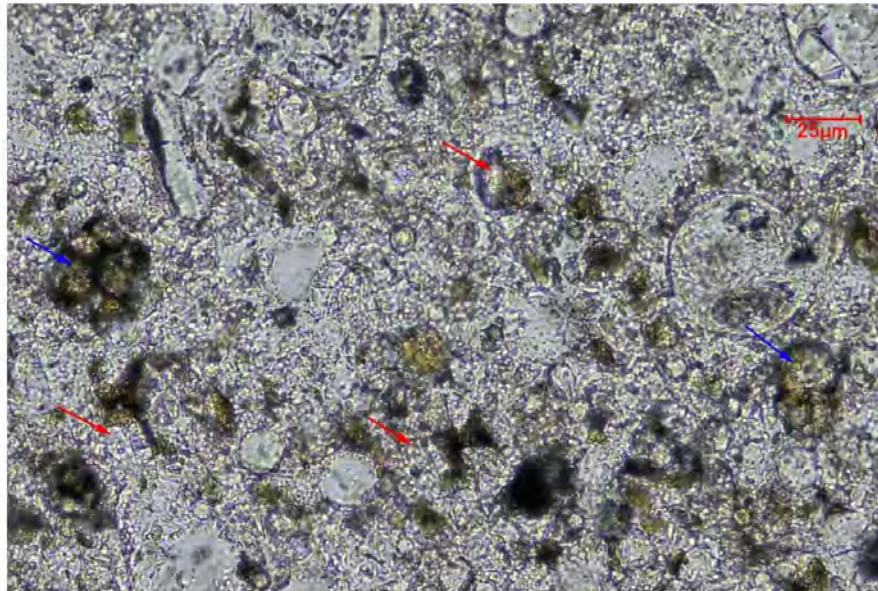**SAMPLE ID:**   521 124B   **DESCRIPTION:**   Moderate to fully hydrated alite portland cement particles/relics (red arrows) and
MAG: 400x   negligible to low hydration of residual belite portland cement particles (blue arrows) in thin section of concrete
viewed with transmitted plane polarized light. Note spherical fly ash pozzolan particles.

PHOTO: 32

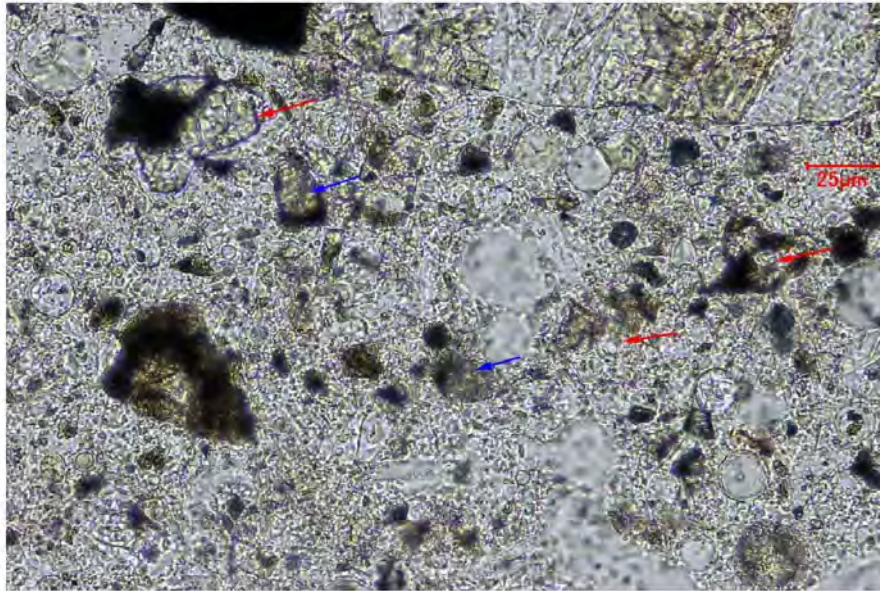**SAMPLE ID:**   521 124W   **DESCRIPTION:**   Moderate to fully hydrated alite portland cement particles/relics (red arrows) and
MAG: 400x   negligible to low hydration of residual multiple belite portland cement particles (blue arrows) in thin section
of concrete viewed with transmitted plane polarized light. Note spherical fly ash pozzolan particles.

AET PROJECT NO: P-0002628   **DATE:**   MAY 21, 2021
PROJECT: PERFORMANCE OF EARLY LOADED CONCRETE SECTIONS AFTER 4 YEARS
                                       STATE PROJECT NO. (SP): 8821-331, TRUNK HIGHWAY NUMBER (TH): 999
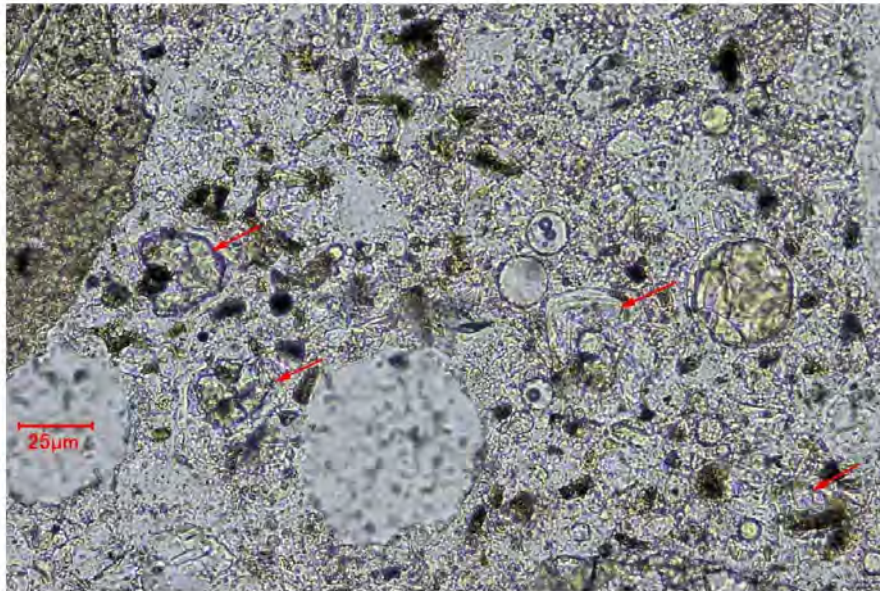
PHOTO: 33

SAMPLE ID: 521 424B   **DESCRIPTION:**   Moderate to fully hydrated alite portland cement particles/relics (red arrows) and
MAG: 400x   negligible to low hydration of residual belite portland cement particles (blue arrows) in thin section of concrete viewed with transmitted plane polarized light. Note spherical fly ash pozzolan particles.

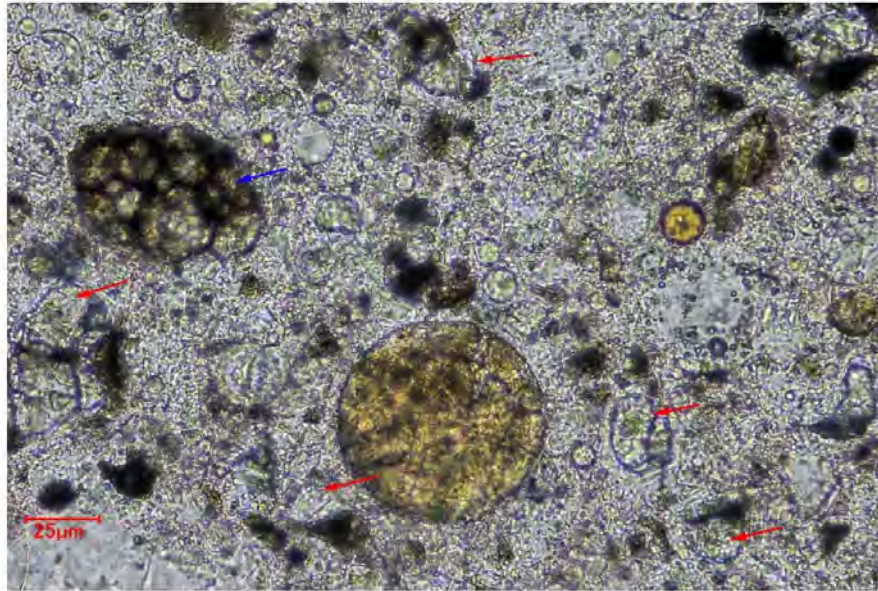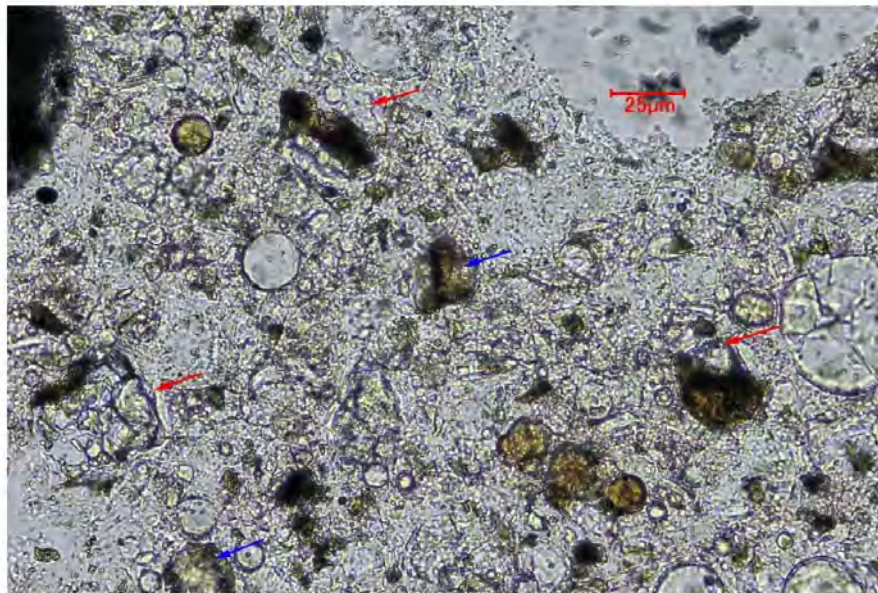**PHOTO: 34**

SAMPLE ID: 521 424W   **DESCRIPTION:**   Moderate to fully hydrated alite portland cement particles/relics (red arrows) in thin
MAG: 400x   section of concrete viewed with transmitted plane polarized light. Note spherical fly ash pozzolan particles.

PHOTO: 35

| SAMPLE ID: | 521 524B | **DESCRIPTION:**   Moderate to fully hydrated alite portland cement particles/relics (red arrows) and |
| MAG: | 400x | negligible hydration of residual multiple belite portland cement particles (blue arrow) in thin section of concrete viewed with transmitted plane polarized light. Note spherical fly ash pozzolan particles. |

PHOTO: 36

| SAMPLE ID: | 521 524W | **DESCRIPTION:**   Moderate to fully hydrated alite portland cement particles/relics (red arrows) and |
| MAG: | 400x | negligible to low hydration of residual belite portland cement particles (blue arrows) in thin section of concrete viewed with transmitted plane polarized light. Note spherical fly ash pozzolan particles. |

Figure H1: Concrete analysis from American Engineering Testing Inc.